Using glaciers to identify, monitor and predict volcanic activity

M D Martin

PhD 2023

Using glaciers to identify, monitor and predict volcanic activity

Michael Dieter Martin

A thesis submitted in partial fulfilment of the requirements of Manchester Metropolitan University for the degree of Doctor of Philosophy

Department of Natural Sciences

Manchester Metropolitan University

2023

Abstract

Globally, ~250 Holocene active volcanoes are either glacier-clad or have glaciers in close proximity. The presence of glaciers on a volcano sometimes masks evidence of volcanic activity and therefore makes direct observations of volcanic activity more challenging if compared to an 'ice-free' volcano. However, it is also possible that glaciers can provide indirect information about the activity of the volcanoes on which they sit. With this in mind, the overall aim of this thesis is to assess the degree to which volcanically triggered impacts on glaciers can be observed from optical satellite imagery, and to consider whether these impacts can be used to help identify, monitor and predict volcanic activity. To achieve this, volcanically triggered changes in glacier surface morphology and glacier surface velocity are studied on ice-clad volcanoes using optical satellite images. Approximately 1400 optical satellite images are investigated from key, well-documented eruptions from 1972 to 2015 (i.e., during the satellite remote sensing era) and around the globe. To investigate volcanically triggered changes in surface velocity, glacier velocimetry is performed on Cone Glacier (Mount Veniaminof, Alaska) using 99 Sentinel-2 band 8 images (near-infrared, central wavelength: 842 nm) covering two volcanically active periods, one from September to December 2018 and one in March/April 2021. This approach includes the extraction of velocities along a profile line (following an inferred ice flowline), the generation of time-series velocities, and the calculation of velocity difference maps. The extensive analysis of optical satellite images around the globe shows that the most common observable volcanic impact on glacier morphology (for both thick and thin ice-masses) is ice cauldron and opening formation, often (but not exclusively) associated with concentric crevassing. Other observable volcanic impacts on glacier morphology include ice bulging and fracturing due to subglacial dome growth, localized crevassing due to supraglacial lava flows and widespread glacier crevassing, presumably, due to meltwater-triggered glacier acceleration and advance. Glacier velocimetry results from Cone Glacier show faster glacier surface velocities ~10 months prior to the 2018 volcanically active period and ~2 months prior to the 2021 volcanically active period. Also, an amplified seasonal cycle of faster-than-usual surface velocities in the summer and slower-than-usual surface velocities in the winter is observed during both years with an eruption.

Volcanically triggered meltwater is considered as a cause of changing the subglacial drainage at Cone Glacier and is therefore argued as a potential cause of the observed surface velocity changes. The wider applicability of the results to other temperate and polythermal glaciers affected by volcanic activity is discussed. In all, this thesis works towards a deeper understanding of volcanic impacts on glacier morphology and dynamics, elaborates main limitations of using optical satellite images to study ice-clad volcanoes and provides advice for best practice for monitoring glaciers in volcanically active areas.

Acknowledgements

This work was funded through a Leverhulme Trust Research Project Grant (Grant ID: RPG-2019-093).

First, I would like to express my sincere gratitude to my principal supervisor Dr Iestyn Barr (Manchester Metropolitan University) for his great support in developing the project and in conducting this research. Major parts of the research presented in this PhD thesis were conducted during the Covid-19 pandemic with only very limited access to university buildings and PhD colleagues. Without Iestyn's permanent availability especially during these isolating times and his exceptional help to overcome the worries of a PhD student, this project would have not been possible.

Next, I would like to state my deepest gratitude to the other members of the supervisory team Prof Matteo Spagnolo (University of Aberdeen), Prof Benjamin Edwards (Dickinson College, Pennsylvania) and Dr Elias Symeonakis (Manchester Metropolitan University) for their permanent advice and support throughout the project. Fruitful discussions with all members of the supervisory team tremendously expanded my horizon in this highly interdisciplinary research field and being part of such a scientifically diverse project team enabled me to both grow professionally and personally.

I would like to express special thanks to Maximilian van Wyk de Vries, who developed the feature tracking software 'Glacier Image Velocimetry (GIV)' used to obtain the feature tracking tracking results presented in Chapter 6. His patient explanations of various concerns related to the use of the software and his help with the following interpretation of feature tracking results on Mount Veniaminof made a real difference.

Also, I would like to thank the numerous people that I met during the 3¼ years of the project on various occasions and who heavily inspired my work. At this point, I also would like to express my appreciation for the invaluable inputs provided by the two anonymous reviewers of the publication associated with this thesis.

I would like to express my deepest gratitude to my girlfriend Linda for her continuous encouragement especially during the process of thesis writing and for patiently listening to me talking about glaciers and volcanoes. Above all, I would like to thank my parents. Without their continuous support I would not have been able to pursue this research journey.

List of contents

Chapter 1 Introduction 1

1.1. Scientific background and rationale for this thesis 1

1.2. Project aim 3

1.3. Objectives 3

1.4. Outline of thesis 4

Chapter 2 Glaciers and volcanoes 7

2.1. Glaciers 7

2.1.1. Glacier dynamics 8

2.1.2. Glacier hydrology 10

2.2. Volcanoes 12

2.2.1. Volcanology 12

2.2.2. Volcanoes and climate 14

2.2.3. Types of volcanoes/Volcanic landforms 15

Chapter 3 Glaciovolcanism 18

3.1. Glacier-volcano interactions 19

3.1.1. Ice surface subsidence (cauldron formation) and concentric crevassing 21

3.1.2. Opening formation 24

3.1.3. Glacier acceleration and advance/Glacier slow-down 25

3.1.4. Glacier area changes/glacier destruction 28

3.1.5. Glacier surface abrasion/Channel formation 30

3.1.6. Glacier crevassing 31

Chapter 4 Methodological framework 33

4.1. Optical satellite remote sensing 33

4.1.1. The basics of passive remote sensing 35

4.1.2. The remote sensing process 36

4.1.3. Multispectral remote sensing 38

4.1.4. Spatial/temporal and radiometric resolution 40

4.1.5. Satellite data archives 41

4.1.6. Image enhancement 44

4.2. Feature tracking 44

4.2.1. Feature tracking in glaciology (Glacier Velocimetry) 45

4.2.2. The GDM-OPT ICE service by CNRS EOST 47

4.2.3. 'Glacier Image Velocimetry' (GIV) software 49

Chapter 5 Assessment of the use of optical satellite images to detect volcanic impacts on glacier surface morphology – (published) 53
5.1. Introduction 53
5.2. Methods 54
5.2.1. Glacierized volcanoes investigated in this thesis 54
5.2.2. Satellite image download/viewing 55
5.3. Results 58
5.3.1. Ice cauldron formation 58
5.3.2. Opening formation 60
5.3.3. Glacier crevassing 62
5.4. Discussion 68
5.4.1. Observable impacts on glaciers 68
5.4.2. Key challenges 70
5.4.3. Guidelines for best practice 73
5.5. Conclusions 75
Author contributions to this chapter 77
Chapter 6 Detection of volcanically triggered changes in surface velocity of a temperate glacier using Sentinel-2 data – a case study on Mount Veniaminof 78
6.1. Introduction 78
6.2. Background 79
6.2.1. Search of suitable glaciers/The choice of Cone Glacier 79
6.2.2. Climate and glaciers in the Aleutian arc 80
6.2.3. Geology and Glaciology of Mount Veniaminof 82
6.2.4. The 2018 and 2021 volcanically active periods 83
6.3. Methods 85
6.3.1. Glacier image velocimetry on Cone Glacier 85
6.3.2. Velocity data analysis 87
6.4. Results 89
6.4.1. Mean flow velocity and flow direction of Cone Glacier 89
6.4.2. Validation with velocity dataset of Millan et al. 2022 90
6.4.3. Velocities along profile line 92
6.4.4. Time-series analysis 94
6.4.5. Velocity difference maps 97
6.5. Discussion 102
6.5.1. Summary of key findings 102
6.5.2. Data quality and comparison to velocity dataset of Millan et al. (2022) 103

6.5.3. Ice melting and volcanic forcing at Mount Veniaminof 104
6.5.4. Implications for subglacial hydrology of Cone Glacier 106
6.5.5. Possible limitations connected to a generalisation of the results of this case study 109
6.6. Conclusions 110
Chapter 7 General conclusions and future research directions 112
7.1. Summary of key chapter results 112
7.2. Future research directions 114
7.2.1. Automated crevasse detection 114
7.2.2. Comparison of our glacier surface velocity data to other glaciers affected by volcanic activity around the globe 115
7.2.3. Subglacial heat flux and subglacial drainage networks 116
7.2.4. Satellite data infrastructure and glacier surface velocity monitoring for volcano observatories 117
7.2.5. Final remarks 119
Data availability statement 120
References 121
Appendix 1 135
Appendix 2 (Publication) 171

List of figures

Fig. 1.1 Glacierized volcanoes around the globe 4
Fig. 2.1 Distribution of glaciers on Earth 7
Fig. 2.2 Crevasse types on a valley glacier 9
Fig. 2.3 Hydrologic system of a temperate glacier 11
Fig. 2.4 Conceptual model of cavities/orifices at the glacier bed 12
Fig. 2.5 Plate boundaries and positions of Holocene active volcanoes 14
Fig. 2.6 Main types of plate boundaries on Earth 14
Fig. 2.7 Common volcanic landforms on Earth 17
Fig. 3.1 Glacierized volcanoes on Earth 19
Fig. 3.2 Illustrations of volcanic impacts on glaciers 20
Fig. 3.3 Glaciovolcanic eruption types (cauldron formation) 22
Fig. 3.4 Ice cauldron (depression formation) on Gjálp (Iceland) 23
Fig. 3.5 Crevassing of glacier ice related to cauldron formation on Gjálp (Iceland) 23
Fig. 3.6 Glacier advance on Vólcan Michinmahuida (Chile) 27

Fig. 3.7 Glacier surface velocity on Glacier Amarillo (Vólcan Michinmahuida) 28
Fig. 3.8 Glacier destruction on Mount St Helens (1980 eruption) 29
Fig. 3.9 Glacier surface scouring by pyroclastic flows (Nevado del Ruiz) 30
Fig. 4.1 Number of near-polar orbiting, land imaging civilian satellites 35
Fig. 4.2 The electromagnetic spectrum 36
Fig. 4.3 Pathways of electromagnetic radiation through the atmosphere 37
Fig. 4.4 Atmospheric transmission of electromagnetic radiation 37
Fig. 4.5 Whisk-broom design of the MSS instrument 39
Fig. 4.6 GIV software main window 50
Fig. 4.7 The feature tracking principle (I) 51
Fig. 4.8 The feature tracking principle (II). 51
Fig. 5.1 Glacierized volcanoes around the globe 54
Fig. 5.2 Ice cauldrons on Katla (Iceland) 59
Fig. 5.3 Ice openings on Vatnajökull (Iceland) 59
Fig. 5.4 Ice openings on Eyjafjallajökull (Iceland). 61
Fig. 5.5 Concentric crevassing on Mount Redoubt (Alaska) 63
Fig. 5.6 Concentric crevassing on Mount Hudson (Chile) 64
Fig. 5.7 Subglacial dome growth on Mount St. Helens (USA) 65
Fig. 5.8 Glacier crevassing on Montagu Island (South Sandwich Islands) 67
Fig. 5.9 Ice cauldron formation on Mount Veniaminof (Alaska) 68
Fig. 6.1 Mount Veniaminof overview image 79
Fig. 6.2 Mount Veniaminof region air temperature curve 81
Fig. 6.3 Cone Glacier terminus position 82
Fig. 6.4 Volcanically active periods on Mount Veniaminof 84
Fig. 6.5 MIROVA data Mount Veniaminof 85
Fig. 6.6 Time difference for successive Sentinel-2 images downloaded.. 86
Fig. 6.7 Region of interest and stable area on Cone Glacier 86
Fig. 6.8 Glacier surface velocity and flow direction of Cone Glacier 89
Fig. 6.9 Percentage error variability of glacier surface velocity. 90
Fig. 6.10 Surface velocity on Cone Glacier by Millan et al. (2022). 91
Fig. 6.11 Velocity difference of our velocities to Millan et al. (2022). 91
Fig. 6.12 Histogram of velocity differences. 92
Fig. 6.13 Profile line on Cone Glacier 93
Fig. 6.14 Velocities along the profile line 94
Fig. 6.15 Time-series velocities, air temperature and precipitation 96

Fig. 6.16 Correlation of time-series velocities and air temperature/precipitation. 96
Fig. 6.17 Velocity changes of volcanically active year 2018.....99
Fig. 6.18 Velocity change of volcanically active year 2021 102

List of figures (Appendix 1)

Figure 1 Velocities along the profile line (all months) 138
Figure 2 Time-series velocities and air temperature (all points) 141
Figure 3 Time-series velocities and precipitation (all points) 144
Figure 4 Velocity changes of volcanically active year 2018 to respective months in reference year 2019 and year 2020 (all months) 147
Figure 5 Velocity changes of volcanically active year 2021 to respective months in reference year 2020 (all months) 155

List of tables (main text and Appendix 1)

Table 1 Ice-clad volcanoes investigated 55
Table 2 Specification of satellites.....57
Table 3: Sentinel-2 images used for feature tracking on Cone Glacier 135
Table 4: Changes from default parameter settings in GIV.....137
Table 5 Glacier-clad volcanoes investigated in this thesis.....156
Table 6 Details on (freely available) satellite remote sensing datasets used.....162
Table 7 Details on commercial images used.....170

Chapter 1 Introduction

This Chapter presents a short introduction to the topic of this thesis and specifies the project aims and objectives. Chapters 2 and 3 (both Literature Review Chapters) develop the scientific background in greater detail. The results of the work of Barr et al. (2018a), who published a literature review of volcanic impacts on glaciers since 1800 AD, feature in Chapter 3 and serve as a precursor and important context for this PhD project. Besides these introductory Chapters, this thesis is otherwise based on optical satellite remote sensing and is concerned with volcanically triggered changes to glacier surface morphology and glacier dynamics (with a special focus on changes in surface velocity). The approach introduced here is new, unique and of low cost, since it is mostly (but not exclusively) based on freely available satellite data. The work presented includes an extensive search of satellite image archives for volcanic impacts on glacier surface morphology. This features in Chapter 5 and was published in 'Remote Sensing' as Martin et al. (2021), see Appendix 2. This thesis also presents glacier-velocimetry work on Mount Veniaminof (Alaska) covering two volcanically active periods in 2018 and 2021. This latter work is also structured in an academic journal article format and features in Chapter 6.

1.1. Scientific background and rationale for this thesis

Many (~250 of ~1400) Holocene volcanoes on Earth are glacier-clad or have glaciers in close proximity (Siebert et al., 2015; Edwards et al., 2020; Global Volcanism Program and Venzke, 2022). Therefore, interactions between volcanic activity and ice are common (e.g., Pierson et al., 1990; Gudmundsson et al., 1997; Magnússon et al., 2012; Bleick et al., 2013; Oddsson et al., 2016). Volcanic activity can impact glacier ice in various ways, e.g., by direct magma-ice contact due to the placement of sub- and supraglacial lava flows (Gudmundsson et al., 2004; Oddsson et al., 2016) and/or growth of a subglacial volcanic dome (Walder et al., 2007, 2008), alongside other factors. However, glacier ice on or in the proximity of volcanoes can also be affected by volcanic activity without direct contact to volcanically erupted material, e.g., due to enhanced geothermal heating (Guðmundsson et al., 2007; Barr et al., 2018a).

There are a variety of possible consequences for a glacier being affected by volcanic activity, with most related to ice melt (Gudmundsson et al., 2004; Barr et al., 2018a), which can result in major changes in glacier surface morphology, such as the formation of ice-cauldrons (see sub-section 3.1.1) and/or glacier crevassing (sub-section 3.1.6). Many, if not all of the changes to the glacier surface morphology have the potential to indicate past, ongoing and future periods of volcanic unrest (Bleick et al., 2013; Barr et al., 2018a). Also, an increased volume of meltwater at the glacier bed can result in increased basal lubrication, which can lead to glacier acceleration/advance (see sub-section 3.1.3). Some research even shows evidence of a pre-eruption glacier acceleration (e.g., Rivera et al., 2012). In contrast, the work of Magnússon et al. (2010) shows a long-lasting (i.e. several years) slow-down of glacier velocity related to efficient drainage and low subglacial water pressure (see sub-section 3.1.3).

Research on volcano-glacier interactions in general is relevant to society, since some of the aforementioned processes can have substantial impacts on human activities and can even lead to a loss of human lives. For example, the rather small-scale and initially subglacial eruption of Eyjafjallajökull in 2010 produced large quantities of fine-grained ash, which disrupted air-traffic in large parts of Europe for several weeks and led to substantial financial losses in the order of 1.3 billion euros (Gudmundsson et al., 2012; Sigurdsson, 2015; Smellie and Edwards, 2016). In 1985, the interaction between snow/ice and pyroclastic flows triggered catastrophic lahars on Nevado del Ruiz, which resulted in the death of ~23,000 people (Naranjo et al., 1986; Pierson et al., 1990). Satellite remote sensing techniques provide a means to investigate these often inaccessible and remote glacier-clad volcanoes from a safe distance and have already played an important role in research on glacier-clad volcanoes. Many different sensor types have been used such as optical (Williams, 1987; Patrick et al., 2005; Martinis, 2007; Rivera et al., 2012; Bleick et al., 2013; Patrick and Smellie, 2013; Muraviev and Muraviev, 2016), thermal (Dehn et al., 2002; Delgado et al., 2014; Lacava et al., 2014; Plank et al., 2018) and SAR-based systems (incl. InSAR) (Alsdorf and Smith, 1999; Björnsson et al., 2001; Scharrer et al., 2008; Delgado et al., 2014; Rossi et al., 2016). Despite the increasing number of studies using satellites to investigate glaciovolcanic processes, observations of glacier-clad volcanoes are often limited to specific places or study areas.

In the recent years, Earth observation satellites carrying optical sensors have seen a continuing increase in spatial and temporal resolution (Belward and Skøien, 2015) and are nowadays often available free of charge. Optical satellite images have also commonly been used to obtain glacier surface velocities and record glacier extents (e.g., Kääb et al., 2002; Paul et al., 2007, 2016; Gjermundsen et al., 2011; Herman et al., 2011; Mouginot and Rignot, 2015; Wilson et al., 2016; Dell et al., 2019; Millan et al., 2019; Van Wyk de Vries and Wickert, 2020), with some studies focusing on ice-clad volcanoes (e.g., Martinis, 2007; Rivera et al., 2012; Muraviev and Muraviev, 2016; Reinthaler et al., 2019). However, there is a lack of a systematic investigation of fluctuations in glacier velocity and terminus position before and during volcanically active periods. Given the considerations above, this thesis aims to make use of the potential of optical satellite images for a systematic study of volcanically impacted morphological changes of glaciers worldwide. Also, this thesis investigates glacier velocities and glacier terminus fluctuations on an active volcano.

1.2. Project aim

The overall aim of this thesis is to assess the degree to which volcanically triggered impacts on glaciers can be observed from optical satellite imagery, and to consider whether these impacts can be used to help identify, monitor and predict volcanic activity.

1.3. Objectives

To achieve the overall project aim, the specific objectives of this thesis are:

Objective 1: Investigation of volcanically triggered changes in glacier surface morphology for 11 well-known eruptive periods on 10 representative ice-clad volcanoes around the globe (Fig. 1.1). This includes an extensive search for volcanic impacts on glacier morphology in archival (mostly freely available) optical satellite imagery from 1972 to 2015 (i.e., during the satellite remote sensing era).

Objective 2: Investigation of the surface velocity and terminus position of Cone Glacier (Mount Veniaminof, Alaska) based on 99 Sentinel-2 images from May 2016 to January 2022 covering two volcanically active periods, one in September-December 2018 and one in March/April 2021.

Objective 3: (Part A) Based on the findings from Objective 1, identification of key challenges and provision of advice for best practice when using optical satellite images to investigate volcanically triggered changes in glacier morphology on glacier-clad volcanoes around the globe. **(Part B)** From the findings of Objective 2, discussion of the results obtained from the glacier velocity analysis on Cone Glacier linked to the dynamics and hydrology of a temperate glacier impacted by volcanic activity.

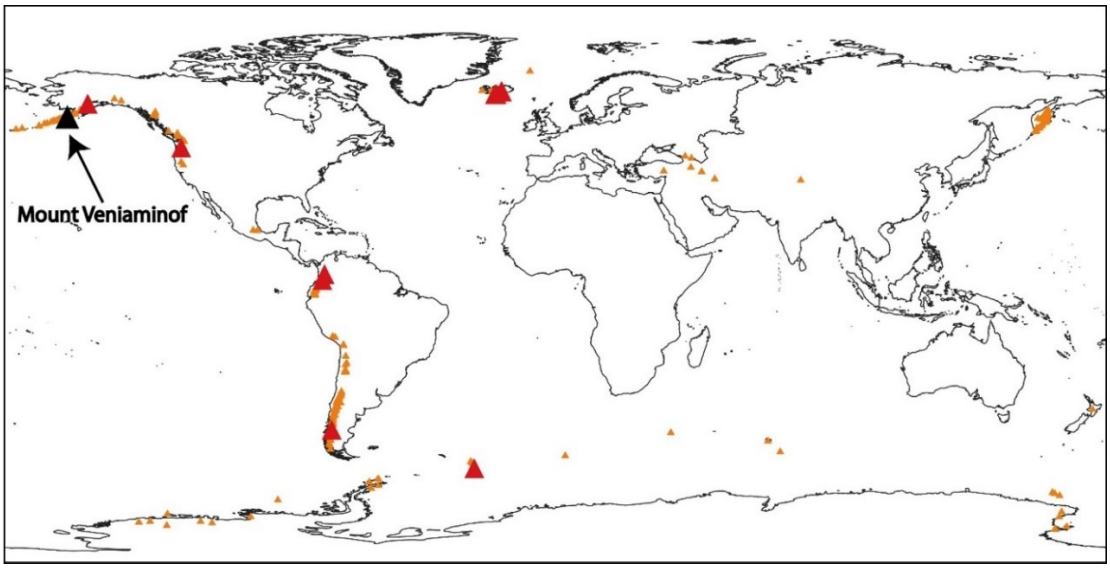

Fig. 1.1 Glacierized volcanoes around the globe (small orange triangles) from Edwards et al. (2020) and volcanoes investigated in this thesis using optical satellite images (red triangles). Glacier velocimetry work was performed on Cone Glacier on Mount Veniaminof (black triangle). Basemap: 'World Continents', accessed on 10/03/2021

1.4. Outline of thesis

Chapters 2 and 3 provide a literature review, and Chapter 4 introduces the methodological framework of this thesis. Given the interdisciplinarity of this thesis, these three Chapters work as an introduction to the topics 'glaciers', 'volcanoes', 'glaciovolcanism' and 'optical satellite remote sensing' separately. Chapters 5 and 6 focus on the thesis results and both are formatted in an academic journal style with introduction, methods, results and conclusions. This thesis ends with a summary of the key chapter results and discusses future research directions in Chapter 7.

In the following, a short outline of the individual Chapters is given:

Chapter 2 presents an introduction to glaciers and volcanoes. Section 2.1 'Glaciers' covers general aspects of glacier dynamics and glacier hydrology. This section has specific emphasis on temperate, polythermal and largely 'warm-based' glaciers and the role of liquid water in the glacial system, since this is crucial to understanding the effects of additional meltwater caused by volcanic activity. Section 2.2 'Volcanoes' works as an introduction to volcanism in general and introduces related volcanic landforms. Also, there is a separate sub-section 2.2.2 'Volcanoes and climate' briefly introducing indirect impacts on glaciers through volcanically triggered climate change (however not the focus of this thesis). The aim of this Chapter is to put the more specific Chapter 3 focusing on 'glaciovolcanism' in a wider context.

Chapter 3 introduces the specific field of research on ice-clad volcanoes (glaciovolcanism). This Chapter is structured according to possible glaciological consequences arising from volcanic activity on ice-clad volcanoes. Some content of the Chapter was published in Martin et al. (2021), see Appendix 2. This Chapter also presents examples from around the globe and therefore contains background information on the glacier-covered volcanoes investigated with optical satellite images in Chapter 5.

Chapter 4 presents an introduction to optical satellite remote sensing and glacier velocimetry based on feature tracking. Section 4.1 provides an overview of the physical basis of optical satellite remote sensing and touches upon multispectral remote sensing and satellite data archives. Section 4.2 introduces the technique of feature tracking as applied in Chapter 6 using the 'Glacier Image Velocimetry' (GIV) software developed by van Wyk de Vries and Wickert (2021).

Chapter 5 addresses Objective 1 and Objective 3 (Part A). This Chapter assesses the usefulness of optical satellite images for detecting volcanic impacts on glacier surface morphology by presenting the results of an extensive search of satellite data archives from ice-clad volcanoes around the globe (Objective 1). Also, key challenges when using optical satellite images to detect volcanically impacted changes on glacier surface morphology are identified and advice for best practice is given (Objective 3 Part A).

The key elements of this Chapter were published in the journal 'Remote Sensing' by Martin et al. (2021), see Appendix 2.

Chapter 6 addresses Objective 2 and Objective 3 (Part B). This Chapter investigates volcanically triggered changes in surface velocity of Cone Glacier (Mount Veniaminof, Alaska) covering two volcanically active periods, one in 2018 and one in 2021 by performing glacier velocimetry using Sentinel-2 satellite images (Objective 2). The generated monthly velocity maps are validated using the global glacier velocity dataset by Millan et al. (2022) (sub-section 6.4.2) and are analysed as monthly velocities along a profile line (sub-section 6.4.3), as time-series velocities (sub-section 6.4.4) and as velocity difference maps (sub-section 6.4.5). This Chapter also presents results of a correlation analysis between air temperature/precipitation data provided by the KNMI Climate Explorer and glacier surface velocities for both the entire time period investigated (i.e., from November 2017 to January 2022) and a time period assumed to be volcanic activity-free (i.e., from April 2019 to December 2020). In the last part, this Chapter discusses implications of our velocity analysis on Cone Glacier for the dynamics and hydrology of a temperate glacier affected by volcanic activity (Objective 3 Part B).

Chapter 7 provides a summary of key chapter results and elaborates future research direction.

Chapter 2 Glaciers and volcanoes

2.1. Glaciers

Approximately 16 million km^2 of Earth is glacierised. Glacier coverage ranges from >50,000 km^2 large ice sheets present in Antarctica and Greenland, ice caps (<50,000 km^2), ice fields, valley and mountain (cirque-type) glaciers (Benn and Evans, 2010). There are a total of ~ 215,000 glaciers on Earth (Fig. 2.1) (RGI, 2017). In simple terms, the existence of glaciers depends on precipitation (snow fall), temperature and topography and glaciers grow where the net (snow and ice) accumulation exceeds ablation (Benn and Evans, 2010). The newly formed snow-pack has to survive at least two consecutive summers to be transformed to perennial ice and glaciers are usually considered as such when they reach an area larger than a football field (10,000 m^2) (Taillant, 2015). Glaciers are complex systems interacting with other components of the Earth's system such as the atmosphere, oceans, rivers and landscape (Benn and Evans, 2010). As such, glaciers have been widely accepted as good indicators of ongoing climate change due to the influence of globally increasing air temperatures on glacier overall global recession (Barry, 2006; Gardner et al., 2013; Zemp et al., 2015; Hock et al., 2019).

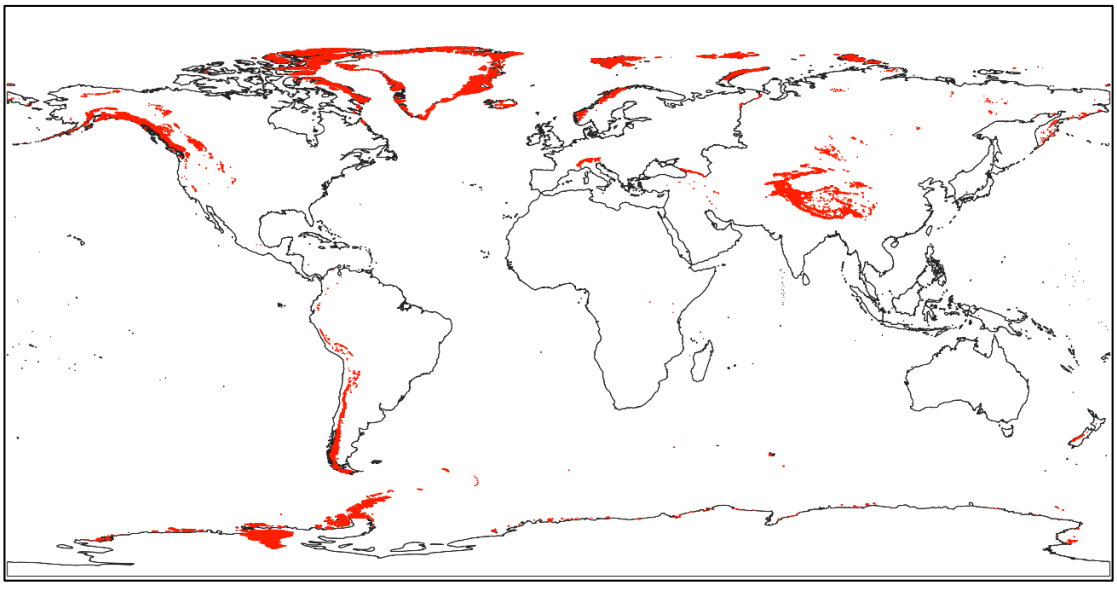

Fig. 2.1 Distribution of glaciers on Earth (glacier outlines, total number ~215000) according to Randolph Glacier Inventory (Version 6.0) (RGI, 2017); Basemap: 'World continents', accessed on 10/03/2021

2.1.1. Glacier dynamics

Glacier ice can technically be seen as a monomineralic metamorphic rock (Colgan et al., 2016) and behaves as a non-compressible, non-linear viscous material. This means, if ice is put under pressure, strain rates increase non-linearly with applied stress (Glen, 1955; Benn and Evans, 2010). Ice deformation works as movement (or gliding) between ice crystals, a mechanism called ice creep, which resembles the behaviour of metals close to their melting point (Benn and Evans, 2010). If forces pulling apart the ice become too large, the ice behaves in a brittle way and crevasses might open up. Crevasses are common on all glaciers, ice sheets and ice shelves and cover a large range of sizes, from millimetre-scale cracks up to 45 m deep crevasses in Antarctica (Benn and Evans, 2010; Colgan et al., 2016). There are a variety of different crevasse types such as transverse crevasses, splaying crevasses, radial crevasses and en-echelon crevasses, dependant on the dominant stress regime. Ice falls are regions of an extensional setting with extremely fast flowing ice. The 'bergschrund' at the head of a valley glacier is assumed to separate cold- from warm-based ice (Fig 2.2) (Benn and Evans, 2010). In general, crevasses are limited in their maximum depth due to the tensile stresses opening them up being outbalanced by increasing compressive stresses at depth (Benn and Evans, 2010). However, hydrofracture in principle is capable of increasing the depth of a crevasse through the entire glacier and finally allowing a crevasse to reach the glacier bed. This was first shown theoretically by Weertman (1973). A special case is the formation of concentric crevasses due to rapid glacier subsidence and local reversal of ice flow towards the subsidence area, which leads to brittle behaviour of the ice (e.g., Gudmundsson et al., 2004; Tuffen, 2007; Barr et al., 2018a). This special type of crevassing is related to volcanic activity and further discussed in sub-section 3.1.1.

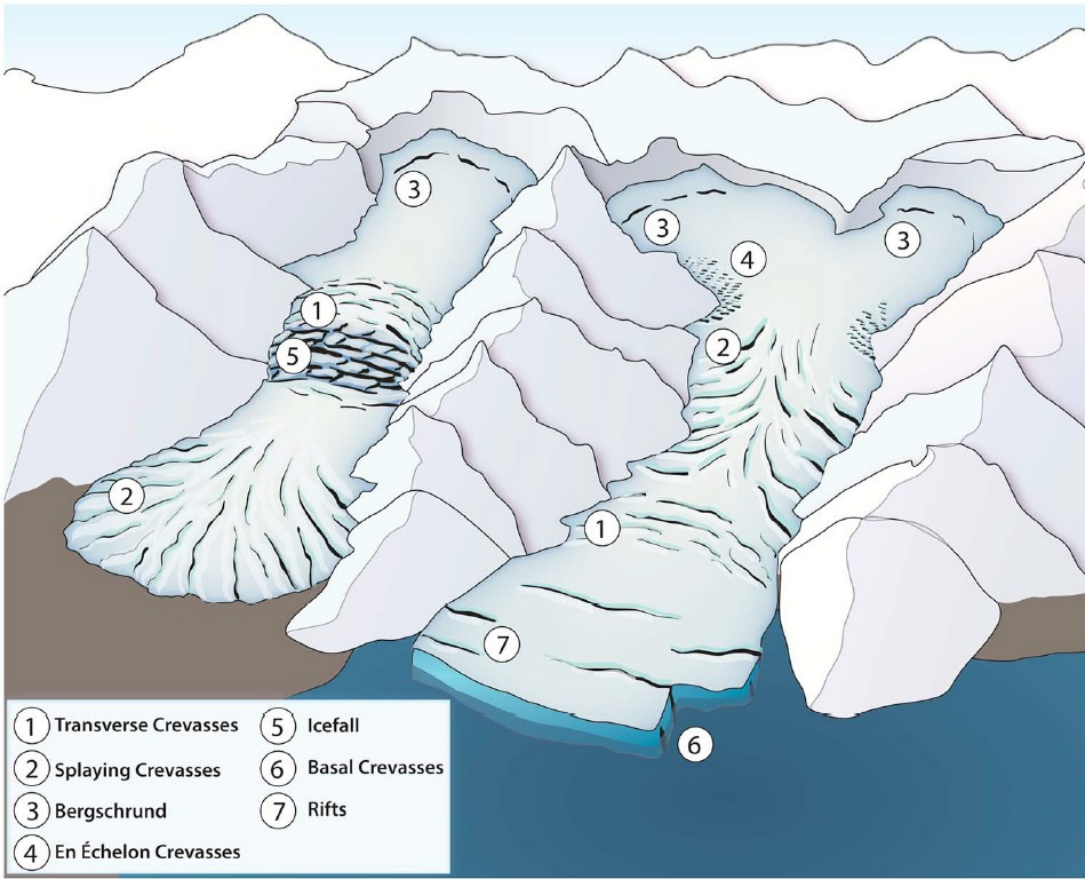

Fig. 2.2 Various types of crevasses present on a valley glacier from Colgan et al. (2016)

Individual glaciers can be divided into an accumulation zone, where annual mass gain exceeds mass losses due to ablation, and an ablation zone, where annual mass losses exceed mass gain (Clarke, 1987). The line on the glacier where annual accumulation equals annual ablation is called equilibrium line altitude (Benn and Evans, 2010). Mass therefore is transferred from the accumulation to the ablation zone resulting in the balance velocity, which, however, commonly differs from measured glacier velocities (Clarke, 1987). Particularly for temperate (warm-based) glaciers, other factors such as regelation melting, basal sliding and the deformation of the glacier bed (dependent on bedrock lithology) also influence observed glacier velocities. In general, the presence of subglacial water has large implications for glacier-bedrock coupling, and glacier motion is affected by a variety of factors such as the amount of water stored at the bed, effective basal water pressure, the efficiency of the drainage network and basal shear stress/basal roughness (Willis, 1995; Fountain and Walder, 1998; Benn and Evans, 2010).

Measured velocities for typical valley glaciers are in the range of several to a few tens of metres per year (e.g., MacGregor et al., 2005), but ice speeds may range up to several kilometres per year as found for the Patagonian icefields (Mouginot and Rignot, 2015).

2.1.2. Glacier hydrology

Cold-based glaciers commonly are present in the High Arctic and Antarctica and commonly have uniform velocities over the year (Waller, 2001; Benn and Evans, 2010). The glaciers presented in this thesis, however, might be mostly both cold- and warm-based (polythermal) glaciers. Warm-based glacier ice is - in contrast to cold-based ice masses - at the pressure melting point (Benn and Evans, 2010). Basal ice temperature therefore has important implications for the availability of meltwater at the glacier bed and affects glacier motion (Benn and Evans, 2010). Glacier speed - for temperate (or warm-based) glaciers - usually is higher in spring and summer than in autumn and winter and is impacted by extended periods of ablation or heavy rainfall (Willis, 1995). At the beginning of the ablation season surface water may access the subglacial drainage system through crevasses or moulins, that have channels linked to them (Fig. 2.3). At that time in the year, a non-arborescent, slow drainage system with channels incised in the bed (Nye channels) and subglacial cavities is present, which is not able to cope with the large amount of meltwater generated at the beginning of the melt season (Hodge, 1974; Walder, 1986; Fountain and Walder, 1998). The resulting high water pressure might lead to increased glacier velocity (Iken and Bindschadler, 1986; MacGregor et al., 2005). A conceptual model of subglacial cavities and related orifices is presented in Fig. 2.4. For example, for Bench Glacier in Alaska, speed-up initiated a few days before peak in water storage and travelled up-glacier from the glacier terminus. Measured surface velocity magnitudes were in the order of 2-4 times the annual mean velocity. Also, an uplift of the glacier of ~8-16 cm related to cavity formation and propagation of the speed-up wave was reported (MacGregor et al., 2005).

In summer, as more water reaches the glacier bed, an arborescent, efficient drainage system with ice-walled conduits (Röthlisberger channels) develops. These transient tunnels are incised into the base of the glacier (in the ice) resulting in low water pressure (Röthlisberger, 1972; Fountain and Walder, 1998).

If water flow is concentrated into a few channels, an increase in water pressure does not necessarily lead to a large increase in velocity (Iken and Bindschadler, 1986). In late fall (autumn), as water discharge decreases, the tunnels are closed by ice creep (Fountain and Walder, 1998). Subglacial water pressure changes in general have to occur over a sufficiently large portion of the glacier bed to enhance basal sliding and therefore affect measured glacier surface velocity (Willis, 1995). To complicate matters more, basal velocities (which are directly affected by the presence of meltwater) do not necessarily have to be transferred to the surface linearly. Balise and Raymond (1985) showed that basal velocity patterns only match surface velocity patterns if the basal velocity anomaly appears over a long spatial scale (~10 times glacier thickness). For smaller scales, transferred surface velocities become attenuated and may even be altered in their spatial patterns (Balise and Raymond, 1985).

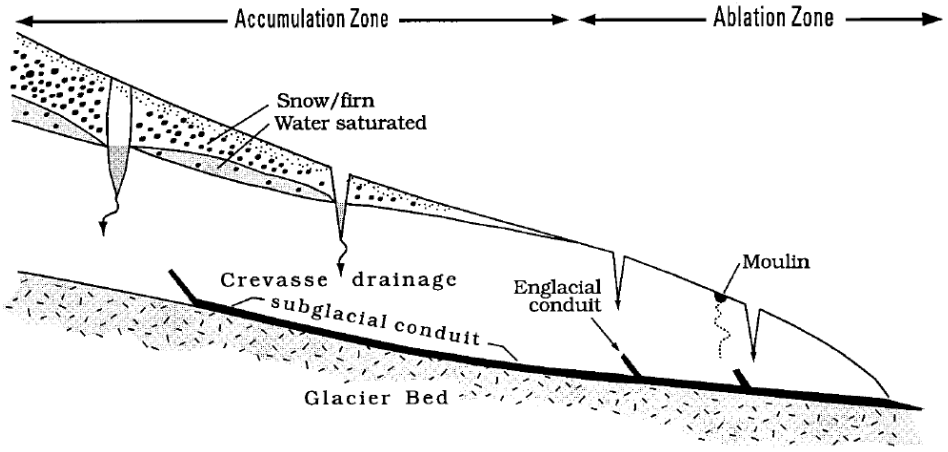

Fig. 2.3 Longitudinal cross section of hydrologic system in a temperate glacier. Water travels along the boundary between impermeable ice and firn in the accumulation zone and flows into crevasses. In the ablation zone, water directly reaches the glacier bed via crevasses/moulins. From Fountain and Walder (1998) based on Figure 10.11. from Röthlisberger and Lang (1987)

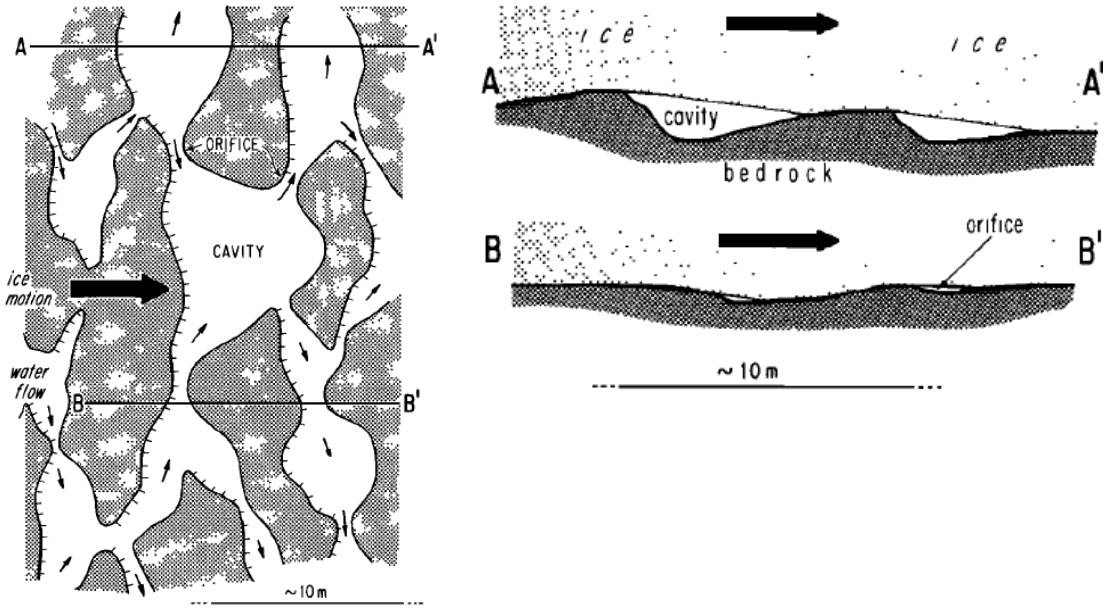

Fig. 2.4 Conceptual model of cavities/orifices at the glacier bed; (left) plan view; (right) vertical cross section; hatched area is where ice is in contact with glacier bed and the large arrow indicates ice motion; subglacial water flow is quasi-perpendicular to ice motion; from Kamb (1987)

2.2. Volcanoes

A 'volcano' is a complex geologic environment and can be described as "surface expression of thermal activity and magmatism in the interior of the planet" (de Silva and Lindsay, 2015). In principle, there are two main types, composite- (or strato-) and shield-volcanoes. A total of ~1400 volcanoes were active during the Holocene (i.e., the last 10,000 years), which are non-randomly distributed on Earth (Fig. 2.5). The exact number, however, remains uncertain and might partly depend on definition. Volcanoes can produce various landforms (see sub-section 2.2.3).

2.2.1. Volcanology

The theory of plate tectonics - developed in the 1960s - forms the basis for explanation of volcano distribution. The tectonic plates represent the broken lithosphere, which comprises the Earth's crust and upper mantle. There are two types of lithosphere, oceanic and continental (Francis and Oppenheimer, 2004; LaFemina, 2015). Magma is generated from the work of moving the plates around on the underlying asthenosphere and rises up buoyantly along the zones of weaknesses due to the density contrast between magma and the mantle material. This is essentially how a volcano is born (LaFemina, 2015; Siebert et al., 2015; Sigurdsson, 2015).

More than 94% of known historical volcanic eruptions can be related to either convergent or divergent plate margins or belong to hot spot locations (Fig. 2.6) (Siebert et al., 2015). Approximately 80% of Earth's volcanism occurs beneath 1-4 km of water along the ~60,000 km long mid-ocean ridges. At a divergent plate boundary, the decrease of overburden pressure leads to passive upwelling of magma and decompression melting (LaFemina, 2015; Siebert et al., 2015; Sigurdsson, 2015). Due to the high water pressure at these depths, primarily pillow lavas are formed and the reaction between magma and water is relatively passive (Sigurdsson, 2015). Besides at mid-ocean ridges, water can interact with magma in a variety of ways ranging from opening up of a vent in a sea or lake, interaction of magma and water in an aquifer, or magma being erupted underneath a glacier (Francis and Oppenheimer, 2004; Edwards et al., 2015). In any case, magma-water interactions in shallow water form violent, phreatic explosions fragmenting the magma. If a larger amount of water comes in contact with magma, highly explosive phreatomagmatic eruptions are the result (Francis and Oppenheimer, 2004; Sigurdsson, 2015).

The complementary process of crust formation at mid-ocean ridges is the recycling of crust material at subduction zones, where the old, dense oceanic crust subducts underneath the less dense continental crust taking with it sediments laden with H_2O bearing minerals (Fig. 2.6) (Grove and Till, 2015; Siebert et al., 2015; Sigurdsson, 2015). Subduction zone volcanism concentrates to a very narrow zone (~100 km) above the subducting slab with the circum-Pacific Ring of Fire forming a prominent system of subduction zone volcanoes (LaFemina, 2015; Siebert et al., 2015; Sigurdsson, 2015). This includes the glacier-covered volcanoes of the Andes, Alaska and Kamchatka.

In addition, there is hot-spot volcanism unrelated to plate boundaries. These mushroom-like structures are thought to originate at the boundary layer between Earth's lower mantle and outer core. They are stationery with respect to the moving plates, thus explaining volcanoes/island chains such as the Hawaiian islands (Siebert et al., 2015; Sigurdsson, 2015). Iceland forms a special case of a mid-ocean ridge being exposed above sea-level, since it involves the interplay between a mid-ocean ridge and a hot-spot (Þor Þorðarson et al., 2014). Transform plate boundaries typically are not related to magmatism/volcanism (LaFemina, 2015).

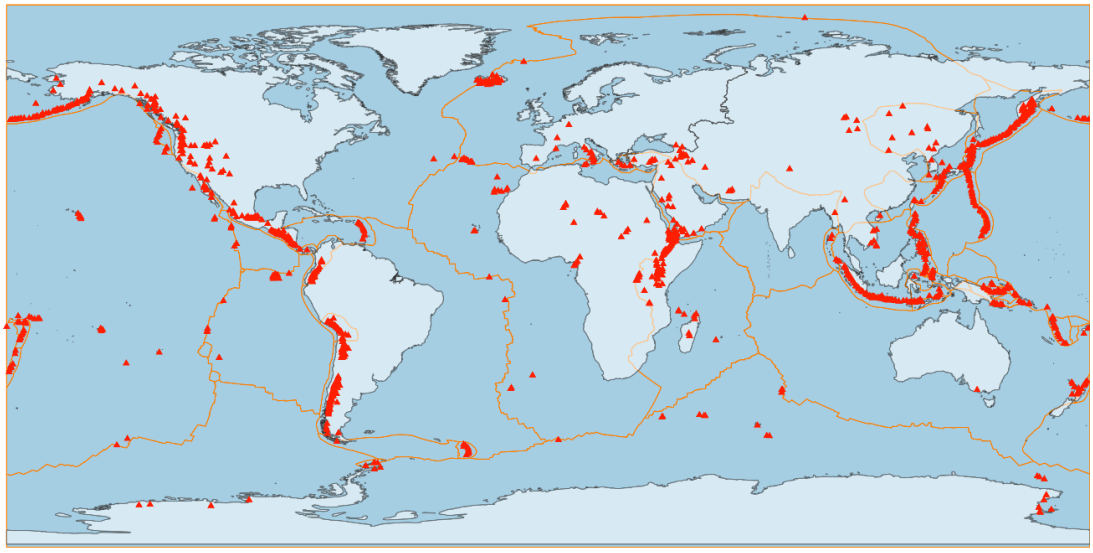

Fig. 2.5 Plate boundaries (orange lines) from Bird (2003) and positions of Holocene active volcanoes (red triangles, total number: 1357) from Smithsonian Institution and Venzke (2013); downloaded 03/12/2021. Basemap: 'World continents', accessed on 10/03/2021

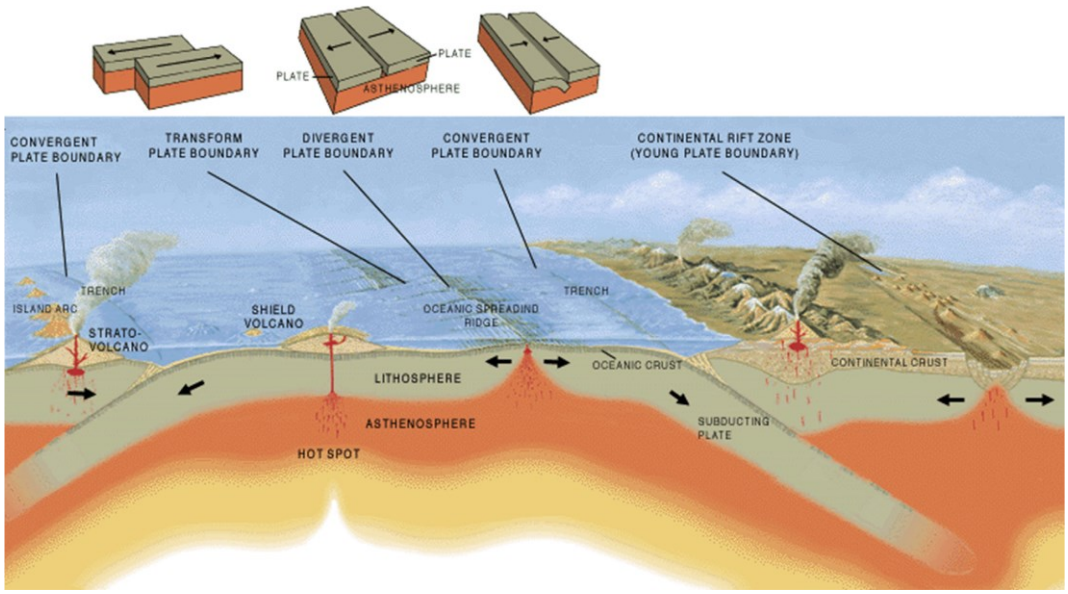

Fig. 2.6 Main types of plate boundaries on Earth and related volcanism. USGS. URL: https://pubs.usgs.gov/gip/dynamic/Vigil.html, accessed on 06/12/2021

2.2.2. Volcanoes and climate

The impact that large volcanic eruptions can have on climate are widely discussed in the literature (e.g., Rampino et al., 1988; Rampino and Self, 1993; Oppenheimer, 2011; Robock, 2015; Sigurdsson, 2015; Cooper et al., 2018). During a volcanic eruption, often large quantities of sulphur dioxide gas are ejected, which – depending on eruption strength – might ultimately reach the stratosphere as sulphuric acid (H_2SO_4) and can circulate around the globe (Oppenheimer, 2011; Robock, 2015; Cooper et al., 2018).

The main impact of sulphuric acid in the stratosphere is backscattering of incoming solar radiation resulting in an overall mild, but statistically significant, decrease in surface temperatures on regional and global scales (commonly <1°C) (Rampino et al., 1988; Robock, 2015; Cooper et al., 2018). During the violent 1991 eruption of Mount Pinatubo, emission of sulfur dioxide gas into the stratosphere resulted in a cloud that travelled around the world within 22 days and resulted in an overall global cooling effect for the two years after the eruption (Oppenheimer, 2011; Robock, 2015; Sigurdsson, 2015). A more extreme example is the 1815 eruption of Tambora, which resulted in a 'year without summer' following the eruption with mean temperatures being ~ 3 °C below average across Europe (Robock, 2015; Sigurdsson, 2015). Sparse measurements after the eruption indicate a substantial drop of the 0°C isotherm and increased snowfall in the Hudson Bay (Rampino and Self, 1993). In the geologic record, the eruption at Toba ~74,000 years BP resulted in surface temperature decreases of ~3-5 °C in the Northern Hemisphere and related possible increased snow fall and ice accumulation in regions sensitive to glaciation (Rampino and Self, 1993). Besides the well-investigated impact of volcanic eruptions on climate, the examples of Tambora (1815) and Toba (~74,000 years BP) show a very likely relationship between large volcanic activity and the growth/shrinkage of glaciers. However, such relationships remain poorly understood since large volcanic eruptions with mass and volatile ejections comparable to those of Tambora and Toba are rare events (see Rampino and Self, 1993). Despite the importance of the discussed (most likely long-term) impacts of volcanically triggered climate change on glaciers, this thesis focuses on more short-term (i.e., within a maximum time period of several years) and direct volcanic impacts on glaciers, also moving the focus from large volcanic activity to smaller events and unrest periods. Several of these direct glaciological consequences of volcanic activity are discussed in Chapter 3.

2.2.3. Types of volcanoes/Volcanic landforms

The appearance of a volcano on the surface is determined by its geologic setting and magma composition. Composite volcanoes typically have a conical shape and are constructed of stacked (layered) lavas and pyroclastic deposits. The magma to produce a composite volcano tends to be SiO_2 rich and andesitic to dacitic in composition to form steep-sided volcanoes (Fig. 2.7A,B) (de Silva and Lindsay, 2015).

Violent explosive eruptions might be followed by the extrusion of a steep-sided lava dome made of viscous, degassed magma (Fig. 2.7E) (Siebert et al., 2015). Composite volcanoes are most typical for subduction zones, but are also present at a divergent plate boundary setting in Iceland (e.g., Askja, Hekla or Torfajökull) (de Silva and Lindsay, 2015) and are the most common volcano type in relation to interaction with glaciers around the world (Edwards et al., 2020). Shield volcanoes are constructed of basaltic, low-viscous lava flows, which give them their typical 'shield' appearance with low-angle slopes. The volcanoes of the Hawaiian and Galapagos Islands are representative for this type (Fig. 2.7D) (de Silva and Lindsay, 2015). In addition, there are maars and calderas representing negative volcano features. A maar is a remnant of a phreatomagmatic explosion, which involves an intensive magma-groundwater interaction (independent of the magma being basaltic or more evolved), resulting in a flat, roughly circular crater in the landscape (Fig. 2.7C) (de Silva and Lindsay, 2015; Zimanowski et al., 2015). After the eruption of large volumes of magma, the crust above the residual magma chamber can collapse to form a caldera. Prominent examples are the Toba caldera (Sumatra, Indonesia) and the Yellowstone caldera (USA) (Branney and Acocella, 2015; de Silva and Lindsay, 2015). In contrast to composite volcanoes, only a fraction of glacier-covered volcanoes are classified as 'shield volcano' or 'caldera' (Edwards et al., 2020).

Another important volcanic landform typical for (palaeo-) glaciovolcanic environments are 'tuyas' and 'tindars'. They typically appear as longer than wide 'table mountains' and are prominent in British Columbia (Canada), Antarctica and Iceland (Fig. 2.7F) (Edwards et al., 2015). Their formation includes both subglacial and subaerial stages of volcanism, which is expressed by successions of pillow lavas, hyaloclastite and tuff-breccia (Edwards et al., 2015; Smellie and Edwards, 2016). Tuyas and tindars are also used to determine the extents and particularly thicknesses of paleo ice sheets and are even thought to be present on Mars, indicating the former occurrence of subglacial volcanism (Edwards et al., 2015; Smellie and Edwards, 2016). Despite their relevance in the field of glaciovolcanism, this thesis is concerned about more recent (i.e., within the past 40 years) interactions between volcanoes and glaciers.

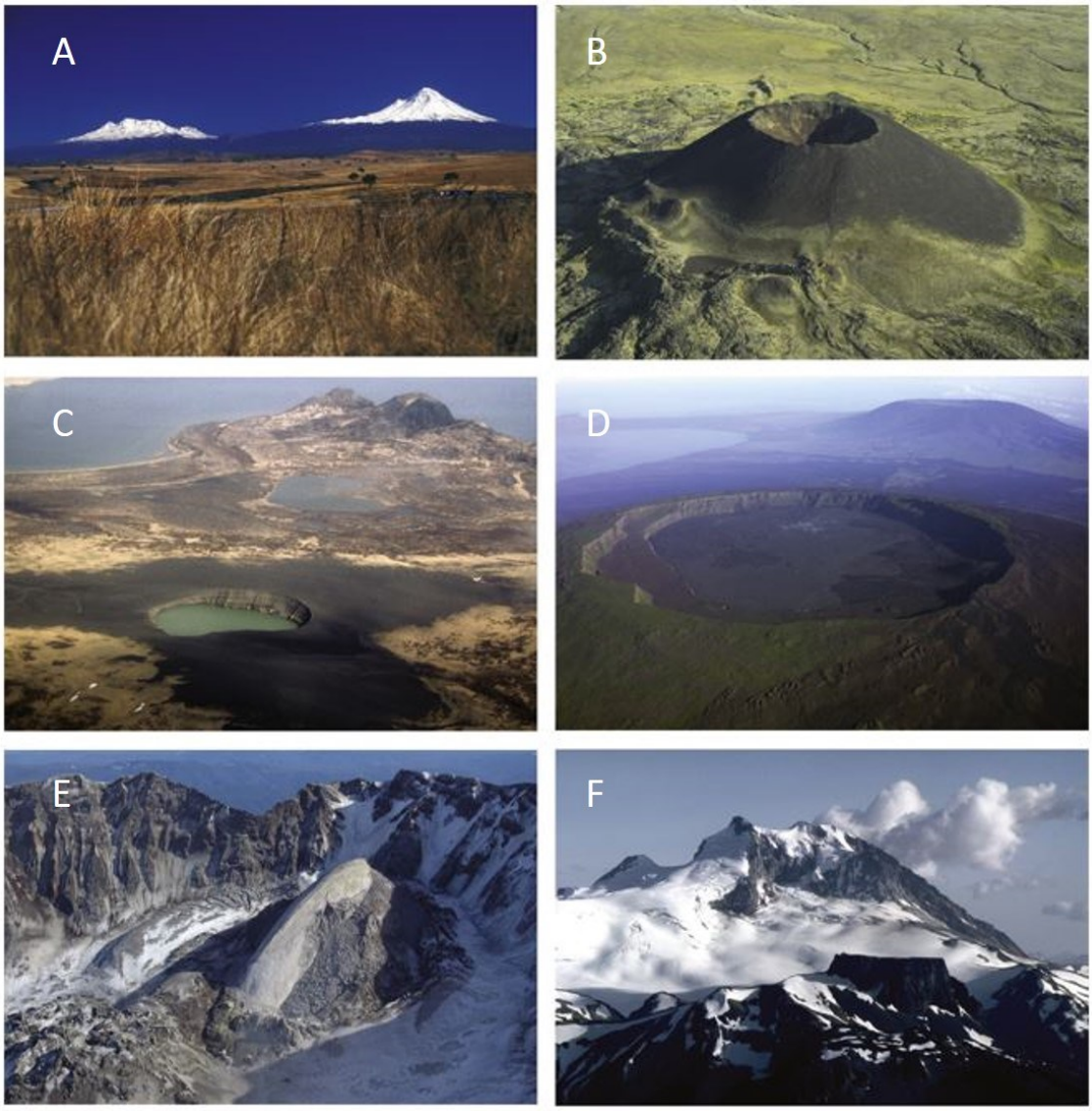

Fig. 2.7 Common volcanic landforms on Earth from Siebert et al. (2015) (A) Stratovolcanoes: Mexico's Popocatepetl volcano (right) and Iztaccihuatl (left); Photo by Lee Siebert (Smithsonian Institution); (B) Pyroclastic cone: Eve Cone on Edziza volcano in Canada; Photo by Ben Edwards (Dickinson College); (C) Maar (with tephra blanket): Alaska; Photo by Chris Nye (Alaska Division of Geology and Geophysics/USGS); (D) Shield volcano: Darwin volcano incl. summit caldera (foreground) and Wolf volcano (background); Galápagos Islands; Photo by Patricio Ramon (Escuela Politecnica, Quito); (E) Lava domes: Mount St. Helens (USA), grown from 1980-86 (lower left) and from 2004-06 (right center); Photo by Steve Schilling, (USGS). (F) Flat-topped tuya or 'table mountain' formed by extrusion of lava under glacial ice; British Columbia, Alaska; Photo by Lee Siebert (Smithsonian Institution).

Chapter 3 Glaciovolcanism

There are currently ~250 Holocene active volcanoes (of a total of ~1400) on Earth that are ice-clad or have glaciers in their proximity (Fig. 3.1) (Siebert et al., 2015; Edwards et al., 2020; Smithsonian Institution and Venzke, 2013) and interactions between volcanoes and ice/snow are therefore common (e.g., Pierson et al., 1990; Gudmundsson et al., 1997; Magnússon et al., 2012; Bleick et al., 2013; Oddsson et al., 2016). The discipline of 'glaciovolcanism' is comparably young but has received increasing attention since the beginning of the 21st century. It is truly interdisciplinary including, but not limited to, many disciplines such as volcanology, sedimentology, glaciology, geomorphology and planetary science (Smellie and Edwards, 2016). The term 'glaciovolcanism' or 'glaciovolcanic' was first formerly defined by Smellie (2006, p. 243):

"[..] glaciovolcanic is used to refer to all types of volcano interactions with ice in all its forms (including snow and firn) and, by implication, any meltwater derived from that ice by volcanic heating."

Thus, this definition does not only refer to truly 'subglacial' eruptions, but also includes interactions taking place above or proximal to the ice (e.g., subaerial lava overriding snow and ice) (Smellie, 2006; Smellie and Edwards, 2016). However, for this thesis, subglacial eruptions are the primary focus. Volcanic eruptions can occur in a variety of glacial settings such as beneath hundreds of metres thick ice (including continental-scale ice sheets such as those in Antarctica), ice filled calderas, ice covered stratovolcanoes or on top or beneath snow (Edwards et al., 2015).

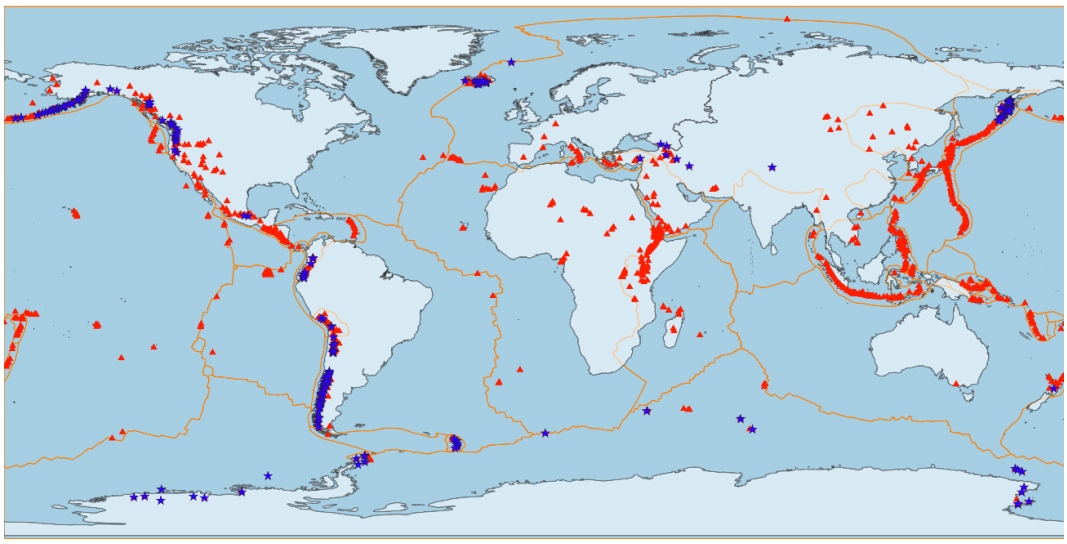

Fig. 3.1 Plate boundaries (orange lines) from Bird (2003) and positions of Holocene active volcanoes (red triangles, total number: 1357) from Smithsonian Institution and Venzke (2013); downloaded 03/12/2021. Blue stars are positions of glacierized volcanoes from Edwards et al. (2020). Basemap: 'World continents', accessed on 10/03/2021

3.1. Glacier-volcano interactions

Glaciers can be affected by volcanic activity in various ways with different consequences for the glacier. Previous publications show that volcanic activity that impact glaciers include (but are not limited to) enhanced geothermal heating, subglacial dome growth, sub- and supra-glacial lava flows, pyroclastic density currents, supraglacial tephra deposition and sub- and supra-glacial flooding/lahar formation (Major and Newhall, 1989; Smellie and Edwards, 2016; Barr et al., 2018a). The aforementioned volcanic impacts can have direct (and immediate) consequences for the glacier such as ice melt/erosion, ice cauldron (depression) formation, ice fracturing/deformation, ice destruction and glacier crevassing, but may also have consequences for the glacier on a longer timescale (i.e., up to decades) such as glacier advance/acceleration and glacier retreat (Fig. 3.2). Also, lava flows emplaced on ice can result in variable ice melting depending on the presence (and thickness) of a debris/tephra layer on the glacier surface (Edwards et al., 2013). Some volcanic processes such as tephra deposition on the glacier surface can affect the glacier by – depending on tephra thickness and tephra continuity – insulating the ice or leading to enhanced ablation due to changes in surface albedo (Fig. 3.2d points 27&28) (Richardson and Brook, 2010; Brook et al., 2011; Barr et al., 2018a).

This can result in increased (or decreased) ice melt and therefore impact glacier velocity/advance (e.g., Rivera et al., 2012). Since tephra deposition has a less direct (and immediate) impact on the glacier, it is not the focus of this thesis.

The following sub-sections discuss (direct) glaciological consequences of volcanic impacts in more detail and present examples from around the globe. Some of the content was published in Martin et al. (2021), see Appendix 2. These sub-sections therefore provide background information to the examples presented in Chapter 5, that are investigated in this thesis using optical satellite imagery.

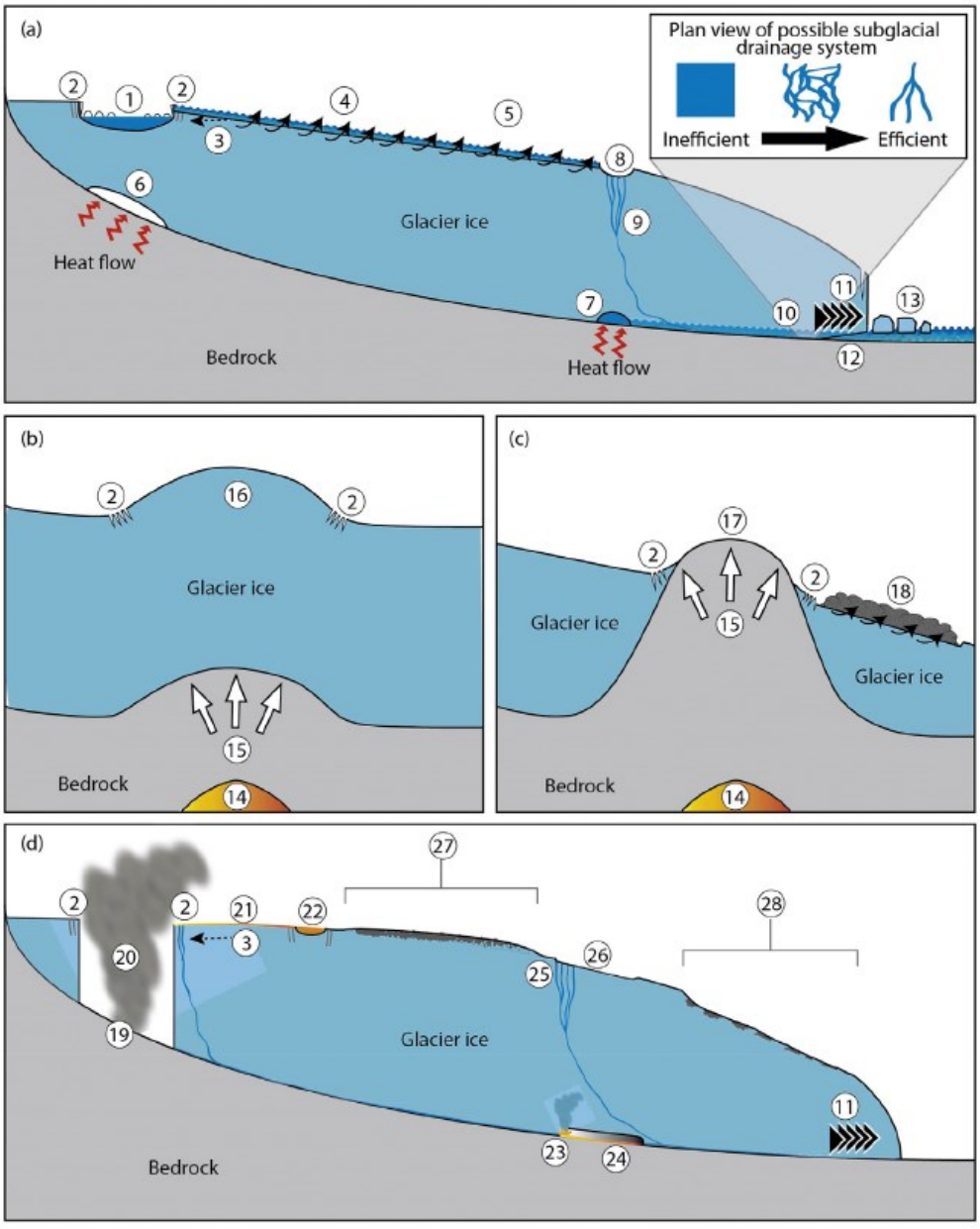

Fig. 3.2 Illustrations of volcanic impacts on glaciers from Barr et al. (2018a). Explanations in the text.

3.1.1. Ice surface subsidence (cauldron formation) and concentric crevassing

The main glaciological impact of enhanced subglacial heat flow is the formation of subglacial cavities or lakes due to ice melting (Fig. 3.2a points 6 and 7), which can result in ice surface subsidence (ice cauldron formation) and ice fracturing (Fig. 3.2a points 1 and 8) (Barr et al., 2018a). Cauldrons are generally caused by heat applied at the glacier base at the location of the vent. The associated rapid basal melting results in subsidence of the overlying ice and ice flow towards the vent (dependent on ice thickness). The term cauldron covers the range from shallow, non-crevassed depressions in the ice surface to steep-sided, heavily crevassed cylindrical chasms, which sometimes extend to bedrock (i.e., to the glacier bed) (Gudmundsson et al., 1997; Guðmundsson et al., 2007).

Dependent on ice thickness and eruption strength, a volcanic eruption can form ice cauldrons surrounded by heavily crevassed and deformed ice (Fig. 3.3a) or can melt all the way through the ice forming an ice crater (Fig. 3.2d point 20 & Fig. 3.3b) (Edwards et al., 2015; Barr et al., 2018a). If the ice is thick (>500 m), reversals in ice flow direction towards the cauldron might result in brittle behaviour of at least the uppermost part of the ice layer, which can result in the formation of concentric crevasses (Fig. 3.3a) (Gudmundsson et al., 2004; Edwards et al., 2015; Barr et al., 2018a). During the initial stages of an eruption, a central block with a non-crevassed (smooth) glacier surface is present, which can collapse to form a subaerial eruption (Gudmundsson et al., 1997, 2004; Tuffen, 2007). At ice-clad volcanoes where the ice is comparatively thin (<200 m), ice craters with steep walls indicate little or no influence on the local ice flow field (Fig. 3.3b) (Edwards et al., 2015). Eruptions beneath intermediate ice thicknesses can show behaviour of both end-members, dependant on magma composition and ice melting rate (Smellie and Edwards, 2016). Cauldron formation (and associated concentric crevassing) is typical for ice-dominant eruptions, where the presence of ice and meltwater has a major influence on the eruption style and behaviour (Edwards et al., 2015; Smellie and Edwards, 2016). Ice cauldron formation (and associated concentric crevassing) typically occurs in Iceland, but also on other glacierized volcanoes around the globe.

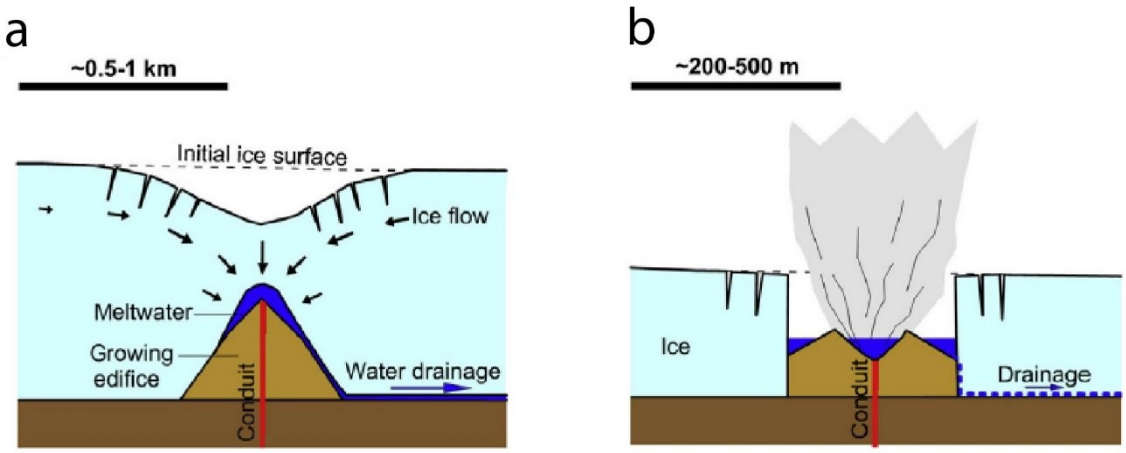

Fig. 3.3 Glaciovolcanic eruption types (classes) from Edwards et al. (2015). (a) Subglacial eruptions under thick (>500 m) ice with growing volcanic edifice (tuya or tindar formation) and deforming ice with reversal of ice flow towards the vent; (b) Eruption beneath thin (<200 m) ice; cauldron formation with steep walls and no reversal of ice flow

3.1.1.1. Iceland (Gjálp 1996, Bárðarbunga 2014-15, Katla 1999-2005)

In October 1996, subglacial melting due to a fissure eruption at the Vatnajökull ice cap between the volcanoes of Bárðarbunga and Grímsvötn (Gjálp) formed an ice cauldron and concentric crevassing overnight (Fig. 3.4 and Fig. 3.5). The cauldron increased from 4 to 7 km in diameter within the first three months of the eruption. The eruption melted through 500 m thick ice in 30 hours in one particular place, other parts remained subglacial. Also, subsidence and crevassing was observed along the meltwater path into Grímsvötn lake, which drained in a large jökulhlaup in November 1996 (Gudmundsson et al., 1997, 2004).

Fig. 3.4 Cauldron (subsidence bowl) as surface expression on the glacier ice along an eruptive fissure during the 1996 Gjálp eruption. Courtesy of R. Axelsson. (Global Volcanism Program, 1996)

Fig. 3.5 Crevassing of glacier ice related to cauldron formation during the 1996 Gjálp eruption. Shadow of the airplane for scale. Courtesy of R. Axelsson. (Global Volcanism Program, 1996)

In 2014–2015, a rifting episode between Bárðarbunga and Askja resulted in the formation of ice cauldrons on Dyngjujökull glacier along the path of a more than 45 km long subglacial dyke, and included the collapse of the Bárðarbunga caldera (Riel et al., 2015; Rossi et al., 2016; Reynolds et al., 2017). These cauldrons formed within a sector of ice 430–670 m thick (Farinotti, 2019).

In 1999–2005, geothermal activity on Katla (Iceland), beneath Mýrdalsjökull glacier, resulted in the formation of very large ice cauldrons, ~1–1.5 km in diameter in 400–700m thick ice (Björnsson and Guðmundsson, 2000; Guðmundsson et al., 2007).

3.1.1.2. Beyond Iceland (Mount Redoubt 2009, Mount Hudson 2011, Mount Veniaminof 2021)

Beyond Iceland, ice cauldrons were observed approximately two months before the eruption on Mount Redoubt in Alaska in March/April 2009 (alongside a variety of other precursors such as crevassing, ice-slurry/debris flows and the emission of ejecta) (Bleick et al., 2013). One of the cauldrons formed in the summit crater of the volcano, where ice is ~150 m thick (Trabant and Hawkins, 1997). These cauldrons were associated with near-vertical walls and despite the ice being below 200 m thick, showed clear concentric crevassing (Schaefer, 2011; Bleick et al., 2013; McGimsey et al., 2014).

Cauldrons associated with the emission of gases and pyroclasts were also reported during the eruption of Mount Hudson (Chile) in October–December 2011 (Amigo et al., 2012).

The recent March–April 2021 eruption of Mount Veniaminof in Alaska also produced a visible cauldron ~1 km in diameter, east of the prominent and active intra-caldera cone within ice that is ~100 m thick (Welch et al., 2007; *Global Volcanism Program. Report on Veniaminof (United States). In: Sennert, S K (ed.)*).

3.1.2. Opening formation

In contrast to ice cauldron formation, openings are associated with meltwater flux through zones of weakness within the ice (e.g., pre-existing crevasses) due to high subglacial water pressures. The openings are formed locally if the meltwater finally reaches the glacier surface and continues flowing supraglacially.

3.1.2.1. Eyjafjallajökull (2010)

As an example, during the Eyjafjallajökull eruption (Iceland) in 2010, ice cauldrons formed in the summit crater and openings appeared in the ice surface along a subglacial flood path down Gígjökull glacier, where the ice thickness was reported to be less than 100 m (Strachan, 2001; Magnússon et al., 2012; Oddsson et al., 2016).

3.1.3. Glacier acceleration and advance/Glacier slow-down

Both enhanced subglacial heat flow and subglacial eruptions will result in increased meltwater production and enhanced bed lubrication, which can ultimately result in enhanced basal sliding due to increased subglacial water pressure (Fig. 3.2a,d point 11) (Magnússon et al., 2007; Barr et al., 2018a). However, there is evidence of the opposite effect occurring in some settings. The work of Magnússon et al. (2010) shows the effect of meltwater leakage from a subglacial lake on ice flow, which can lower water pressure and reduce sliding. Whether increased subglacial meltwater results in changes in glacier velocity, however, depends on the nature of the subglacial hydrological drainage system. For example, glaciers may not change their (surface) velocity considerably if the bed is already wet and if a well-developed subglacial drainage system is present (see sub-section 2.1.2 and references therein). In general, various (climatically driven) factors influencing glacier speed have to be considered to determine if a particular glacier has accelerated and/or advanced due to volcanic activity. It remains unclear if an (volcanically triggered) accelerating glacier also advances and most studies focus on (volcanically triggered) glacier advances (Sturm et al., 1991; Benson et al., 2007; Muraviev and Muraviev, 2016; Reinthaler et al., 2019). The relationship between glacier advance and acceleration seems to be highly dependent on ice flux and therefore (changes in) glacier slope and debris cover. This relationship has been investigated for an advance/repeat cycle for alpine 'non-volcanic' glaciers, but is beyond of the scope of this thesis (e.g., Herman et al., 2011)

3.1.3.1. Mount Wrangell (1964 – present), Klyuchevskoy Volcanic Group (after 2005), Volcán Michinmahuida (2007-2009), Gjálp (1996)

Globally, there are a small number of examples of glacier advance and/or acceleration and glacier slow-down due to increased melting caused by volcanic activity. Following the Great Alaskan earthquake in March 1964, glaciers on the northeast flank of Mount Wrangell (Alaska) steadily advanced (at least until 2003) at 5-18 m/year and showed season-independent flow velocities, whereas glaciers on the western flank did not show any sign of advance (Sturm et al., 1991; Benson et al., 2007). The steady advance of these glaciers is thought to be due to changes in heatflux after the earthquake and an abundance of subglacial meltwater (Sturm et al., 1991; Benson et al., 2007).

In Kamchatka, glacier advance related to volcanic heating was reported in the Klyuchevskoy volcanic group. For example, Shmidta glacier has advanced since 2007, which is thought to be related to the 2005-10 eruptive period of Klyuchevskoy volcano (Muraviev and Muraviev, 2016; Barr et al., 2018b).

In South America, Glacier Amarillo (located on Volcán Michinmahuida) was reported to have accelerated several months before the eruption of nearby Volcán Chaitén in May 2008. Increased geothermal heatflux due to the existence of hotspots under Michinmahuida volcano is proposed to have resulted in increased melting and enhanced basal sliding, which translates into glacier advance of up to ~200 m (Fig. 3.6) and faster glacier surface velocities (Fig. 3.7). The advance of Glacier Amarillo was not mirrored by glaciers on 'non-volcanic' mountains (e.g., Monte Inexplorado and Monte Tronador) in the region (Rivera et al., 2012). In contrast, persistent leakage from Grímsvötn following the Gjálp eruption and related jökulhlaup in 1996 resulted in more efficient channelized drainage and reduction in basal water pressure – causing considerable drop in ice flow velocity on Skeiðarárjökull for a time period of at least four years (Magnússon et al., 2010).

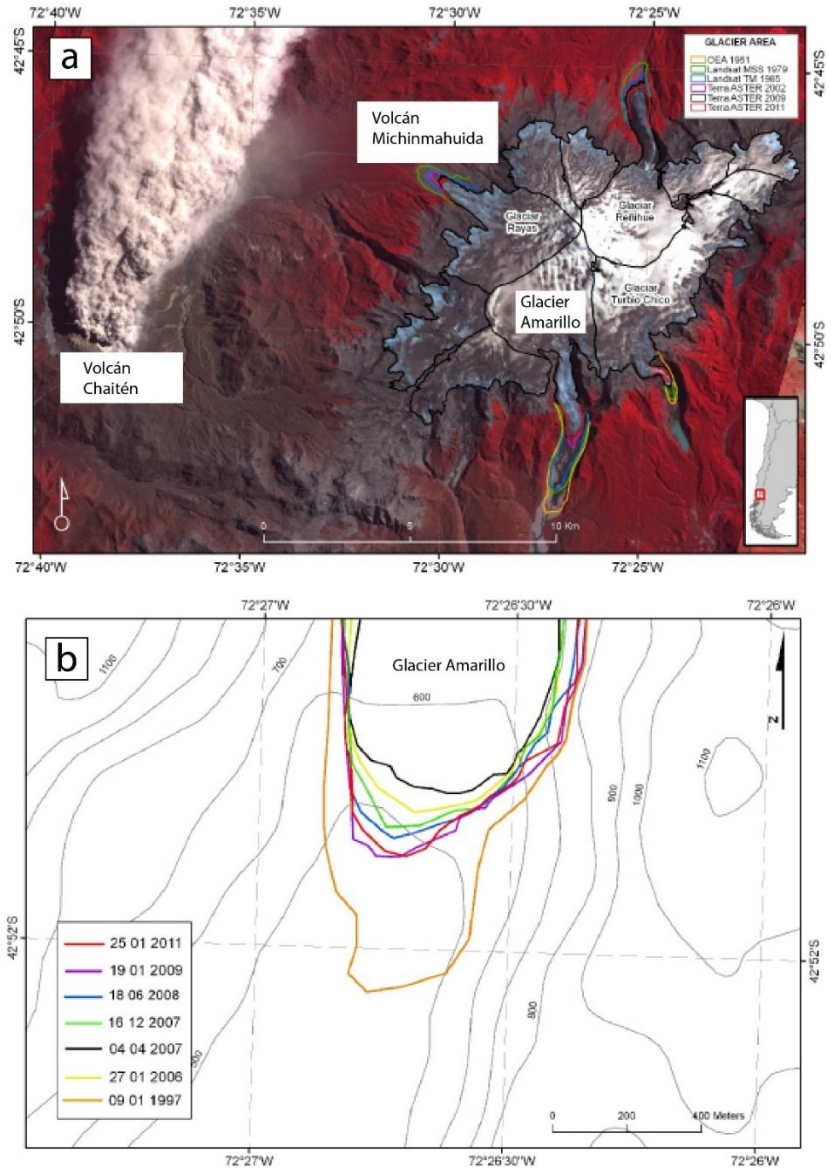

Fig. 3.6 Advance of Glacier Amarillo on Vólcan Michinmahuida (Chile) related to the volcanic active period at nearby Volcán Chaitén in May 2008 (a) ASTER VNIR overview image of Vólcan Chaitén (left) and Vólcan Michinmahuida with Glacier Amarillo (right); (b) Frontal changes of Glacier Amarillo with clearly visible glacier advance during 2007-09; from Rivera et al. (2012)

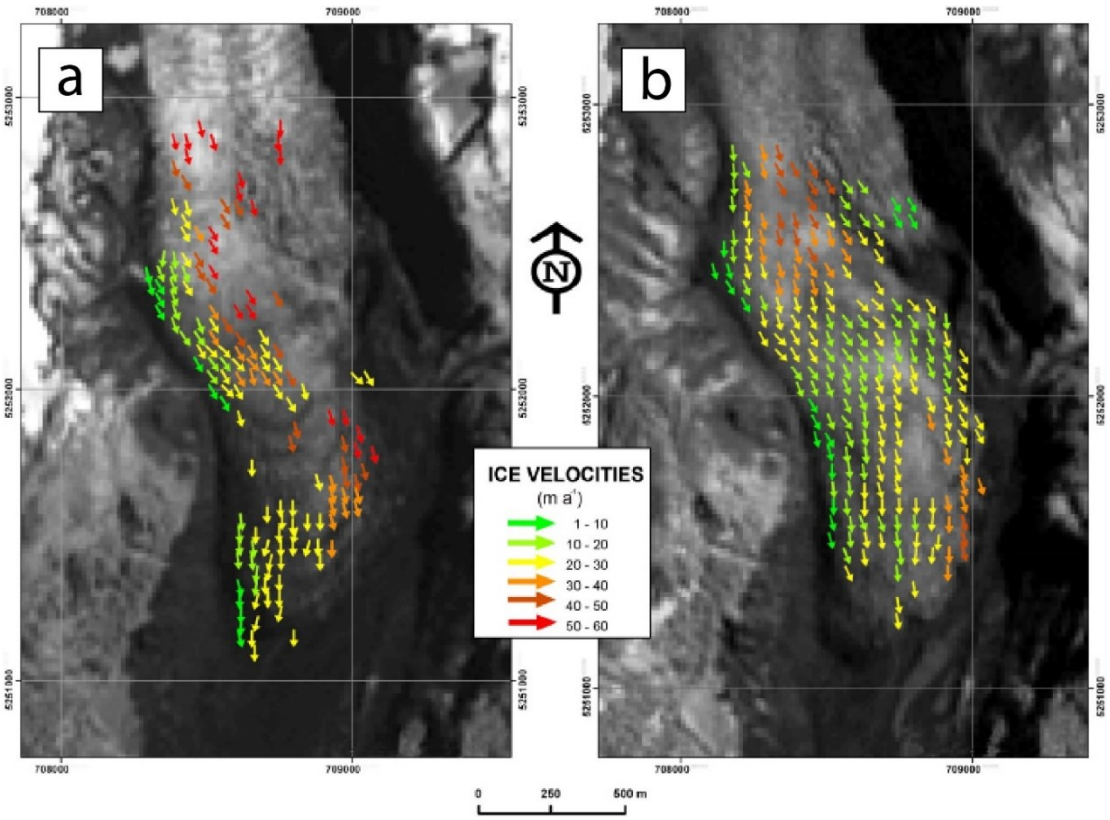

Fig. 3.7 Glacier surface velocities at Glacier Amarillo's lower tongue. The eruptive period on Volcán Chaitén was in May 2008. (a) Glacier velocities during glacier advance (December 2007 to January 2009). (b) Glacier velocities between January 2009 and January 2011 (after main glacier advance); from Rivera et al. (2012)

3.1.4. Glacier area changes/glacier destruction

The reduction of glacier area (and volume) due to volcanic activity is commonly reported around the world. This might be due to various volcanic impacts such as enhanced subglacial heatflow/subglacial eruptions, the formation of lahars/pyroclastic density currents and/or deposition of supraglacial tephra/debris (Barr et al., 2018a).

3.1.4.1. Nevado del Huila (2007-2012), Nevado del Ruiz (1985)

During the 2007-12 active period at Nevado del Huila, several of the aforementioned processes resulted in the loss of a portion of El Oso glacier tongue and a ~30% loss of the glacier surface area within two years of the volcanically active period (Rabatel et al., 2013; Granados et al., 2015).

During the eruption on Nevado del Ruiz in 1985, the surface area of ice and snow was reduced by 4.2 km^2 (16%) from its pre-eruptive area of 25 km^2 and 9% of the total volume of ice and snow was lost (Pierson et al., 1990; Thouret, 1990).

3.1.4.2. Mount St. Helens (1980)

An extreme case of a glacier area change can include partial or complete glacier destruction. Both glacier destruction and glacier beheading (i.e., destruction of a glacier's accumulation zone) are common for subglacial eruptions and are often directly related to volcanic blasts (Barr et al., 2018a). A notable example occurred during the eruption of Mount St. Helens in 1980, when four of the 13 glaciers present prior to the eruption were left beheaded and two glaciers were completely destroyed (Fig. 3.8) (Brugman and Post, 1981). Glaciers left beheaded often do not quickly retreat, since deposits insulate the ice resulting in ice stagnation (indirect impact). However, over the timescale of decades, these glaciers have been observed to disappear entirely (e.g., for some of the beheaded glaciers on Mount St. Helens) (Barr et al., 2018a).

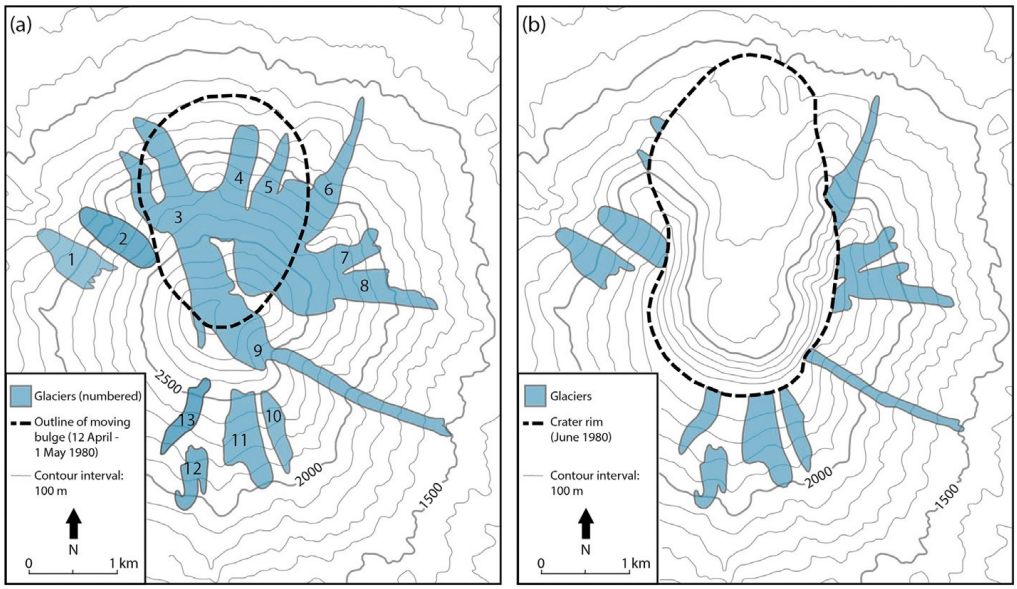

Fig. 3.8 Glaciers on Mount St. Helens from (a) before and (b) after the 1980 eruption. Glaciers 4 and 5 were completely destroyed, glaciers 6,7,8 and 9 were left beheaded. Figure from Barr et al. (2018a) based on Brugman and Post (1981)

3.1.5. Glacier surface abrasion/Channel formation

3.1.5.1. Nevado del Ruiz (1985), Nevado del Huila (2007-2012)

Pyroclastic density currents can both abrade and incise channels in a glacier's surface. During the comparably small eruption of Nevado del Ruiz (Colombia) in 1985, pyroclastic density currents effectively entrained snow and ice, rounded seracs and abraded the glacier surface (Fig. 3.9). Related to this, up to 100 m wide and 2-4 m deep channels were formed in the ice surface of Nereidas, Azufrado and Lagunillas glaciers. Effective mixing and heat transfer to snow and ice generated large volumes of meltwater, which ultimately resulted in a 4 times larger volume lahar after incorporation of sediments along its way down the volcano. Injection of pyroclastic debris into pre-existing crevasses resulted in additional fracturing of the glacier surface (Naranjo et al., 1986; Pierson et al., 1990).

Comparably, during the active volcanic period at Nevado del Huila (Colombia) in the years 2007-12, ice melting resulted in the formation of a lahar, which incised channels in the glacier surface (Monsalve et al., 2011; Granados et al., 2015).

Fig. 3.9 Scoured surface of Nereidas glacier (Nevado del Ruiz) by pyroclastic flows. Seracs (3-5 m high) are rounded or almost completely abraded. From Pierson et al. (1990)

3.1.6. Glacier crevassing

Most of the volcanic impacts on glaciers presented in the above sub-sections will result in crevassing of the glacier surface. The following sub-sections intend to describe various volcanic active periods that have glacier crevassing as their main impact (excluding ice cauldron formation, which is discussed separately in sub-section 3.1.1).

3.1.6.1. Crevassing due to Subglacial lava dome growth

Volcanic domes consist of viscous lava and rocks that are extruded and piled up around a volcanic vent. They can form over time periods of days to weeks, but their formation can also last for years to decades. Their size can range from a few tens of metres to a few kilometres in diameter (Calder et al., 2015). If extruded underneath/through or beside glacier ice, direct impacts on the surrounding ice can include ice deformation and fracturing (Fig. 3.2c points 2,14, 15,17). Also, glacier displacement and squeezing has been reported (Walder et al., 2007, 2008). In general, reported instances of glacier deformation related to subglacial dome growth remain comparably rare (Barr et al., 2018a).

3.1.6.1.1. Mount St. Helens (2004-2006)

Following the eruption of Mount St. Helens in 1980, a volcanic dome episodically grew until October 1986 (Swanson and Holcomb, 1990). Alongside, a small 'amphitheatre-like' glacier began to grow after the eruption and reached a maximum thickness of 200 m in September 2001 (Schilling et al., 2004). New doming activity began in October 2004 and heavily impacted the crater glacier. The dome split the glacier in two parts and squeezed the ice against the crater walls (Walder et al., 2007, 2008). This led to heavy crevassing and even local doubling in the thickness of the two glacier parts (Walder et al., 2008).

3.1.6.2. Localized Crevassing Due to Supraglacial Lava Flows

The formation of sub- and/or supraglacial lava flows is common for most glaciovolcanic eruptions and the primary impact on the glacier is ice melt (Fig. 3.2d points 21,22). Supraglacial lava flows can form visible ice surface channels, whereas subglacial lava flows are more difficult to observe. Both types of lava flows can be kilometres long. Subglacial melting related to lava flows can be violent due to water being vaporised when interacting with lava, however, ice melting due to lava flows most likely remains localised and therefore only has limited impact on glacier behaviour (Barr et al., 2018a).

3.1.6.2.1. Heard Island (2006-2008), Montagu Island (2001-2007)

Examples of pronounced ice surface channels and/or depression formation due to supraglacial lava flows come from the volcanic eruptive phases on Heard Island (Mawson Peak; South Indian Ocean) and on Montagu Island (Mount Belinda; South Sandwich Islands) in the years 2006-08 and 2001-07, respectively. The emplacement of a lava flow on Mount Belinda most likely resulted in a carved gully in the ice cover and heavy crevassing at the flow front (Patrick et al., 2005; Patrick and Smellie, 2013)

3.1.6.3. Widespread Crevassing Due to Glacier Acceleration/Advance

3.1.6.3.1. Montagu Island (2001-2007)

Glacier acceleration/advance can lead to increased crevassing of a glacier surface. For example, active lava flows and subglacial melt are presumed to have promoted glacier acceleration (due to basal lubrication) during a low-intensity volcanically active period in the years 2001 to 2007 on Mount Belinda (Montagu Island). This is presumed to have caused the glacier's surface to become extensively crevassed (Patrick et al., 2005; Patrick and Smellie, 2013).

Chapter 4 Methodological framework

4.1. Optical satellite remote sensing

This Chapter provides an overview of the satellite remote sensing methodological framework used to study ice-clad volcanoes in this thesis. 'Remote Sensing' as defined by Campbell and Wynne (2011) "is the practice of deriving information about the Earth's land and water surfaces using images acquired from an overhead perspective, using electro-magnetic radiation in one or more regions of the electromagnetic spectrum, reflected or emitted from the Earth's surface." It is noteworthy that remote sensing in a broader sense also includes meteorological and extraterrestrial investigations as well as sensing of the Earth's magnetic field (Campbell and Wynne, 2011). The definition above includes both active and passive remote sensing. Sensors of active systems, such as synthetic aperture radar (SAR), are constructed to actively illuminate the Earth's surface and record the energy scattered back to the sensor. In contrast, passive systems rely on the Sun as an illuminator and record the reflected or emitted energy from the Earth's surface (Campbell and Wynne, 2011). The focus of this thesis is on passive, optical satellite remote sensing (i.e., in the visible part of the electromagnetic spectrum).

The term 'remote sensing' was first used with the launch of the first Television and Infrared Observation satellite (TIROS) in April 1960, which was a weather satellite designed to monitor cloud patterns and equipped with a TV and an infrared camera (Campbell and Wynne, 2011). The launch of the first satellite of the Landsat ('land satellite') program in 1972 allowed for the first time broad-scale and systematic repetitive observations of the Earth's land surface in digital format (Campbell and Wynne, 2011). Landsat has the longest collection of space-based, moderate resolution land remote sensing data (Emery and Camps, 2017) and has 3 active missions at the time of writing (i.e., Landsat 7, Landsat 8 and the latest satellite Landsat 9 being launched on 27 September 2021, https://www.usgs.gov/landsat-missions/landsat-9, accessed on 08/12/2022). Other Landsat-like satellite systems such as the SPOT satellite series were developed and launched in the 1980s and 90s. Very-high-resolution satellites (e.g., IKONOS, GeoEye and WorldView) were launched in the late 90s and early 2000s (Campbell and Wynne, 2011).

Satellite remote sensing (including both active and passive systems) nowadays has a wide range of applications in agriculture, geology, forestry, mapping and global change research (Emery and Camps, 2017).

Remote sensing based techniques can be used to discriminate between landcover types (e.g., Symeonakis et al., 2018, 2020); to identify minerals that are indicative for exploitable ore deposits (e.g., Enton, 2017; Shirmard et al., 2022) and to map flood extents (e.g., Klemas, 2015), amongst many other applications. Thermal remote sensing allows, for example, the detection of hotspots on active volcanoes and the mapping of lava flow (e.g., Wright et al., 2004; Coppola et al., 2020). Most importantly (for this thesis), optical remote sensing techniques are routinely used to map glacier extents (e.g., Kääb et al., 2002; Paul et al., 2007, 2016; Gjermundsen et al., 2011) and velocities (e.g., Herman et al., 2011; Mouginot and Rignot, 2015; Wilson et al., 2016; Dell et al., 2019; Millan et al., 2019; Van Wyk de Vries and Wickert, 2020). The continuous availability of satellite remote sensing data for the last ~40 years allows time-series analysis to investigate changes in glacier extents on longer timescales (e.g., Reinthaler et al., 2019). Also, remote sensing based maps of global glacier extents and velocities have now become available. For example, the Randolph Glacier Inventory is a collection of digital outlines of glaciers around the globe (excluding the Greenland and Antarctic ice sheets) (Pfeffer et al., 2014) and the work by Millan et al. (2022) provided glacier surface velocities for 98% of all glaciers on Earth. Most satellite based techniques are developed to study glaciers and volcanoes separately, however, there are a few studies using optical satellite data to investigate morphological changes of glaciers and volcanically triggered glacier advance/acceleration (e.g., Williams, 1987; Björnsson and Einarsson, 1990; Sturm et al., 1991; Patrick et al., 2005; Martinis, 2007; Rivera et al., 2012; Bleick et al., 2013; Patrick and Smellie, 2013). In this thesis, we focus on optical satellite data (rather than other datasets, including SAR) since only optical satellite data cover almost half a century and the past decade has seen a rapid increase in the variety of free and commercial datasets potentially suitable for glacier-volcano monitoring (Fig. 4.1) (see Belward and Skøien, 2015).

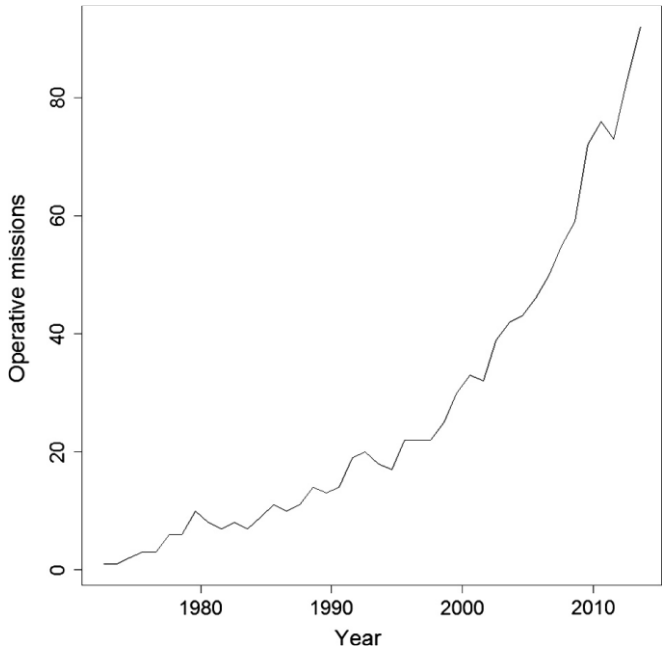

Fig. 4.1 Number of near-polar orbiting, land imaging civilian satellites from August 1972 to 2013 from (Belward and Skøien, 2015)

4.1.1. The basics of passive remote sensing

Passive Remote Sensing makes use of electromagnetic energy that is reflected or emitted from the Earth's surface to the sensor. Electromagnetic energy is transmitted in the form of an electromagnetic wave (i.e., an oscillating electric and magnetic field) moving at the speed of light (299,729 km/s) (Campbell and Wynne, 2011; Emery and Camps, 2017). The wave's frequency (ν) and wavelength (λ) are inversely proportional and are related to the wave's speed (c) via the following equation:

$$c = \lambda * \nu \qquad \textbf{(4.1)}$$

The electromagnetic wave provides its energy in discrete quantities (photons), which are described with Planck's general equation:

$$E = h * \nu \qquad \textbf{(4.2)}$$

Where E is the photon energy, h is Planck's constant (h = 6.62607×10^{-34} J·s) and ν represents frequency (Emery and Camps, 2017). The distribution of photon energies (or frequencies) is presented in the electromagnetic spectrum (Fig. 4.2) (Emery and Camps, 2017).

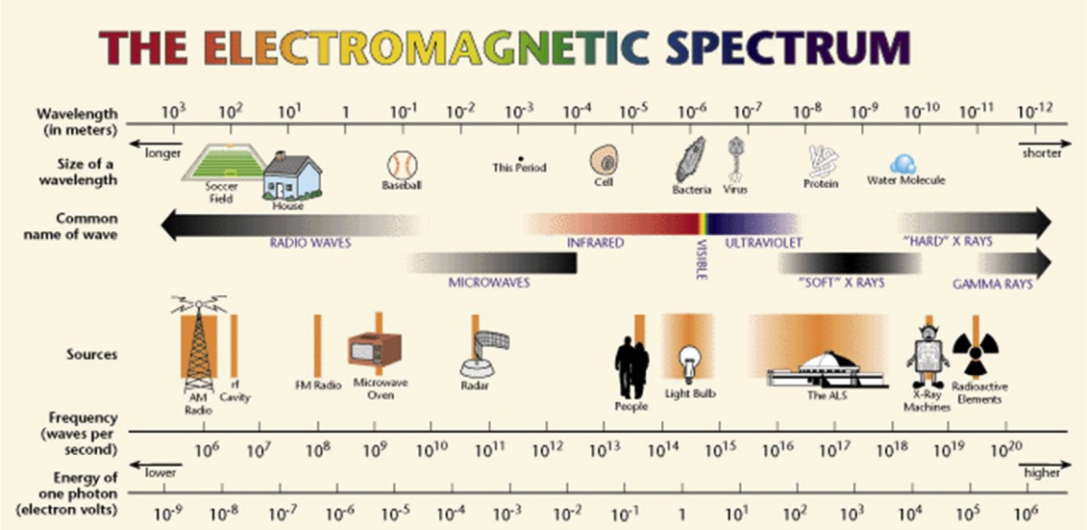

Fig. 4.2 The electromagnetic spectrum from (Emery and Camps, 2017)

The wavelengths relevant to remote sensing begin with the ultraviolet region and range up to the microwave region (Campbell and Wynne, 2011). This thesis is mostly concerned with satellite remote sensing in the visible part of the spectrum (i.e., ranging from ~400 to ~700 nm). Remote sensing techniques in general make use of differences in spectral signatures, such as varying reflection or emission properties of objects on the Earth's surface (e.g., vegetation, minerals, glaciers etc.) to identify and distinguish between them (Campbell and Wynne, 2011; Emery and Camps, 2017).

4.1.2. The remote sensing process

In contrast to airborne remote sensing, electromagnetic radiation recorded with a satellite has a complex pathway through the entire depth of the atmosphere including absorption, reflection, scattering and up/downwelling processes due to the interaction with atmospheric molecules and/or particles. Of course, radiation can also be transmitted through the atmosphere to the sensor without further interaction (Fig. 4.3) (Campbell and Wynne, 2011; Emery and Camps, 2017). In fact, radiation reaching a satellite can also be spontaneously emitted by the atmosphere or the Earth's surface (upwelling radiation) (Emery and Camps, 2017). For remote sensing in the VIS and NIR part of the electromagnetic spectrum, transmission, reflection and scattering processes are most important (Emery and Camps, 2017).

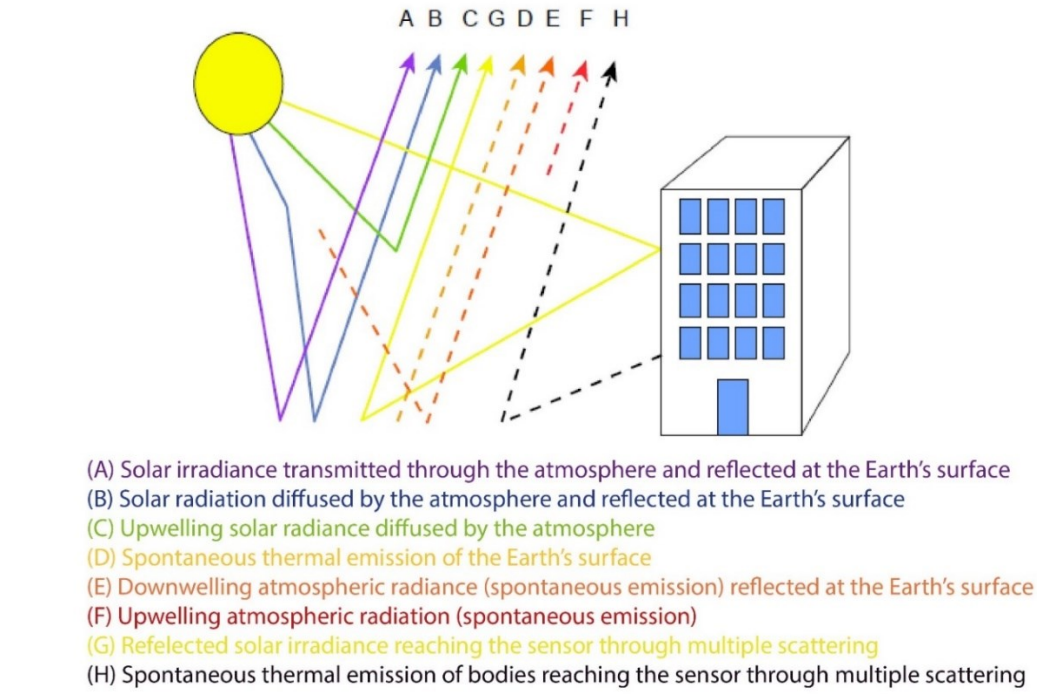

Fig. 4.3 Possible pathways of electromagnetic radiation through the atmosphere reaching a space sensor from Emery and Camps (2017) based on Schott (2007)

Absorption is the process that leads to the strong attenuation of energy on its way through the atmosphere and is mainly caused by atmospheric gases, such as O_3, CO_2 and most importantly H_2O (Campbell and Wynne, 2011; Emery and Camps, 2017). The atmosphere has multiple 'atmospheric windows', through which electromagnetic energy can pass without much attenuation (Emery and Camps, 2017). Satellite remote sensing instruments mostly work in these windows (Fig. 4.4) (Emery and Camps, 2017)

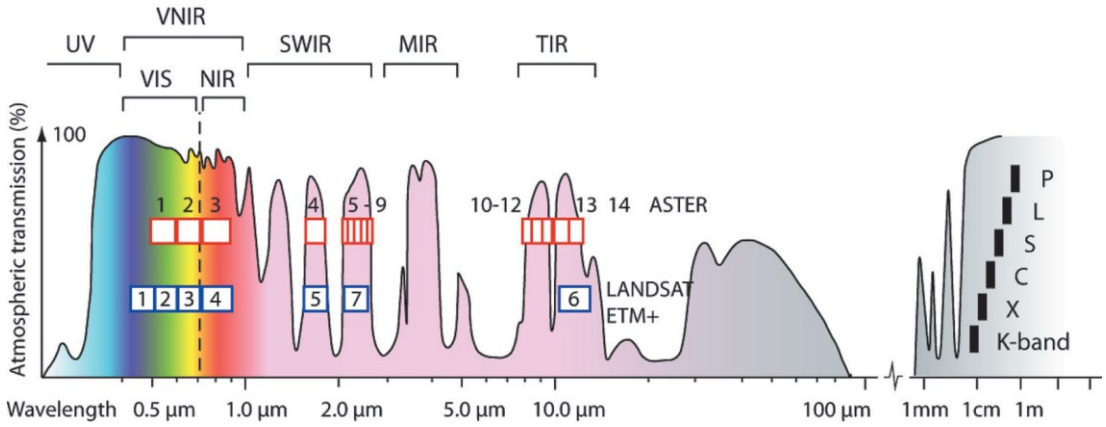

Fig. 4.4 Atmospheric transmission in the wavelength range relevant for satellite remote sensing and wavelength ranges of channels of ASTER and Landsat ETM+ sensors superimposed; UV: ultraviolet, VIS: visible, NIR: near-infrared, SWIR: shortwave infrared, MIR: middle infrared, TIR: thermal infrared, P-K: radar bands (for active remote sensing) from Kääb et al. (2014)

Despite the sensors being designed to lie within atmospheric windows, scattering by atmospheric particles causes limitations to satellite remote sensing in various ways. Scattering means the re-direction of electromagnetic radiation by particles present in the atmosphere, and is dependent on particle size and abundance, the wavelength of the radiation and the depth of the atmosphere (Campbell and Wynne, 2011). Rayleigh scattering occurs if electromagnetic radiation interacts with atmospheric particles that are small relative to the radiation-wavelength (Campbell and Wynne, 2011; Emery and Camps, 2017). It is highly wavelength-dependent and affects UV and blue light more than light of longer wavelengths. Therefore, UV und blue light is generally not considered for remote sensing (Campbell and Wynne, 2011; Emery and Camps, 2017). Mie scattering is caused by large atmospheric particles (e.g., dust, pollen, smoke and water droplets) and mostly affects wavelengths similar to the particle's size (Campbell and Wynne, 2011; Emery and Camps, 2017). It influences a broad range of wavelengths in and near the visible spectrum (Campbell and Wynne, 2011; Emery and Camps, 2017). Non-selective (wavelength-independent) scattering occurs if particles are much larger than the radiation-wavelength and can result in a decrease in contrast in satellite imagery (whitish or greyish haze) due to scattering of light outside the sensor's field of view towards it (Campbell and Wynne, 2011; Emery and Camps, 2017).

4.1.3. Multispectral remote sensing

Multispectral sensors observe the Earth's surface within specified (rather broad) wavelength ranges or bands (e.g., red, green and blue for the VIS range). In contrast, hyperspectral remote sensors (which are not the focus of this thesis) have the capability to collect data within 200 or more channels (e.g., EO-1 Hyperion) (Campbell and Wynne, 2011). In principle, there are two distinct image acquisition designs that are used to collect multi-spectral data with a satellite namely whisk-broom and push-broom scanners. Whisk-broom scanning relies on the principle of an oscillating mirror that scans the Earth's surface in an across-track direction (Schott, 2007; Campbell and Wynne, 2011). Data are collected with each mirror sweep in different bands or channels (i.e., wavelength ranges) along a swath (e.g., measuring 185 km for Landsat), just as dust is swept into a dust pan (Fig. 4.5) (Schott, 2007). The ground spot of the sensor at nadir is called the ground instantaneous field of view (GIFOV), which is directly related to the spatial resolution of the final satellite imagery products (Schott, 2007).

The Multi-Spectral Scanner (MSS) instrument on board Landsat 1-5 (GIFOV ~80 m) collected data with six different detectors, whereas the more advanced Thematic Mapper (TM) sensor on board Landsat 4-5 had the capability to scan in both directions and made use of 16 smaller detectors to increase spatial resolution (to 30 m) (Schott, 2007). The ETM+ sensor onboard Landsat 7 has a similar design to the TM sensor, but additionally allows the acquisition of imagery in panchromatic mode (15 m spatial resolution). In contrast to the above, push-broom scanners allow the simultaneous collection of entire lines of data with increased signal-to-noise ratios (Schott, 2007). They have the advantage of not having movable parts; however, they only achieve smaller ground swaths (e.g., 60 km for SPOT) (Schott, 2007). High-resolution instruments such as IKONOS or QuickBird have push-broom designs and the trend for new sensors is towards this instrument type, e.g., for the Operational Land Imager (OLI) on board Landsat 8 (Schott, 2007; Emery and Camps, 2017).

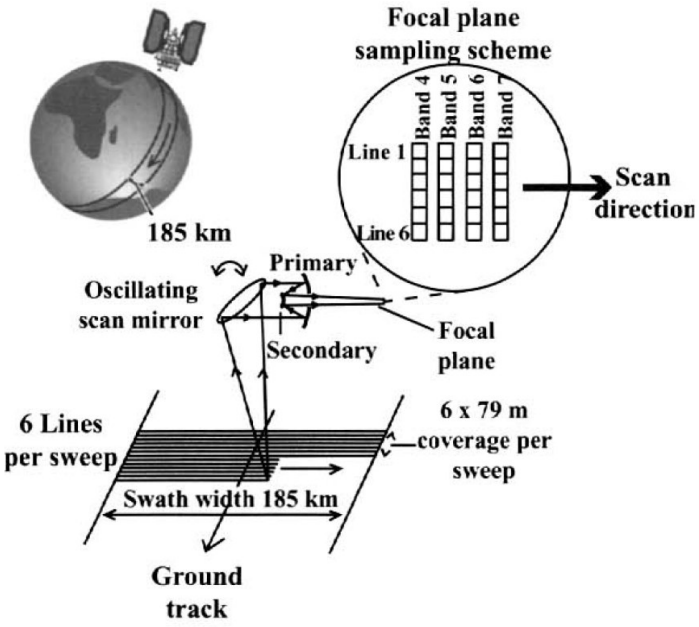

Fig. 4.5 Whisk-broom design of MSS instrument (as used with Landsat1-5 satellites) from (Schott, 2007)

The collected data stripes are stored as rectangular (2D) arrays of pixels (i.e., a digital image) in a satellite scene (e.g., measuring 185 km by 170 km for a Landsat scene) (Campbell and Wynne, 2011). In the case of multispectral remote sensing, digital images can have several layers of the same scene acquired in different bands (Liu and Mason, 2009).

The combined effect of spacecraft forward motion and rotation of the Earth skews the scene, which has to be corrected for to obtain a proper ground projection (Schott, 2007; Campbell and Wynne, 2011).

In order to ensure comparable brightness of features within scenes for a particular location on Earth, satellites are typically put in a sun-synchronous orbit (i.e., they acquire imagery for a given location on the same local sun time) (Campbell and Wynne, 2011). Despite placing satellites in sun-synchronous orbits, each pixel within a scene only represents a numeric value of relative brightness within the respective scene, so the calculation of true radiance and reflectance requires additional corrections for instrumental gain and offset, illumination conditions and atmospheric absorption/scattering (Campbell and Wynne, 2011; Kääb et al., 2014). Satellite data are distributed at different processing levels (see sub-section 4.1.5), which, dependent on the processing level, include the corrections mentioned above.

4.1.4. Spatial/temporal and radiometric resolution

Satellites/sensors are designed with a range of spatial, temporal and radiometric resolutions to serve various requirements. Very broad-scale sensors at coarse resolutions (i.e., >250 m) often have the capability to image the entire Earth at least once a day and serve meteorological applications or were designed to study the thermal balance of land surfaces (e.g., AVHRR, MODIS) (Schott, 2007; Campbell and Wynne, 2011). The next group of satellites/sensors may be classified as 'Landsat-like' systems with broad geographic coverage at moderate resolution (i.e., ~10-100 m) for the investigation of land surfaces (e.g., Landsat, ASTER, EO-1 ALI, SPOT, Sentinel-2). Repeat cycles are in the order of days (Campbell and Wynne, 2011). Finally, fine-resolution satellite systems were designed to serve very specific purposes such as urban infrastructure analysis, transportation planning and construction support and can have spatial resolutions smaller than ~1 m (e.g., IKONOS-2, QuickBird-2, GeoEye-1 or the WorldView satellite series) (Campbell and Wynne, 2011). The definition of what is considered 'low', 'medium' and 'high' resolution imagery is largely dependent on the application. In this thesis, we follow the definition of Elliot et al. (2016), who uses the term 'low-resolution' for image resolutions of 10–100 m, 'medium-resolution' for image resolutions of 1–10 m and 'high-resolution' for images of less than 1 m resolution.

Radiometric resolution refers to how sensitive a sensor is to variations in electromagnetic energy, or the number of grey-scale values the sensor can distinguish between. Since a satellite scene is a digital image, this information is stored in bits, so, e.g., a 8-bit ASTER satellite image would result in 256 potential grey-scale values (https://www.nrcan.gc.ca/maps-tools-and-publications/satellite-imagery-and-air-photos/tutorial-fundamentals-remote-sensing/satellites-and-sensors/radiometric-resolution/9379, accessed on 08/12/2022). This thesis is mostly based on imagery from the low-resolution (but freely available) 'Landsat-like' systems with various radiometric resolutions (e.g., 8 bit for Landsat 7 ETM+, ASTER; 16 bit for EO-1 ALI). Additionally, several high spatial and spectral resolution (commercial) images were purchased for specific sites to study volcanic impacts on glaciers in greater detail (see results presented in Chapter 5).

4.1.5. Satellite data archives

Currently, images from a variety of satellites are available free of charge via numerous image providers. This includes optical, SAR and thermal remote sensing data from satellites such as ASTER, Landsat 1-9, Sentinel-1 and 2, MODIS and many more. An extensive list of image providers and available datasets, named 'Volcano Remote Sensing Cheat Sheet', can be accessed via the Global Volcano Monitoring Infrastructure Database (GVMID) website (https://wovodat.org/about/cov_timeline.php, accessed on 08/12/2022). Satellite images in archives are often provided at different processing levels. Level 1 data typically show at sensor, top-of-atmosphere radiance and include radiometric and geometric corrections, which can include the use of DEMs and/or ground control points. Level 2 data are further processed with atmospheric corrections to obtain bottom-of-atmosphere reflectance and can, e.g., provide information on surface temperature. Level 3 products are available, e.g., for the Landsat satellites with analysis ready data on, e.g., surface water extent or snow coverage. Specific processing steps performed within a certain processing level vary with satellite/sensor and respective information on processing levels for specific satellites can be found, e.g., at the USGS (www.usgs.gov, accessed on 08/12/2022), LP DAAC (https://lpdaac.usgs.gov/, accessed on 08/12/2022) and ESA (https://sentinel.esa.int/web/sentinel/home, accessed 08/12/2022) websites and available satellite product specifications.

Most satellite image providers have an easy-to-use interface that allow the user to search for images of a specific satellite, draw regions of interest (ROIs) and allow the search to be limited via dates of interest (such as start and end-date). Most providers also allow the results to be filtered with a cloud cover range. Often, the same images of a specific satellite are available via different image providers. The aforementioned image search capabilities also apply to commercial image providers; however, the process of ordering images is not always straightforward and available images might be limited to a comparably small number of satellites. Image providers (both for freely available and commercial products) used in this thesis are quickly presented here.

- The EarthExplorer developed by the United States Geological Survey (USGS) (https://earthexplorer.usgs.gov/, accessed on 08/12/2022) is a user interface providing a variety of satellite and aircraft-based data such as, e.g., ASTER, MODIS, EO-1 ALI satellite data, aerial imagery, UAS data and processed maps (e.g., vegetation maps).
- Google Earth Engine (GEE) (https://developers.google.com/earth-engine/guides/playground, accessed on 08/12/2022) provides options to view and download satellite images and even has capabilities to perform sophisticated planetary-scale geospatial analysis (Gorelick et al., 2017). Google Earth Engine can be accessed via an application programming interface (API) and an associated javascript-based interactive development environment (IDE) and hosts a public data catalogue with multi-petabyte of analysis-ready data within Google's high performance computing resources (Gorelick et al., 2017). This includes a large variety of satellite (derived) data such as SAR and optical satellite data (e.g., Sentinel-1 and 2), DEMs (e.g., ArcticDEM), climate/vegetation data (e.g., global temperature/precipitation and vegetation maps) and a small set of hyperspectral data from EO-1 Hyperion at different processing levels. The wide range of functions available in/accessible through GEE also include filtering and sorting similar to the search capabilities of 'typical' providers described above. In contrast to 'typical' image providers, GEE displays satellite images in full native, spatial resolution and bit depth (Gorelick et al., 2017).

- The image provider Planet (https://www.planet.com/, accessed on 08/12/2022) hosts commercial (medium-resolution) images from RapidEye, PlanetScope and SkySat satellites. Planet allows free of charge data access of 5,000 km^2/month through its Education and Research program (https://www.planet.com/markets/education-and-research/, accessed on 08/12/2022).
- Commercial (medium- and high-resolution) satellite images from, e.g., GeoEye-1, IKONOS, QuickBird or the WorldView satellites were downloaded from geocento (https://geocento.com/, accessed on 08/12/2022), which also provides an easy-to-use user-interface with the capability to select single images similar to the USGS EarthExplorer or Planet.

In contrast to image providers, virtual globes seamlessly mosaic images from a variety of (often high-resolution) sources and allow the Earth's surface to be viewed in 3D (Yu and Gong, 2012). Several virtual globes such as Google Earth (https://earth.google.com/web/, accessed on 22/12/2022), NASA World Wind (https://worldwind.arc.nasa.gov/, accessed on 22/12/2022) or Skyline Globe (https://www.skylinesoft.com/, accessed on 08/12/2022) are currently available. In this thesis, Google Earth proved particularly valuable to check a particular glacier's suitability for feature-tracking but was also used to search evidence of volcanic impacts on glacier morphology. Google Earth allows a user to zoom in and out, to change perspective and to display historical images (i.e., move through time). However, as with all virtual globes, it does not provide the option to download the underlying satellite images (in full resolution) for further GIS analysis.

Satellite images in this thesis were viewed and processed in GEE and the Open Source Geographic Information System QGIS versions 3.10. and 3.22. QGIS has an easy-to-use graphical user interface (GUI) and supports vector as well as raster data such as satellite images. It can be run on most Unix platforms, Windows and macOS ('QGIS Desktop 3.22 User Guide,' 2022).

4.1.6. Image enhancement

Since satellite images are acquired in digital format, their digital number (DN) values can be presented in a histogram. Contrast enhancement or histogram modification is a common technique to optimize image contrast and brightness and was heavily used in this thesis (Liu and Mason, 2009).

The contrast enhancement technique newly distributes the pixel DN values within an image using new minimum and maximum values and changing the distance between histogram bars (Liu and Mason, 2009; Campbell and Wynne, 2011). After loading a respective satellite scene in QGIS, the software automatically stretches to MinMax values to match the 8-bit (0-255) system for display on a computer screen ('QGIS Desktop 3.22 User Guide,' 2022).

Automatic stretching specifically becomes necessary if, e.g., 12-bit Sentinel-2 images are loaded. To further enhance contrast, the histograms of DN values were stretched based on user-defined minimum and maximum values. Doing so, all color values below the defined minimum value are assigned to the lowest gradient color and all values above the defined maximum value are assigned with the highest gradient color (GISP, 2016), which makes it possible to better distinguish between features, e.g., a dark crevasse on the bright glacier surface. Since most of the work in this thesis was done in the visible and near-infrared range of the electromagnetic spectrum, most satellite images were rendered as 'Multiband color' (for 3 band display as a combination of red, green and blue) or as 'Singleband grey' (e.g., for panchromatic images). The image viewing capabilities of GEE were used to view either 'Singleband-grey' or 'RGB composite' images and the range of DN values was limited to better display image contrast/visibility. Satellite image brightness and contrast was further enhanced using the respective Image Adjustment capabilities of Adobe Photoshop where necessary.

4.2. Feature tracking

Feature tracking techniques based on satellite imagery (or photographs) have been widely applied to address Earth science related problems such as the measurement of co-seismic ground displacement (Leprince et al., 2007), river flow (Muste et al., 2008), ocean surface currents (Breaker et al., 1994) or to measure the trajectory of pyroclasts during volcanic eruptions (Gaudin et al., 2016).

In the literature, feature tracking is widely applied to obtain glacier surface velocities (e.g., Herman et al., 2011; Mouginot and Rignot, 2015; Wilson et al., 2016; Dell et al., 2019; Millan et al., 2019; Van Wyk de Vries and Wickert, 2020).

Feature tracking also proved useful to determine velocity changes on glaciers located on active volcanoes. For example, Rivera et al. (2012) detected faster than usual surface velocities on a glacier on Volcán Michinmahuida (Chile) prior to the eruption of nearby Volcán Chaitén in 2008 using feature-tracking on ASTER VNIR satellite images (see Fig. 3.6 sub-section 3.1.3). Similarly, Martinis et al. (2007) found an increase in the velocity of Skeiðarárjökull glacier during the 2004 Grímsvötn eruption (Iceland) using image cross-correlation on ASTER images. Currently, there is a variety of different feature-tracking software available such as IMCORR (Scambos et al., 1992), COSI-CORR (Leprince et al., 2007), ImGRAFT (Messerli and Grinsted, 2015), autoRIFT (Lei et al., 2021), GIV (Van Wyk de Vries and Wickert, 2020) and some others.

In principle, feature-tracking (or image cross-correlation) techniques are based on particle image velocimetry (PIV), which was developed in the 1980s to investigate fluid motion with the help of small tracer particles (Westerweel, 1997; Adrian, 2005). PIV systems work with a pulsed laser, which produces a light sheet to illuminate particles in the flowing fluid. The emitted light is scattered by the particles into a lens oriented at 90° to the light sheet and recorded on a photograph, video or (since the advent of digital photography) on a charge-coupled device (CCD) (Adrian, 1991, 2005; Westerweel, 1997). The idea of auto- and cross-correlation of successive images to automatically extract particle displacement of recorded images has been developed since the 1980s and 90s. This included the division of the image into a grid of interrogation spots to find the mean displacement of multiple particles within each cell (Adrian, 2005).

4.2.1. Feature tracking in glaciology (Glacier Velocimetry)

The work of Bindschadler and Scambos (1991) and Scambos (1992) transferred the ideas of image cross-correlation to glaciology to measure glacier surface velocities on Ice Stream E in Antarctica. A very important pre-requisite for successful feature tracking on glacier surfaces is as precise as possible co-registration of the images (Scambos et al., 1992; Leprince et al., 2007; Kääb et al., 2016).

This stems from the problem of satellite images being acquired under variable illumination conditions and slightly different incidence angles, which contrasts the controlled laser lightning used in PIV laboratory settings (Berthier et al., 2005; Kääb et al., 2016; Van Wyk de Vries and Wickert, 2020).

To precisely co-register successive satellite images, early studies relied heavily on the presence of non-moving ground-control points (GCP) such as exposed bedrock (see references in Bindschadler and Scambos, 1991). However, with the cross-correlation technique, it was possible to circumvent the use of GCPs and use long-wavelength topographic undulations on the Antarctic ice stream to co-register satellite images. This even allowed the tracking of subtle surface features such as crevasse scars without sharp boundaries (Bindschadler and Scambos, 1991; Scambos et al., 1992).

To ultimately find displacements within successive images, the co-registered images are broken down into small rectangular image areas (so called 'chips') and the brightness pattern of a particular chip in one image is searched for in a successive image (see Fig. 4.7 and Fig. 4.8) (Bindschadler and Scambos, 1991; Scambos et al., 1992). Even with the early work of Bindschadler and Scambos (1991) and Scambos (1992) it was possible to measure displacements with better than one-pixel accuracy. The respective software package IMCORR is currently available as a SAGA-GIS module (https://saga-gis.sourceforge.io/saga_tool_doc/2.1.3/grid_analysis_19.html, accessed on 08/12/2022). Modern feature tracking software differ in the way they perform image correlation. Some rely on a normalized cross-correlation (NCC) approach operating in the spatial domain (described above), others operate in the frequency domain using a Fast Fourier Transform (FFT) (Heid and Kääb, 2012).

Satellite images today are commonly available as orthorectified (and geolocated) products (i.e., corrected for platform viewing geometry), which includes the use of (often global) digital elevation models (DEM) to move pixels back to their true positions and provide pixels with real-world ground coordinates (e.g., see Messerli and Grinsted, 2015; Kääb et al., 2016). This makes orthorectified satellite images in principle useful for glacier velocimetry without further image co-registration. The work of Kääb et al. (2016) investigated the geometric and radiometric performance of Sentinel-2 Level 1C images and their potential usability for glacier velocity measurements.

Vertical elevation errors of the DEMs used for image orthorectification can translate into horizontal offsets in the ortho-rectified product (so called co-registration accuracy) (Nuth and Kääb, 2011; Kääb et al., 2016).

These errors are particularly large for mountainous areas with steep slopes and – on a rapidly changing glacier surface – the DEMs used for orthorectification are quickly outdated (Berthier et al., 2005; Kääb et al., 2016).

The images also contain radiometric noise due to imperfect detector calibration, which can express itself in along-track stripes (Kääb et al., 2016). Both errors affect the accuracy of displacement measurements, since they can result in lateral offsets unrelated to glacier motion (Kääb et al., 2016). For Sentinel-2 data, these errors can be mitigated by the use of images from the same relative orbit (repeat orbit), which have the same pattern of DEM misinterpretations and therefore errors become eliminated in an offset field generated from these data (Kääb et al., 2016).

The tested, overall good radiometric and geometric performance of Sentinel-2 Level 1C data and the high co-registration accuracy of 1/10 of a pixel (i.e., 1-2 m) (Kääb et al., 2016) motivated their use for obtaining glacier velocities on Mount Veniaminof, Alaska, within this thesis. For this work, we used the feature tracking software 'Glacier Image Velocimetry' (GIV) developed by van Wyk de Vries and Wickert (2020). Sub-Section 4.2.3 presents a more in-depth explanation of practical feature tracking as applied within this software.

4.2.2. The GDM-OPT ICE service by CNRS EOST

In this thesis, two pieces of software were tested to obtain glacier velocities on Mount Veniaminof. Besides GIV (see sub-section 4.2.3), the GDM-OPT ICE (formerly called MPIC-OPT-ICE) service provided by the Centre National de la Recherche Scientifique (CNRS) and the Ecole et Observatoire des Sciences de la Terre (EOST) was extensively tested. The service provides access to a High Performance Computer (HPC) infrastructure through the ESA Geohazards Exploitation Platform (GEP) and can be purchased with an 'Advanced' GEP service pack. GDM-OPT ICE relies on the multiple-pairwise image matching (MPIC) of Sentinel-2 images and the user can process up to 100 images per request (with a maximum of 40 requests per month). Users can choose between two image cross correlation functions, MicMac and GeFolKi.

MicMac is a photogrammetry software originally designed for extraction of 3D information from 2D images. It has been developed by the National Institute of Geographic and Forestry Information (IGN) and the National School of Geographic Sciences (ENSG) since 2003. The software, comparable to other image cross correlation software, calculates similarity between images from a normalized cross correlation coefficient; however, it relies on multiple images rather than a single image pair (Rupnik et al., 2017).

GeFolKi is based on computation of optical flow and was developed by the French Aeronautics, Space and Defense Research Lab (ONERA) (Brigot et al., 2016; Provost et al., 2021). In contrast to MicMac, GeFolKi relies on the apparent motion of objects on two images caused by the relative motion between sensor and scene (Brigot et al., 2016). GeFolKi performs image co-registration on a pixel-by-pixel basis over a local window centred around that pixel (Brigot et al., 2016; Charrier et al., 2020). The GDM-OPT ICE service relies on the MPIC principle, which refers to pairwise matching of satellite images with different acquisition dates and calculation of mean displacement for a stack of images (Stumpf et al., 2017). The built-in time-series inversion capability enables the user to generate time-series inverted mean velocities, which rely on least squares inversion of the individual displacement measurements for each pixel (Bontemps et al., 2018).

On the platform, the user can select the input images directly (without a need to download a single satellite image) and, besides the image cross correlation function, can choose between several parameters such as Sentinel-2 image band, minimum and maximum image matching range and region of interest. A more in-depth description of the GDM-OPT ICE service can be found in the respective terradue documentation (https://docs.terradue.com/geohazards-tep/tutorials/GDM-OPT-ICE.html#use-case-ice-velocity-of-the-european-alps-glaciers-mont-blanc-massif, accessed on 08/12/2022).

The user can view outputs such as mean velocity fields (in N-S and E-W direction or overall velocity magnitude), mean velocities after inversion of the displacement time-series (in N-S and E-W direction or overall velocity magnitude) and some quality measures (e.g., vector coherence) directly on the platform.

Also, there is access to all individual displacement fields generated and all data can be downloaded from the platform.

In this thesis, we tested the overall usefulness of the GDM-OPT ICE service to obtain glacier velocities on glacierized volcanoes. We performed several test runs on Mount Hudson (Chile) and Mount Veniaminof (Alaska) with variable parameter settings. In principle, the obtained mean velocity fields look realistic, and we appreciate the image processing capability without the need to download a single satellite image.

In practice, however, we experienced long processing times (in the order of one day for ~10 satellite images) and frequent task failures using the service. To us, it seems like the overall purpose of GDM-OPT ICE is to produce as accurate as possible mean velocities based on image stacking and time-series inversion. Since the aim of the project presented in this thesis is to investigate pre-, syn- and post-eruption velocities, displacements have to be generated with a much higher temporal resolution. This could, in principle, be accomplished by downloading and further processing of the individual displacement maps, however, this would result in large data quantities (e.g., ~190 GB for the Tutorial region in the European Alps based on 73 Sentinel-2 images). We appreciate the capabilities of GDM-OPT ICE towards generation of accurate velocity maps; however, given the considerations above, we found the GIV software by van Wyk de Vries and Wickert (2021) to better serve our purpose. This software can process a series of ~100 satellite images in the order of ~20 min on a usual laptop/computer and comes with the capability to directly extract monthly velocities. GIV software is introduced more thoroughly in sub-section 4.2.3.

4.2.3. ‘Glacier Image Velocimetry’ (GIV) software

The freely available feature tracking software package ‘Glacier Image Velocimetry’ (GIV) was specifically developed to calculate surface velocities of glaciers from satellite images. GIV is not designed to co-register images, but relies on already orthorectified products (in UTM coordinates) such as Level 1C Sentinel-2 images (Van Wyk de Vries and Wickert, 2020). Along with the feature tracking procedure itself, the software is quickly introduced here, but for a full description see van Wyk de Vries and Wickert (2020) and the ‘Glacier Image Velocimetry User Manual’ provided as Supplement to the publication.

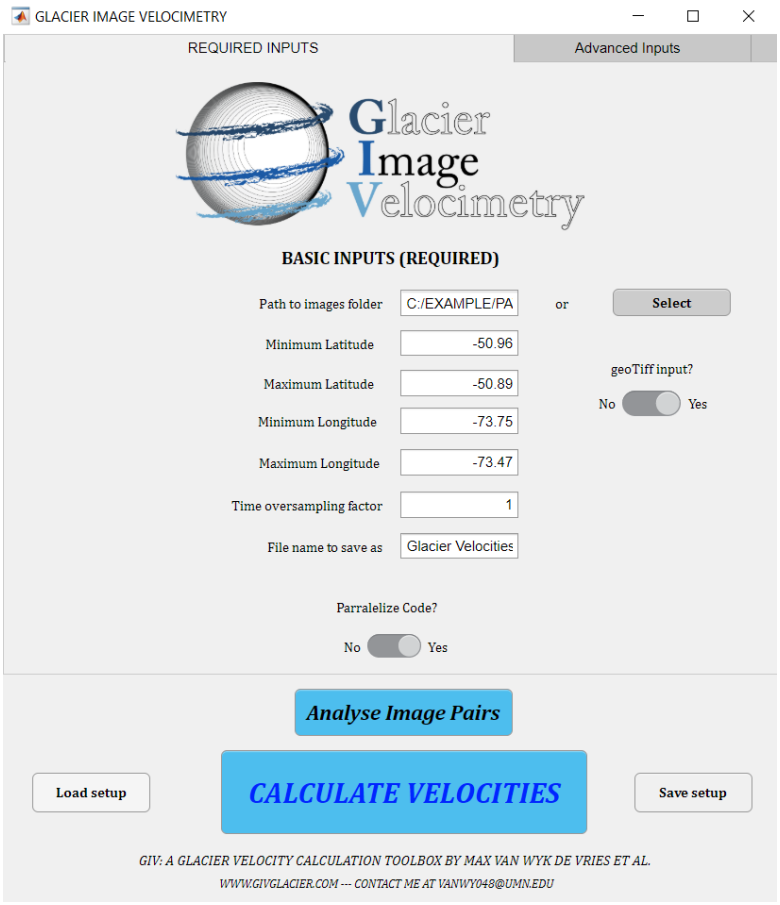

Fig. 4.6 GIV GUI main window with options to set the path to the images folder, add minimum and maximum latitude/longitude values (not required for geotiff input), set the time oversampling factor and 'Analyse image Pairs' (which calculates the 'Total number of image pairs' and the 'Number of image pairs per individual oversample')

GIV is written in Matlab and can be run on any usual computer using a GUI (Fig. 4.6) or a standalone app. The software is able to compute multiple displacement fields in parallel, dependent on the number of physical cores on the user's computer. It reads satellite images both in geotiff and jpg formats and extracts acquisition year, month and day directly from the filenames (if named in yyyymmdd format).

The coordinates are directly read from the UTM geocoded satellite image. The area of a glacier of interest is extracted from a modified satellite image, which has the respective area drawn on in pure white (255,255,255). The software allows minimum and maximum time separation to be set, which ensures a reasonably high number of image pairs with good coherence. A reasonable choice of time separation depends on an initial estimation of the glacier velocity to ensure detectable glacier displacement within a certain time interval (Scambos et al., 1992).

This means that, if the glacier moves very slowly and time separation between image pairs is too low, geometric errors might be larger than detectable glacier displacement. However, if the glacier moves too fast, a respective image pair with too large time separation might lose coherence (Van Wyk de Vries and Wickert, 2020). The software also allows a temporal oversampling factor to be set, which enables velocity maps to be generated for both consecutive and non-consecutive image pairs. This allows to control the number of total image pairs generated. As with IMCORR mentioned in section 4.2, satellite images are broken down in a grid of chips (Fig. 4.7).

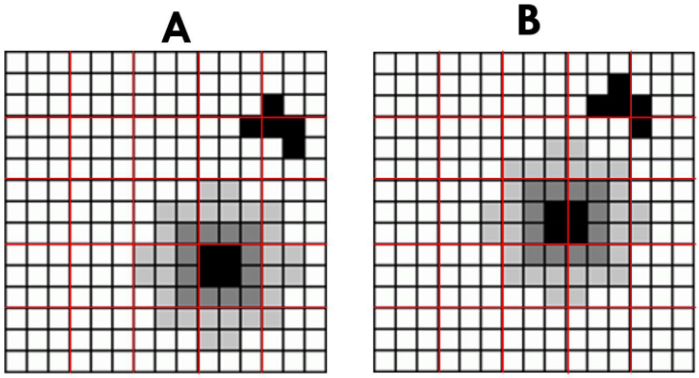

Fig. 4.7 Features in image (A) are displaced to a different location in image (B). Grid of 'chips' presented as red rectangles. Figure from 'Glacier Image Velocimetry User Manual' (Van Wyk de Vries and Wickert, 2020)

Each chip in one image is compared to all the chips in a second image and a correlation coefficient using a fast Fourier transform (FFT) is calculated for each of the chips. In a next step, a Gaussian curve is fitted to the correlation coefficients to find the peak location at sub-pixel accuracy (i.e., independent of chip-size) (Fig. 4.8).

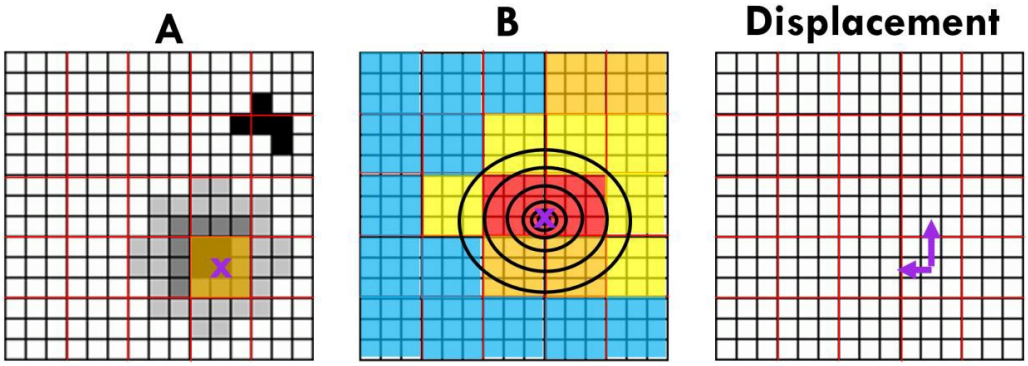

Fig. 4.8 Location of the purple x in image (A) is found in image (B) after calculation of correlation coefficients for all the image chips (blue: low correlation, red: high correlation) and fitting of a Gaussian peak (black ellipses). From this, the displacement vectors of the chip are determined (purple arrows in image 'Displacement'). Figure from 'Glacier Image Velocimetry User Manual' (Van Wyk de Vries and Wickert, 2020).

The final velocity is calculated from the displacement and the time difference between image A and B (which is calculated from the extracted dates of the filenames). Several filters are included in GIV to reduce noise, to emphasize trackable features (i.e., to increase contrast) and to extract features even on cloudy images. A built-in multi-pass method makes use of reducing window sizes to increase the signal-to-noise ratio. In post-processing, the software automatically detects outliers via outlier detection functions and allows the user to both set a maximum velocity threshold and to limit the range of possible flow directions. Also, the software provides the option to define a stable (i.e., non-moving) region to correct for systematic georeferencing errors.

The software re-calculates the raw displacement fields by a weighted mean approach to obtain monthly velocity fields. Output files are saved as Matlab arrays and output images are presented both as quick-view png figures and georeferenced velocity maps in geotiff format, that can directly be loaded into GIS systems. Additionally, the software optionally allows to extract time-series data for flow velocity and flow direction for user-selected points on the glacier of interest.

Chapter 5 Assessment of the use of optical satellite images to detect volcanic impacts on glacier surface morphology – (published)

This Chapter presents the results on the investigation of the visibility (i.e., necessary temporal and spatial resolution) of volcanic impacts on glacier surface morphology in optical satellite imagery for a selection of representative ice-clad volcanoes from around the globe. These results were published in Martin et al. (2021), see Appendix 2. Please find a list of the author contributions at the end of this chapter. A more detailed description of the examples presented in this Chapter can be found in Chapter 3 and Table 5 in the Appendix 1.

5.1. Introduction

The potential of glaciers possibly providing precursory information on volcanic activity through changed patterns of crevassing, glacier velocities, glacier thicknesses and/or glacier runoff has been noted quite early (e.g., Brugman and Post, 1981). Early studies used the first available Landsat 1 images to survey the Vatnajökull ice cap in Iceland using digital image enhancement techniques. Elliptical supraglacial calderas and depressions were identified in these images and linked to subglacial volcanic activity (Williams, 1987; Björnsson and Einarsson, 1990). Even after the early studies mentioned above, optical satellite images have played an important role in investigating volcanically triggered changes to glacier morphology. For example, Bleick et al. (2013) observed the formation of supraglacial holes and a prominent ice-cauldron with associated concentric crevassing prior to the 2009 Mount Redoubt (Alaska) eruption with the help of high-resolution Quickbird satellite images and aerial photographs (Bleick et al., 2013). Patrick et al. (2005) and Patrick and Smellie (2013) investigated volcanically triggered changes to glaciers in remote Antarctica and glaciated islands in the southern oceans using both low-resolution ASTER, Landsat 7, EO-1 ALI and high-resolution IKONOS and Quickbird satellite images. Based on these images, lava flows/lakes, tephra cover and snow-free zones (often coinciding with fumarolic activity) were identified due to their distinct appearance relative to snow-covered surfaces (Patrick et al., 2005; Patrick and Smellie, 2013).

Additionally, it was possible to detect potentially volcanically triggered glacier surface crevassing on Montagu Island due to the emplacement of a lava flow (Patrick and Smellie, 2013).

Observed large-scale crevassing of the glacier surface was related to the flow of basal meltwater, which likely destabilized the overlying ice (Patrick and Smellie, 2013). The studies by Patrick et al. (2005) and Patrick and Smellie (2013) generally show the value of investigating volcanic activity with optical satellite images for remote/inaccessible places on Earth and point to a more systematic exploitation as presented in the following (sub-)sections of this thesis.

5.2. Methods

5.2.1. Glacierized volcanoes investigated in this thesis

The literature reveals a total of ~69 instances of documented volcanic impacts on glaciers at ~43 volcanoes globally from 1972 to 2015 (i.e., during the optical satellite era) (Barr et al., 2018a). Detailed analysis of each of these instances included satellite image viewing of the surface expression of the respective volcanic impact and literature search. This thesis focuses on a selection of the best-documented examples that potentially represent major volcanic impacts on glacier surface morphology from 1972 to 2015 and are therefore considered representative (see Fig. 5.1 and Table 1). Table 5 in the Appendix 1 reports the geology/glaciology of the respective glacier-clad volcanoes and the eruption dates/characteristics.

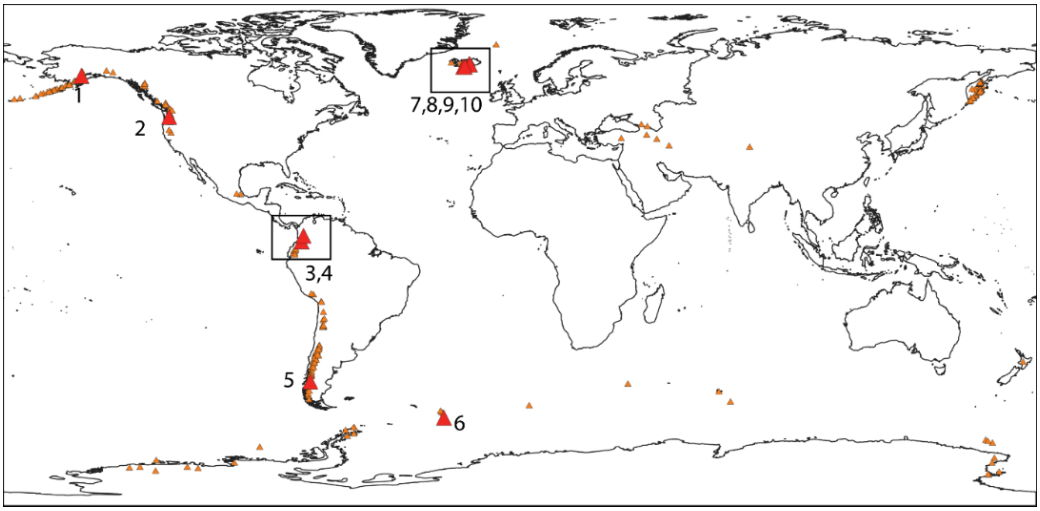

Fig. 5.1 Glacierized volcanoes around the globe (small orange triangles), (Edwards et al., 2020) and volcanoes investigated in this study (red triangles, numbered). For some volcanoes, multiple events are investigated. Volcano names are detailed in Table 1. Basemap: 'World Continents'

Table 1 Ice-clad volcanoes investigated in this thesis (volcano numbers relate to Fig. 5.1, Table 5 and Table 6 in the Appendix 1). Examples illustrated in Chapter 5 are shown in bold.

Volcano number	Volcano name	Volcano type	Region/country	Coordinates (lat, lon)	Period of activity
1	**Mount Redoubt**	**Stratovolcano**	**Alaska (US)**	**60.485, -152.742**	**03/2009–04/2009**
2	**Mount St. Helens**	**Stratovolcano**	**United States**	**46.2, -122.18**	**03/1980–10/1980 09/2004–2006**
3	Nevado del Ruiz	Stratovolcano	Colombia	4.892, -75.324	11/1985
4	Nevado del Huila	Stratovolcano	Colombia	2.93, -76.03	02/2007–05/2009
5	**Mount Hudson**	**Stratovolcano**	**Chile**	**-45.9, -72.97**	**10/2011–12/2011**
6	**Mount Belinda (Montagu Island)**	**Shieldvolcano**	**South Sandwich-Islands (UK)**	**-58.445, -26.374**	**10/2001–09/2007**
7	**Eyjafjallajökull**	**Central volcano**	**Iceland**	**63.633, -19.633**	**03/2010–06/2010**
8	**Katla (Mýrdalsjökull)**	**Subglacial central volcano**	**Iceland**	**63.633, -19.083**	**1999–2005**
9	Grímsvötn (Gjálp)	Subglacial volcanic fissure	Iceland	64.416, -17.316	09/1996–10/1996
10	**Bárðarbunga**	**Subglacial central volcano**	**Iceland**	**64.633, -17.516**	**08/2014–02/2015**

5.2.2. Satellite image download/viewing

In this thesis, ~1400 freely available low- to medium-resolution, and a limited number of commercial, high-resolution, optical satellite images were investigated. We obtained freely available (non-commercial) images mostly through Google Earth Engine (GEE) (https://developers.google.com/earth-engine/guides/playground, accessed on 08/12/2022) and USGS EarthExplorer (https://earthexplorer.usgs.gov/, accessed on 08/12/2022). An example of a GEE javascript code for an ASTER image search during the 2009 active period of Mount Redoubt is provided in the github repository of this thesis (https://github.com/mmartin17/glaciovolcanism).

This thesis made use of the full ASTER, Landsat and Sentinel-2 archives included in the GEE data catalogue. We mostly used the USGS Earth Explorer to obtain EO-1 ALI data, which are not included in the Google Earth Engine catalogue at the time of writing.

We viewed/downloaded ASTER, Landsat, EO-1 ALI and Sentinel-2 data at processing Level 1 (see sub-section 4.1.5) and obtained commercial satellite images through geocento (https://geocento.com/, accessed on 08/12/2022) and Planet (https://www.planet.com/, accessed on 08/12/2022) satellite image providers (see Table 7 in the Appendix 1). We accessed Planet images for free through Planet's Education and Research Program (https://www.planet.com/markets/education-and-research/, accessed on 08/12/2022). Table 2 summarizes the satellites used in this thesis. Table 6 in the Appendix 1 details the datasets/data providers and the number of available (and useful) satellite images per investigation site. We viewed the images in the visible and near-infrared range of the electromagnetic spectrum (including panchromatic bands) and enhanced the images for better visibility using contrast enhancement/histogram stretch (where appropriate) in QGIS 3.10 (QGIS.org, 2021. QGIS Geographic Information System. QGIS Association. (https://qgis.org/en/site/, accessed on 08/12/2022). More information on the satellite data archives used and the image enhancement technique applied can be found in sub-sections 4.1.5 and 4.1.6, respectively.

Table 2 Specification of satellites used in this thesis based on information from ESA (https://earth.esa.int/, accessed on 08/12/2022), ESA Earth Observation Portal (https://eoportal.org/, accessed on 08/12/2022), Satellite Imaging Corporation (https://www.satimagingcorp.com/, accessed on 08/12/2022), USGS (https://www.usgs.gov/, accessed on 08/12/2022) and Sentinel-Hub (https://docs.sentinel-hub.com/api/latest/, accessed on 08/12/2022)

Satellite Name	**sensor**	**Launch**	**Decomission**	**spatial resolution multispectral [m]**	**spatial resolution panchromatic [m]**	**revisit time/repeat cycle [days]**
Non-commercial satellites						
Terra	ASTER	December 18th 1999	in operation	15	N/A	16
Landsat 2	Multispectral Scanner (MSS)	January 22nd 1975	July 27th 1983	80	N/A	18
Landsat 3	Multispectral Scanner (MSS)	March 5th 1978	September 7th 1983	80	N/A	18
Landsat 4	Multispectral Scanner (MSS)	July 16th 1982	June 15th 2001	80	N/A	16
	Thematic Mapper (TM)			30	N/A	16
Landsat 5	Multispectral Scanner (MSS)	March 1st 1984	June 5th 2013	80	N/A	16
	Thematic Mapper (TM)			30	N/A	16
Landsat 7	Thematic Mapper (ETM+)	Apr 15 th 1999	in operation	30	15	16
Landsat8	Operational Land Imager (OLI)	February 11th 2013	in operation	30	15	16
EO-1	Advanced Land Imager (ALI)	November 21st 2000	Feb 22nd 2017	30	10	16
Sentinel-2	MultiSpectral Instrument (MSI)	Sentinel-2A: June 23rd 2015, Sentinel-2B: March 7th 2017	in operation	10	N/A	5
RapidEye	RapidEye Earth Imaging System (REIS)	August 29th 2008	Mar 2020	6.5	N/A	5.5

PlanetScope	Four-band frame Imager	June 22 2016 (launch of first satellites)	in operation	3.7-4.0	N/A	1
Commercial satellites						
IKONOS-2	Optical sensor assembly (OSA)	Sept 24th 1999	March 31st 2015	3.2	0.82	1-4
QuickBird2	Ball Global Imaging System 2000 (BGIS 2000)	October 18th 2001	January 27th 2015	2.62	0.65	1-3.5
WorldView-1	WorldView-60 camera (WV60)	Sep 18th 2007	in operation	N/A	0.5	1.7
WordView-2	WordView-110 camera (WV110)	October 8th 2009	in operation	1.8	0.46	up to 1.1
GeoEye-1	GeoEye Imaging System (GIS)	Sep 6 2008	in operation	1.64	0.41	1.7

5.3. Results

5.3.1. Ice cauldron formation

In principle, ice cauldrons are readily detectable with low-resolution satellite imagery, particularly within thick ice. With satellite sensors operating in the visible and near-infrared range (including multispectral and panchromatic bands), cauldrons appear as dark (shaded) areas against the bright ice surface. Ice cauldrons, despite heavily related to the appearance of concentric crevassing, are treated separately in this Chapter due to their different appearance in optical satellite imagery. A period of geothermal activity beneath Mýrdalsjökull (Katla) between 1999 and 2005 led to the formation of large ice cauldrons, which are identifiable on ASTER visible and near-infrared (VNIR) images (15 m resolution, Fig. 5.2). During the 2014–2015 Bárðarbunga eruption, three cauldrons developed on the surface of Dyngjujökull glacier in the northern part of the Vatnajökull ice cap. These cauldrons are clearly visible as shadows against the snow-covered ice in a true-colour composite EO-1 ALI image (30 m resolution; Fig. 5.3b).

However, in a snow-free EO-1 ALI image (Fig. 5.3c), the cauldrons are not visible, since transmitted radiance from the cauldrons region is not distinguishable from the surrounding dirty ice (even though the cauldrons are present at the time of image capture, as shown by Reynolds et al. (2017) using aerial- and TerraSAR-X imagery). An enlarged view of the northernmost cauldron shows evidence of faint concentric crevassing (Fig. 5.3d).

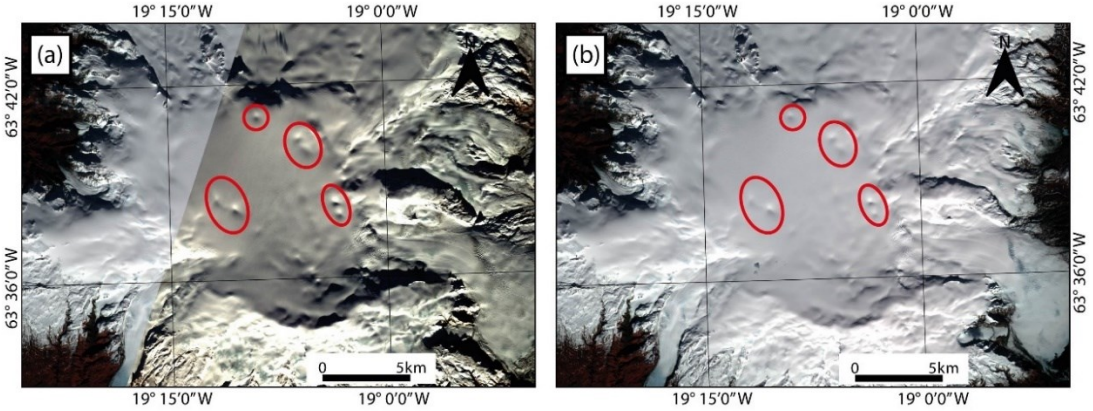

*Fig. 5.2 ASTER VNIR images (15 m resolution) of Mýrdalsjökull (Katla volcano beneath ice cap). (**a**) from 7 November 2002 and (**b**) from 17 March 2004. Both images show cauldrons over-active geothermal areas (encircled in red).*

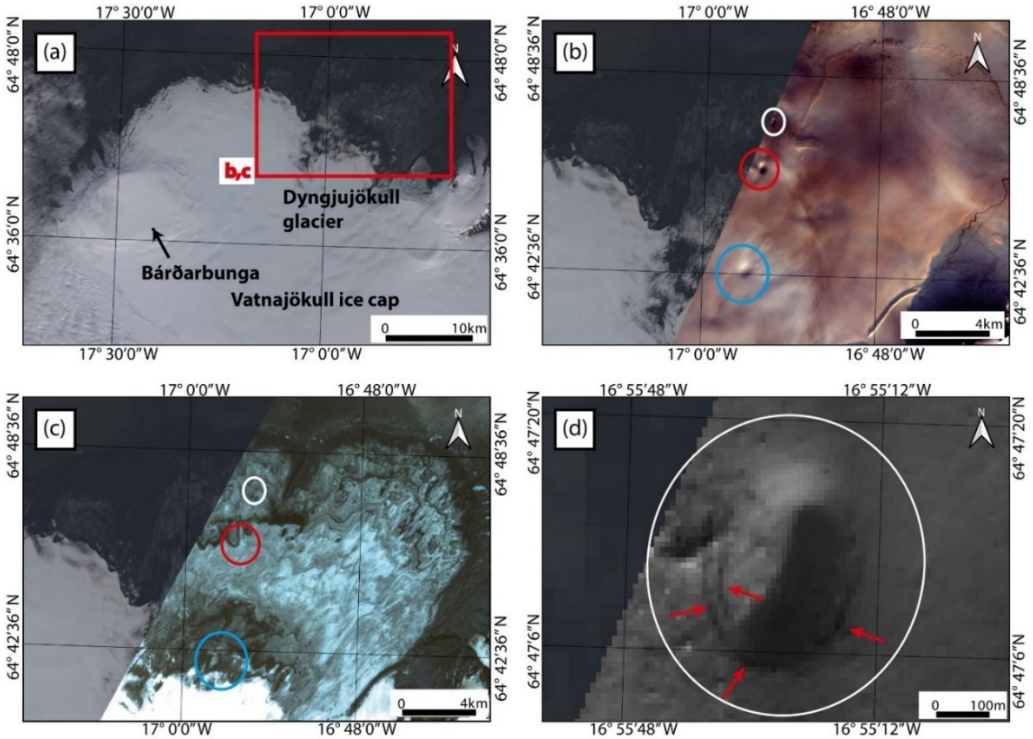

Fig. 5.3 (a) Landsat 8 overview image (30 m resolution) of the northern part of Vatnajökull ice cap. Red rectangle shows the study area on Dyngjujökull glacier (subfigures b and c). (b) EO-1 ALI true-colour composite images (30 m resolution) from 4 November 2014 (snow-covered) and (c) 20 September 2014 (non- snow-covered) showing Dyngjujökull glacier. For both images, three cauldrons are encircled in white, red and blue. Background image (non snow-covered) from Landsat 8 for all images (b–d). (d) EO-1 ALI panchromatic image (10 m resolution) from 4 November 2014, enlarged to show a cauldron with faint concentric crevassing (crevasses indicated with red arrows).

5.3.2. Opening formation

Volcanically triggered openings on the glacier surface are in principle observable with low-resolution images (>15 m resolution), however, they are best observed with at least medium-resolution images (~5 m resolution or better) due to the surface texture making it difficult to distinguish between openings and other features on the glacier surface. A notable example comes from Eyjafjallajökull (Fig. 5.4a), where the 2010 eruption, besides melting through the entire ice column in the main crater, produced openings on Gígjökull glacier (Fig. 5.4b,c). A view from April 2010 shows the intact surface of the glacier before the explosive phase of the eruption (inset Fig. 5.4a). Several openings (without concentric crevassing) developed in the upper part of Gígjökull glacier during the eruption due to subglacial meltwater flow (Oddsson et al., 2016), and are visible in low-resolution ASTER images (Fig. 5.4b), but better seen with WorldView-1 imagery (2 m resolution) acquired on the same day (red arrows, Fig. 5.4c).

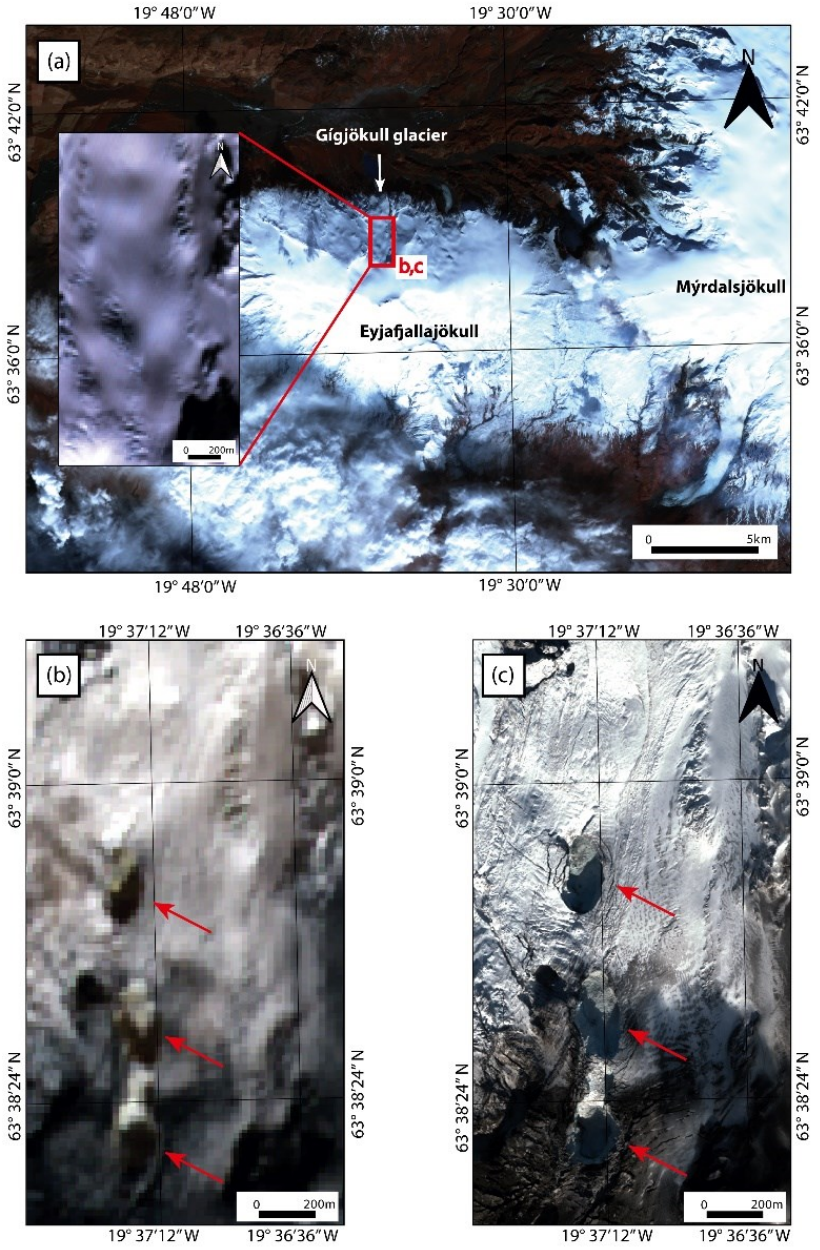

*Fig. 5.4 (**a**) ASTER VNIR (15 m resolution) overview image of Eyjafjallajökull from 01 April 2010, with a small box showing the study area on Gígjökull glacier. The ASTER VNIR image (15 m resolution) in the inset shows the intact glacier surface before the summit eruption. (**b**) ASTER VNIR (15 m resolution) image and (**c**) WorldView-1 visible image (2 m resolution), both acquired on 19 April 2010 during the summit eruption showing at least three openings on the glacier surface (red arrows);WorldView-1 image: DigitalGlobe Products. WorldView-1 © 2010 DigitalGlobe, Inc., a Maxar company, Westminster, CO, USA.*

5.3.3. Glacier crevassing

In this section, volcanic activity that leads to crevassing of glacial ice is considered. Ice cauldron formation is commonly associated with concentric crevassing (sub-section 5.3.3.1).Other volcanic factors that can lead to glacier crevassing include subglacial lava dome growth (sub-section 5.3.3.2), localized crevassing adjacent to supraglacial lava flows (sub-section 5.3.3.3) and widespread (glacier-wide) crevassing due to glacier acceleration/advance triggered by increased meltwater at the ice-bed interface (sub-section 5.3.3.4).

5.3.3.1. Concentric crevassing due to Ice Cauldron Formation

Concentric crevasses related to cauldron formation on ice-covered stratovolcanoes are observed with medium- to high-resolution images, but are too small to be identified with low-resolution images alone. In principle, crevasses can be identified in satellite images as dark fissures on the bright coloured glacial ice and snow. Fig. 5.5a shows Mount Redoubt shortly before its eruption in March 2009, and Fig. 5.5b–d reveal the capabilities of medium- and high-resolution images for ice-cauldron/crevassing detection at this volcano. In this example, the low-resolution ASTER image (Fig. 5.5c) and high-resolution IKONOS- 2 image (Fig. 5.5d, 0.8 m resolution) were acquired on the same day. The ice cauldron and concentric crevasses are more clearly visible in the IKONOS-2 image than in the ASTER image due to its high spatial resolution. With high-resolution images, it is not only possible to identify concentric crevasses, but also to accurately monitor their evolution (including changes in their number, length and width). This becomes clear if Fig. 5.5b is compared to Fig. 5.5d. The satellite image in Fig. 5.5b was acquired several days before those of Fig. 5.5c,d and shows a smaller, less evolved cauldron and fewer/smaller crevasses (blue arrows).

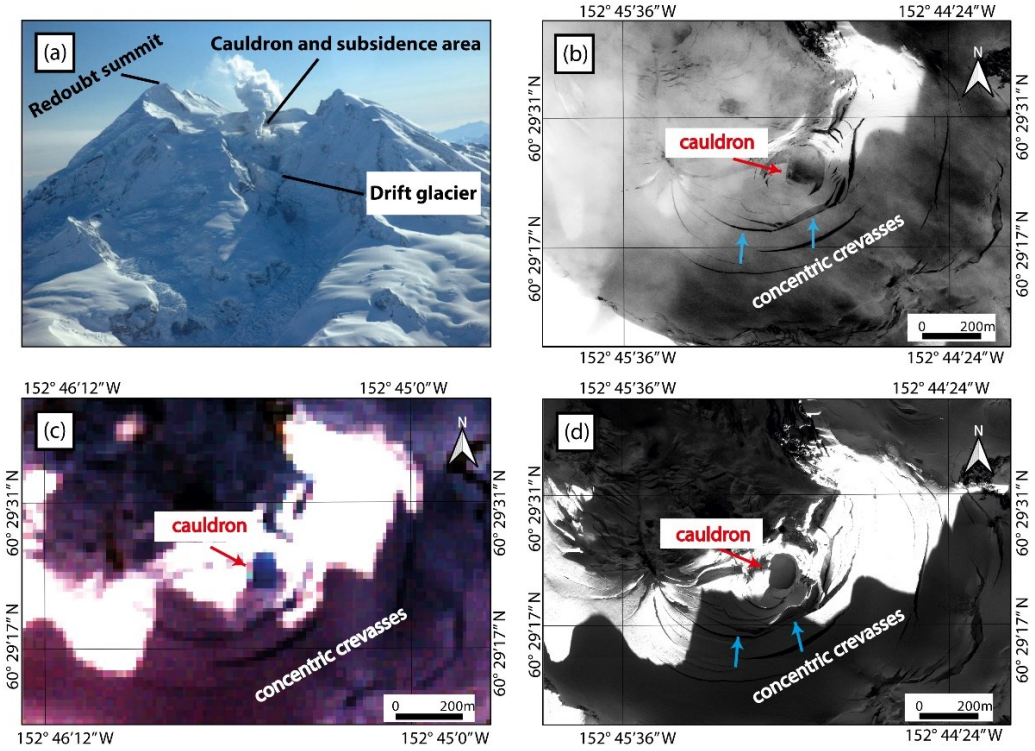

*Fig. 5.5 (**a**) photograph of north flank of Mount Redoubt from 15 March 2009 (shortly before its eruption; photo by H. Bleick AVO/USGS). The study site shown in panels (**b**–**d**) lies within the cauldron and subsidence area. (**b**) IKONOS-2 panchromatic image (0.8 m resolution) from 19 February 2009 showing an ice-cauldron and concentric crevasses. (**c**) ASTER VNIR image (15 m resolution). (**d**) IKONOS-2 panchromatic image (0.8 m resolution) showing a large ice-cauldron and concentric crevassing. Blue arrows show the locations of growing crevasses/increased number of crevasses. Images (**c**) and (**d**) were both acquired on 02 March 2009, and all subfigures (**b**–**d**) cover the same spatial area. IKONOS-2 products: DigitalGlobe Products. IKONOS-2 © 2009 DigitalGlobe, Inc., a Maxar company, Westminster, CO, USA.*

In contrast to the cauldrons on Mount Redoubt presented above, in some cases, cauldrons lack a clearly-identifiable central melt-pit and are therefore only indicated by concentric crevassing. This is the case for Mount Hudson during its 2011 eruption, as revealed by Rapid-Eye imagery (5 m resolution, Fig. 5.6).

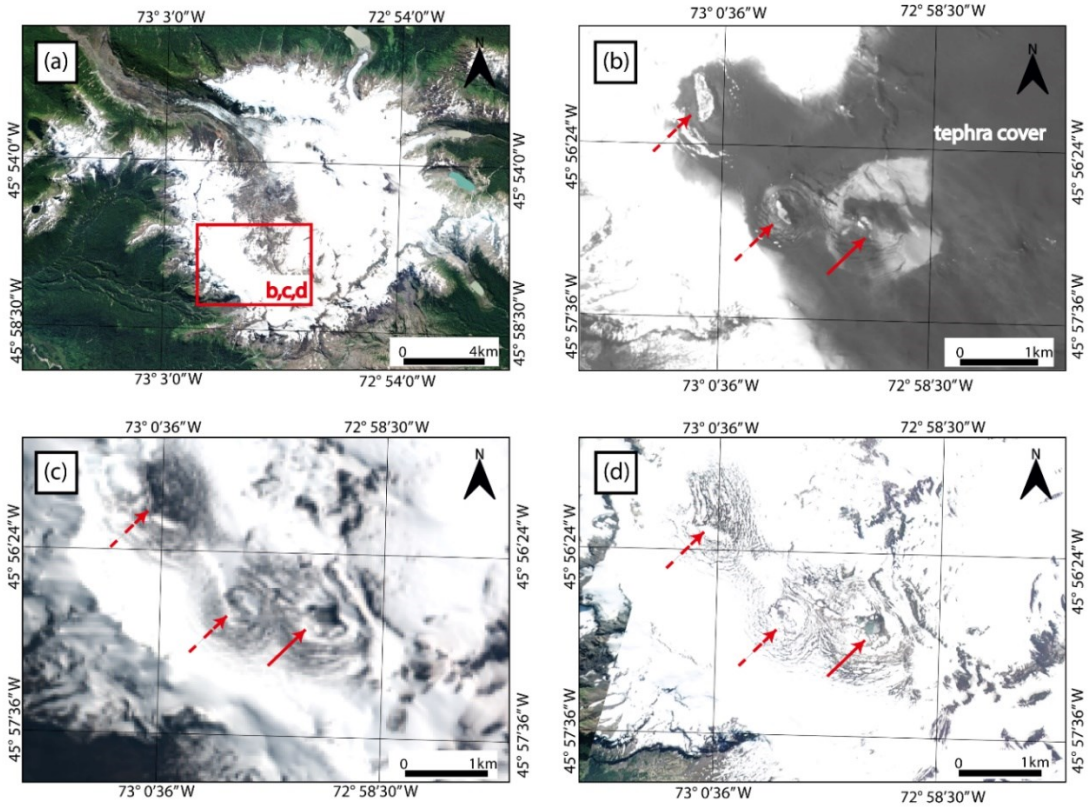

*Fig. 5.6 (**a**) Rapid-Eye true-colour overview image (5 m resolution) of Mount Hudson from 19 February 2011, (**b**) EO-1 ALI panchromatic image (10 m resolution) from 01 Novemer 2011, (**c**) EO-1 ALI true-colour image (30 m resolution) from 30 Novemer 2011 and (**d**) Rapid-Eye true-colour image (5 m resolution) from 01 December 2011. All subfigures (**b**–**d**) show the same extent and show one cauldron (red bold arrow) and the (possible) location of two more cauldrons (red dashed arrows); Rapid-Eye image: Planet Team (2017), https://www.planet.com/ , accessed on 22 December 2022).*

5.3.3.2. Crevassing due to Subglacial Lava Dome Growth

Subglacial dome growth on ice-covered stratovolcanoes commonly results in small-scale crevassing, which is often only visible in medium- to high-resolution images. During the eruption of Mount St. Helens from 2004 to 2006, a lava dome gradually developed beneath a small crater-occupying glacier. In the initial stage of the eruption in early October 2004, a melt hole formed in the glacier surface (red arrow in Fig. 5.7b) and parts of East Crater glacier became crevassed due to the onset of lava dome growth (Fig. 5.7b). As the lava dome continued to grow, it extruded through the ice, resulting in the deformation and heavy crevassing of East Crater glacier (Fig. 5.7c,d). The impact of dome growth (ice displacement, crevassing and melt-hole formation) on very small glaciers (~1 km2, 200 m thick) such as the one described are best viewed with at least medium-resolution images such as QuickBird 2 (Fig. 5.7c, 2.4 m).

High-resolution images (such as QuickBird-2 panchromatic, 0.6 m) might be required particularly when it comes to small scale crevassing (Fig. 5.7b). The impacts mentioned are less clear in medium-resolution EO-1 ALI panchromatic images (10 m resolution, Fig. 5.7d), and almost impossible to observe in low-resolution imagery (>10 m resolution).

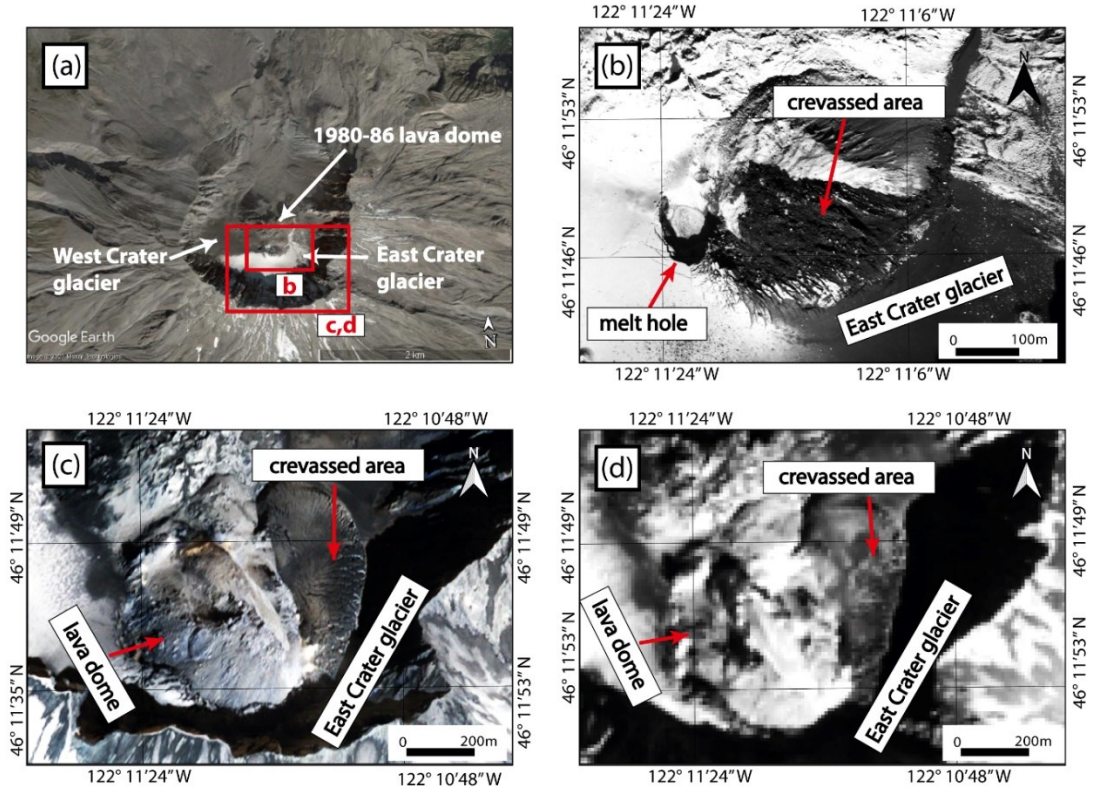

*Fig. 5.7 (a) GoogleEarth image from 03 October 2004 showing the Mount St. Helens summit crater (© 2021 Maxar Technologies). (b) QuickBird 2 panchromatic image (0.6 m resolution) from 05 October 2004. (**c**) QuickBird-2 visible image (2.4 m resolution) from 13 March 2005. (**d**) EO-1 ALI panchromatic image (10 m resolution) from 15 March 2005. All images show the impacts (crevassing, melt-hole formation) on East Crater glacier due to subglacial lava dome growth (DigitalGlobe Products. QuickBird-2 © 2004, 2005 DigitalGlobe, Inc., a Maxar company, Westminster, CO, USA).*

5.3.3.3. Localized Crevassing Due to Supraglacial Lava Flows

Medium-resolution satellite images (i.e., with resolutions of ~10 m or better) are sufficient to detect crevasses caused by supraglacial lava flows. For example, from 2001–2007, a (mostly effusive) eruption at Mount Belinda (Montagu Island) (Fig. 5.8a) resulted in supraglacial lava flows, which are clearly visible in medium-resolution EO-1 ALI panchromatic imagery (Fig. 5.8b). This medium-resolution imagery also reveals localised crevasses surrounding the supraglacial lava flow (reported by Patrick and Smellie, 2013; see Fig. 5.8b).

These crevasses presumably indicate that the lava melted deep channels/gullies into the glacier surface (Patrick et al., 2005; Patrick and Smellie, 2013; Smellie and Edwards, 2016). These melt-gullies are difficult to observe directly, but their impact on the surrounding ice is observed in medium-resolution imagery.

5.3.3.4. Widespread Crevassing Due to Glacier Acceleration/Advance

During the 2001–2007 eruption at Mount Belinda, the outlet glacier which drains the volcano's northern flank experienced widespread (i.e., glacier-wide) crevassing. This crevassing is thought to reflect glacier acceleration and advance (i.e., 'surging') in response to subglacial meltwater release during the eruption (Smellie and Edwards, 2016). The Landsat-7 panchromatic image (15 m resolution) in Fig. 5.8a shows the largely intact (i.e., minimally crevassed) glacier surface ~9 months before the onset of volcanic activity. By contrast, the EO-1 ALI panchromatic images in Fig. 5.8c,d, acquired during the eruptive period, shows widespread crevassing of the glacier surface. Thus, unlike localized crevassing related to ice cauldrons or volcanic dome growth (e.g., sub-sections 5.3.3.1 and 5.3.3.2), widespread glacier crevassing at Mount Belinda is identifiable even without access to high-resolution imagery.

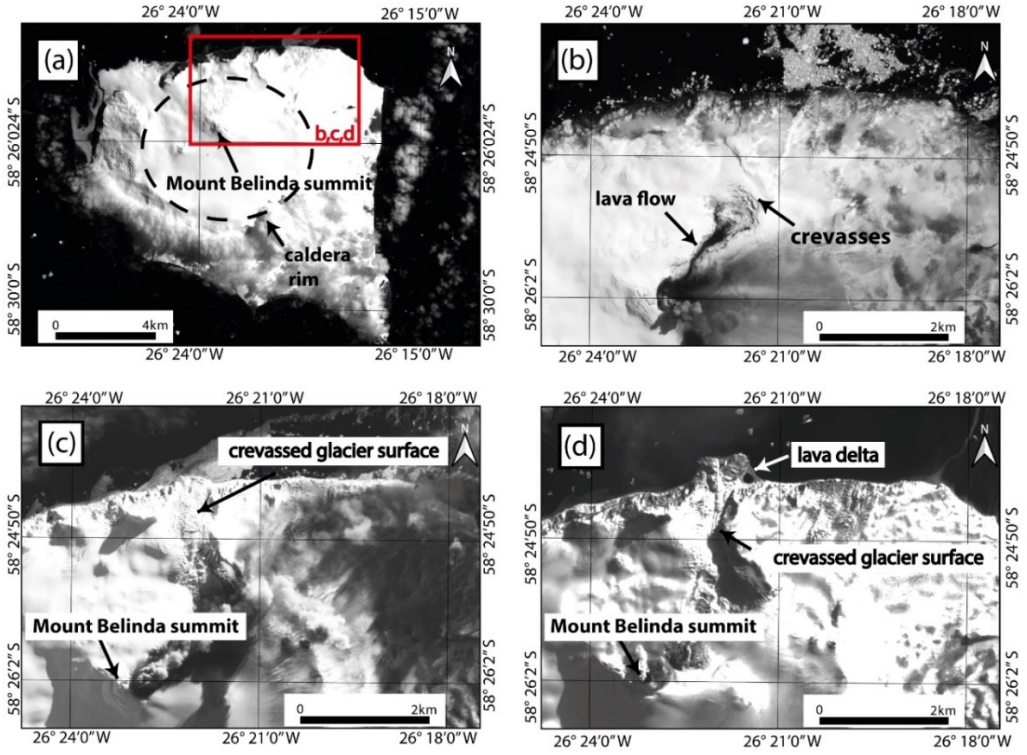

*Fig. 5.8 (**a**) Landsat 7 panchromatic image (15 m resolution) acquired on 24 January 2001 showing Montagu Island before the start of an eruptive period at Mount Belinda. (**b**) EO-1 ALI panchromatic image (10 m resolution) from 07 December 2003 showing a supraglacial lava flow, and associated crevassing. (**c**) EO-1 ALI panchromatic image (10 m resolution) from 06 August 2005. (**d**) EO-1 ALI panchromatic image (10 m resolution) from 18 August 2007. Subfigures (**c**) and (**d**) show widespread glacier crevassing. All subfigures (**b**–**d**) cover the same region of the northern part of the caldera.*

5.3.3.5. Mount Veniaminof: A Recent Example

In this sub-section, we document changes in glacier surface morphology on Mount Veniaminof (Alaska) during its very recent active period from March–April 2021. Emission of ash-plumes, (potential) lava effusion under the intra-caldera glacier and subsidence of glacier ice was reported (*Global Volcanism Program. Report on Veniaminof (United States). In: Sennert, S K (ed.)*). Both low spatial resolution Landsat-8 panchromatic images (15 m resolution) and medium spatial resolution Sentinel-2 images (10 m resolution) are sufficient to detect a newly developed ice cauldron and concentric crevasses in the glacier surface (Fig. 5.9).

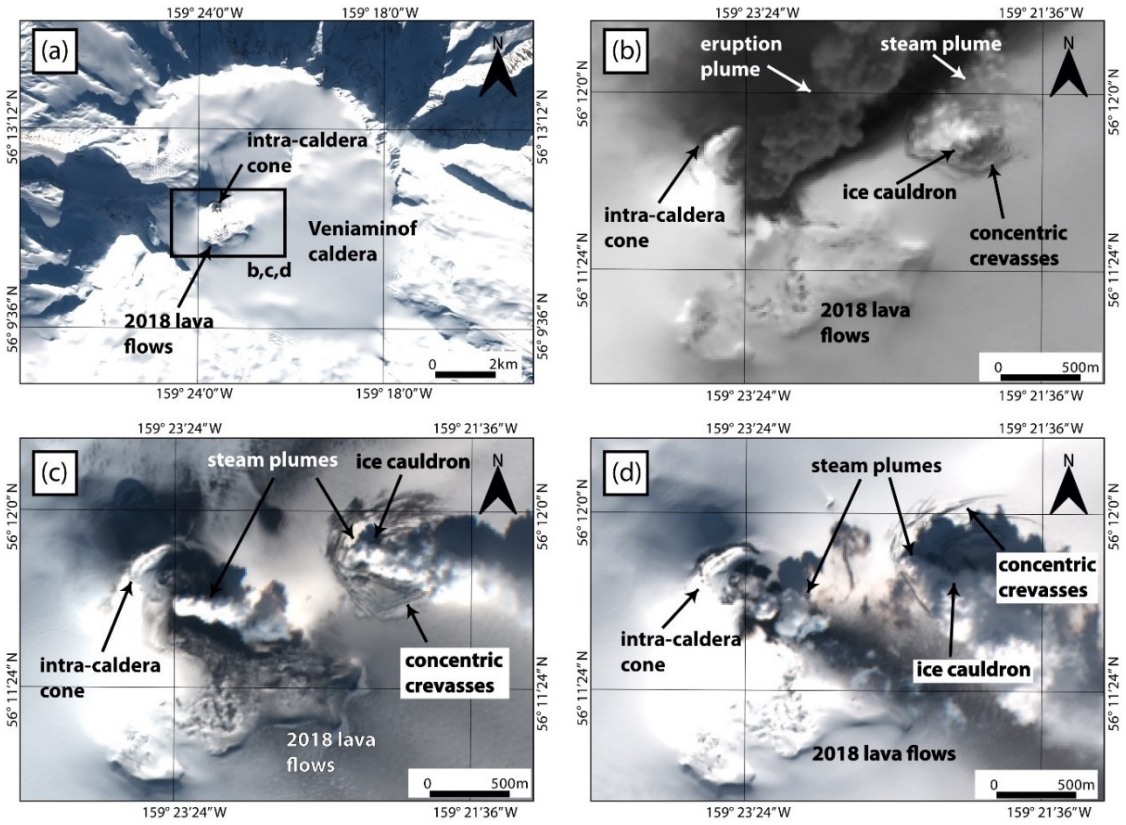

*Fig. 5.9. Recent volcanic activity on Mount Veniaminof: (**a**) Sentinel-2 true-colour overview image (10 m resolution) of the Veniaminof caldera from 04 February 2021 with an intra-caldera volcanic cone and (mostly snow-covered) 2018 lava flows; (**b**) Landsat-8 panchromatic image from 09 March 2021 (15 m resolution); (**c**,**d**) Sentinel-2 true-colour images from 11 March 2021 and 21 March 2021, respectively (both 10 m resolution). All subfigures (**b**–**d**) show an ice-cauldron and concentric crevasses related to the March 2021 active period as zoom-ins on the intra-caldera volcanic cone.*

5.4. Discussion

5.4.1. Observable impacts on glaciers

5.4.1.1. Ice cauldron/Opening formation

Ice cauldrons are the most common volcanic impact on glaciers observable from optical satellite images. For small subglacial eruptions (e.g., Bárðarbunga 2014–2015) or above geothermally active regions (e.g., Mýrdalsjökull) with large ice-thickness, these cauldrons tend not to extend to bedrock (i.e., to the glacier bed), but form depressions that are much wider than deep, typically up to 3-km in diameter (see Guðmundsson et al., 2007). In optical images, these glacier surface depressions are often observable due to shadowing, which results in areas (inside parts of the ice cauldrons) that are distinct from the usually brighter glacier surface.

Due to these often-conspicuous contrasts in surface shading, large surface cauldrons are, in principle, readily observable even in low-resolution satellite images (Fig. 5.3). In some cases, more energetic eruptions can produce ice cauldrons that extend to bedrock. For example, at Gjálp in 1996 ice cauldrons melted through up to 500 m of ice (Gudmundsson et al., 1997). Though large, these cauldrons can be difficult to observe during, or shortly after eruptions, since the explosive events that lead to their formation also produce ash-laden eruption plumes, preventing direct observation of the ice surface using optical remote sensing sources (e.g., no suitable optical images show the cauldron in the main caldera at Eyjafjallajökull in 2010). Ice cauldron formation is also common at volcanoes with thinner and less extensive ice cover, and cauldrons often extend to bedrock. Using optical satellite images, it is possible to detect these cauldrons on Mount Redoubt during and following its active period in 2009 (Fig. 5.5) and on Mount Hudson during and following its active period in 2011 (Fig. 5.6). The detection of cauldrons on only partially ice-covered volcanoes creates some difficulties due to an often restricted cauldron size (Fig. 5.5), combined with a highly variable surface texture, topography and colour at the summit. However, cauldrons are often visible in medium- and high-resolution imagery and appear as either dark spots (<a few pixels) or regions (multiple pixels), depending on image resolution (see Figures Fig. 5.3 and Fig. 5.4). Particularly large lahars might be generated by eruptions through crater lakes depending on the amount of lake water involved (Major and Newhall, 1989). Similarly, large amounts of water stored in ice cauldrons formed before a large eruptive event might increase the likelihood of large lahars, emphasising the importance of identifying ice cauldrons.

5.4.1.2. Crevassing

Glacier crevassing is another volcanic impact on glaciers commonly observable from optical satellite images. These crevasses are often localized and concentric (e.g., encircling ice cauldrons), but can also be more widespread, and irregular or linear in form. In fact, all volcanic impacts on glaciers discussed in this paper are, to some degree, associated with crevassing. In principle, crevasses are visible as dark stripes in optical satellite images (Fig. 5.8c), though their detection depends on a notable colour contrast between the crevasse and the surrounding glacial ice and snow.

Various approaches have been used to detect widespread regions of crevassing on 'non-volcanic' glaciers, using low- to high-resolution optical satellite images (Krimmel and Meier, 1975; Glasser and Scambos, 2008; Colgan et al., 2011, 2016; Rivera et al., 2014; Bhardwaj et al., 2016). However, some volcanically generated glacier crevasses (e.g., those forming around the margins of ice caldrons or those forming related to subglacial dome growth) are often small and comparatively isolated (rather than widespread), meaning that individual landform identification can be challenging, and requires medium- to high-resolution imagery. In addition, when investigating glacierized volcanoes, being able to monitor crevasse development (e.g., crevasses appearing where they were formerly absent) and evolution (e.g., growth) is important. This generally requires imagery with both high spatial and temporal resolution, and is easier for glaciers that are not already heavily crevassed (see Fig. 5.8).

5.4.2. Key challenges

5.4.2.1. Spatial and temporal resolution/Satellite image availability

In general, effective studies on landcover changes based on optical satellite remote sensing require image acquisition frequencies and spatial resolutions that are suitable for the research question to be addressed. As presented in sub-section 4.1.4, there are a variety of systems with different spatial and temporal resolutions available. For example, very coarse-spatial (i.e., >250 m), but high temporal resolution images with image acquisition at least once a day (e.g., MODIS) form the basis to observe volcanic hotspots and to map lava flow extents (e.g., Wright et al., 2004; Coppola et al., 2020). However, this image type is commonly not used to study glacier surfaces. The results of this thesis show that some low spatial resolution optical imagery (i.e., 10-100 m) is useful for identifying and monitoring some larger volcanic impacts on glacier surface morphology, but is unable to resolve smaller features including some crevasses, cauldrons, ice domes and supraglacial channels. Observing volcanic impacts on small (thin) glaciers can also be particularly challenging, since these glaciers typically have steep, and heavily crevassed surfaces (due to the influence of steep and undulating bed topography), with frequent bedrock protrusions sometimes difficult to distinguish from glacial ice and volcanic extruding features.

Given these issues with scale, detailed investigation of volcanic impacts on glaciers often requires medium-resolution imagery of at least ~5 m. At present, this has cost implications, since freely available imagery often is of low-resolution.

A further problem of image availability is that historical eruptions are typically poorly covered by satellite imagery. This applies most notably to volcanic active periods that occurred prior to the widespread availability of imagery from Landsat 7 and ASTER satellites (both launched in 1999). This leads to a strong temporal bias towards more recent eruptions (see examples presented in this study) and prevents studies on some important eruptions such as, e.g., Gjálp 1996 or the eruption on Nevado del Ruiz 1985.

5.4.2.2. Clouds/eruption plumes

There are also some major challenges when using optical satellite images related to cloud cover, which is related to optical satellite systems being unable to receive radiation from a cloud-covered ground surface. This limit also tremendously affects the usability of optical satellite images to study glaciers, e.g. to map glacier extents or to study surface properties of glaciers (e.g., Kääb et al., 2002, 2014; Paul et al., 2016). On volcanoes, eruption plumes and/or tephra cover can additionally cover portions of the glacier surface making it impossible to study them with optical satellite images (e.g., Bleick et al., 2013; Patrick and Smellie, 2013). In this thesis, the presence of clouds, eruption plumes and/or tephra cover only left a fraction of the investigated images useful to detect surface changes on ice-clad volcanoes (see Table 6).

One potential solution (though not the focus of this thesis) is to use SAR satellite data operating in the microwave region of the electromagnetic spectrum, which can penetrate clouds due to a larger wavelength used. For example, crevassing of the glacier surface yields an increased backscatter of amplitude SAR data used to identify ice cauldrons and meltwater tunnels on Mýrdalsjökull (Scharrer et al., 2008).

5.4.2.3. Supraglacial snow cover

Supraglacial snow cover also introduces difficulties with observing volcanic impacts on glaciers from optical imagery, since details of the ice surface are often obscured. This is particularly relevant for volcanic events that occur during winter (or the snow season). However, in some cases, snow cover can be an advantage, since it creates a homogeneous surface of low contrast, making subtle changes in topography (e.g., ice surface cauldrons) easier to identify (see Fig. 5.3).

5.4.2.4. Optimal images acquisition frequency

In general, it is also difficult to assess the required (or optimal) frequency of image acquisition for successful monitoring of glacier-clad volcanoes. The timescales that apply for the formation of the features discussed in this thesis vary considerably from several minutes to months/years. For instance, the formation of new ice cauldrons in the summit area of Eyjafjallajökull in 2010 took place within minutes (Magnússon et al., 2012), whereas squeezing of glacier ice and related crevasse formation on the Crater glacier during the extrusion of a volcanic dome on Mount St. Helens continued for approximately two years (Walder et al., 2007, 2008). The time frame for widespread crevassing of a glacier due to increased generation of basal meltwater (as observed on Mount Belinda) likely lies somewhere between those two endmembers. Therefore, in some quickly evolving instances images would ideally be acquired very frequently (~several per day), whereas other instances could, in principle, be sufficiently well monitored based on the common repeat cycle of ~16 days for Landsat or ASTER, though issues with cloud cover and eruption plumes remain.

5.4.2.5. Identification of the nature of volcano-glacier interactions

When viewing optical satellite imagery, it is sometimes difficult to discern the precise nature of volcano-glacier interactions. For example, supraglacial flow paths of volcanically triggered floods and lahars are typically easy to distinguish because the debris deposited contrasts with the bright glacier surface. However, using satellite imagery alone, it is difficult to establish whether these events incised channels into the ice, or just flowed across the glacier surface.

This also applies to supraglacial lava flows, which are often notably darker than the surrounding ice, but optical images provide little information about whether the glacier surface has been melted/incised. In this latter example, crevasses radiating from a subaerial lava flow terminus (e.g., Mount Belinda, Fig. 5.8b) can provide some indication that, through melting, the lava has had an impact on the glacier surface morphology (also see Patrick and Smellie, (2013)). However, to prove this, some knowledge about the efficiency of heat transfer from the subaerial lava to the ice is required. In the case of Mount Belinda, the emplacement of subglacial lava flows might also have resulted in the described changes to glacier morphology, since e.g., during the 2010 Eyjafjallajökull eruption, melting of ice by a subglacial lava flow resulted in an ice canyon with subaerial lava (Oddsson et al., 2016). Part of this challenge in observing volcanic impacts on glaciers using optical satellite imagery is the lack of quantitative information on changing ice surface elevations (a key indicator of ice melt, fracture, doming, etc.).

This clearly points to digital elevation models (DEMs) as potentially useful sources (though not the focus of this study), particularly when multiple high-resolution DEMs representing conditions before and after periods of volcanic unrest are available. For example, Rossi et al. (2016) used pre- and post-event DEMs to identify and measure supraglacial ice cauldrons formed during the 2014–2015 Bárðarbunga eruption.

5.4.3. Guidelines for best practice

For the purposes of monitoring glacier-clad volcanoes, being able to detect volcanic impacts on the surface morphology of glaciers is important. With that in mind, here we outline a set of general guidelines for anyone undertaking (or wishing to undertake) this task using optical satellite imagery.

5.4.3.1. Site overview and image availability

For a particular volcano, glacier and volcanically active period, satellite image availability is a key factor determining which volcanic impacts on glaciers are identifiable. For historical analysis (rather than monitoring), this is primarily determined by the period of interest. For example, for older events (but still within the satellite era), e.g., those that occurred between 1972 (the launch year of Landsat 1) and 1999, imagery is mostly of low spatial resolution, and choice of satellites is very limited (e.g., Landsat 1-5 and SPOT 1-4) (Elliott et al., 2016).

For events that have occurred since 1999, the range and resolution (spatial and temporal) of available images improves dramatically, particularly in recent years. Some free, but low-resolution, sources (e.g., Landsat 7, ASTER) are available throughout this period. Medium-and high-resolution images are also available (e.g., since the launch of IKONOS in 1999), but are typically commercial, rather than accessible for free.

Given the costs associated with obtaining high-resolution imagery, for the purposes of observing volcanic impacts on glaciers, lower resolution, but freely available, imagery can serve as a foundation. These images can then be supplemented with 'targeted' and judiciously selected (i.e., covering specific areas and time periods) commercial imagery. Free and commercial imagery is available via various websites, and some image types (e.g., Landsat and ASTER) are often easiest to access through platforms such as Google Earth Engine (Gorelick et al., 2017). In some cases, freeware virtual globes (e.g., Google Earth and NASA Worldwind) and web mapping services (e.g., Bing Maps and Google Maps) can provide access to high-resolution images (with plugins available to export images into GIS packages such as QGIS). Thus, virtual globes and web mapping services allow access to high-resolution imagery, without the costs associated with commercial data. However, due to the limited availability of images, and the lack of user choice in image selection, these platforms rarely have images (and certainly not multiple images) covering a particular time period of interest (c.f., Barr et al. (2018a)), and are of limited use when considering highly dynamic environments (such as those associated with active volcanism).

5.4.3.2. User Experience

The ability to identify volcanic impacts on glaciers using optical satellite imagery partly depends on user experience. For most users (particularly those with comparatively limited experience), examining 'known' (or documented) examples, such as those highlighted in this paper, is likely to be useful. This might involve observing volcanic impacts in the field, from existing ground-based or aerial photographs, or by looking at medium- to high-resolution satellite imagery. This is likely to be particularly useful for distinguishing between bedrock protrusions and features related to volcanic activity.

Once familiar with the types of features that are present, previously undocumented volcanic impacts on glaciers can be searched for, using lower resolution imagery if necessary.

5.4.3.3. Using Multi-Temporal Images

Since observing volcanic impacts on glaciers effectively involves change detection (e.g., the development of glacier crevasses where they were previously absent), observing satellite images from a range of time periods (pre-, syn- and post-volcanic activity) is important. This is often possible by generating a time-series of images (in native resolution), e.g., using Google Earth Engine Code Editor, which requires some java script knowledge (Gorelick et al., 2017). When producing such a time-series, image availability (see sub-section 5.4.3.1) might be a limiting factor; however, where possible, images which show the glacier surface in its 'natural' (i.e., non-volcanically impacted) state are key. This is particularly true of images from the same season (but perhaps a different year) as the period of volcanic unrest. How long before, or after, a period of activity images are useful/relevant is unclear, though some glaciers are known to have experienced changes in surface morphology months prior to eruptions (e.g., Mount Redoubt, 2009), and many impacts were still observable years after (Barr et al., 2018a). As the spatial and temporal resolution of imagery continue to improve over coming years, monitoring volcanic impacts on glaciers will likely be easier (particularly obtaining cloud-free images) and possible with greater detail than for historical events. In many cases, images are likely to be available on cloud-based platforms such as Sentinel Hub Playground (https://apps.sentinel-hub.com/sentinel-playground/, accessed on 18 March 2021), which allow data visualisation and manipulation (e.g., producing different band combinations) without having to download.

5.5. Conclusions

Recent years have seen a rapid increase in freely available and commercial optical satellite images, covering large parts of the Earth. In this study, this global data source has been searched for evidence of volcanic impacts on glacier surface morphology, with a focus on well-known (documented) examples from the literature. The main conclusions are:

- The most common volcanic impact on glacier surface morphology observable in optical satellite imagery is the formation of ice cauldrons (i.e., depressions in the glacier surface). Depending on eruption energy/type, ice thickness and image resolution, these cauldrons often appear as dark points/areas or as regions of distinct shadowing which contrast with the usually bright glacier surface.
- Other observable volcanic impacts on glacier surface morphology are widespread glacier crevassing, localized crevassing (e.g., adjacent to supraglacial lava flows or ice cauldrons) and ice bulging and fracturing due to subglacial dome growth.
- All volcanic impacts on glaciers investigated in this work are, to some degree, associated with crevassing, which is commonly visible as dark stripes on optical satellite images.
- The key challenge when using optical satellite images to study volcano-glacier interactions is the availability of cloud- and plume-free images with sufficient spatial and temporal resolution to observe (and monitor) the evolution of (sometimes) small-scale changes in glacier surface morphology. Useful imagery is increasingly available, but this does not help when observing historical eruptions, and the widespread use of commercial imagery is usually prohibitively expensive. Lower resolution imagery is often freely available, but identifying and interpreting changes in glacier morphology from these sources requires greater user experience.
- Overall, optical satellite imagery is a useful source for studying changes in glacier morphology caused by volcanic activity, particularly in remote and inaccessible parts of the world. This suggests that global-scale analysis and monitoring are possible. However, due to the costs of high-resolution (spatial and temporal) imagery, and the limited quantitative information that can be extracted, optical satellite imagery is best used in combination with DEMs, radar data, aerial images (derived from planes and/or drones) and ground-based observations.

Author contributions to this chapter

Conceptualization	Iestyn Barr, Benjamin Edwards, Elias Symeonakis, Matteo Spagnolo
Methodology	**Michael Dieter Martin (PhD student)**
Investigation	**Michael Dieter Martin (PhD student)**
writing—original draft preparation	**Michael Dieter Martin (PhD student)**, Iestyn Barr
writing—review and editing	Benjamin Edwards, Elias Symeonakis, Matteo Spagnolo, Sanaz Vajedian
supervision	Iestyn Barr, Benjamin Edwards, Elias Symeonakis, Matteo Spagnolo
funding acquisition	Iestyn Barr, Benjamin Edwards, Elias Symeonakis, Matteo Spagnolo

Chapter 6 Detection of volcanically triggered changes in surface velocity of a temperate glacier using Sentinel-2 data – a case study on Mount Veniaminof

6.1. Introduction

Mount Veniaminof (56.2°N, 159.4°W) is a large glacierized, 2507 m high basalt-to-dacite stratovolcano of Quaternary age (Waythomas, 2021). It is located on the Alaska Peninsula in the Aleutian arc (between Alaska and Russia) 240 km northeast of Cold Bay. Mount Veniaminof is one of the largest and most active volcanoes in the Aleutian arc with several explosive eruptions over the past 25,000 years and at least 19 eruptions from 1830 until now (Welch et al., 2007; Waythomas, 2021). Volcanic activity is mostly limited to small to moderate Strombolian events (VEI 1-3) including lava fountaining, low-level gas emissions and occasional lava flows (Waythomas, 2021). The volcano is covered by 273 km^2 of glacial ice and comprises an 8 by 10 km ice-filled summit caldera (Waythomas, 2021). There are two volcanic cones (cone A and cone B) within the caldera, however, all historical eruptions took place on cone A, which is snow- and ice-free all year round (Fig. 6.1) (Waythomas, 2021). The active cone (cone A) rises 250 m above the surrounding ice, whereas the dormant cone is completely buried by ice (Welch et al., 2007). There are 4 glaciers draining the caldera, however, this thesis focuses on Cone Glacier, which is Mount Veniaminof's largest glacier draining the caldera to the west (Fig. 6.1).

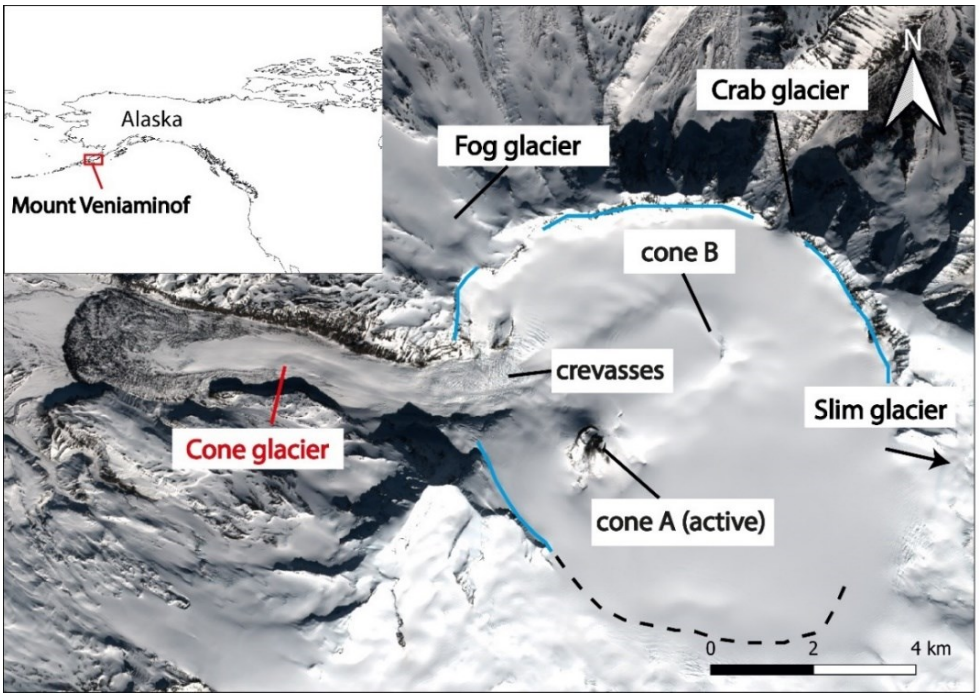

Fig. 6.1 Sentinel-2 true-colour composite image of Mount Veniaminof from 25/03/2017 with cone A and B and its outlet glaciers breaching the caldera. The volcano is located in the Aleutian Arc (see inset). The caldera rim is shown as a blue line and the inferred caldera rim is shown as a black dashed line (from Yount et al. (1985) and Neal et al. (1995)).

6.2. Background

6.2.1. Search of suitable glaciers/The choice of Cone Glacier

Cone Glacier was selected based on a set of criteria, which included an extensive search for suitable glacierized volcanoes around the globe. We based our search on the dataset of Edwards et al. (2020), who reports all Holocene eruptions on glacierized volcanoes worldwide and the dataset of Barr et al. (2018a), who reported observed impacts on glacierized volcanoes since 1800 AD. We restricted both datasets to eruptions during the remote sensing era (i.e., since the launch of Landsat-1 in 1972). We explored the eruption characteristics for each volcano using the Smithsonian Volcano Institution reports (*Global Volcanism Program. Report on Veniaminof (United States). In: Sennert, S K (ed.)*) and the information given in the dataset of Barr et al. (2018a). We were looking for glacier-clad volcanoes with suitable (i.e., lasting for years) time gaps to be able to record a particular glacier returning to a 'background' velocity state after having been impacted by volcanic activity.

We then investigated the suitability of the glacier surfaces for feature tracking (e.g., glacier extent, appearance of glacier surface) and inspected the satellite image availability for suitable sites (e.g., cloud cover, visibility of features on the glacier surface etc.). Since Sentinel-2 images turned out to be most suitable for use with GIV software, we further restricted our dataset to all reported instances of glaciers being affected by volcanic activity since ~2015 (i.e., the launch date of the Sentinel-2A satellite). For Mount Veniaminof, enough suitable Sentinel-2 images are available after 2015 to cover two volcanically active periods, one in 2018 and one in 2021 and the surface of Cone Glacier fulfilled most of the criteria to perform feature tracking on. Additionally, based on information from the Smithsonian Institution reports (*Global Volcanism Program. Report on Veniaminof (United States). In: Sennert, S K (ed.)*) and Middle Infrared Observations of Volcanic Activity system (MIROVA) data (Coppola et al., 2020), Mount Veniaminof reveals a time gap of ~1 ¾ years (from April 2019 to December 2020) between its two volcanically active phases. This time gap works as a reference period, which is assumed to reflect glacier surface velocities largely unaffected by volcanic activity (see sub-section 6.2.4).

6.2.2. Climate and glaciers in the Aleutian arc

The climate in the Aleutian range is cool, wet and windy and average temperatures are ~5-10°C in summer and near freezing in winter (Rodionov et al., 2005). The eastern Aleutians (where Mount Veniaminof is located) generally experienced a shift towards a warmer climate since 1977, however, climate patterns in the Aleutians are pretty variable and the closest station at Cold Bay (~240 km from Mount Veniaminof) even reported a decrease in mean annual temperature from 1977 (Rodionov et al., 2005; Molnia, 2007). KNMI Near-Surface Air Temperature monthly re-analysis data (http://climexp.knmi.nl/select.cgi?era5_t2m, accessed on 02/05/2022) from 2000-2021 for the Mount Veniaminof region showed a slight increase of air temperatures from 2013 until 2018 and a slight decrease after 2018; however, there is no general shift towards higher temperatures (Fig. 6.2).

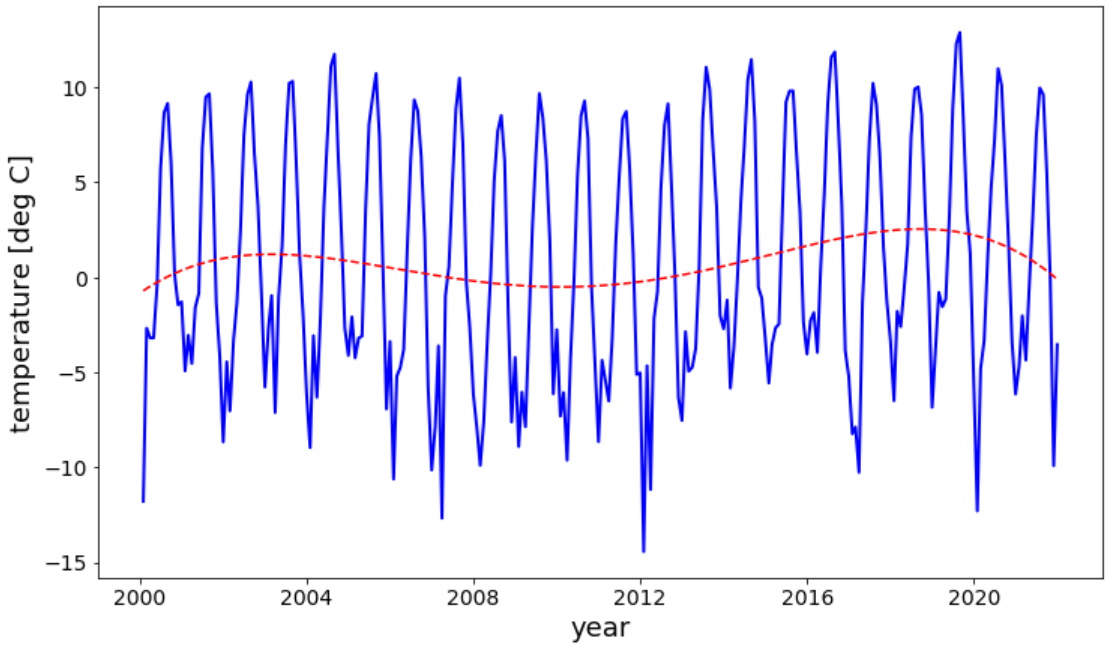

Fig. 6.2 Temperature curve for Mount Veniaminof based on KNMI re-analysis data (blue line) and temperature trendline based on 4th order polynomial (red dashed line)

There is a reported general trend towards more precipitation in Alaska during the 20th century and the annual precipitation in the Aleutian range varies widely from 530 mm to 2080 mm (Rodionov et al., 2005; Molnia, 2007). For the region of Mt Veniaminof, KNMI Precipitation monthly re-analysis data showed variations in precipitation ranging from ~1500-1900 mm/year for the study period from 2016 to 2022 (https://climexp.knmi.nl/select.cgi?era5_tp, accessed on 02/05/2022). Essentially all Alaskan glaciers are reported to be temperate, which means that changes in temperature and precipitation and therefore the availability of meltwater at the glacier bed will have a large impact on glacier dynamics (Molnia, 2007; Benn and Evans, 2010). Thinning and retreating is reported for all valley and outlet glaciers in the Aleutian arc at the end of the 20th century and at the beginning of the 21st century (Molnia, 2007). By contrast, Cone Glacier turns out to be remarkably stable over the time period of interest from May 2016 to January 2022. We digitized the glacier tongue margin on 14 suitable Sentinel-2 images to investigate changes in the glacier terminus position (Fig. 6.3). The glacier tongue fluctuation was limited to ~40-70 m for most places and only ranged above ~100 m in a few places.

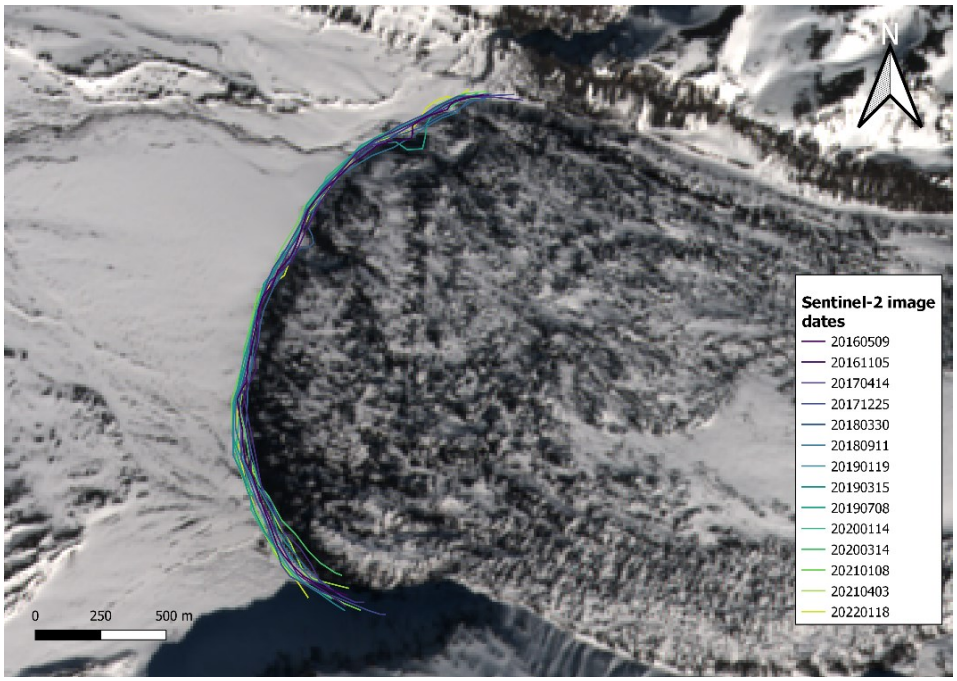

Fig. 6.3 Margin of Cone Glacier from May 2016 to January 2022 for the Sentinel-2 image dates given in the legend. Background Sentinel-2 image from 25/03/2017.

6.2.3. Geology and Glaciology of Mount Veniaminof

According to the geological map of Alaska, the region around Mount Veniaminof consists of unconsolidated surficial deposits and the volcano itself is made of Quaternary and possibly latest Tertiary volcanic rocks ranging from rhyolite to basalt (Wilson et al., 2015). A deep-penetrating radio-echo sounding (RES) survey conducted in July 2005 revealed the caldera floor to be very flat and possibly covered by a thick layer of permeable scoria and ash (Welch et al., 2007). The same study by Welch et al. (2007) determined the geothermal heat flux in the caldera to be ~19 W/m^2, which is considered to be comparable to active hydrothermal vents in volcanic lakes.

The 8 by 10 km caldera is filled with ~260 m thick ice on average, which ranges up to 475 m in some places in the southern basin (Welch et al., 2007). The ice is very clear with almost parallel to sub-horizontal RES reflectors throughout the caldera (Welch et al., 2007). Unfortunately, the radar survey conducted by Welch et al. (2007) did not cover the Cone Glacier area, but ice thicknesses range from 100-150 m in the ice fall area and up to ~200 m for the lower glacier area according to the global consensus estimate of ice thicknesses published by Farinotti et al. (2019).

Based on ASTER GDEM data (https://www.jpl.nasa.gov/images/pia12090-asters-global-digital-elevation-model-gdem, accessed on 19/04/2022), the glacier tongue is located at ~480 m above sea level and the mean elevation of the ice field (where the head of Cone Glacier is located) is at 1860 m above sea level (Welch et al., 2007). The equilibrium line altitude of glaciers draining the caldera are reported to be ~1300 m above sea level (Welch et al., 2007). Given the glacier's altitude and latitude, Cone Glacier is most likely temperate (Welch et al., 2007).

6.2.4. The 2018 and 2021 volcanically active periods

Prior to the 2018 and 2021 volcanically active periods, Mount Veniaminof had some remarkable and well- documented eruptions in 1983-84, 1993-94 and 2013 including ash emission, lava flows, ice melt and the formation of melt pits (e.g., see Yount et al., 1985; Neal et al., 1995; Waythomas, 2021). In this thesis, we focus on the latest two volcanically active periods, one in 2018 and one in 2021, which are covered by available Sentinel-2 imagery (with the Sentinel-2A satellite being launched in June 2015) (Fig. 6.4). We investigated the volcanically active phases of 2013, 2018 and 2021 using the respective Smithsonian Institution reports for the years 2013-2021 (*Global Volcanism Program. Report on Veniaminof (United States). In: Sennert, S K (ed.)*), the work of Waythomas et al. (2021) and data from the Middle Infrared Observations of Volcanic Activity (MIROVA) system (Coppola et al., 2020; pers. comm. to D. Coppola).

In between the 2013 and the 2018 volcanically active periods, the volcano was reported to be in a relatively quiet state with only some minor steam emissions in October 2015. In September 2018, a new eruption (VEI=2) started with low-level ash emissions, lava fountaining and the formation of small lava flows. The first thermal anomaly was detected by MIROVA on September 9th. The eruption was located at 2 summit vents (with 5-10 m in diameter) and at some smaller flank vents. By September 14th, the lava flow was ~ 800 m long and reached a length of 1.2 km by October 25th. Fractures in the ice are reported during November 7-13th due to the presence of meltwater under the ice, and steam plumes indicated interaction between snow/ice and lava. By December 2018, a total of 3 lava lobes had formed covering an area of 0.6 km^2. The 2018 eruptive phase was reported to have lasted ~ 4 months from September to December 2018.

In between the 2018 and the 2021 active periods, the volcano showed some low-level tremor and a steam plume in July/August 2019 but returned to background activity by the end of August 2019. Seismic tremor again was above the background state in June 2020 for ~3 days. Both instances were not detected by the MIROVA system.

The 2021 eruption (VEI=1) started with a small explosion in March 2021 and lasted until early April 2021 (i.e., ~1 month). The eruption included the formation of low-level ash plumes and highly elevated surface temperatures visible in satellite imagery around the eruption location. The first thermal signal of the eruption was detected by MIROVA on March 7th. The active phase included the subglacial eruption of lava from a subglacial vent 1100 m east of cone A, which most likely travelled ~1 km east of the cone's summit under the ice and resulted in the formation of a small ice cauldron. The cauldron broadened and reached 550 to 600 m in diameter by mid-March. By early April 2021, a cluster of three vents and three separate lava flows became visible in the ice cauldron.

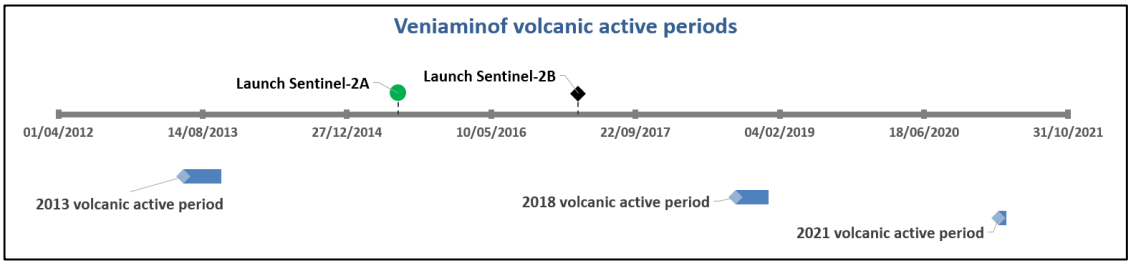

Fig. 6.4 Volcanically active periods on Mount Veniaminof from 2013 to 2021 and launch dates of Sentinel-2A and Sentinel-2B satellites.

Both, the comparison between KNMI Explorer climate data and our time-series glacier velocity curves and the analysis of our extracted velocities along a profile line demonstrate that Cone Glacier was affected by volcanic activity beyond the activity periods reported by the Smithsonian Institution reports and MIROVA. Some of our data show glacier surface velocities to be comparably slow for ~3 months after the end of reported volcanic activity in December 2018 and therefore we consider the volcano to be still active within these ~ 3 months (see sub-section 6.4.3 and 6.4.4). Also, some data indicate faster than usual surface velocities ~ 3 months prior to the onset of reported volcanic activity in 2021 and we therefore assume the volcano to be active ~3 months before the period of reported volcanic activity (see sub-section 6.4.3 and 6.4.4). For a discussion of the reasons why both slower- and faster-than-usual glacier surface velocities could indicate volcanic activity, please refer to sub-section 6.5.4.1.

Based on our findings, we finally assumed the time period from April 2019 to December 2020 to be mainly unaffected by volcanic activity (Fig. 6.5).

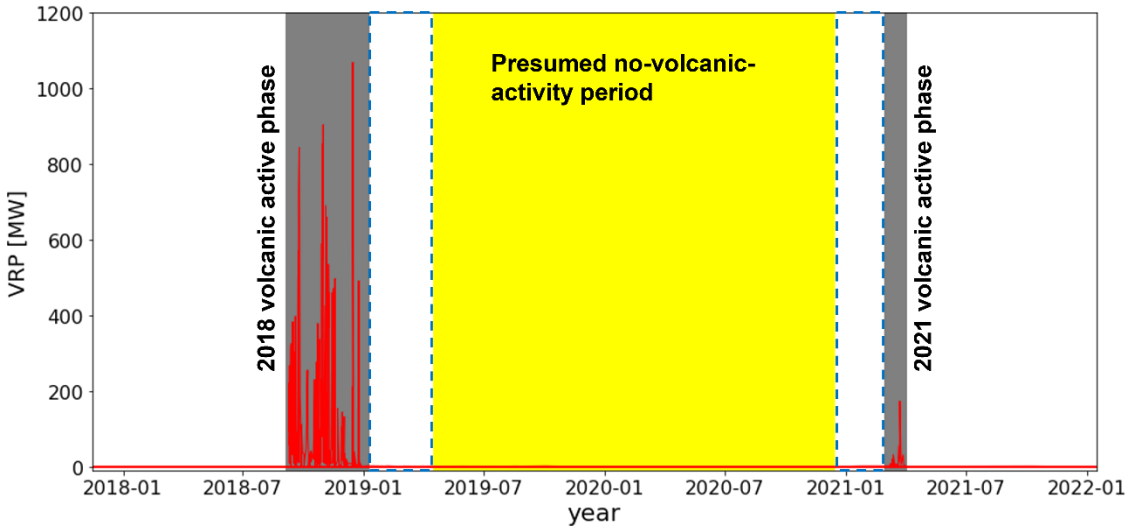

Fig. 6.5 MIROVA volcanic radiative power (VRP) data (red line) and time periods of reported volcanically active phases in 2018 and 2021 (grey bars). From glacier surface velocity inferred volcanic activity (blue dashed line box). Presumed time period of no volcanic activity (yellow bar). MIROVA data from pers. comm. to Diego Coppola.

6.3. Methods

6.3.1. Glacier image velocimetry on Cone Glacier

In this thesis, 99 suitable (i.e., cloud-free) Sentinel-2 Level-1C images from June 2015 until January 2022 were manually selected and downloaded using Google Earth Engine. Since the first suitable image was only available in May 2016, the dataset presented in this thesis covers the time period from May 2016 until January 2022. A list of all images used is provided in Table 3 in the Appendix 1. We restricted the satellite scenes to a region of interest covering Cone Glacier and downloaded the images in UTM projection (EPSG: 32604). We used the NIR band 8 (central wavelength: 842 nm) of the Sentinel-2 images with 10 m spatial resolution, which is minimally affected by along-track stripes (Kääb et al., 2016). We restricted our search to images from the same relative orbit (orbit number 29) to mitigate lateral offsets between images due to along-track stripes or DEM misinterpretations (Kääb et al., 2016). The time difference (temporal resolution) in the dataset for successive suitable images varies from 5 to 100 days.

The overall number of suitable images increased and the time separation between successive suitable images tremendously decreased ~8 months after the launch of the Sentinel-2B satellite (Fig. 6.6). We performed several test runs in GIV using a Lenovo laptop with an Intel(R) Core(TM) i7-8565U CPU @ 1.80 GHz Processor and 16 GB RAM. We varied the temporal oversampling, minimum and maximum time intervals for the image pairs, the image filtering and output resolutions. We obtained results minimally affected by noise by choosing an output resolution of 100 m and by limiting the time separation for image pairs to a minimum of 21 days and a maximum of 1 year. We set the time oversampling factor to 30, which resulted in a maximum possible number of 1569 image pairs. All changes from the default setting of the software are detailed in Table 4 in Appendix 1. We defined a region of interest on the glacier surface, where surface velocities were calculated, and we additionally defined an area of stable (i.e., non-moving) surface around Cone Glacier by directly erasing the respective pixels in Microsoft Paint (Fig. 6.7).

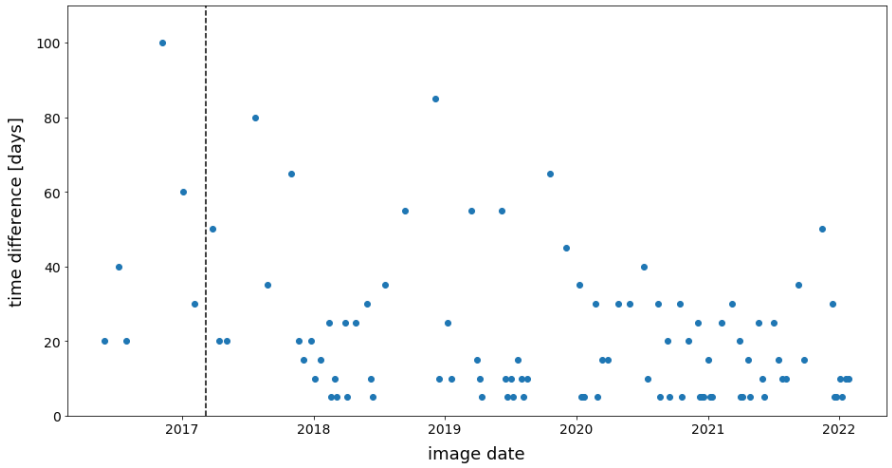

Fig. 6.6 Time difference in days for successive suitable Sentinel-2 images downloaded. Dashed line: launch date of Sentinel-2B satellite (07/03/2017).

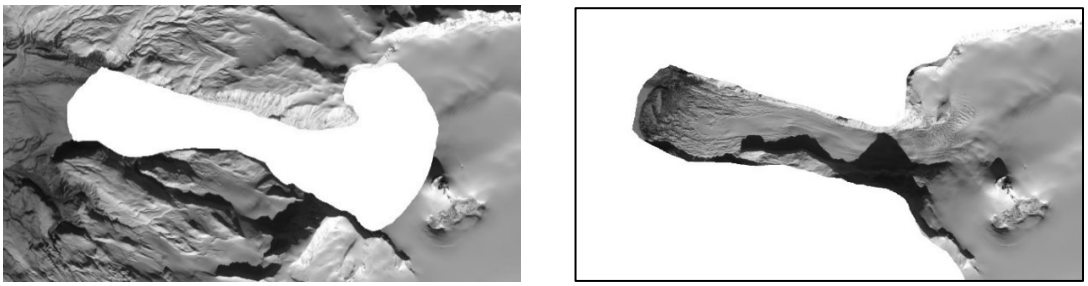

Fig. 6.7 (left): Mask defining the Cone Glacier region on Mount Veniaminof where glacier velocities are calculated. (right): stable (non-moving) surface. Due to GIV software requirements, both are drawn in pure white (see sub-section 4.2.3). Background image: Sentinel-2 (band 8) image from 15/10/2020

6.3.2. Velocity data analysis

We obtained (georeferenced) mean velocity fields and mean flow direction fields (including respective standard deviation and error fields) as direct outputs from the GIV software. We validated our mean velocity data using the global glacier velocity dataset for the years 2017 and 2018 published by Millan et al. (2022). Since there are no significant changes in climate for the Veniaminof region over the period of investigation from 2016 to 2022 (see sub-section 6.2.2), we assumed our mean velocities to be comparable to the results of Millan et al. (2022). We present our results on mean velocity and flow direction (including validation with the dataset by Millan et al. (2022)) in sub-sections 6.4.1. and 6.4.2.

Alongside mean velocity and flow direction fields, the software provides (georeferenced) monthly velocity fields, which we used to obtain velocities along a profile line ranging from the glacier tongue to the glacier head (see Fig. 6.1 and Fig. 6.13). We extracted the velocities with the help of the 'Profile Line Tool' in QGIS. The results are presented in sub-section 6.4.3.

Since we can assume Cone Glacier to be temperate and temperature and precipitation usually has a large influence on these glacier types (see sub-sections 2.1.2 and 6.2.3), we investigated these climatic parameters for the Mount Veniaminof region from January 2000 through December 2021 using monthly re-analysis Near-Surface Temperature (http://climexp.knmi.nl/select.cgi?era5_t2m, accessed on 02/05/2022) and Precipitation (https://climexp.knmi.nl/select.cgi?era5_tp, accessed on 02/05/2022) data. The respective datasets were downloaded from the KNMI Climate Explorer (https://climexp.knmi.nl/start.cgi, accessed on 02/05/2022) with 0.25 deg resolution. At the time of writing, the KNMI datasets are available from January 1950 through July 2022. Information on general temperature and precipitation trends in the Aleutian arc from before 2000 is taken from the work of Molnia (2007) and Rodionov et al. (2005).

We obtained time-series data for 10 points along our profile line from the GIV built-in time-series capability and performed a correlation analysis of our time-series velocities and the KNMI Near-Surface Temperature and Precipitation data.

We considered the separate investigation of the entire time-series and a potentially 'activity-free' time-period from April 2019 to December 2020 (see sub-section 6.2.4) necessary to understand the relationship between air temperature/precipitation and Cone Glacier's surface velocity both during active volcanic phases and during a (presumed) non-volcanic phase. We excluded all velocities from before November 2017 (i.e., 8 months after the launch of the Sentinel-2B satellite), since they turned out to be unrealistically high or low for most points. The final results of our time-series analysis are presented in sub-section 6.4.4.

We quantified the (presumably volcanically triggered) velocity change as observed in the time-series curves and our velocities along the profile line by producing monthly 'velocity difference' and 'velocity percentage change' maps. For the 2018 active phase, we calculate the 'velocity differences' and 'percentage velocity change' from November 2017 to March 2019 to the respective months in 2019 and 2020 (assumed to be activity free). For the 2021 active phase, we calculated 'velocity differences' and 'percentage velocity change' for each month in 2021 and in January 2022 to the respective months in year 2020 (assumed to be activity free). We used the following equation to obtain the 'velocity difference (m/year)' for each month:

$$velocity\ difference\ = velocity\ (activity\ year) - velocity\ (non - activity\ year) \qquad \textbf{(6.1)}$$

Also, we calculated the 'percentage velocity change (%)' for each month using the following equation:

$$percentage\ velocity\ change\ [\%] = \frac{velocity\ difference}{velocity\ (non - activity\ year)} * 100 \qquad \textbf{(6.2)}$$

Our velocity difference and percentage velocity difference maps can be viewed in sub-section 6.4.5. Most of the analytical work was performed in Python and Matlab. We make all code available in a github repository accessible under the GNU General Public License v3.0 via the following link: (https://github.com/mmartin17/glaciovolcanism).

6.4. Results

6.4.1. Mean flow velocity and flow direction of Cone Glacier

The mean flow velocity on Cone Glacier for the entire period of investigation from May 2016 to January 2022 ranges from ~10-20 m/year on the glacier tongue up to ~630 m/year for the highly crevassed glacier head (Fig. 6.8). Velocity standard deviations are generally in the order of ~70-100 m/year for the crevassed region but can range up to ~200 m/year in some places. For the slowest portions of the glacier (such as the glacier tongue), the velocity standard deviation is in the order of ~10-15 m/year.

The velocity percentage error variability (i.e., standard deviation divided by mean velocity for each pixel) is lowest for the heavily crevassed and fastest flowing region on the glacier (in the order of ~15%). It generally is lower for inner parts of the glacier (up to ~40%) and can range up to ~100% (or more) for the glacier edges (Fig. 6.9).

The flow direction is towards west to north-west (~260°-290°) for the lower glacier area and southwest for the fastest flowing region (~220°-260°). There is inflow of ice towards Cone Glacier south of the heavily crevassed region with flow directions ranging from west to north-west (~270°-310°) and inflow of ice from the north-east with flow directions ranging from ~220°-240°. Standard deviations for flow direction are in the order of ~2.5° for the heavily crevassed region and range up to 35° for the glacier's edges.

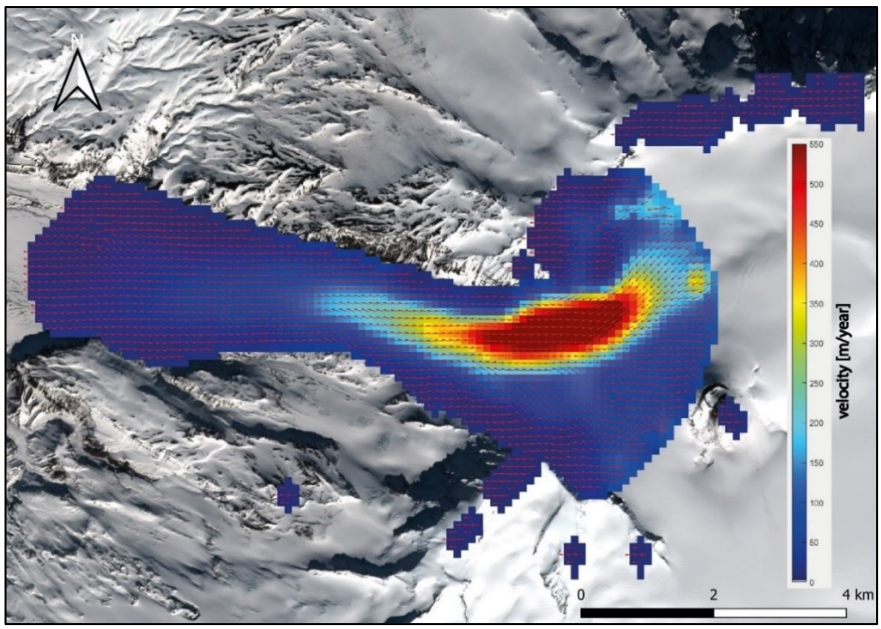

Fig. 6.8 Mean flow velocity and flow direction of Cone Glacier for the period of investigation from May 2016 to January 2022. Background image: Sentinel-2 true colour image from 25/03/2017.

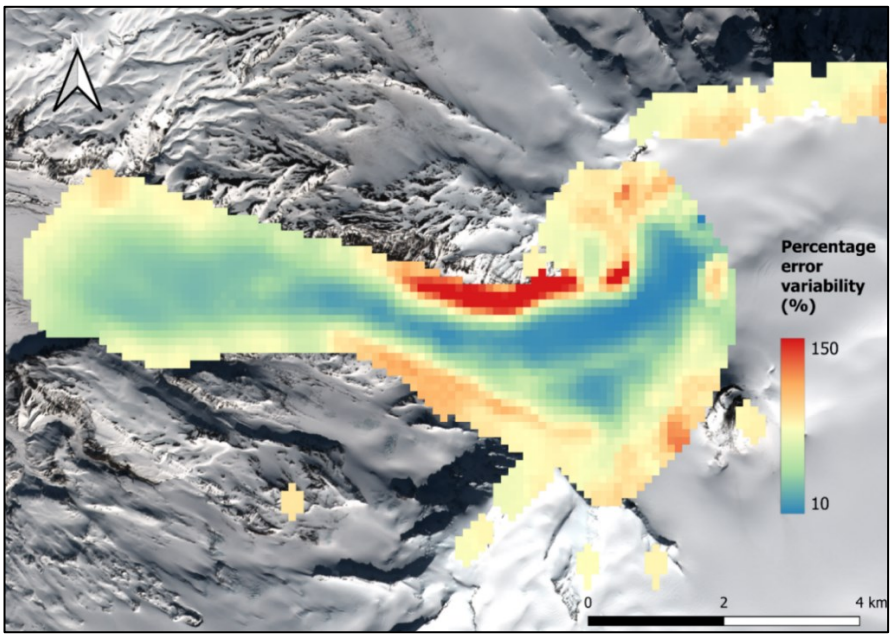

Fig. 6.9 Percentage error variability of velocities on Cone Glacier. Background image: Sentinel-2 true colour image from 25/03/2017.

6.4.2. Validation with velocity dataset of Millan et al. 2022

We validate our mean velocities on Cone Glacier with the global glacier velocity dataset for the years 2017 and 2018 published by Millan et al. (2022) (Fig. 6.10). Similar to the mean velocity derived in this thesis (Fig. 6.8), the dataset reveals the highest velocities (up to ~550 m/year) on the highly crevassed zone and the lowest velocities on the glacier tongue. Overall, we find the largest differences to our dataset (up to ~300 m/year) for the highly crevassed zone and the smallest differences for the glacier tongue (generally not more than ~±20 m/year) (Fig. 6.11). We observe an overall slight bias towards higher velocities in our dataset if compared to the dataset presented by Millan et al. (2022) (Fig. 6.12).

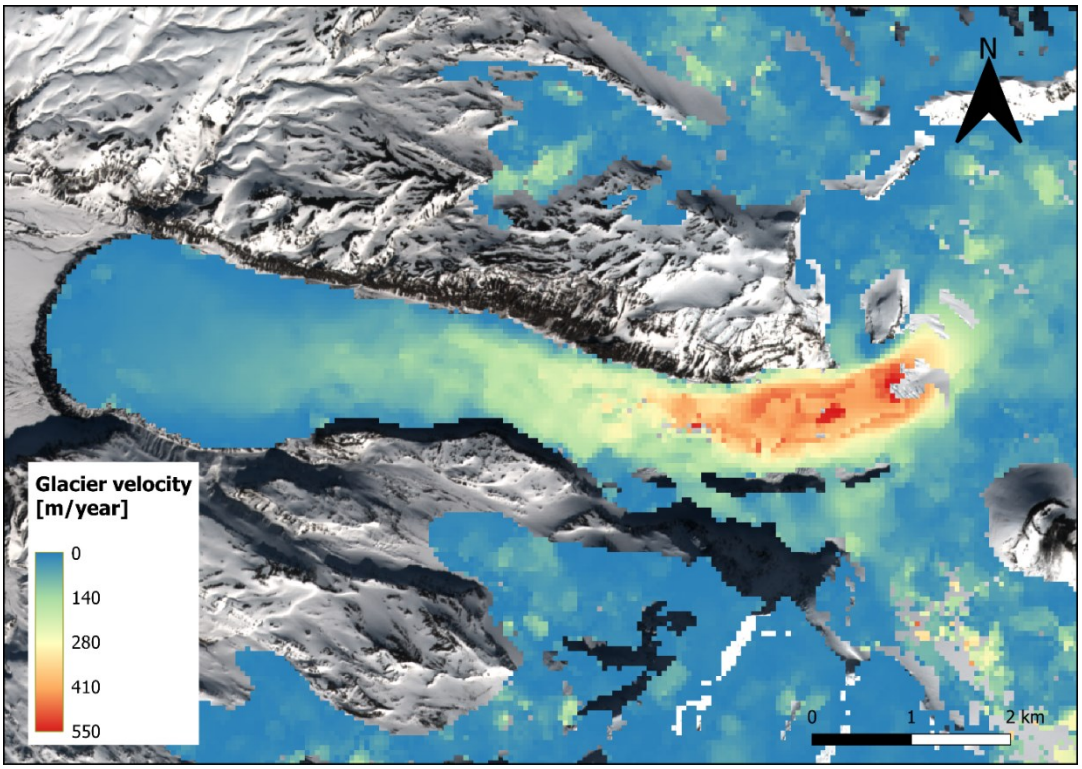

Fig. 6.10 Mean surface velocity on Cone Glacier by Millan et al. (2022) for the years 2017 to 2018. Background image: Sentinel-2 true colour image from 25/03/2017.

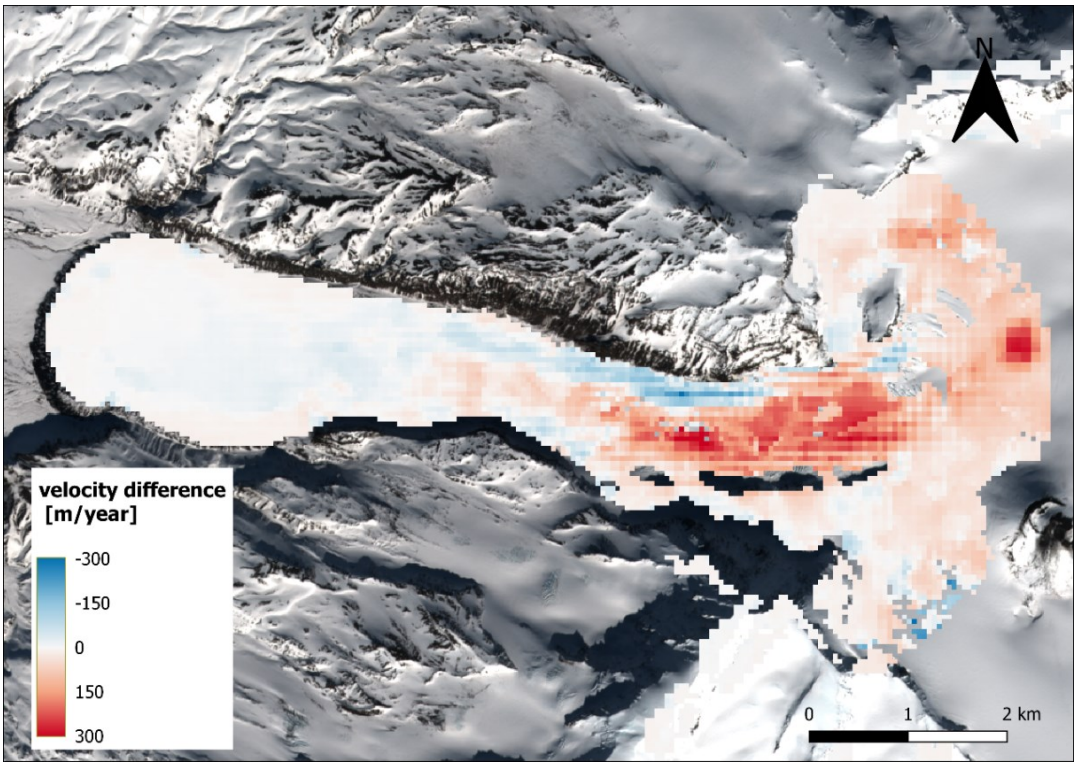

Fig. 6.11 Velocity difference of our dataset (Fig. 6.8) to the dataset presented by Millan et al. (2022) (Fig. 6.10). Red colour represents higher velocities in our dataset. Background image: Sentinel-2 true colour image from 25/03/2017.

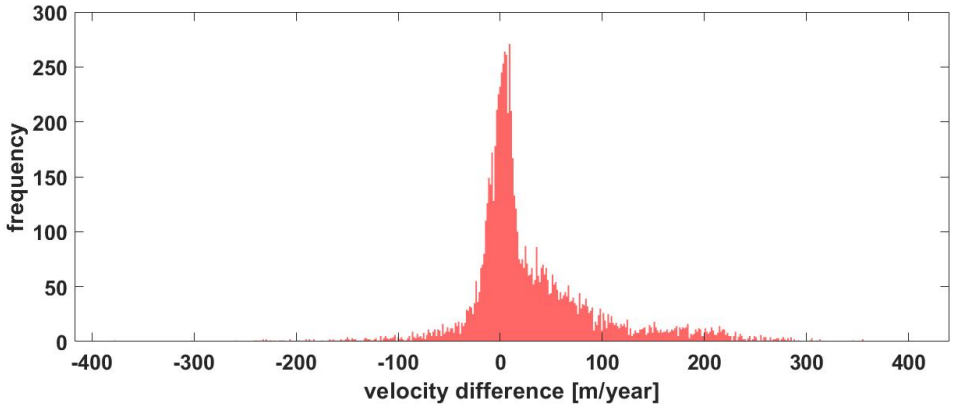

Fig. 6.12 Histogram of velocity differences of our dataset and the dataset presented by Millan et al. (2022) (see Fig. 6.11).

6.4.3. Velocities along profile line

We extracted monthly velocities along a profile line ranging from the glacier tongue to the glacier head for the years 2017-2021 (Fig. 6.13). The monthly velocities along the profile line and the velocity differences to the years 2019 and 2020 (presumed to be mainly activity-free) for all months (i.e., January through December) are shown in Figure 1 in the Appendix 1.

In this sub-section, we show the monthly velocities along the profile line (Fig. 6.14, upper row) and the velocity differences to the (mainly activity-free) years 2019 and 2020 for the months March and October, respectively (Fig. 6.14, lower rows). We find that velocities above the equilibrium line altitude are up to ~150 m/year higher from November 2017 through June 2018 (i.e., prior to the start of the eruption in September 2018) if compared to the years 2019 and 2020. In this glacier area, velocities tend to be up to ~150 m/year slower in 2018 from October through December (i.e., during the eruptive period). Additionally, there is a remarkable slow-down in mid-glacier areas (below the equilibrium line altitude) in 2018 from July through December with up to ~400 m/year slower velocities (Fig. 6.14). Slower velocities mainly above the equilibrium line altitude are preserved until March 2019 (i.e., after the volcanically active period). Above the equilibrium line altitude, we find a similar pattern of up to ~150 m/year higher velocities from January to June 2021 (including the active period in March 2021) and a tendency to slower velocities from October through December 2021 (after the active period in March 2021).

For mid-glacier areas, the signal we observe for the year 2021 also is similar to the year 2018, however, with only up to ~250 m/year slower velocities and the peak of the signal seems to be restricted to a region close to the equilibrium line altitude.

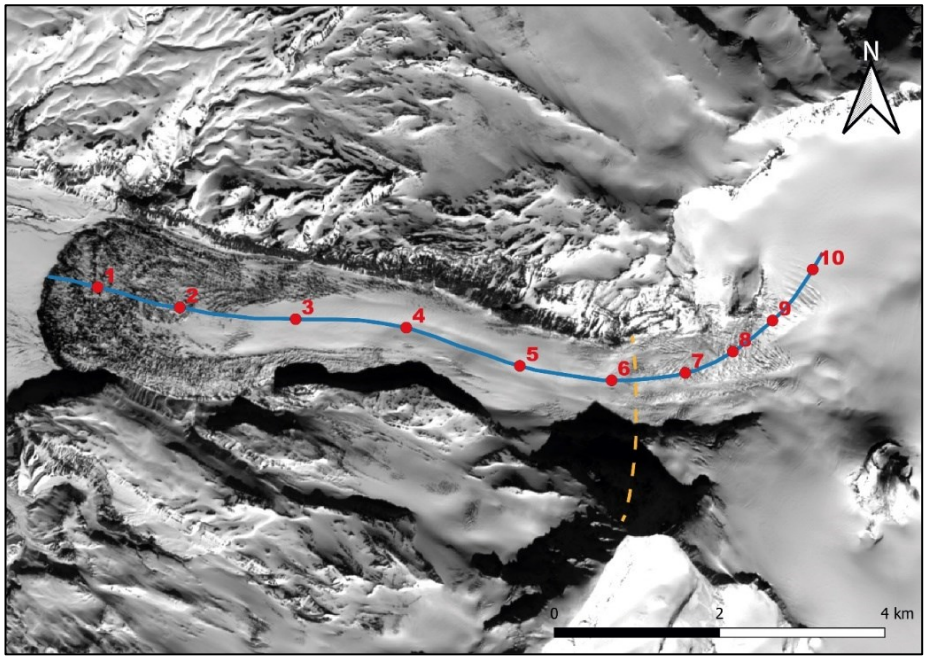

Fig. 6.13 Profile line (blue) along Cone Glacier with points for time-series analysis (red numbered dots) and approximate location of equilibrium line altitude (orange dashed line). The position of the equilibrium line altitude is determined based on data from Welch et al. (2007) and ASTER GDEM data (https://www.jpl.nasa.gov/images/pia12090-asters-global-digital-elevation-model-gdem, accessed on 19/04/2022). Background image: Sentinel-2 true colour image from 25/03/2017

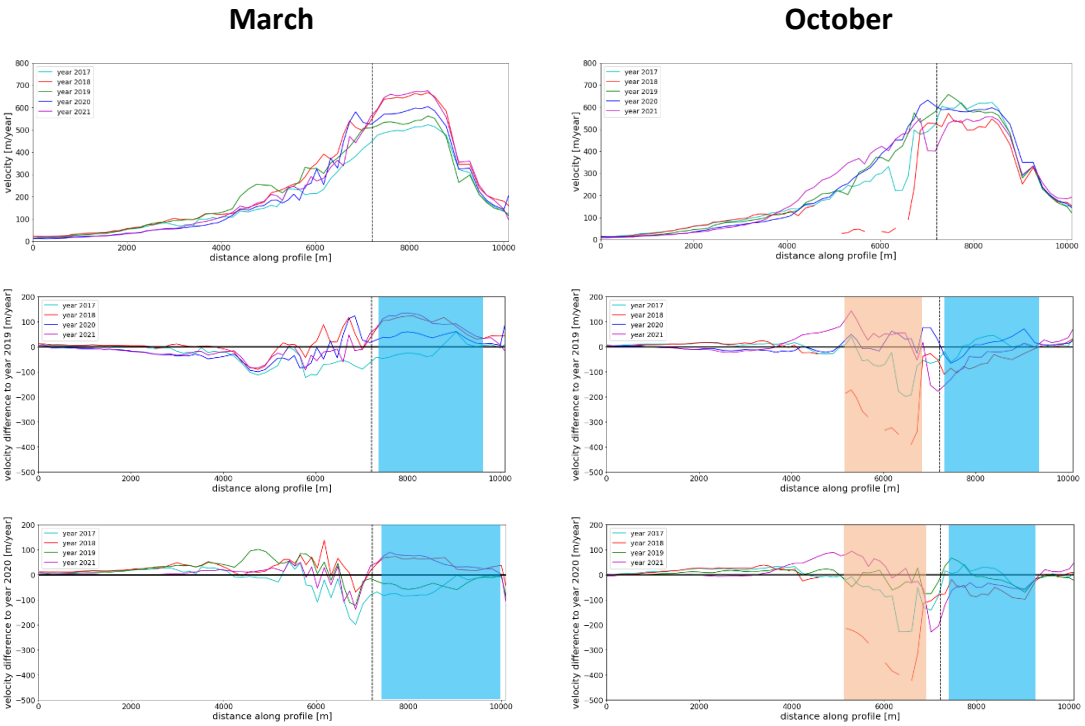

Fig. 6.14 Upper row: Velocities along the profile line presented in Fig. 6.13 for March (left) and October (right). Middle row: Velocity difference to the year 2019 for March (left) and October (right). Lower row: Velocity difference to the year 2020 for March (left) and October (right). Dashed line: equilibrium line altitude. Blue bar: Heavily crevassed region, Orange bar: mid-glacier region. The velocities and velocity differences to non-volcanic years for all months can be found in Figure 1 in the Appendix 1.

6.4.4. Time-series analysis

We generated time-series velocity data for 10 points along the profile line presented in sub-section 6.4.3 for the time period from November 2017 through January 2022 (Fig. 6.13) and compared our velocity curves with the seasonal pattern of KNMI air temperature/precipitation data for the Veniaminof region. Figure 2 and Figure 3 in the Appendix 1 present the velocity curves versus air temperature/precipitation and the correlation plots for both the entire time period investigated (i.e., November 2017 through January 2022) and the time period with presumed no volcanic activity (i.e., April 2019 until December 2020) for all 10 points separately. In this sub-section, we show the time-series velocities versus air temperature/precipitation (incl. correlation plots) for Point 3 (glacier tongue) and Point 7 (high-velocity zone) (Fig. 6.15).

For the glacier tongue (i.e., points 1-3), time-series velocities reveal no significant seasonal pattern. For areas higher up on the glacier, a seasonal velocity pattern with faster velocities in summer and slower velocities in winter can be observed, which is most prominent for large parts of the highly crevassed zone (i.e., points 5-8).

In principle, we find the highest correlation (R^2 values) of air temperature with glacier velocity for the fast-flowing and highly crevassed zone of the glacier and the lowest correlation for the slow-flowing lower glacier areas. The R^2 values for the high-velocity zone (i.e., points 5-8) significantly increase for the presumed phase of no volcanic activity (Fig. 6.16). There is an average increase of 0.174 for the correlation between glacier velocity and air temperature for the non-volcanic phase if compared to the entire investigated time period.

We also observe a remarkable shift towards increased monthly velocities for the heavily-crevassed region (points 6-9) prior to the volcanically active periods in 2018 and 2021. The signal becomes obvious if the velocity curves are compared with the respective air temperature curves (labels a and b in Fig. 6.15). The shift is much more prominent for the ~4 month lasting 2018 volcanically active period than it is for the ~1 month lasting 2021 volcanically active period. Additionally, there is an amplified slow-down of glacier velocities in upper glacier areas during and shortly after the 2018 volcanically active period (label c in Fig. 6.15). In general, both signals (speed-up and slow-down) become attenuated for lower glacier areas and cannot be observed on the glacier tongue.

For precipitation, we find an overall inverse relationship of precipitation and glacier velocity, which is highest for the heavily-crevassed region (i.e., points 6-9). For the lower glacier areas, almost no correlation can be observed. Restricting the dataset to the presumed activity-free period does not significantly change the correlation pattern both for lower glacier areas and the heavily crevassed zone (Fig. 6.16).

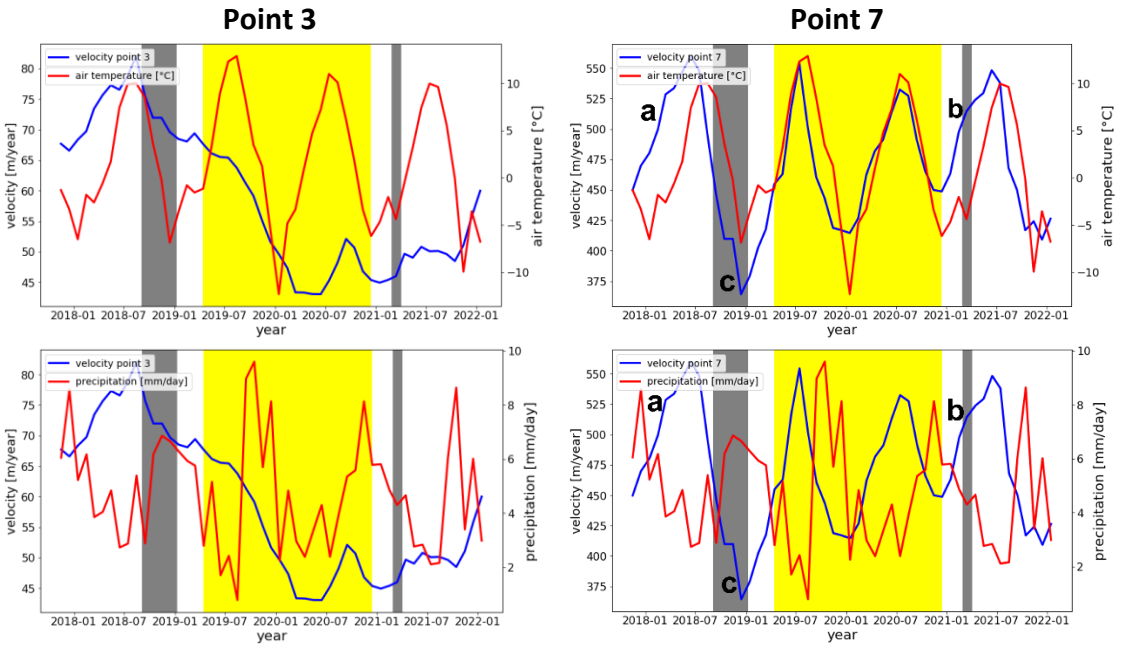

Fig. 6.15 Time-series velocities for point 3 (left column) and 7 (right column) versus air temperature (upper row) and precipitation (lower row). Grey bars: reported periods of volcanic activity in 2018 and 2021. Yellow bar: presumed no volcanic activity phase. Labels a,b,c indicate presumed volcanic signal in the velocity curve. Please note an order of magnitude higher velocities for point 7 if compared to point 3. Velocity curves versus air-temperature/precipitation for all points can be found in Figure 2 and Figure 3 in the Appendix 1.

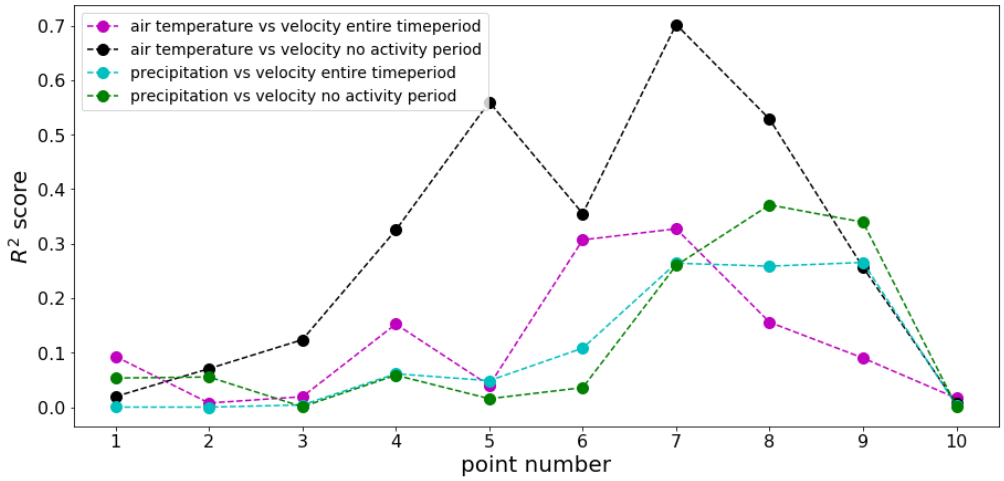

Fig. 6.16 Correlation (R^2 scores) of time-series velocity and air temperature/precipitation for points 1-10. Correlation values are presented for the entire time period (dashed purple and cyan lines) and the time period with no volcanic activity (dashed black and green lines).

6.4.5. Velocity difference maps

We generated monthly velocity difference and velocity change maps for the time periods with volcanic activity to the respective time period we assume to be activity-free (i.e., from April 2019 to December 2020). All monthly velocity difference and velocity percentage change maps for the 2018 and 2021 active periods can be viewed in Appendix 1 in Figure 4 and Figure 5.

6.4.5.1. The 2018 volcanically active period (September to December 2018)

For the 2018 active period (from September to December 2018), we compare the monthly velocity maps from November 2017 to March 2019 to the respective monthly velocity map of the (assumed) activity-free period. We observe the largest percentage velocity changes of over ~150% in some places from March until June 2018 (i.e., before the start of the eruption in September 2018); however, there are limited areas of large percentage velocity changes in each month located at the glacier's margins. It remains noteworthy that we can not observe considerably faster flow velocities in direct vicinity to the active cone throughout the entire active period.

6.4.5.1.1. Pre-eruption glacier velocity changes (November 2017 to August 2018)

From November 2017 to June 2018, for most places in the upper glacier area, we observe ~10-50 m/year faster velocities, which ranges up to ~150 m/year in some limited regions of the highly crevassed zone. Also, we find up to ~200 m/year faster velocities in the region of the equilibrium line altitude. Interestingly, the velocity change in general is relatively low for the upper glacier area (~10-20% or lower) and only exceeds ~50% in a few places there. For lower glacier areas and the glacier tongue, we observe ~10-40 m/year faster velocities; however, and especially from March until June 2018, this amounts to over ~60% of velocity change in considerable parts of the lower glacier area. Fig. 6.17 (left column) presents the velocity differences and percentage velocity change (%) for March 2018 (i.e., before the start of the 2018 active period in September 2018). By July and August 2018 (shortly before the start of the 2018 active period), we observe over ~50 m/year slower velocities for large parts of the mid- and upper glacier area, which amounts to ~80% of velocity change. Interestingly, in the lower glacier area, there are no significant changes by July and August 2018 if compared to the previous months (both for velocity difference and velocity percentage change).

6.4.5.1.2. Syn-eruption glacier velocity changes (September 2018 to December 2018)

From September to November 2018, we observe a similar velocity difference pattern if compared to August 2018 (shortly before the start of the 2018 eruptive period); however, with an enlarged region of up to ~150 m/year slower velocities in mid- to up-glacier areas, which amounts to ~70% of velocity change. Interestingly, this signal of slower velocities becomes weaker in December 2018 (towards the end of the eruptive period) with mostly below ~100 m/year (~50%) slower velocities. Fig. 6.17 (right column) presents the velocity differences and velocity changes (%) for October 2018 (during the 2018 active period). From September to December 2018, the glacier still flows ~10-40 m/year (~60%) faster in most places in the lower glacier area; however, there is a tendency to overall lower velocity differences and the largest velocity difference values tend to be restricted to a region close to the glacier's centreline. From September to December 2018, some limited areas along the glacier edges show no velocity difference or even slightly slower velocities in the order of a few m/year (up to ~40%).

6.4.5.1.3. Post-eruption glacier velocity changes (January 2019 to March 2019)

From January to March 2019, we observe slower velocities in the upper glacier area, in the order of ~30-60 m/year (~5-10%) and a limited region of up to ~100 m/year (~80%) faster velocities in the mid-glacier area. The lower glacier area shows ~10-25 m/year (up to ~40%) faster velocities for most of the glacier surface; however, some limited regions at the glacier's edges shows slightly slower velocities of a few m/year (~20-30%). From January 2019 to March 2019, we observe the overall lowest variability in glacier velocity differences and the overall lowest percentage velocity changes for the entire glacier area if compared to the pre- and syn- eruptive phases.

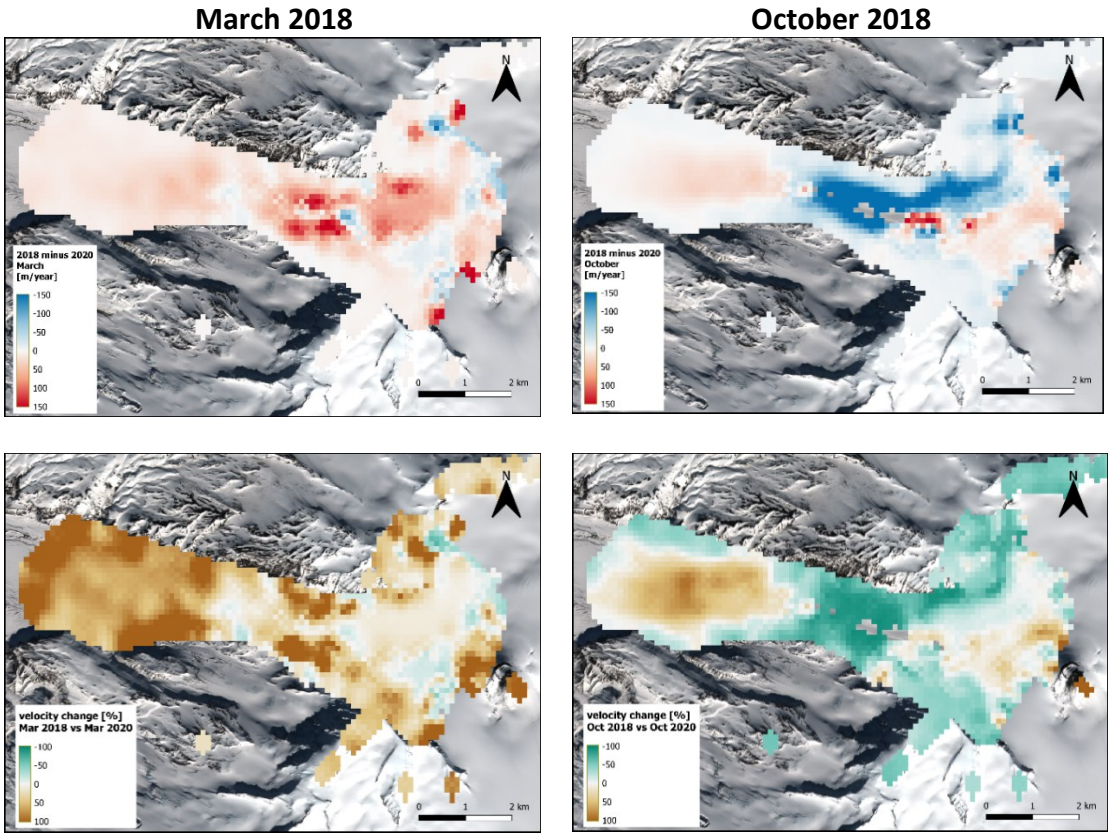

Fig. 6.17 Velocity change of year 2018 to year 2020 in March (left column) and October (right column). Velocity differences are presented in the upper row (red colours represent faster velocities in the activity year), relative velocity changes (%) are presented in the lower row. Background image: Sentinel-2 true colour image from 25/03/2017.

6.4.5.2. The 2021 volcanically active period (March/April 2021)

For the 2021 active period in March/April 2021, we compare the monthly velocity maps from January 2021 to January 2022 to the respective monthly velocity maps of the presumed 'activity-free' time period in year 2020. In contrast to the 2018 active period, which shows significant velocity changes for large parts of the glacier surface, the velocity changes for the 2021 active period is much less pronounced and most parts of the glacier area (incl. the lower glacier areas) show no velocity difference or only minor velocity changes.

6.4.5.2.1. Pre-eruption glacier velocity changes (January 2021 to February 2021)

In January and February 2021, most of the highly crevassed zone shows ~10-80 m/year (5-10%) faster velocities with some areas showing no velocity changes or even ~20-60 m/year (~up to 20%) slower velocities. We observe a restricted zone of up to ~150 m/year (above 100%) faster velocities in mid-glacier areas. For the lower glacier area, velocity differences are generally limited to ± 10 m/year (<20%) with some exceptions at the glacier edges, which show larger percentage velocity changes of up to 40%.

6.4.5.2.2. Syn-eruption glacier velocity changes (March 2021 to April 2021)

For March-April 2021, we observe up to ~80 m/year (~10%) faster glacier velocities mainly restricted to the highly crevassed zone and there is almost no area with extremely large velocity differences. For most of the up-glacier area no velocity changes or even 30-40 m/year slower velocities are observed. In mid-glacier area, a zone of ~40-80 m/year (~25%) slower velocity begins to develop in direct vicinity of a restricted region of above ~100 m/year (80-100%) faster velocities. For the lower glacier area, velocity differences are still limited to small values of ~ 10 m/year (<20%) (with some exceptions at the glacier edges); however, there are no negative velocity differences present any more. Also, we observe a pronounced zone of up to ~30 m/year (~200%) faster velocities in some limited areas at the southern glacier edge of the lower glacier area. Fig. 6.18 (left column) presents the velocity differences and velocity changes (%) for March 2021

6.4.5.2.3. Post-eruption glacier velocity changes (May 2021 to January 2022)

From May 2021 until August 2021, the zone of slower velocities in the mid-glacier area enlarges towards the up-glacier area and by August 2021, there are only limited areas of positive velocity differences in the up- and mid-glacier area. For most of the up-glacier area, velocities are ~50-90 m/year (~5-15%) slower; however, a considerable part of the mid-glacier area shows above ~200 m/year (~70%) slower velocities. For the lower glacier area, the glacier velocities still tends to have positive velocity differences of a few m/year. However, the velocity differences and percentage velocity change both tends towards zero (or even slightly negative values) by August 2021.

Interestingly, a zone of up to ~60 m/year (~25%) larger velocity differences is persistent in the lower mid-glacier area close to the centreline of the glacier. In September and October 2021, a zone of mainly negative velocity differences with up to ~200 m/year (~70%) slower velocities is present in the up- and mid-glacier area. For the lower glacier area, we find mainly negative velocity differences in the order of a few m/year. Fig. 6.18 (right column) presents the velocity differences and velocity changes (%) for October 2021. By November and December 2021, we find ~30-40 m/year (up to ~10%) slower velocities for major parts of the up-glacier area. Interestingly, the signal of faster velocities in the lower mid-glacier area increases to up to ~100 m/year (60%) by December 2021. For the lower glacier area, the tendency of negative velocity differences is reversed to positive velocity differences of a few m/year by December 2021. In January 2022, we find the glacier to have at least ~20 m/year (~10%) faster velocities if compared to January 2020 for major parts of the up- to mid-glacier area with some exceptions of up to ~140 m/year (~50-80%) faster velocities. Also, we observe large areas of large percentage velocity changes over ~100% on all parts of the glacier and the lower glacier area almost entirely shows positive velocity differences of a few m/year.

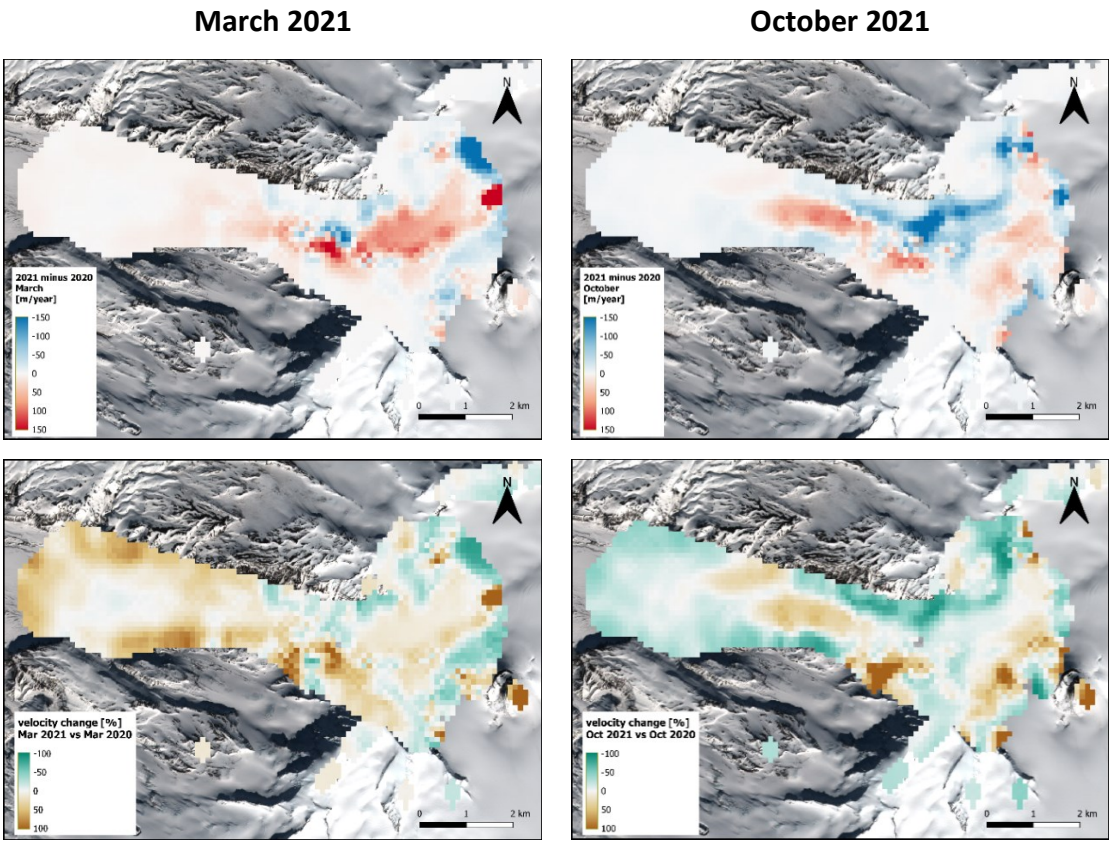

Fig. 6.18 Velocity change of year 2021 to year 2020 in March (left column) and October (right column). Velocity differences are presented in the upper row (red colours represent faster velocities in the activity year), relative velocity changes (%) are presented in the lower row. Background image: Sentinel-2 true colour image from 25/03/2017.

6.5. Discussion

6.5.1. Summary of key findings

This Chapter is concerned about volcanically triggered surface velocity changes of Cone Glacier (Mount Veniaminof, Alaska) based on Sentinel-2 data. Our dataset covers two volcanically active periods, one in 2018 (from September to December 2018) and one in 2021 (in March/April 2021). The mean surface velocity on Cone Glacier ranges from ~10-20 m/year on the glacier tongue to up to ~630 m/year for a highly crevassed zone close to the glacier's head. Validation of our glacier velocities with data from Millan et al. (2022) showed up to ± 300m/year different velocities for the highly crevassed part of the Cone Glacier area and not more than ± 20 m/year different velocities for the glacier tongue. The glacier's main flow direction is to the west (~220-290°). We find a pronounced seasonal velocity cycle for the upper Cone Glacier area (high correlation between air temperature and glacier surface velocity).

Comparison of our time-series velocities with air temperature data and velocities extracted along a profile line indicate up to ~150-200 m/year faster velocities ~10 months prior to the 2018 volcanic active period and ~10-80 m/year faster velocities at least ~2 months prior to the 2021 volcanically active period for the middle- and upper Cone Glacier region. Also, we find up to ~150 m/year slower velocities during and at least ~3 months after the 2018 volcanic active period and up to ~150-200 m/year slower velocities at least ~9 months after the 2021 volcanic active period. This signal is confirmed with our velocity difference data (i.e., monthly velocity differences from a year with volcanic activity to a year without volcanic activity). Overall, we find faster velocities in the early months (i.e., January to June) and slower velocities in the late months (i.e., July to December) of a year with an eruption if compared to a year without volcanic activity.

6.5.2. Data quality and comparison to velocity dataset of Millan et al. (2022)

The overall mean velocity we derived for Cone Glacier is comparable to the velocities derived by Millan et al. (2022) (Fig. 6.7). Compared to other Alpine-type glaciers around the globe, the glacier's mean velocity is relatively high (especially for the ice-fall area). Despite the majority of the Alaskan glaciers flowing at slower velocities, some glaciers, e.g., in the St Elias or Wrangell mountains have velocities comparable to, or even higher than the mean velocity we report for Cone Glacier (e.g., Burgess et al., 2013; Millan et al., 2022). The higher velocities in our dataset compared to the results of Millan et al. (2022) may be explained by the different time periods considered for the measurements and different sensors used. The mean velocity of our dataset covers the time period from 2016-2022 (including both the 2018 and 2021 volcanically active periods), whereas the dataset of Millan et al. (2022) covers the years 2017-18 (possibly including the 2018 volcanically active period). It is therefore possible that our mean velocity data record mostly higher glacier velocities associated to both events. Also, different sensors and offset tracking techniques/software can lead to differences. Our velocity data are derived from hand-selected (and overall cloud-free) Sentinel-2 band-8 images. The study of Millan et al. (2022) relied on both Landsat-8 and Sentinel-2 (optical) images, but the authors also used radar data (Sentinel-1) in regions with low correlation for optical images. This might lead to slightly variable results (see Huang and Li, 2011).

Since this thesis is mostly concerned with temporal differences in velocity, the absolute velocity values can be assumed to be less important and therefore a (possible) consistent bias towards faster velocities will have a minimal effect on the results presented.

We chose to use the 'percentage error variability' reported by the software to evaluate the overall performance of our results. As expected for feature tracking derived surface velocities, the software seems to have the largest errors with velocity calculation along the edges of the glacier due to, e.g., topographic shadows (e.g., see Kääb et al., 2002; Heid and Kääb, 2012; Van Wyk de Vries and Wickert, 2020). We may therefore assume velocities in the centre parts of the glacier to be most reliable. In general, the 'percentage error variability' is able to work as a first-order quality measure, but must be interpreted with caution, since it can both reflect high error and/or high temporal variability (i.e., the signal we are looking for) (pers. comm. with M. van Wyk de Vries).

6.5.3. Ice melting and volcanic forcing at Mount Veniaminof

In order to effectively determine if a volcanic signal is present in our velocity analysis, it is necessary to consider the climatic conditions in the Mount Veniaminof area. The KNMI temperature curve for the Veniaminof region shows a well-developed seasonal pattern but does not show a significant trend towards warmer (or colder) temperatures throughout our study period from 2016-2022 (Fig. 6.2). Therefore, we might expect additional melting for climate change reasons and therefore climatically induced changes in glacier surface velocity throughout the study period to be minimal. Due to its location in the Aleutian range with its overall wet climate, a large mass turnover for Cone Glacier and an overall temperate behaviour can be assumed. In principle, the wet conditions in the Veniaminof area might imply that Cone Glacier is less sensitive to possible (small-scale) volcanic forcing, since the presence of meltwater at the bed can be assumed all year round (i.e., a channelised, rather than distributed, subglacial drainage system is likely present). However, our analysis of glacier extents and surface velocities indicate the opposite, based on several reasons. First, we found Cone Glacier to be remarkably stable (i.e., only limited fluctuations of the glacier terminus) over the time period of investigation.

This contrasts findings of, e.g., Molnia et al. (2007), who reported glacier retreat and thinning for essentially all Alaskan glaciers by the end of the 21st century. Second, the relationship between air temperature and glacier velocity stands out more during a time period assumed to be volcanically 'activity-free'. Third, time-series velocity shift towards increased surface velocities before both volcanically active periods. This signal is further confirmed by higher velocities prior to volcanically active periods we found in our velocities along the profile line and our velocity difference maps.

Throughout the study period, the Smithsonian Institution reports on Mount Veniaminof from 2016-2022 show that volcanic periods in 2018 and 2021 both included active ice melting (demonstrated by, e.g., fractures in the ice and ice cauldron formation). Unfortunately, there are no data on the volume of melted ice available for either volcanically active period. However, the 1983 volcanically active period resulted in ~0.07 km^3 of ice melted with an area covered by lava flows smaller than during the 2018 active period (Yount et al., 1985; Waythomas, 2021). During the 2021 volcanically active period, three lava flows and the vents became visible in the formed ice cauldron, which indicates that a considerable part (if not all) of the ~100-150m thick ice at this location was melted (Farinotti, 2019; Waythomas, 2021). Besides ice melting due to direct lava-ice contact, increased geothermal heatflux, potentially spanning a wide range from several tens of Watt per square metre (e.g., Wrangell Mountains, Benson et al. (2007)) to several tens of kilo-Watts per square metre (e.g., Katla, Guðmundsson et al. (2007c)), can actively melt ice. For Mount Veniaminof, it might be reasonable to take the value of 19 W/m^2 derived from RES profiling as a lower boundary, since the related field campaign by Welch et al. (2007) was conducted in July 2005 (a time period with only minor volcanic activity). This value still is ~150-500 times larger than the average geothermal flux in Alaska (Batir et al., 2015) and is almost certainly sufficient to melt a considerable portion of the ice, since e.g., the work of Salamatin et al. (2000) showed that even a volcanic heat flux of ~1.0-1.8 W/m^2 can melt up to 25% of ice accumulated in a crater. Also, literature shows that subsoil temperatures can significantly increase prior to even small-scale volcanic eruptions (e.g., Liaudat et al., 2014).

The overall geologic conditions in principle favour meltwater routing underneath Cone Glacier, since the ice cap (and the glacier) is most likely underlain by permeable scoria and ash (Welch et al., 2007).

Subglacial water drainage (in westward direction) underneath Cone Glacier has also been postulated by Yount et al. (1985) in relation to the 1983-84 volcanically active period. Meltwater drainage underneath Cone Glacier is further supported by the lack of evidence for subglacial water tunnels towards the south and east and therefore favouring drainage into the Cone Glacier system (Welch et al., 2007).

6.5.4. Implications for subglacial hydrology of Cone Glacier

6.5.4.1. Upper Cone Glacier response to volcanic activity

The overall spatial pattern of highest velocities up-glacier (and in the highly crevassed zone) and slowest-velocities at Cone Glacier's terminus matches the velocity pattern of a common temperate glacier (e.g., Hodge, 1974; Macgregor et al., 2005). Most temperate glaciers around the globe also have an expressed seasonal cycle with higher summer than winter velocities (Willis, 1995; Benn and Evans, 2010). This seasonal cycle, however, can only be found in the highly crevassed zone on Cone Glacier. Our time-series velocity curves and our velocities extracted along the profile line show increased velocities for at least ~2 months prior to the 2021 volcanic activity (taking place in March/April 2021). For the 2018 volcanically active period, some time-series velocity curves and extracted velocities along the profile line indicate faster velocities at least ~10 months prior to the onset of reported volcanic activity (in September 2018); however, reliable velocities could only be generated from November 2017 and it is therefore not possible to determine for how long before November 2017 the velocity signal is present. Some time-series velocity curves and our extracted velocities along the profile line suggest that the glacier most likely remained affected at least ~3 months after the volcanically active period in 2018. In general, we can see the same pattern of higher velocities in the early months and slower velocities in the late months of a year for both years with volcanic activity (i.e., 2018 and 2021), irrespectively of the time the reported volcanic activity actually took place. For example, for the 2018 active phase, there is a glacier speed-up in the upper glacier areas from January to June 2018 and a remarkable slow-down ~3 months before the start of the volcanically active period in September 2018.

The year 2021 shows roughly the same pattern of higher velocities from January to roughly June 2021 and slower velocities from July to December 2021, despite the volcanically active period being in March 2021. In contrast to the 2018 active phase, the glacier seems to be affected at least ~9 months after the volcanically active period ended in April 2021. This would point to an overall amplified seasonal velocity cycle for a glacier being affected by volcanic activity (i.e., higher than usual velocities in spring/summer and lower than usual velocities in autumn/winter) if compared to an 'activity-free' year.

Also, our data suggest that glacier surface velocity changes might be observable more than 10 months before a volcanically active period only if the volcanically active phase takes place in the late months of the year (i.e., ~September to December) and glacier surface velocity changes are only observable for up to 3 months after the active period ended in that case. In contrast, if a volcanically active phase takes place in the early months of the year (i.e., Januar to April), glacier surface velocity changes might only be observable shortly (i.e., ~2-3 months) before the onset of an active volcanic period. However, the volcanic signal on glacier surface velocities might be observed even several months after the volcanically active phase ended.

Given the considerations above, we hypothesize that enhanced geothermal heating and/or direct ice melting resulted in changed conditions at the glacier's bed during the volcanically active years. Since temperate glaciers tend to have a poorly developed subglacial drainage system at the beginning of the melt season (i.e., in spring/early summer), additional meltwater can effectively lead to enhanced basal lubrication and glacier speed-up during that time of the year (see Barr et al., 2018a). For Cone Glacier, this would explain the higher surface velocities we observed from November 2017 through June 2018 before the start of the volcanic eruptive period in September 2018. In contrast, the distinct slow-down of glacier velocities from July 2018, particularly for an area of the glacier close to the equilibrium line altitude, can be explained by the development of an efficient subglacial drainage system, which at that time of the year is much better evolved if compared with the same time of a 'non-volcanic' year and in this case further developed by the presence of additional meltwater because of the volcanic activity.

Due to the continuous (volcanically generated) water input of the previous months, the subglacial drainage system can be assumed to consist of larger than normal R-type tunnels and therefore is capable of efficiently transporting large amounts of meltwater. As a consequence, the glacier might move at a slower velocity if compared to the same time of a 'non-volcanic' year. The above described volcanically impacted seasonal evolution of the subglacial system most likely also applies to the year 2021 (with its active phase in March 2021) and might be able to explain the slow glacier velocities we observed several months after the end of the volcanically active period.

6.5.4.2. Lower Cone Glacier response to volcanic activity

We shall now consider the lower Cone Glacier area with no (or almost no) seasonal cycle present. This behaviour is different to most 'typical' temperate glaciers, which commonly show the largest seasonal velocity variations in the lower ablation area. However, there are many exceptions (Willis, 1995), e.g., some Alaskan glaciers are reported to have the fastest velocities in spring and the lowest in fall while others have no seasonal velocity variation at all (Burgess et al., 2013). From a hydrological point of view, the availability of meltwater at the glacier bed due to surface melting is larger in the lower than in the upper glacier areas (Fountain and Walder, 1998). Since we consider Cone Glacier to be temperate, we can assume a larger amount of meltwater to be present at Cone Glacier's lower area than in the upper glacier area. It is therefore likely that Cone Glacier's subglacial drainage system is generally much more efficient in lower than in upper glacier areas and might be able to cope much better with additional volcanically generated meltwater. Although there are phases of less volcanic activity on Mount Veniaminof, Cone Glacier most likely is 'always' more or less impacted by volcanically generated meltwater. This persistent 'background activity' might explain the lack of seasonal surface velocity variations at Cone Glacier's lower areas. It remains noteworthy, however, that the large velocity changes particularly prior to the 3 months lasting 2018 volcanically active period clearly shows the glacier being at 'unrest' even at lower glacier areas. Interestingly, this signal cannot be observed for the 2021 volcanically active period and might be related to the shorter duration (i.e., ~1 month) of the 2021 volcanically active phase with less meltwater produced.

Unfortunately, there are no run-off data available at the 'Unnamed river' draining Cone Glacier, which would have been very useful to verify our hypotheses. The next station available in the USGS National Water Dashboard is Cold Bay (~240 km away), which is too far to record a significant signal related to the processes described above (https://dashboard.waterdata.usgs.gov/app/nwd/en/?aoi=default, accessed on 08/12/2022).

6.5.5. Possible limitations connected to a generalisation of the results of this case study

Our results show the large impact volcanic activity can have on glacier surface velocities, which has also been shown for a limited number of ice-clad volcanoes in the literature (e.g., Martinis, 2007; Rivera et al., 2012). However, there are some limitations that might restrict the validity of our results.

This thesis focuses on Sentinel-2 images, which provided reliable surface velocity data from November 2017 through 2022. With this, the first velocity data were only available 10 months prior to the start of the 2018 eruption in September 2018. Given the lack of velocity data before November 2017, it is in principle possible that our dataset in fact shows a reduction of velocity after the 2018 eruption even for areas of Cone Glacier above the equilibrium line altitude. However, since the second year after the eruption (2020) shows the same pattern of velocity differences as the first year after the eruption (2019) for all months (see Figure 1 Appendix), it is more likely that the dataset shows a real velocity increase for 2018 and 2021. The lower Glacier area might indeed show a long-lasting (i.e. for at least two years) post-eruption glacier slow-down, which might be related to a much more efficient drainage system (as discussed in sub-section 6.5.4.2). A similar case of long-lasting post-eruption glacier slow-down has been observed for Skeiðarárjökull after the 1996 eruption at Gjálp (see Magnússon et al., 2010).

A second limitation might be due to our results being specific to a glacier that is temperate, which implies that additional heat supplied to the glacier bed results in additional meltwater at the bed. For polythermal- and cold-based glaciers, the required amount of energy provided to the glacier bed most likely is higher to lift subglacial temperatures above the pressure melting point and therefore favour enough meltwater generation to return a large enough signal that can be picked up by the satellites.

Since most Holocene active volcanoes are located beyond the High Arctic and Antarctica (where most cold-based ice is present), glacier ice located on most active volcanoes is likely to be temperate or polythermal (Benn and Evans, 2010; Edwards et al., 2020). This would point to a more general validity of our results for a large group of glaciers located on active volcanoes.

Another limiting factor might be due to most of the volcanic signal being limited to a highly crevassed area on Mount Veniaminof. This region of the glacier coincides with the highest mean velocities in our dataset and points to being an icefall with exceptional glaciological conditions such as extreme ice extension and non-laminar ice flow (Benn and Evans, 2010; Colgan et al., 2016). At a first glance, this might suggest our results are only valid for the specific case of extremely rapid flowing ice. However, there is no good glaciological reason to assume a volcanic signal in a glacier surface velocity field is easier (or exclusively) detectable on extremely rapid flowing ice. It is possible that our results present the specific case of volcanic activity interacting with an icefall.

However, it is likely that a similar (and possibly enhanced) type of signal is observable on 'volcanic' glaciers without highly crevassed zones as well.

6.6. Conclusions

This Chapter investigated volcanically triggered surface velocity changes of Cone Glacier (Mount Veniaminof, Alaska) using Sentinel-2 data. Our dataset covers two volcanically active periods, one in 2018 (September to December 2018) and one in 2021 (March/April 2021). The main conclusions are:

- All the three, our time-series velocities, our velocities extracted along a profile line and our velocity difference maps indicate that the time period of how long before and after a volcanically active period glacier surface velocities are impacted by volcanic activity is dependent on the time of the year (i.e., the season) the activity took place.
- Our results suggest widespread changes to the subglacial hydrologic system underneath Cone Glacier. Based on our findings, we make the following conclusions:

  - For the upper- and middle Cone Glacier area, additional meltwater meets a non-well established hydrologic network in the early months (i.e., from January to June) of a year with volcanic activity resulting in widespread basal lubrication and glacier speed-up. For the late months of a year with an eruption (i.e., from July to December) a well-established subglacial drainage system (due to the water input from the previous months) is able to efficiently transport large quantities of meltwater and results in glacier slow-down.
  - For the lower Cone Glacier area, the lack of velocity variation indicates that a well-developed subglacial drainage system is present all year round and therefore additional volcanically generated meltwater is transported very efficiently resulting in overall homogeneous (i.e., season-independent) velocities. However, more subtle changes in glacier velocity indicate the lower glacier area also is at 'unrest' at least ~10 months prior to the 2018 volcanically active period.

- Since most glaciers located on active volcanoes most likely are polythermal or temperate (such as Cone Glacier), we expect a large group of glaciers impacted by volcanic activity to experience comparable changes to the subglacial drainage system and therefore show a similar velocity behaviour to our results.
- Our results add to a deeper understanding of the dynamics and the hydrology of a glacier impacted by volcanic activity and therefore contribute towards monitoring and prediction of volcanic eruptions on glacier-clad volcanoes.

Chapter 7 General conclusions and future research directions

The overall aim of this PhD project was to assess the degree to which volcanically triggered impacts on glaciers can be observed from optical satellite imagery, and to consider whether these impacts can be used to help identify, monitor and predict volcanic activity. The first objective was to investigate volcanically triggered changes on glacier surface morphology for a selection of representative ice-clad volcanoes around the globe based on optical satellite imagery from 1972 to 2015 (i.e., during the satellite remote sensing era). The second objective was to investigate volcanically triggered changes in the surface velocity and terminus position of Cone Glacier (Mount Veniaminof, Alaska) based on 99 Sentinel-2 images covering two volcanic active periods, one in September-December 2018 and one in March/April 2021. The third objective was to identify key challenges when using optical satellite images to detect volcanic impacts on glacier surface morphology and to present advice for best practice. This last objective also includes implications of our glacier velocity analysis for the dynamics and the subglacial drainage system of a temperate glacier impacted by volcanic activity.

This Chapter summarizes the key results of the thesis and outlines future research directions with the main focus on if and how glaciers might be used to identify, monitor and predict volcanic activity.

7.1. Summary of key chapter results

Chapter 5: Assessment of the use of optical satellite images to detect volcanic impacts on glacier surface morphology – (published)

Based on the work of Barr et al. (2018a), we focus on a selection of the best documented examples of volcanic impacts on glacier surface morphology from around the globe. For the 11 case examples selected, we examine ~1400 freely available satellite images and a small number of commercial images. This thorough analysis allows us to identify the most readily observable volcanic impacts on glacier surface morphology with optical satellite imagery and allows us to determine necessary temporal and spatial image resolutions.

We find that some larger cauldrons are readily observable with low-resolution (i.e., 10-100m) images, however, smaller cauldrons and crevasses often require medium (i.e., 1-10m) to high (i.e., >1m) spatial resolution images. Since the time period for the formation of the investigated features varies considerably from minutes to months/years, satellite images often have to be acquired very frequently (~several per day) to successfully monitor a particular volcanic impact. Besides image resolution, we identify cloud cover, general image availability (especially for older events) and the high costs for high-resolution images to be major limiting factors for successful detection of volcanic impacts on glacier surface morphology. Due to the reasons given above, we emphasize that a certain user knowledge/experience is often necessary to successfully identify and interpret volcanic impacts on glaciers using satellite images. Given the continuously improving spatial and temporal resolution of optical satellite images and the development of easy-to-use image access platforms, we conclude that optical satellite images are a useful source for studying changes in glacier morphology caused by volcanic activity in the future.

Chapter 6: Detection of volcanically triggered changes in surface velocity of a temperate glacier using Sentinel-2 data – a case study on Mount Veniaminof

We select Cone Glacier for our velocity analysis based on a set of glaciological criteria and eruption characteristics described in the literature (e.g., Barr et al., 2018a; Edwards et al., 2020) and the weekly volcanic activity reports by the Smithsonian Volcano Institution (*Global Volcanism Program. Report on Veniaminof (United States). In: Sennert, S K (ed.)*). The investigated time period from 2015-2022 covers two volcanically active phases, one in 2018 and one in 2021. From our glacier velocimetry results based on Sentinel-2 images, we extract monthly velocities along a profile line, we calculate time-series velocities, and we obtain velocity difference maps. Comparison of the seasonal cyclicity in our time-series velocities to climatological data gives evidence for a pre-, syn- and post eruption volcanic impact on the glacier surface velocities, which we support with the help of velocity measurements along a profile line and with velocity difference maps. For example, in mid and upper glacier areas, we find monthly glacier velocities to be up to ~150-200 m/year higher several months prior to the 2018 active period if compared to the same month during years presumed to be volcanic activity-free.

In contrast, we find glacier velocities to be up to ~200m/year slower shortly before and during the 2018 volcanic active period. These surface velocity changes are interpreted in terms of geothermal heatflux and/or direct ice melting on Mount Veniaminof to causing changes in the Cone Glacier subglacial drainage system. Dependent on the amount of (volcanically generated) meltwater available and the efficiency of the subglacial drainage network, basal lubrication might result in higher glacier surface velocities if compared to years presumed to be volcanic activity-free. In contrast, larger than normal R-type tunnels can result in effective subglacial water drainage and therefore slower surface velocities. Based on several glaciological considerations, we conclude that our results might be representative of a number of temperate glaciers affected by volcanic activity around the globe.

7.2. Future research directions

The results presented in this thesis suggest that glaciers are potentially useful indicators of volcanic activity. However, this thesis also reveals that much more research needs to be done to be able to use glaciers to identify, monitor and predict volcanic activity. This applies to research on subglacial heat flux and drainage systems, improvements in crevasse detection systems and data infrastructure, with the overall aim to ensure data access to a wide community of researchers and volcano observatories. We suggest future research should focus on the following topics:

7.2.1. Automated crevasse detection

The results of this thesis show that almost all volcanic impacts on glaciers investigated are associated with various degrees of (additional and often small-scale) crevassing. It is therefore clear, that, from both the perspective of monitoring and predicting volcanic activity on ice-clad volcanoes, future research should focus on effective (and automated) crevasse detection. Automated crevasse detection has been successfully tested using airborne laser scanning (Kodde et al., 2007), airborne LiDAR/DEMs (Foroutan et al., 2019) and ground-penetrating radar (GPR) (Walker and Ray, 2019). However, as with all field- or airborne-based methods, these techniques in general are much more expensive than satellite remote sensing based techniques and they need a comparably high level of logistical effort.

Therefore, attempts have been made towards automated crevasse detection, e.g. by using characteristic thermal properties detectable in Landsat thermal bands (Bhardwaj et al., 2016) and based on texture differences (i.e., changes in grey-scale levels) of ASTER satellite images (Xu et al., 2011).

However, and as presented in this thesis, most volcanically caused crevasses are rather small and comparatively isolated and therefore resolutions of ASTER and Landsat images in the order of ~10-30 m are not sufficient to detect them. Similar to the results of our work using optical satellite images, the automated detection results of Bhardwaj et al. (2016) and Xu et al. (2011) are limited to large-scale crevasses with minimum sizes in the order of one pixel of the sensor (i.e., ~10-30 m). Also, bad weather conditions (clouds) and eruption plumes make efficient monitoring using this data type challenging. In principle, SAR signals can effectively penetrate clouds and therefore operate independent of weather conditions and/or eruption plumes. In recent work, Zhao et al. (2022) successfully detected crevasses in Antarctica using a deep learning method based on Sentinel-1 SAR images. However, as with the studies of Bhardwaj et al. (2016) and Xu et al. (2011), the spatial resolution (20 x 40 m) of the Sentinel-1 images limit the applicability of the technique for small crevasses (Zhao et al., 2022). These limitations indicate that medium- to high-resolution optical satellite images (e.g., RapidEye, GeoEye, IKONOS-2) or medium- to high-resolution SAR satellite images (e.g., TerraSAR-X) should be used for future work on automated crevasse detection. However, to date, medium- and high-resolution satellite images typically have high costs, which most likely hinders research efforts to automate the detection of crevasses.

7.2.2. Comparison of our glacier surface velocity data to other glaciers affected by volcanic activity around the globe

This thesis for the first time investigated volcanically impacted glacier surface velocity changes with a monthly resolution, which proved to be sufficient for detecting potential volcanic impacts on glacier surface velocity. Results from the Cone Glacier study are likely representative of other temperate glaciers. However, additional studies of volcanic impacts on glacier surface velocities from other settings are needed to further validate and corroborate our results.

7.2.3. Subglacial heat flux and subglacial drainage networks

This thesis supports evidence for glacier surface velocity being affected by changes in its subglacial drainage system, (most likely because of altered) subglacial heat flux. It is commonly accepted that changes in geothermal heat flux have a large impact on glacier dynamics (e.g., Marmoni et al., 2021 and references therein) and the relationship between changes in subglacial heat flux and glacier surface velocity has been assumed by various researchers (e.g., Sturm et al., 1991; Benson et al., 2007; Rivera et al., 2012). Both, fieldwork and thermal remote sensing are required to measure variations in geothermal heatflux. For example, the work of Girona et al. (2021) investigated large-scale changes in brightness-temperatures on several volcanoes around the globe using MODIS band 31 long-wave infrared (LWIR) data (Girona et al., 2021). The results show long-term (i.e., in the order of years) and large-scale (i.e., tens of square kilometres) subtle heating of the ground surrounding a volcano, regardless of the presence of ice (Girona et al., 2021). In principle, a thermal signal could even be observable on glacierised areas, since some researchers report heat flux through ice, e.g., for the West-Antarctic Ice Sheet (e.g., Fisher et al., 2015). However, the physical basis behind this is not yet clear (see Bhardwaj et al., 2017). In terms of field-based methods, the soil temperature gradient method has proven to be a reliable tool to determine geothermal heat fluxes (e.g., Wang et al., 2019; Wang and Pang, 2022). This method was successfully applied on glacier-clad Peteroa volcano (Chile) (Liaudat et al., 2014). Both, satellite-based techniques and field-based methods could help to better quantify changes in volcanic heat flux and therefore help to better understand results obtained from the study of glacier surface velocity.

The results of this thesis on Cone Glacier point towards a control on glacier surface velocity by changes in the glacier's subglacial drainage network (see sub-section 6.5.3.). Most research on volcanically triggered changes in subglacial drainage, was conducted with a focus on Icelandic glaciers related to subglacial lake formation and jökulhlaups (Björnsson, 2003; Gudmundsson et al., 2004; Magnússon et al., 2007). These instances include the accumulation of large amounts of quickly generated meltwater in subglacial lakes, which often drains away from the eruption site through subglacial tunnels and typically results in large-scale flooding (Björnsson, 2003; Gudmundsson et al., 2004).

The situation in Iceland might not be representative of other volcanic glaciers around the globe (including Cone Glacier investigated in this thesis) because of Iceland's unique tectonic and climatic setting (i.e., high geothermal heat, high volcanic activity and large ice masses). However, literature shows that changes in subglacial drainage networks are common on most temperate glaciers around the globe (including those on ice-clad volcanoes) and impact observed glacier surface velocities (e.g., Iken and Bindschadler, 1986; Willis, 1995; Mair, 2002; Macgregor et al., 2005). Various approaches such as, e.g., water level measurements in drillholes, dye tracing experiments and ground penetrating radar have been used to study subglacial drainage systems (e.g., Iken and Bindschadler, 1986; Mair, 2002; Willis et al., 2009; Schroeder et al., 2020). However, these studies mostly focused on changes of subglacial drainage systems related to changes in meltwater input due to seasonal air temperature changes (and not volcanically triggered meltwater) and therefore more research with existing methodology could help to understand changes in subglacial drainage networks before, during and after volcanic active periods on ice-clad volcanoes.

Both, enhanced research efforts on changes in volcanic heat flux and on changes in subglacial drainage systems of ice-clad volcanoes will help to obtain a better understanding of the (short and long term) impact a particular volcano has on its glacier(s) and might lead to the use of glacier surface velocities for eruption monitoring and prediction.

7.2.4. Satellite data infrastructure and glacier surface velocity monitoring for volcano observatories

Most satellite remote sensing based software/techniques for glacier monitoring still require a high level of expert knowledge and do not necessarily meet the requirements for effective monitoring on ice-clad volcanoes. Therefore, they are not included in monitoring frameworks such as the National Volcano Early Warning System (NVEWS) established by the Consortium of U.S. Volcano Observatories (CUSVO) (Ewert et al., 2005, 2018). This thesis presents some easy-to-use and available software and tools (some web-based) that enable quick satellite image viewing, and might be of particular interest and usefulness for staff in volcano observatories.

Satellite remote sensing data already form an integral part of routine volcano monitoring in observatories, however, only the combination of seismic, geodetic, gas, hydrologic and remote sensing techniques will result in optimum monitoring results (Ewert et al., 2005; Moran et al., 2008; Miller and Jolly, 2014). Despite all monitoring techniques being important, the results of this thesis reveal that optical satellite remote sensing is a valuable additional tool for both long-term monitoring (e.g., via volcanically triggered changes in glacier surface velocity) and short-term monitoring (e.g., due to volcanically induced crevasse formation) on ice-clad volcanoes. Most satellite image providers, unfortunately, do not offer images in native resolution and staff at volcano observatories might not wish to download large satellite image files. With cloud-based providers such as Sentinel Hub Playground (https://apps.sentinel-hub.com/sentinel-playground, accessed on 08/12/2022) or GoogleEarth Engine (https://developers.google.com/earth-engine/guides/playground, accessed on 22/12/2022), users can view images from, e.g., Sentinel-1, 2 and Landsat 8-9 satellites in full (native) resolution as true- or false-colour composites without having to download. However, and as discussed in sub-section 5.4.2.1., the low-resolution of the satellite images enables only large volcanic impacts on a particular glacier to be observed. This thesis shows there is a high potential in using medium- to high-resolution (commercial) satellite images to investigate small-scale volcanic impacts on glaciers (e.g., additional crevassing), which is, however, often associated with high costs. If it is possible to use medium- to high-resolution images, these can be easily purchased from online providers such as Planet (https://www.planet.com/, accessed on 08/12/2022) or geocento (https://geocento.com/, accessed on 08/12/2022). The provider Planet additionally allows access to images directly via user applications such as QGIS and via application programming interfaces (API) and Web Mapping Services (WMS).

Most glacier velocimetry software requires downloading of large image numbers. Therefore, web-based services such as the freely available NASA MEaSUREs ITS_LIVE project (https://its-live.jpl.nasa.gov, accessed on 08/12/2022) or the GDM-OPT ICE service (discussed in sub-section 4.2.3., associated with costs) can, in principle, serve as easy-access platforms to obtain glacier surface velocity data around the globe. The ITS_LIVE project covers a large number of glaciers on Earth and allows the extraction of time-series velocities on a particular glacier in a jupyter notebook environment.

As shown in this thesis, in principle, monthly generated glacier velocity maps are sufficiently temporally resolved to study volcanically triggered changes in glacier surface velocity. The GDM-OPT ICE service does not provide high enough temporally resolved outputs to enable effective glacier monitoring on an ice-clad volcano. However, the time-series velocity function available with the ITS_LIVE project might be a useful tool to be included in observatory work, since the user can freely set the maximum time interval for generated image pairs (and therefore control temporal resolution) and velocity data are available to the present.

Despite some easy-to-access software and tools already available, the above considerations point towards an urgent need for improvements in data accessibility (both for medium- to high-resolution satellite images and high temporal resolution glacier surface velocity data) for these to be implemented in the monitoring strategy of volcano observatories.

7.2.5. Final remarks

Future research on satellite remote sensing applications for ice-clad volcanoes should prioritise the automated detection of changes on the glacier morphology (mainly additional crevassing), e.g., based on medium- to high-resolution optical satellite images. Also, there is an urgent need for better data infrastructure including easily accessible, high temporal resolution glacier velocity data on ice-clad volcanoes. Improvements on easy-to-access data infrastructure, both for change detection and glacier surface velocity, could facilitate better data access for a larger scientific community (including volcano observatories). Also, more research on changes in subglacial heatflux and subglacial drainage systems will provide better understanding of volcanically triggered changes in glacier surface velocity. This thesis demonstrates the potential of optical satellite imagery for research on ice-clad volcanoes and the results will hopefully inspire future research efforts towards using glaciers to identify, monitor and predict volcanic activity.

Data availability statement

Landsat and EO-1 data available from the USGS Earth Resources Observation and Science (EROS) Center; ASTER data are distributed by the Land Processes Distributed Active Archive Center (LP DAAC), located at USGS/EROS, Sioux Falls, SD. http://lpdaac.usgs.gov (accessed on 19/12/2022); Sentinel-2 data available from European Space Agency (ESA)/Copernicus; RapidEye and PlanetScope images obtained via planet: Planet Team (2017), Planet Application Program Interface: In Space for Life on Earth. San Francisco, CA. https://www.planet.com/ (accessed on 22/12/2022).

References

Adrian, R. J. (1991) 'Particle-Imaging Techniques for Experimental Fluid Mechanics.' *Annu. Rev. Fluid Mech.*, 23 pp. 261–304.

Adrian, R. J. (2005) 'Twenty years of particle image velocimetry.' *Experiments in Fluids*, 39(2) pp. 159–169.

Alsdorf, D. E. and Smith, L. C. (1999) 'Interferometric SAR observations of ice topography and velocity changes related to the 1996, Gjalp subglacial eruption, Iceland.' *International Journal of Remote Sensing*, 20(15–16) pp. 3031–3050.

Amigo, Á., Silva, C., Orozo, G., Bertin, D. and Lara, L. E. (2012) 'La crisis eruptiva del volcán Hudson durante octubre-noviembre 2011.' *XII Congreso Geológico Chileno, Antofagasta* pp. 457–459.

Balise, M. J. and Raymond, C. F. (1985) 'Transfer of Basal Sliding Variations to the Surface of a Linearly Viscous Glacier.' *Journal of Glaciology*, 31(109) pp. 308–318.

Barr, I. D., Lynch, C. M., Mullan, D., De Siena, L. and Spagnolo, M. (2018a) 'Volcanic impacts on modern glaciers: A global synthesis.' *Earth-Science Reviews*, 182, July, pp. 186–203.

Barr, I., Dokukin, M., Kougkoulos, I., Livingstone, S., Lovell, H., Małecki, J. and Muraviev, A. (2018b) 'Using ArcticDEM to Analyse the Dimensions and Dynamics of Debris-Covered Glaciers in Kamchatka, Russia.' *Geosciences*, 8(6) p. 216.

Barry, R. G. (2006) 'The status of research on glaciers and global glacier recession: a review.' *Progress in Physical Geography: Earth and Environment*, 30(3) pp. 285–306.

Batir, J., Blackwell, D. and Richards, M. (2015) 'Updated heat flow map of Alaska: Developing a regional scale map for exploration from limited data.' *In Proceedings from World Geothermal Congress*.

Belward, A. S. and Skøien, J. O. (2015) 'Who launched what, when and why; trends in global land-cover observation capacity from civilian earth observation satellites.' *ISPRS Journal of Photogrammetry and Remote Sensing*, 103, May, pp. 115–128.

Benn, D. I. and Evans, D. J. A. (2010) *Glaciers & glaciation*. 2nd ed, London: Hodder education.

Benson, C., Motyka, R., McNutt, S., Lüthi, M. and Truffer, M. (2007) 'Glacier–volcano interactions in the North Crater of Mt Wrangell, Alaska.' *Annals of Glaciology*, 45 pp. 48–57.

Berthier, E., Vadon, H., Baratoux, D., Arnaud, Y., Vincent, C., Feigl, K. L., Rémy, F. and Legrésy, B. (2005) 'Surface motion of mountain glaciers derived from satellite optical imagery.' *Remote Sensing of Environment*, 95(1) pp. 14–28.

Bhardwaj, A., Sam, L., Singh, S. and Kumar, R. (2016) 'Automated detection and temporal monitoring of crevasses using remote sensing and their implications for glacier dynamics.' *Annals of Glaciology*, 57(71) pp. 81–91.

Bhardwaj, A., Singh, S., Sam, L., Bhardwaj, A., Martín-Torres, F. J., Singh, A. and Kumar, R. (2017) 'MODIS-based estimates of strong snow surface temperature anomaly related to high altitude earthquakes of 2015.' *Remote Sensing of Environment*, 188, January, pp. 1–8.

Bindschadler, R. A. and Scambos, T. A. (1991) ‘Satellite-Image-Derived Velocity Field of an Antarctic Ice Stream.’ *Science*, 252(5003) pp. 242–246.

Bird, P. (2003) ‘An updated digital model of plate boundaries: UPDATED MODEL OF PLATE BOUNDARIES.’ *Geochemistry, Geophysics, Geosystems*, 4(3).

Björnsson, H. (2003) ‘Subglacial lakes and jökulhlaups in Iceland.’ *Global and Planetary Change*, 35(3–4) pp. 255–271.

Björnsson, H. and Einarsson, P. (1990) ‘Volcanoes beneath Vatnajökull, Iceland: Evidence from radio echo-sounding, earthquakes and jökulhlaups.’ *Jökull*, 40 pp. 147–168.

Björnsson, H. and Guðmundsson, M. T. (2000) ‘Surface and bedrock topography of Mýrdalsjökull, Iceland: the Katla caldera, eruption sites and routes of jökulhlaups.’ *Jökull*, 49 pp. 29–46.

Björnsson, H., Rott, H., Gudmundsson, S., Fischer, A., Siegel, A. and Gudmundsson, M. T. (2001) ‘Glacier–volcano interactions deduced by SAR interferometry.’ *Journal of Glaciology*, 47(156) pp. 58–70.

Bleick, H. A., Coombs, M. L., Cervelli, P. F., Bull, K. F. and Wessels, R. L. (2013) ‘Volcano–ice interactions precursory to the 2009 eruption of Redoubt Volcano, Alaska.’ *Journal of Volcanology and Geothermal Research*, 259, June, pp. 373–388.

Bontemps, N., Lacroix, P. and Doin, M.-P. (2018) ‘Inversion of deformation fields time-series from optical images, and application to the long term kinematics of slow-moving landslides in Peru.’ *Remote Sensing of Environment*, 210, June, pp. 144–158.

Branney, M. and Acocella, V. (2015) ‘Calderas.’ *In The Encyclopedia of Volcanoes*. Elsevier, pp. 299–315.

Breaker, L. C., Rao, D. B., Krasnopolsky, V. M. and Yan, X.-H. (1994) ‘The Feasibility of Estimating Ocean Surface Currents on an Operational Basis Using Satellite Feature Tracking Methods.’ *Bulletin of the American Meteorological Society*, 75(11) pp. 2085–2095.

Brigot, G., Colin-Koeniguer, E., Plyer, A. and Janez, F. (2016) ‘Adaptation and Evaluation of an Optical Flow Method Applied to Coregistration of Forest Remote Sensing Images.’ *IEEE Journal of Selected Topics in Applied Earth Observations and Remote Sensing*, 9(7) pp. 2923–2939.

Brook, M. S., Dean, J. F. and Keys, H. J. R. (2011) ‘Response of a mid-latitude cirque glacier to climate over the last two decades: Mangaehuehu Glacier, Mt Ruapehu: CIRQUE GLACIER RESPONSE TO CLIMATE.’ *Earth Surface Processes and Landforms*, 36(14) pp. 1973–1980.

Brugman, M.M. and Post, A. (1981) ‘Effects of volcanism on the glaciers of Mount St. Helens.’ *Geol. Survey Circular*, (850-D) pp. 1–11.

Burgess, E. W., Forster, R. R. and Larsen, C. F. (2013) ‘Flow velocities of Alaskan glaciers.’ *Nature Communications*, 4(1) p. 2146.

Calder, E. S., Lavallée, Y., Kendrick, J. E. and Bernstein, M. (2015) ‘Lava Dome Eruptions.’ *In The Encyclopedia of Volcanoes*. Elsevier, pp. 343–362.

Campbell, J. B. and Wynne, R. H. (2011) *Introduction to remote sensing*. 5th ed, New York London: Guilford Press.

Charrier, L., Godet, P., Rambour, C., Weissgerber, F., Erdmann, S. and Koeniguer, E. C. (2020) 'Analysis of dense coregistration methods applied to optical and SAR time-series for ice flow estimations.' *In 2020 IEEE Radar Conference (RadarConf20)*. Florence, Italy: IEEE, pp. 1–6.

Clarke, G. K. C. (1987) 'Fast glacier flow: Ice streams, surging, and tidewater glaciers.' *Journal of Geophysical Research*, 92(B9) p. 8835.

Colgan, W., Rajaram, H., Abdalati, W., McCutchan, C., Mottram, R., Moussavi, M. S. and Grigsby, S. (2016) 'Glacier crevasses: Observations, models, and mass balance implications: Glacier Crevasses.' *Reviews of Geophysics*, 54(1) pp. 119–161.

Colgan, W., Steffen, K., McLamb, W. S., Abdalati, W., Rajaram, H., Motyka, R., Phillips, T. and Anderson, R. (2011) 'An increase in crevasse extent, West Greenland: Hydrologic implications: INCREASED CREVASSE EXTENT WEST GREENLAND.' *Geophysical Research Letters*, 38(18) p. n/a-n/a.

Cooper, C. L., Swindles, G. T., Savov, I. P., Schmidt, A. and Bacon, K. L. (2018) 'Evaluating the relationship between climate change and volcanism.' *Earth-Science Reviews*, 177, February, pp. 238–247.

Coppola, D., Laiolo, M., Cigolini, C., Massimetti, F., Delle Donne, D., Ripepe, M., Arias, H., Barsotti, S., Parra, C. B., Centeno, R. G., Cevuard, S., Chigna, G., Chun, C., Garaebiti, E., Gonzales, D., Griswold, J., Juarez, J., Lara, L. E., López, C. M., Macedo, O., Mahinda, C., Ogburn, S., Prambada, O., Ramon, P., Ramos, D., Peltier, A., Saunders, S., de Zeeuw-van Dalfsen, E., Varley, N. and William, R. (2020) 'Thermal Remote Sensing for Global Volcano Monitoring: Experiences From the MIROVA System.' *Frontiers in Earth Science*, 7, January, p. 362.

Dehn, J., Dean, K., Engle, K. and Izbekov, P. (2002) 'Thermal precursors in satellite images of the 1999 eruption of Shishaldin Volcano.' *Bulletin of Volcanology*, 64(8) pp. 525–534.

Delgado, F., Pritchard, M., Lohman, R. and Naranjo, J. A. (2014) 'The 2011 Hudson volcano eruption (Southern Andes, Chile): Pre-eruptive inflation and hotspots observed with InSAR and thermal imagery.' *Bulletin of Volcanology*, 76(5).

Dell, R., Carr, R., Phillips, E. and Russell, A. J. (2019) 'Response of glacier flow and structure to proglacial lake development and climate at Fjallsjökull, south-east Iceland.' *Journal of Glaciology*, 65(250) pp. 321–336.

Edwards, B., Kochtitzky, W. and Battersby, S. (2020) 'Global mapping of future glaciovolcanism.' *Global and Planetary Change*, 195, December, p. 103356.

Edwards, B. R., Gudmundsson, M. T. and Russell, J. K. (2015) 'Glaciovolcanism.' *In The Encyclopedia of Volcanoes*. Elsevier, pp. 377–393.

Edwards, B. R., Karson, J., Wysocki, R., Lev, E., Bindeman, I. and Kueppers, U. (2013) 'Insights on lava–ice/snow interactions from large-scale basaltic melt experiments.' *Geology*, 41(8) pp. 851–854.

Elliott, J. R., Walters, R. J. and Wright, T. J. (2016) 'The role of space-based observation in understanding and responding to active tectonics and earthquakes.' *Nature Communications*, 7(1) p. 13844.

Emery, B. and Camps, A. (2017) *Introduction to satellite remote sensing: atmosphere, ocean and land applications*.

Enton, B. (2017) ‘The use of hyperspectral remote sensing for mineral exploration: a review.’ *Journal of Hyperspectral Remote Sensing*, 7(4) pp. 189–211.

Ewert, J. W., Diefenbach, A. K. and Ramsey, D. W. (2018) *2018 Update to the U.S. Geological Survey National Volcanic Threat Assessment*. U.S. Geological Survey (Scientific Investigations Report), p. 40.

Ewert, J. W., Guffanti, M. and Murray, T. L. (2005) *An Assessment of Volcanic Threat and Monitoring Capabilities in the United States: Framework for a National Volcano Early Warning System*. USGS.

Farinotti, D. (2019) ‘A consensus estimate for the ice thickness distribution of all glaciers on Earth - dataset.’ ETH Zurich.

Fisher, A. T., Mankoff, K. D., Tulaczyk, S. M., Tyler, S. W., Foley, N., and and the WISSARD Science Team (2015) ‘High geothermal heat flux measured below the West Antarctic Ice Sheet.’ *Science Advances*, 1(6) p. e1500093.

Foroutan, M., Marshall, S. J. and Menounos, B. (2019) ‘Automatic mapping and geomorphometry extraction technique for crevasses in geodetic mass-balance calculations at Haig Glacier, Canadian Rockies.’ *Journal of Glaciology*, 65(254) pp. 971–982.

Fountain, A. G. and Walder, J. S. (1998) ‘Water flow through temperate glaciers.’ *Reviews of Geophysics*, 36(3) pp. 299–328.

Francis, P. and Oppenheimer, C. (2004) *Volcanoes*. 2nd ed, Oxford ; New York: Oxford University Press.

Gardner, A. S., Moholdt, G., Cogley, J. G., Wouters, B., Arendt, A. A., Wahr, J., Berthier, E., Hock, R., Pfeffer, W. T., Kaser, G., Ligtenberg, S. R. M., Bolch, T., Sharp, M. J., Hagen, J. O., van den Broeke, M. R. and Paul, F. (2013) ‘A Reconciled Estimate of Glacier Contributions to Sea Level Rise: 2003 to 2009.’ *Science*, 340(6134) pp. 852–857.

Gaudin, D., Taddeucci, J., Houghton, B. F., Orr, T. R., Andronico, D., Del Bello, E., Kueppers, U., Ricci, T. and Scarlato, P. (2016) ‘3-D high-speed imaging of volcanic bomb trajectory in basaltic explosive eruptions: 3-D IMAGING OF VOLCANIC BOMB TRAJECTORY.’ *Geochemistry, Geophysics, Geosystems*, 17(10) pp. 4268–4275.

Girona, T., Realmuto, V. and Lundgren, P. (2021) ‘Large-scale thermal unrest of volcanoes for years prior to eruption.’ *Nature Geoscience*, 14(4) pp. 238–241.

GISP, K. M. (2016) *Mastering QGIS - Second Edition.* Packt Publishing.

Gjermundsen, E. F., Mathieu, R., Kääb, A., Chinn, T., Fitzharris, B. and Hagen, J. O. (2011) ‘Assessment of multispectral glacier mapping methods and derivation of glacier area changes, 1978–2002, in the central Southern Alps, New Zealand, from ASTER satellite data, field survey and existing inventory data.’ *Journal of Glaciology*, 57(204) pp. 667–683.

Glasser, N. F. and Scambos, T. A. (2008) ‘A structural glaciological analysis of the 2002 Larsen B ice-shelf collapse.’ *Journal of Glaciology*, 54(184) pp. 3–16.

Glen, J. W. (1955) ‘The creep of polycrystalline ice.’ *Proceedings of the Royal Society of London. Series A. Mathematical and Physical Sciences*, 228(1175) pp. 519–538.

Global Volcanism Program (1996) ‘Report on Grimsvotn (Iceland).’ Wunderman, R. (ed.) *Bulletin of the Global Volcanism Network*, 21(9).

Global Volcanism Program. Report on Veniaminof (United States). In: Sennert, S K (ed.) Smithsonian Institution and US Geological Survey (multiple reports from 2013 until 2021 were considered)

Global Volcanism Program and Venzke, E. (2022) ‘Volcanoes of the World, v.5.’ Smithsonian Institution.

Gorelick, N., Hancher, M., Dixon, M., Ilyushchenko, S., Thau, D. and Moore, R. (2017) ‘Google Earth Engine: Planetary-scale geospatial analysis for everyone.’ *Remote Sensing of Environment*, 202, December, pp. 18–27.

Granados, H. D., Miranda, P. J., Núñez, G. C., Alzate, B. P., Mothes, P., Roa, H. M., Cáceres Correa, B. E. and Ramos, J. C. (2015) ‘Hazards at Ice-Clad Volcanoes.’ *In Snow and Ice-Related Hazards, Risks and Disasters*. Elsevier, pp. 607–646.

Grove, T. L. and Till, C. B. (2015) ‘Melting the Earth’s Upper Mantle.’ *In The Encyclopedia of Volcanoes*. Elsevier, pp. 35–47.

Gudmundsson, A., Lecoeur, N., Mohajeri, N. and Thordarson, T. (2014) ‘Dike emplacement at Bardarbunga, Iceland, induces unusual stress changes, caldera deformation, and earthquakes.’ *Bulletin of Volcanology*, 76(10) p. 869.

Guðmundsson, M. s T., Högnadóttir, Þ., Kristinsson, A. B. and Guðbjörnsson, S. (2007a) ‘Geothermal activity in the subglacial Katla caldera, Iceland, 1999–2005, studied with radar altimetry.’ *Annals of Glaciology*, 45 pp. 66–72.

Guðmundsson, M. s T., Högnadóttir, Þ., Kristinsson, A. B. and Guðbjörnsson, S. (2007b) ‘Geothermal activity in the subglacial Katla caldera, Iceland, 1999–2005, studied with radar altimetry.’ *Annals of Glaciology*, 45 pp. 66–72.

Guðmundsson, M. s T., Högnadóttir, Þ., Kristinsson, A. B. and Guðbjörnsson, S. (2007c) ‘Geothermal activity in the subglacial Katla caldera, Iceland, 1999–2005, studied with radar altimetry.’ *Annals of Glaciology*, 45 pp. 66–72.

Gudmundsson, M. T., Sigmundsson, F. and Björnsson, H. (1997) ‘Ice–volcano interaction of the 1996 Gjálp subglacial eruption, Vatnajökull, Iceland.’ *Nature*, 389(6654) pp. 954–957.

Gudmundsson, M. T., Sigmundsson, F., Björnsson, H. and Högnadóttir, T. (2004) ‘The 1996 eruption at Gjálp, Vatnajökull ice cap, Iceland: efficiency of heat transfer, ice deformation and subglacial water pressure.’ *Bulletin of Volcanology*, 66(1) pp. 46–65.

Gudmundsson, M. T., Thordarson, T., Höskuldsson, Á., Larsen, G., Björnsson, H., Prata, F. J., Oddsson, B., Magnússon, E., Högnadóttir, T., Petersen, G. N., Hayward, C. L., Stevenson, J. A. and Jónsdóttir, I. (2012) ‘Ash generation and distribution from the April-May 2010 eruption of Eyjafjallajökull, Iceland.’ *Scientific Reports*, 2(1) p. 572.

Heid, T. and Kääb, A. (2012) ‘Evaluation of existing image matching methods for deriving glacier surface displacements globally from optical satellite imagery.’ *Remote Sensing of Environment*, 118, March, pp. 339–355.

Herman, F., Anderson, B. and Leprince, S. (2011) 'Mountain glacier velocity variation during a retreat/advance cycle quantified using sub-pixel analysis of ASTER images.' *Journal of Glaciology*, 57(202) pp. 197–207.

Hock, R., G., Rasul, C., Adler, B., Cáceres, S., Gruber, Y., Hirabayashi, M., Jackson, A., Kääb, A., Kang, S., Kutuzov, A., Milner, U., Molau, S. and Morin (2019) *High Mountain Areas. In: IPCC Special Report on the Ocean and Cryosphere in a Changing Climate*.

Hodge, S. M. (1974) 'Variations in the Sliding of a Temperate Glacier.' *Journal of Glaciology*, 13(69) pp. 349–369.

Huang, L. and Li, Z. (2011) 'Comparison of SAR and optical data in deriving glacier velocity with feature tracking.' *International Journal of Remote Sensing*, 32(10) pp. 2681–2698.

Iken, A. and Bindschadler, R. A. (1986) 'Combined measurements of Subglacial Water Pressure and Surface Velocity of Findelengletscher, Switzerland: Conclusions about Drainage System and Sliding Mechanism.' *Journal of Glaciology*, 32(110) pp. 101–119.

Kääb, A., Bolch, T., Casey, K., Heid, T., Kargel, J. S., Leonard, G. J., Paul, F. and Raup, B. H. (2014) *In* Kargel, J. S., Leonard, G. J., Bishop, M. P., Kääb, A., and Raup, B. H. (eds) *Global Land Ice Measurements from Space*. Berlin, Heidelberg: Springer Berlin Heidelberg, pp. 75–112.

Kääb, A., Huggel, C., Paul, F., Wessels, R., Raup, B., Kieffer, H. and Kargel, J. (2002) 'GLACIER MONITORING FROM ASTER IMAGERY: ACCURACY AND APPLICATIONS.' *In Proceedings of E ARSeL-LISSIG-Workshop Observing our Cryosphere from Space*. Bern, pp. 43–53.

Kääb, A., Winsvold, S., Altena, B., Nuth, C., Nagler, T. and Wuite, J. (2016) 'Glacier Remote Sensing Using Sentinel-2. Part I: Radiometric and Geometric Performance, and Application to Ice Velocity.' *Remote Sensing*, 8(7) p. 598.

Kamb, B. (1987) 'Glacier surge mechanism based on linked cavity configuration of the basal water conduit system.' *Journal of Geophysical Research*, 92(B9) p. 9083.

Klemas, V. (2015) 'Remote Sensing of Floods and Flood-Prone Areas: An Overview.' *Journal of Coastal Research*, 314, July, pp. 1005–1013.

Kodde, M. P., Pfeifer, N., Gorte, B. G. H., Geist, T. and Höfle, B. (2007) 'Automatic glacier surface analysis from airborne laser scanning.' *International Archives of the Photogrammetry, Remote Sensing and Spatial Information Sciences*, 36.3/W52 pp. 221–226.

Krimmel, R. M. and Meier, M. F. (1975) 'Glacier Applications of Erts Images.' *Journal of Glaciology*, 15(73) pp. 391–402.

Lacava, T., Marchese, F., Arcomano, G., Coviello, I., Falconieri, A., Faruolo, M., Pergola, N. and Tramutoli, V. (2014) 'Thermal Monitoring of Eyjafjöll Volcano Eruptions by Means of Infrared MODIS Data.' *IEEE Journal of Selected Topics in Applied Earth Observations and Remote Sensing*, 7(8) pp. 3393–3401.

LaFemina, P. C. (2015) 'Plate Tectonics and Volcanism.' *In The Encyclopedia of Volcanoes*. Elsevier, pp. 65–92.

Lei, Y., Gardner, A. and Agram, P. (2021) 'Autonomous Repeat Image Feature Tracking (autoRIFT) and Its Application for Tracking Ice Displacement.' *Remote Sensing*, 13(4) p. 749.

Leprince, S., Ayoub, F., Klinger, Y. and Avouac, J.-P. (2007) 'Co-Registration of Optically Sensed Images and Correlation (COSI-Corr): an operational methodology for ground deformation measurements.' *In 2007 IEEE International Geoscience and Remote Sensing Symposium*. Barcelona, Spain: IEEE, pp. 1943–1946.

Liaudat, D. T., Penas, P. and Aloy, G. (2014) 'Impact of volcanic processes on the cryospheric system of the Peteroa Volcano, Andes of southern Mendoza, Argentina.' *Geomorphology*, 208, March, pp. 74–87.

Liu, J. G. and Mason, P. (2009) *Essential Image Processing and GIS for Remote Sensing*.

Lopez Arenas, C. D. and Ramirez Cadena, J. (2010) *Glaciares, nieves y hielos de America Latina: cambio climatico y amenazas.* Bogotá: Ingeominas.

Macgregor, K. R., Riihimaki, C. A. and Anderson, R. S. (2005) 'Spatial and temporal evolution of rapid basal sliding on Bench Glacier, Alaska, USA.' *Journal of Glaciology*, 51(172) pp. 49–63.

Magnússon, E., Björnsson, H., Rott, H. and Pálsson, F. (2010) 'Reduced glacier sliding caused by persistent drainage from a subglacial lake.' *The Cryosphere*, 4(1) pp. 13–20.

Magnússon, E., Gudmundsson, M. T., Roberts, M. J., Sigurðsson, G., Höskuldsson, F. and Oddsson, B. (2012) 'Ice-volcano interactions during the 2010 Eyjafjallajökull eruption, as revealed by airborne imaging radar: ICE-VOLCANO INTERACTIONS.' *Journal of Geophysical Research: Solid Earth*, 117(B7) p. n/a-n/a.

Magnússon, E., Rott, H., Björnsson, H. and Pálsson, F. (2007) 'The impact of jökulhlaups on basal sliding observed by SAR interferometry on Vatnajökull, Iceland.' *Journal of Glaciology*, 53(181) pp. 232–240.

Mair, D. (2002) 'Influence of subglacial drainage system evolution on glacier surface motion: Haut Glacier d'Arolla, Switzerland.' *Journal of Geophysical Research*, 107(B8) p. 2175.

Major, J. J. and Newhall, C. G. (1989) 'Snow and ice perturbation during historical volcanic eruptions and the formation of lahars and floods: A global review.' *Bulletin of Volcanology*, 52(1) pp. 1–27.

Marmoni, G. M., Martino, S., Salvatore, M. C., Gaeta, M., Perinelli, C., Scarascia Mugnozza, G. and Baroni, C. (2021) 'Numerical modelling of geothermal heat flux and ice velocity influencing the thermal conditions of the Priestley Glacier trough (northern Victoria Land, Antarctica).' *Geomorphology*, 394, December, p. 107959.

Martin, M. D., Barr, I., Edwards, B., Spagnolo, M., Vajedian, S. and Symeonakis, E. (2021) 'Assessing the Use of Optical Satellite Images to Detect Volcanic Impacts on Glacier Surface Morphology.' *Remote Sensing*, 13(17) p. 3453.

Martinis, S. (2007) 'Influences of the 2004 Jokulhlaup on Ice Dynamics of Skeidararjokull, Iceland, Using Terra-ASTER Imagery.' *Photogrammetrische Fernerkundung Geoinformation*, 5 pp. 337–347.

McGimsey, R. G., Neal, C. A., Girina, O. A., Chibisova, M. V. and Rybin, A. V. (2014) '2009 Volcanic activity in Alaska, Kamchatka, and the Kurile Islands—Summary of events and response of the Alaska Volcano Observatory.'

Messerli, A. and Grinsted, A. (2015) 'Image georectification and feature tracking toolbox: ImGRAFT.' *Geoscientific Instrumentation, Methods and Data Systems*, 4(1) pp. 23–34.

Millan, R., Mouginot, J., Rabatel, A., Jeong, S., Cusicanqui, D., Derkacheva, A. and Chekki, M. (2019) 'Mapping Surface Flow Velocity of Glaciers at Regional Scale Using a Multiple Sensors Approach.' *Remote Sensing*, 11(21) p. 2498.

Millan, R., Mouginot, J., Rabatel, A. and Morlighem, M. (2022) 'Ice velocity and thickness of the world's glaciers.' *Nature Geoscience*, 15(2) pp. 124–129.

Miller, C. A. and Jolly, A. D. (2014) 'A model for developing best practice volcano monitoring: a combined threat assessment, consultation and network effectiveness approach.' *Natural Hazards*, 71(1) pp. 493–522.

Molnia, B. F. (2007) 'Late nineteenth to early twenty-first century behavior of Alaskan glaciers as indicators of changing regional climate.' *Global and Planetary Change*, 56(1–2) pp. 23–56.

Monsalve, M. L., Pulgarín, B. A., Mojica, J., Santacoloma, C. C. and Cardona, C. E. (2011) 'INTERPRETACIÓN DE LA ACTIVIDAD ERUPTIVA DEL VOLCÁN NEVADO DEL HUILA (COLOMBIA), 2007 – 2009: ANÁLISIS DE COMPONENTES DE MATERIALES EMITIDOS.' *Boletín de Geología*, 33(2) pp. 73–93.

Moran, S. C., Freymueller, J. T., LaHusen, R. G., McGee, K. A., Poland, M. P., Power, J. A., Schmidt, D. A., Schneider, D. J., Stephens, G., Werner, C. A. and White, R. A. (2008) *Instrumentation Recommendations for Volcano Monitoring at U.S. Volcanoes Under the National Volcano Early Warning System*. USGS, p. 47.

Mouginot, J. and Rignot, E. (2015) 'Ice motion of the Patagonian Icefields of South America: 1984–2014.' *Geophysical Research Letters*, 42(5) pp. 1441–1449.

Muraviev, A. Ya. and Muraviev, Ya. D. (2016) 'Fluctuations of glaciers of the Klyuchevskaya group of volcanoes in the 20th –21st centuries.' *Ice and Snow*, 56(4) pp. 480–492.

Muste, M., Fujita, I. and Hauet, A. (2008) 'Large-scale particle image velocimetry for measurements in riverine environments: LARGE-SCALE PARTICLE VELOCIMETRY.' *Water Resources Research*, 44(4).

Naranjo, J. L., Sigurdsson, H., Carey, S. N. and Fritz, W. (1986) 'Eruption of the Nevado del Ruiz Volcano, Colombia, On 13 November 1985: Tephra Fall and Lahars.' *Science*, 233(4767) pp. 961–963.

Neal, C. A., Doukas, M. P. and McGimsey, R. G. (1995) *VOLCANIC ACTIVITY IN ALASKA: SUMMARY OF EVENTS AND RESPONSE OF THE ALASKA VOLCANO OBSERVATORY 1993*.

Nuth, C. and Kääb, A. (2011) 'Co-registration and bias corrections of satellite elevation data sets for quantifying glacier thickness change.' *The Cryosphere*, 5(1) pp. 271–290.

Oddsson, B., Gudmundsson, M. T., Edwards, B. R., Thordarson, T., Magnússon, E. and Sigurðsson, G. (2016) 'Subglacial lava propagation, ice melting and heat transfer during emplacement of an intermediate lava flow in the 2010 Eyjafjallajökull eruption.' *Bulletin of Volcanology*, 78(7) p. 48.

Oppenheimer, C. (2011) *Eruptions that Shook the World.* Cambridge: Cambridge University Press.

Patrick, M. R. and Smellie, J. L. (2013) 'Synthesis A spaceborne inventory of volcanic activity in Antarctica and southern oceans, 2000–10.' *Antarctic Science*, 25(4) pp. 475–500.

Patrick, M. R., Smellie, J. L., Harris, A. J. L., Wright, R., Dean, K., Izbekov, P., Garbeil, H. and Pilger, E. (2005) 'First recorded eruption of Mount Belinda volcano (Montagu Island), South Sandwich Islands.' *Bulletin of Volcanology*, 67(5) pp. 415–422.

Paul, F., Kääb, A. and Haeberli, W. (2007) 'Recent glacier changes in the Alps observed by satellite: Consequences for future monitoring strategies.' *Global and Planetary Change*, 56(1–2) pp. 111–122.

Paul, F., Winsvold, S., Kääb, A., Nagler, T. and Schwaizer, G. (2016) 'Glacier Remote Sensing Using Sentinel-2. Part II: Mapping Glacier Extents and Surface Facies, and Comparison to Landsat 8.' *Remote Sensing*, 8(7) p. 575.

Pfeffer, W. T., Arendt, A. A., Bliss, A., Bolch, T., Cogley, J. G., Gardner, A. S., Hagen, J.-O., Hock, R., Kaser, G., Kienholz, C., Miles, E. S., Moholdt, G., Mölg, N., Paul, F., Radić, V., Rastner, P., Raup, B. H., Rich, J., Sharp, M. J., and The Randolph Consortium (2014) 'The Randolph Glacier Inventory: a globally complete inventory of glaciers.' *Journal of Glaciology*, 60(221) pp. 537–552.

Pierson, T. C., Janda, R. J., Thouret, J.-C. and Borrero, C. A. (1990) 'Perturbation and melting of snow and ice by the 13 November 1985 eruption of Nevado del Ruiz, Colombia, and consequent mobilization, flow and deposition of lahars.' *Journal of Volcanology and Geothermal Research*, 41(1–4) pp. 17–66.

Plank, S., Nolde, M., Richter, R., Fischer, C., Martinis, S., Riedlinger, T., Schoepfer, E. and Klein, D. (2018) 'Monitoring of the 2015 Villarrica Volcano Eruption by Means of DLR's Experimental TET-1 Satellite.' *Remote Sensing*, 10(9) p. 1379.

Provost, F., Malet, J.-P., Michea, D., Doin, M.-P., Lacroix, P., Boissier, E., Pointal, E. and Bally, P. (2021) 'Terrain Deformation Measurements from Optical Satellite Imagery: On-Line Processing Services for Geohazards Monitoring.' *In 2021 IEEE International Geoscience and Remote Sensing Symposium IGARSS*. Brussels, Belgium: IEEE, pp. 1907–1910.

'QGIS Desktop 3.22 User Guide' (2022).

Rabatel, A., Francou, B., Soruco, A., Gomez, J., Cáceres, B., Ceballos, J. L., Basantes, R., Vuille, M., Sicart, J.-E., Huggel, C., Scheel, M., Lejeune, Y., Arnaud, Y., Collet, M., Condom, T., Consoli, G., Favier, V., Jomelli, V., Galarraga, R., Ginot, P., Maisincho, L., Mendoza, J., Ménégoz, M., Ramirez, E., Ribstein, P., Suarez, W., Villacis, M. and Wagnon, P. (2013) 'Current state of glaciers in the tropical Andes: a multi-century perspective on glacier evolution and climate change.' *The Cryosphere*, 7(1) pp. 81–102.

Rampino, M. R. and Self, S. (1993) 'Climate-Volcanism Feedback and the Toba Eruption of ~74,000 Years Ago.' *Quaternary Research*, 40(3) pp. 269–280.

Rampino, M. R., Self, S. and Stothers, R. B. (1988) 'Volcanic Winters.' *Annual Review of Earth and Planetary Sciences*, 16(1) pp. 73–99.

Reinthaler, J., Paul, F., Granados, H. D., Rivera, A. and Huggel, C. (2019) 'Area changes of glaciers on active volcanoes in Latin America between 1986 and 2015 observed from multi-temporal satellite imagery.' *Journal of Glaciology*, 65(252) pp. 542–556.

Reynolds, H. I., Gudmundsson, M. T., Högnadóttir, T., Magnússon, E. and Pálsson, F. (2017) 'Subglacial volcanic activity above a lateral dyke path during the 2014–2015 Bárdarbunga-Holuhraun rifting episode, Iceland.' *Bulletin of Volcanology*, 79(6).

RGI (2017) 'Randolph Glacier Inventory 6.0.' NSIDC.

Richardson, J. M. and Brook, M. S. (2010) 'Ablation of debris-covered ice: some effects of the 25 September 2007 Mt Ruapehu eruption.' *Journal of the Royal Society of New Zealand*, 40(2) pp. 45–55.

Riel, B., Milillo, P., Simons, M., Lundgren, P., Kanamori, H. and Samsonov, S. (2015) 'The collapse of Bárðarbunga caldera, Iceland.' *Geophysical Journal International*, 202(1) pp. 446–453.

Rivera, A., Bown, F., Carrión, D. and Zenteno, P. (2012) 'Glacier responses to recent volcanic activity in Southern Chile.' *Environmental Research Letters*, 7(1) p. 014036.

Rivera, A., Cawkwell, F., Wendt, A. and Zamora, R. (2014) 'Mapping Blue-Ice Areas and Crevasses in West Antarctica Using ASTER Images, GPS, and Radar Measurements.' *In* Kargel, J. S., Leonard, G. J., Bishop, M. P., Kääb, A., and Raup, B. H. (eds) *Global Land Ice Measurements from Space*. Berlin, Heidelberg: Springer Berlin Heidelberg, pp. 743–757.

Robock, A. (2015) 'Climatic Impacts of Volcanic Eruptions.' *In The Encyclopedia of Volcanoes*. Elsevier, pp. 935–942.

Rodionov, S. N., Overland, J. E. and Bond, N. A. (2005) 'Spatial and temporal variability of the Aleutian climate.' *Fisheries Oceanography*, 14(s1) pp. 3–21.

Rossi, C., Minet, C., Fritz, T., Eineder, M. and Bamler, R. (2016) 'Temporal monitoring of subglacial volcanoes with TanDEM-X — Application to the 2014–2015 eruption within the Bárðarbunga volcanic system, Iceland.' *Remote Sensing of Environment*, 181, August, pp. 186–197.

Röthlisberger, H. (1972) 'Water Pressure in Intra- and Subglacial Channels.' *Journal of Glaciology*, 11(62) pp. 177–203.

Röthlisberger, H. and Lang, H. (1987) 'Glacial hydrology.' *In Glacio-fluvial Sediment Transport*. A. M. Gurnell and M. J. Clark, New York: John Wiley, pp. 207–284.

Rupnik, E., Daakir, M. and Pierrot Deseilligny, M. (2017) 'MicMac – a free, open-source solution for photogrammetry.' *Open Geospatial Data, Software and Standards*, 2(1) p. 14.

Salamatin, A. N., Murav'yev, Y. D., Shiraiwa, T. and Matsuoka, K. (2000) 'Modelling dynamics of glaciers in volcanic craters.' *Journal of Glaciology*, 46(153) pp. 177–187.

Scambos, T. A., Dutkiewicz, M. J., Wilson, J. C. and Bindschadler, R. A. (1992) 'Application of image cross-correlation to the measurement of glacier velocity using satellite image data.' *Remote Sensing of Environment*, 42(3) pp. 177–186.

Schaefer, J. R. (2011) 'The 2009 eruption of Redoubt Volcano, Alaska.' *Report of Investigations*, 5 p. 45.

Scharrer, K., Spieler, O., Mayer, Ch. and Münzer, U. (2008) 'Imprints of sub-glacial volcanic activity on a glacier surface—SAR study of Katla volcano, Iceland.' *Bulletin of Volcanology*, 70(4) pp. 495–506.

Schilling, S. P., Carrara, P. E., Thompson, R. A. and Iwatsubo, E. Y. (2004) 'Posteruption glacier development within the crater of Mount St. Helens, Washington, USA.' *Quaternary Research*, 61(3) pp. 325–329.

Schott, J. R. (2007) *Remote sensing: the image chain approach*. New York: Oxford University Press.

Schroeder, D. M., Bingham, R. G., Blankenship, D. D., Christianson, K., Eisen, O., Flowers, G. E., Karlsson, N. B., Koutnik, M. R., Paden, J. D. and Siegert, M. J. (2020) 'Five decades of radioglaciology.' *Annals of Glaciology*, 61(81) pp. 1–13.

Shirmard, H., Farahbakhsh, E., Müller, R. D. and Chandra, R. (2022) 'A review of machine learning in processing remote sensing data for mineral exploration.' *Remote Sensing of Environment*, 268, January, p. 112750.

Siebert, L., Cottrell, E., Venzke, E. and Andrews, B. (2015) 'Earth's Volcanoes and Their Eruptions: An Overview.' *In The Encyclopedia of Volcanoes*. Elsevier, pp. 239–255.

Sigurdsson, H. (2015) 'Introduction.' *In The Encyclopedia of Volcanoes*. Elsevier, pp. 1–12.

de Silva, S. and Lindsay, J. M. (2015) 'Primary Volcanic Landforms.' *In The Encyclopedia of Volcanoes*. Elsevier, pp. 273–297.

Smellie, J. (2006) 'The relative importance of supraglacial versus subglacial meltwater escape in basaltic subglacial tuya eruptions: An important unresolved conundrum.' *Earth-Science Reviews*, 74(3–4) pp. 241–268.

Smellie, J. L. and Edwards, B. R. (2016) *Glaciovolcanism on Earth and Mars: products, processes, and palaeoenvironmental significance*. Cambridge: Cambridge University Press.

Smithsonian Institution and Venzke, E. (2013) 'Volcanoes of the World, v. 4.3.4.' Global Volcanism Program.

Strachan, S. M. (2001) *A geophysical investigation of the Eyjafjallajökull glaciovolcanic system, South Iceland, using radio echo sounding*. PhD thesis. Dep. of Geogr., Univ. of Edingburgh.

Stumpf, A., Malet, J.-P. and Delacourt, C. (2017) 'Correlation of satellite image time-series for the detection and monitoring of slow-moving landslides.' *Remote Sensing of Environment*, 189, February, pp. 40–55.

Sturm, M., Hall, D. K., Benson, C. S. and Field, W. O. (1991) 'Non-climatic control of glacier-terminus fluctuations in the Wrangell and Chugach Mountains, Alaska, U.S.A.' *Journal of Glaciology*, 37(127) pp. 348–356.

Swanson, D. A. and Holcomb, R. T. (1990) 'Regularities in Growth of the Mount St. Helens Dacite Dome, 1980–1986.' *In* Fink, J. H. (ed.) *Lava Flows and Domes*. Berlin, Heidelberg: Springer Berlin Heidelberg (IAVCEI Proceedings in Volcanology), pp. 3–24.

Symeonakis, E., Higginbottom, T., Petroulaki, K. and Rabe, A. (2018) 'Optimisation of Savannah Land Cover Characterisation with Optical and SAR Data.' *Remote Sensing*, 10(4) p. 499.

Symeonakis, E., Korkofigkas, A., Vamvoukakis, G., Stamou, G. and Arnau-Rosalén, E. (2020) 'DEEP LEARNING MONITORING OF WOODY VEGETATION DENSITY IN A SOUTH AFRICAN SAVANNAH REGION.' *The International Archives of the Photogrammetry, Remote Sensing and Spatial Information Sciences*, XLIII-B3-2020, August, pp. 1645–1649.

Taillant, J. D. (2015) *Glaciers: the politics of ice*.

Thouret, J.-C. (1990) 'Effects of the November 13, 1985 eruption on the snow pack and ice cap of Nevado del Ruiz volcano, Colombia.' *Journal of Volcanology and Geothermal Research*, 41(1–4) pp. 177–201.

Trabant, D. C. and Hawkins, D. B. (1997) *Glacier Ice-Volume Modeling and Glacier Volumes on Redoubt Volcano, Alaska*. U.S. Geological Survey Water-Resources Investigation Report 97-4187, pp. 1–29.

Tuffen, H. (2007) 'Models of ice melting and edifice growth at the onset of subglacial basaltic eruptions.' *Journal of Geophysical Research*, 112(B3) p. B03203.

Van Wyk de Vries, M. and Wickert, A. D. (2020) *Glacier Image Velocimetry: an open-source toolbox for easy andrapid calculation of high-resolution glacier-velocity fields*. Glaciers/Remote Sensing.

Van Wyk de Vries, M. and Wickert, A. D. (2021) 'Glacier Image Velocimetry: an open-source toolbox for easy and rapid calculation of high-resolution glacier velocity fields.' *The Cryosphere*, 15(4) pp. 2115–2132.

Walder, J. S. (1986) 'Hydraulics of Subglacial Cavities.' *Journal of Glaciology*, 32(112) pp. 439–445.

Walder, J. S., LaHusen, R. G., Vallance, J. W. and Schilling, S. P. (2007) 'Emplacement of a silicic lava dome through a crater glacier: Mount St Helens, 2004–06.' *Annals of Glaciology*, 45 pp. 14–20.

Walder, J. S., Schilling, S. P., Vallance, J. W. and LaHusen, R. G. (2008) *In* Sherrod, D. R., Scott, W. E., and Stauffer, P. H. (eds) *A volcano rekindled: the renewed eruption of Mount St. Helens, 2004-2006*. Reston, Va: U.S. Dept. of the Interior, U.S. Geological Survey (Professional paper, 1750), pp. 257–276.

Walker, B. and Ray, L. (2019) 'Multi-Class Crevasse Detection Using Ground Penetrating Radar and Feature-Based Machine Learning.' *In IGARSS 2019 - 2019 IEEE International Geoscience and Remote Sensing Symposium*. Yokohama, Japan: IEEE, pp. 3578–3581.

Waller, R. I. (2001) 'The influence of basal processes on the dynamic behaviour of cold-based glaciers.' *Quaternary International*, 86(1) pp. 117–128.

Wang, Y. and Pang, Z. (2022) 'Heat flux in volcanic and geothermal areas: Methods, principles, applications and future directions.' *Gondwana Research*, September, p. S1342937X22002623.

Wang, Y., Pang, Z., Hao, Y., Fan, Y., Tian, J. and Li, J. (2019) 'A revised method for heat flux measurement with applications to the fracture-controlled Kangding geothermal system in the Eastern Himalayan Syntaxis.' *Geothermics*, 77, January, pp. 188–203.

Waythomas, C. (2021) 'Simultaneous effusive and explosive cinder cone eruptions at Veniaminof Volcano, Alaska.' *Volcanica*, 4(2) pp. 295–307.

Weertman, J. (1973) ‘Can a water-filled crevasse reach the bottom surface of a glacier?,’ 95 pp. 139–145.

Welch, B. C., Dwyer, K., Helgen, M., Waythomas, C. F. and Jacobel, R. W. (2007) ‘Geophysical survey of the intra-caldera icefield of Mt Veniaminof, Alaska.’ *Annals of Glaciology*, 45 pp. 58–65.

Westerweel, J. (1997) ‘Fundamentals of digital particle image velocimetry.’ *Measurement Science and Technology*. IOP Publishing, 8(12) pp. 1379–1392.

Williams, R. S. (1987) ‘Satellite Remote Sensing of Vatnajökull, Iceland.’ *Annals of glaciology*. Cambridge, UK: Cambridge University Press, 9(Journal Article) pp. 127–135.

Willis, I. C. (1995) ‘Intra-annual variations in glacier motion: a review.’ *Progress in Physical Geography: Earth and Environment*, 19(1) pp. 61–106.

Willis, I., Lawson, W., Owens, I., Jacobel, B. and Autridge, J. (2009) ‘Subglacial drainage system structure and morphology of Brewster Glacier, New Zealand.’ *Hydrological Processes*, 23(3) pp. 384–396.

Wilson, F. H., Hults, C. P., Mull, C. G. and Karl, S. M. (2015) *Geologic map of Alaska*. (Scientific Investigations Map), p. 197.

Wilson, R., Mernild, S. H., Malmros, J. K., Bravo, C. and Carrión, D. (2016) ‘Surface velocity fluctuations for Glaciar Universidad, central Chile, between 1967 and 2015.’ *Journal of Glaciology*, 62(235) pp. 847–860.

Wright, R., Flynn, L. P., Garbeil, H., Harris, A. J. L. and Pilger, E. (2004) ‘MODVOLC: near-real-time thermal monitoring of global volcanism.’ *Journal of Volcanology and Geothermal Research*, 135(1–2) pp. 29–49.

Xu, T., Yang, W., Liu, Y., Zhou, C. and Wang, Z. (2011) ‘Crevasse Detection in Antarctica Using ASTER Images.’ *In* Kamel, M. and Campilho, A. (eds) *Image Analysis and Recognition*. Berlin, Heidelberg: Springer Berlin Heidelberg (Lecture Notes in Computer Science), pp. 370–379.

Yount, E. M., Miller, T. P., Emanuel, R. P. and Wilson, F. H. (1985) *Eruption in an ice-filled caldera, Mount Veniaminof, Alaska Peninsula: A section in The United States Geological Survey in Alaska: Accomplishments during 1983*. US Geologcial Survey (Circular).

Yu, L. and Gong, P. (2012) ‘Google Earth as a virtual globe tool for Earth science applications at the global scale: progress and perspectives.’ *International Journal of Remote Sensing*, 33(12) pp. 3966–3986.

Zemp, M., Frey, H., Gärtner-Roer, I., Nussbaumer, S. U., Hoelzle, M., Paul, F., Haeberli, W., Denzinger, F., Ahlstrøm, A. P., Anderson, B., Bajracharya, S., Baroni, C., Braun, L. N., Cáceres, B. E., Casassa, G., Cobos, G., Dávila, L. R., Delgado Granados, H., Demuth, M. N., Espizua, L., Fischer, A., Fujita, K., Gadek, B., Ghazanfar, A., Ove Hagen, J., Holmlund, P., Karimi, N., Li, Z., Pelto, M., Pitte, P., Popovnin, V. V., Portocarrero, C. A., Prinz, R., Sangewar, C. V., Severskiy, I., Sigurđsson, O., Soruco, A., Usubaliev, R. and Vincent, C. (2015) ‘Historically unprecedented global glacier decline in the early 21st century.’ *Journal of Glaciology*, 61(228) pp. 745–762.

Zhao, J., Liang, S., Li, X., Duan, Y. and Liang, L. (2022) ‘Detection of Surface Crevasses over Antarctic Ice Shelves Using SAR Imagery and Deep Learning Method.’ *Remote Sensing*, 14(3) p. 487.

Zimanowski, B., Büttner, R., Dellino, P., White, J. D. L. and Wohletz, K. H. (2015) 'Magma–Water Interaction and Phreatomagmatic Fragmentation.' *In The Encyclopedia of Volcanoes*. Elsevier, pp. 473–484.

Þor Þorðarson, Þor Þorðarson, Armann Hoskuldsson and Hoskuldsson, A. (2014) *Iceland*. 2. ed, Edinburgh: Dunedin (Classic geology in Europe, 3).

Appendix 1

Table 3: Sentinel-2 image dates used to perform feature tracking on Cone Glacier (99 images in total)

Image number	Satellite	Processing Level	GEE code	acquisiton date
1	Sentinel-2	Level-1C	COPERNICUS/S2	2016-05-09
2	Sentinel-2	Level-1C	COPERNICUS/S2	2016-05-29
3	Sentinel-2	Level-1C	COPERNICUS/S2	2016-07-08
4	Sentinel-2	Level-1C	COPERNICUS/S2	2016-07-28
5	Sentinel-2	Level-1C	COPERNICUS/S2	2016-11-05
6	Sentinel-2	Level-1C	COPERNICUS/S2	2017-01-04
7	Sentinel-2	Level-1C	COPERNICUS/S2	2017-02-03
8	Sentinel-2	Level-1C	COPERNICUS/S2	2017-03-25
9	Sentinel-2	Level-1C	COPERNICUS/S2	2017-04-14
10	Sentinel-2	Level-1C	COPERNICUS/S2	2017-05-04
11	Sentinel-2	Level-1C	COPERNICUS/S2	2017-07-23
12	Sentinel-2	Level-1C	COPERNICUS/S2	2017-08-27
13	Sentinel-2	Level-1C	COPERNICUS/S2	2017-10-31
14	Sentinel-2	Level-1C	COPERNICUS/S2	2017-11-20
15	Sentinel-2	Level-1C	COPERNICUS/S2	2017-12-05
16	Sentinel-2	Level-1C	COPERNICUS/S2	2017-12-25
17	Sentinel-2	Level-1C	COPERNICUS/S2	2018-01-04
18	Sentinel-2	Level-1C	COPERNICUS/S2	2018-01-19
19	Sentinel-2	Level-1C	COPERNICUS/S2	2018-02-13
20	Sentinel-2	Level-1C	COPERNICUS/S2	2018-02-18
21	Sentinel-2	Level-1C	COPERNICUS/S2	2018-02-28
22	Sentinel-2	Level-1C	COPERNICUS/S2	2018-03-05
23	Sentinel-2	Level-1C	COPERNICUS/S2	2018-03-30
24	Sentinel-2	Level-1C	COPERNICUS/S2	2018-04-04
25	Sentinel-2	Level-1C	COPERNICUS/S2	2018-04-29
26	Sentinel-2	Level-1C	COPERNICUS/S2	2018-05-29
27	Sentinel-2	Level-1C	COPERNICUS/S2	2018-06-08
28	Sentinel-2	Level-1C	COPERNICUS/S2	2018-06-13
29	Sentinel-2	Level-1C	COPERNICUS/S2	2018-07-18
30	Sentinel-2	Level-1C	COPERNICUS/S2	2018-09-11
31	Sentinel-2	Level-1C	COPERNICUS/S2	2018-12-05
32	Sentinel-2	Level-1C	COPERNICUS/S2	2018-12-15
33	Sentinel-2	Level-1C	COPERNICUS/S2	2019-01-09
34	Sentinel-2	Level-1C	COPERNICUS/S2	2019-01-19
35	Sentinel-2	Level-1C	COPERNICUS/S2	2019-03-15
36	Sentinel-2	Level-1C	COPERNICUS/S2	2019-03-30
37	Sentinel-2	Level-1C	COPERNICUS/S2	2019-04-09
38	Sentinel-2	Level-1C	COPERNICUS/S2	2019-04-14
39	Sentinel-2	Level-1C	COPERNICUS/S2	2019-06-08
40	Sentinel-2	Level-1C	COPERNICUS/S2	2019-06-18
41	Sentinel-2	Level-1C	COPERNICUS/S2	2019-06-23
42	Sentinel-2	Level-1C	COPERNICUS/S2	2019-07-03

43	Sentinel-2	Level-1C	COPERNICUS/S2	2019-07-08
44	Sentinel-2	Level-1C	COPERNICUS/S2	2019-07-23
45	Sentinel-2	Level-1C	COPERNICUS/S2	2019-08-02
46	Sentinel-2	Level-1C	COPERNICUS/S2	2019-08-07
47	Sentinel-2	Level-1C	COPERNICUS/S2	2019-08-17
48	Sentinel-2	Level-1C	COPERNICUS/S2	2019-10-21
49	Sentinel-2	Level-1C	COPERNICUS/S2	2019-12-05
50	Sentinel-2	Level-1C	COPERNICUS/S2	2020-01-09
51	Sentinel-2	Level-1C	COPERNICUS/S2	2020-01-14
52	Sentinel-2	Level-1C	COPERNICUS/S2	2020-01-19
53	Sentinel-2	Level-1C	COPERNICUS/S2	2020-01-24
54	Sentinel-2	Level-1C	COPERNICUS/S2	2020-02-23
55	Sentinel-2	Level-1C	COPERNICUS/S2	2020-02-28
56	Sentinel-2	Level-1C	COPERNICUS/S2	2020-03-14
57	Sentinel-2	Level-1C	COPERNICUS/S2	2020-03-29
58	Sentinel-2	Level-1C	COPERNICUS/S2	2020-04-28
59	Sentinel-2	Level-1C	COPERNICUS/S2	2020-05-28
60	Sentinel-2	Level-1C	COPERNICUS/S2	2020-07-07
61	Sentinel-2	Level-1C	COPERNICUS/S2	2020-07-17
62	Sentinel-2	Level-1C	COPERNICUS/S2	2020-08-16
63	Sentinel-2	Level-1C	COPERNICUS/S2	2020-08-21
64	Sentinel-2	Level-1C	COPERNICUS/S2	2020-09-10
65	Sentinel-2	Level-1C	COPERNICUS/S2	2020-09-15
66	Sentinel-2	Level-1C	COPERNICUS/S2	2020-10-15
67	Sentinel-2	Level-1C	COPERNICUS/S2	2020-10-20
68	Sentinel-2	Level-1C	COPERNICUS/S2	2020-11-09
69	Sentinel-2	Level-1C	COPERNICUS/S2	2020-12-04
70	Sentinel-2	Level-1C	COPERNICUS/S2	2020-12-09
71	Sentinel-2	Level-1C	COPERNICUS/S2	2020-12-14
72	Sentinel-2	Level-1C	COPERNICUS/S2	2020-12-19
73	Sentinel-2	Level-1C	COPERNICUS/S2	2021-01-03
74	Sentinel-2	Level-1C	COPERNICUS/S2	2021-01-08
75	Sentinel-2	Level-1C	COPERNICUS/S2	2021-01-13
76	Sentinel-2	Level-1C	COPERNICUS/S2	2021-02-07
77	Sentinel-2	Level-1C	COPERNICUS/S2	2021-03-09
78	Sentinel-2	Level-1C	COPERNICUS/S2	2021-03-29
79	Sentinel-2	Level-1C	COPERNICUS/S2	2021-04-03
80	Sentinel-2	Level-1C	COPERNICUS/S2	2021-04-08
81	Sentinel-2	Level-1C	COPERNICUS/S2	2021-04-23
82	Sentinel-2	Level-1C	COPERNICUS/S2	2021-04-28
83	Sentinel-2	Level-1C	COPERNICUS/S2	2021-05-23
84	Sentinel-2	Level-1C	COPERNICUS/S2	2021-06-02
85	Sentinel-2	Level-1C	COPERNICUS/S2	2021-06-07
86	Sentinel-2	Level-1C	COPERNICUS/S2	2021-07-02
87	Sentinel-2	Level-1C	COPERNICUS/S2	2021-07-17
88	Sentinel-2	Level-1C	COPERNICUS/S2	2021-07-27
89	Sentinel-2	Level-1C	COPERNICUS/S2	2021-08-06

90	Sentinel-2	Level-1C	COPERNICUS/S2	2021-09-10
91	Sentinel-2	Level-1C	COPERNICUS/S2	2021-09-25
92	Sentinel-2	Level-1C	COPERNICUS/S2	2021-11-14
93	Sentinel-2	Level-1C	COPERNICUS/S2	2021-12-14
94	Sentinel-2	Level-1C	COPERNICUS/S2	2021-12-19
95	Sentinel-2	Level-1C	COPERNICUS/S2	2021-12-24
96	Sentinel-2	Level-1C	COPERNICUS/S2	2022-01-03
97	Sentinel-2	Level-1C	COPERNICUS/S2	2022-01-08
98	Sentinel-2	Level-1C	COPERNICUS/S2	2022-01-18
99	Sentinel-2	Level-1C	COPERNICUS/S2	2022-01-28

Table 4: Changes from default parameter settings applied within GIV for results presented in this thesis

Parameter	**Value**
Time oversampling factor	30
Output resolution (in metres)	100
Minimum interval for image pairs (in years)	0.058
Maximum interval for image pairs (in years)	1
Excluded angle minimum 1 (in degrees)	0
Excluded angle maximum 1 (in degrees)	210
Excluded angle minimum 2 (in degrees)	330
Excluded angle maximum 2 (in degrees)	360
Stable area	yes

January

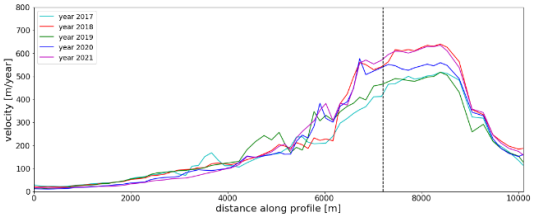

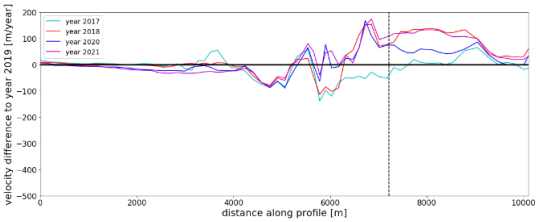

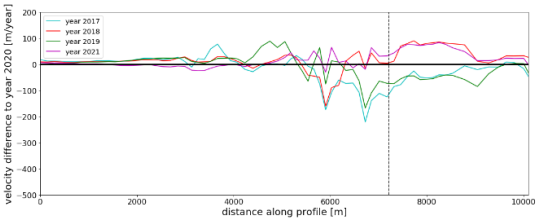

February

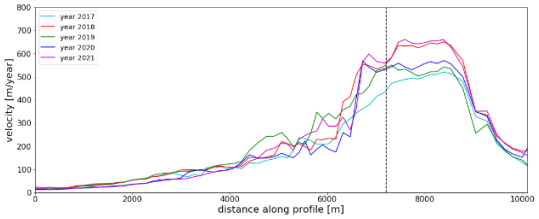

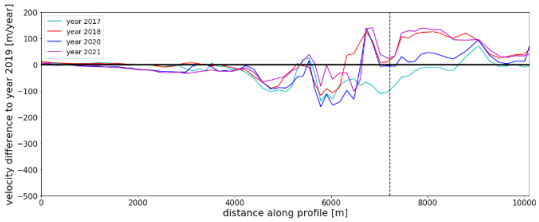

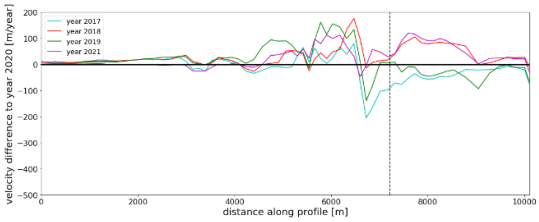

March

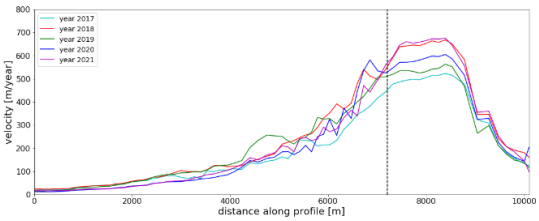

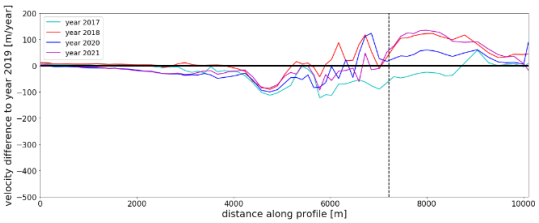

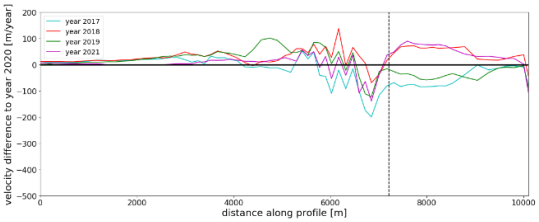

April

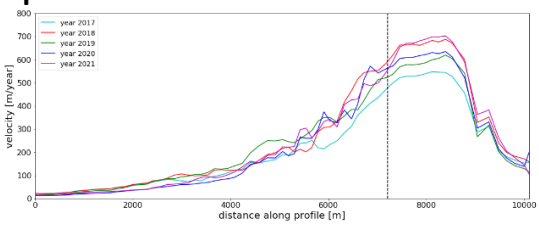

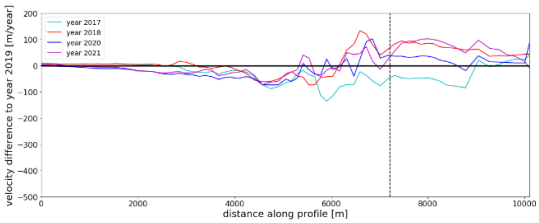

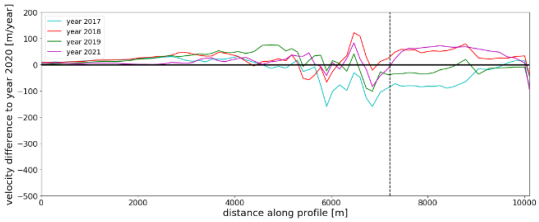

May

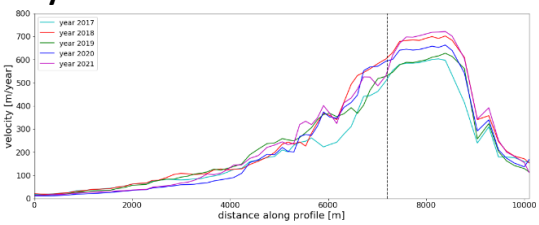

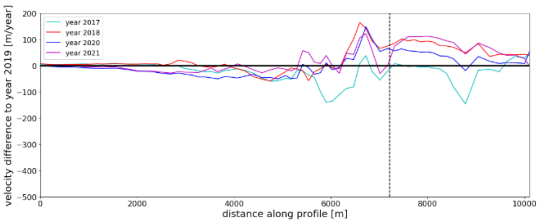

June

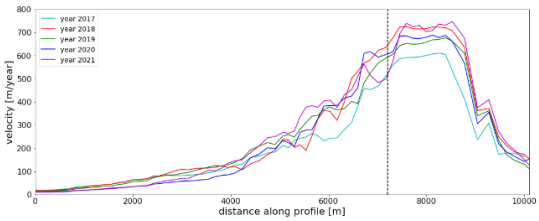

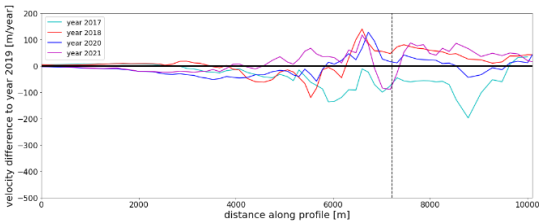

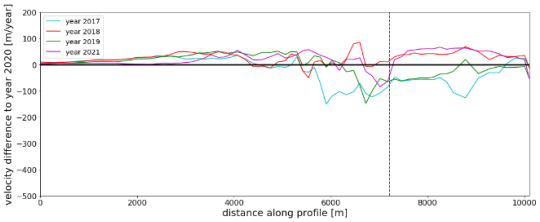

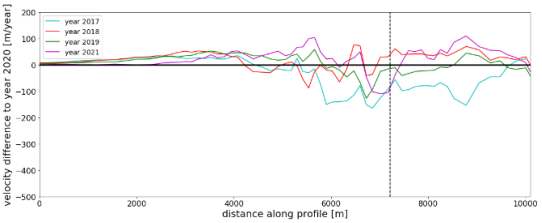

July

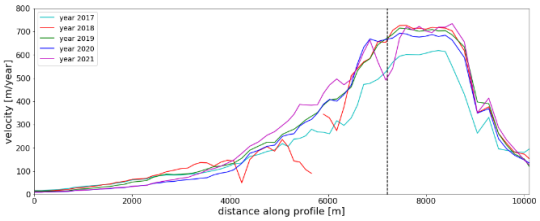

August

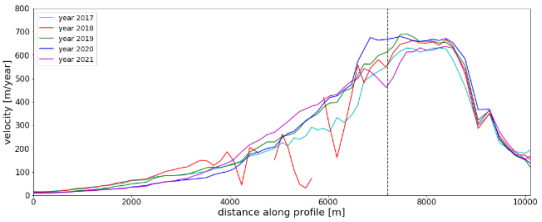

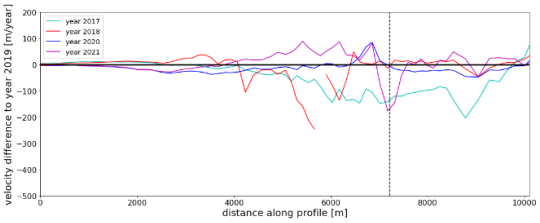

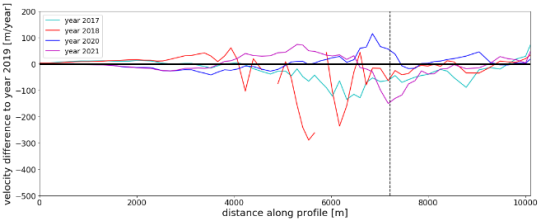

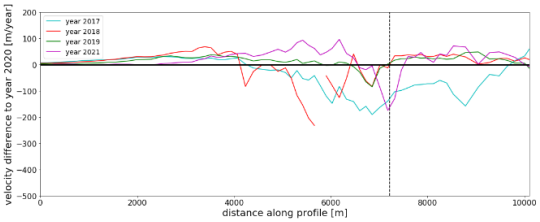

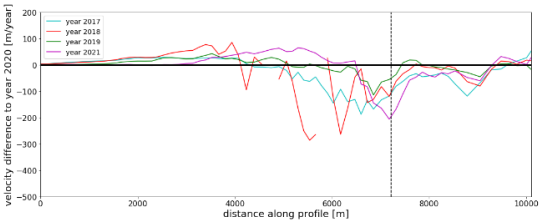

September

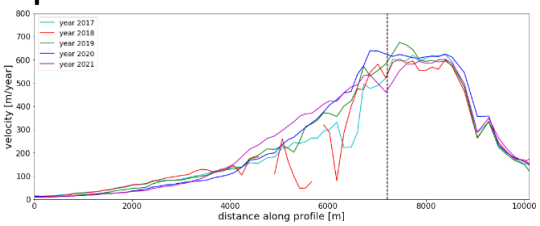

October

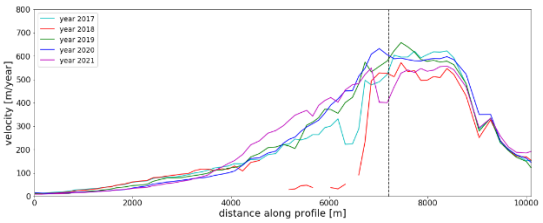

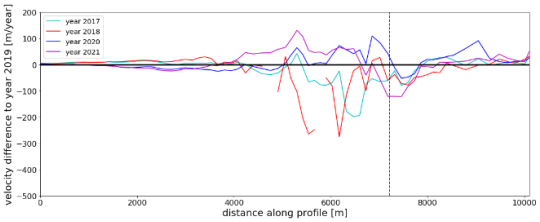

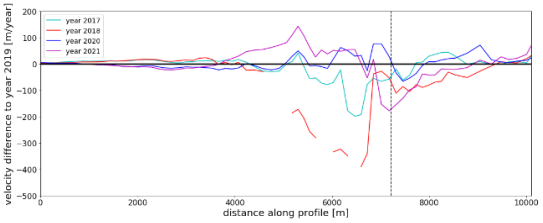

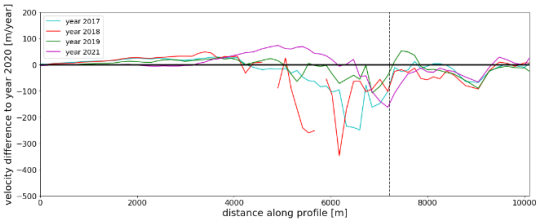

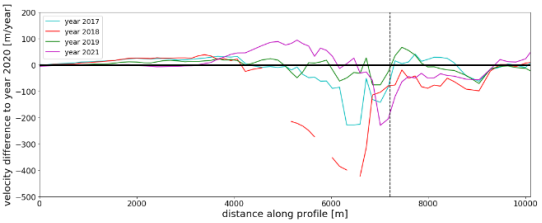

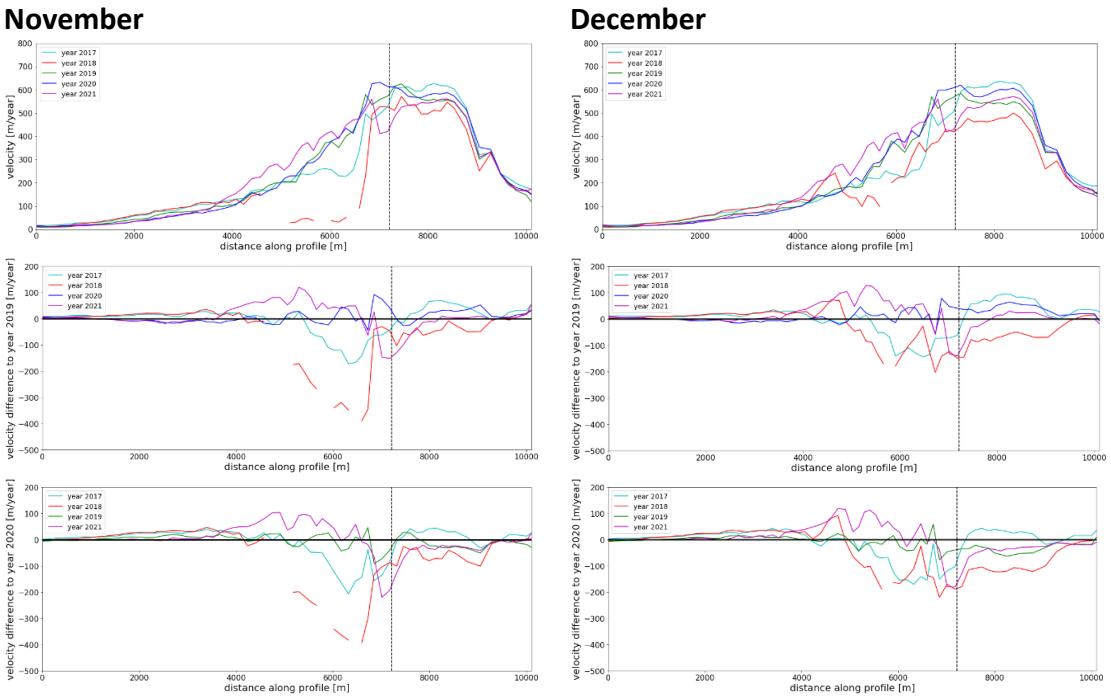

Figure 1 Upper row: Velocities along the profile line presented in Fig. 6.13 for the months January to December. Middle row: Velocity difference to the year 2019 for each month. Lower row: Velocity difference to the year 2020 for each month.

Point 1

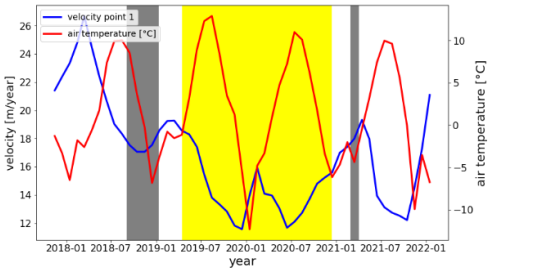

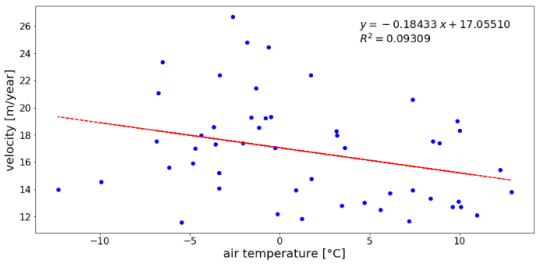

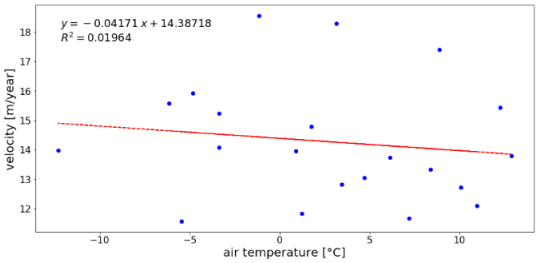

Point 2

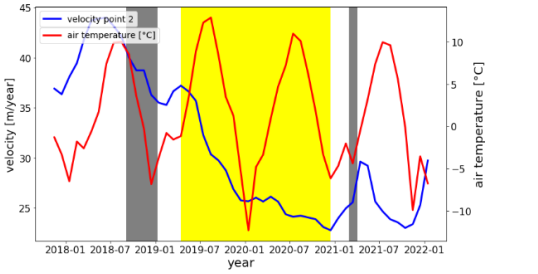

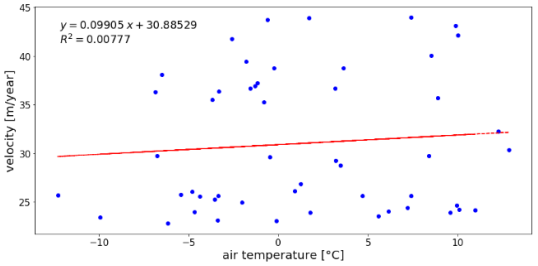

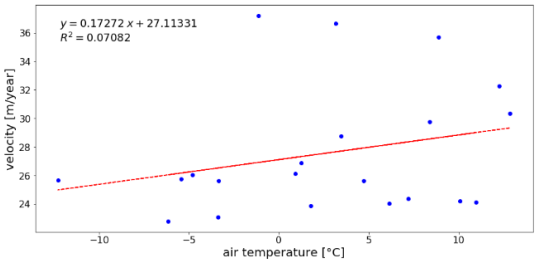

Point 3

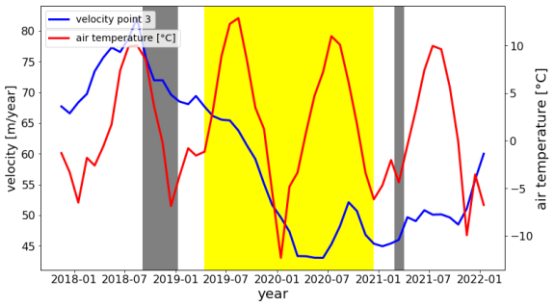

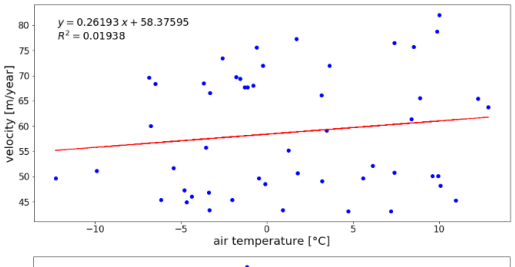

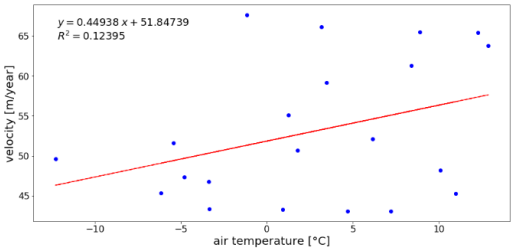

Point 4

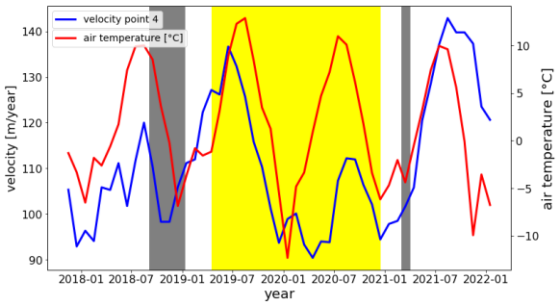

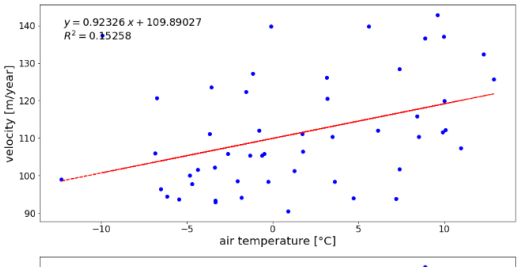

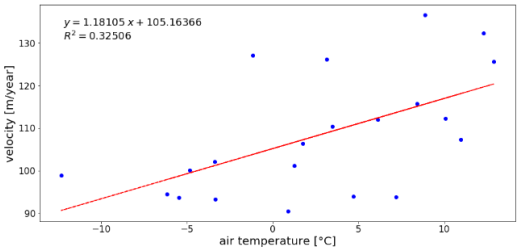

Point 5

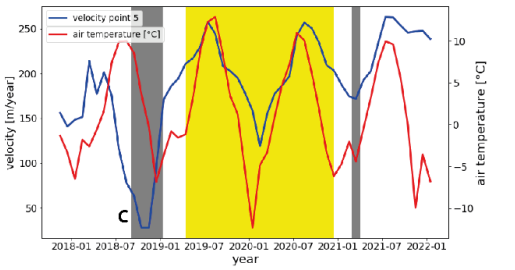

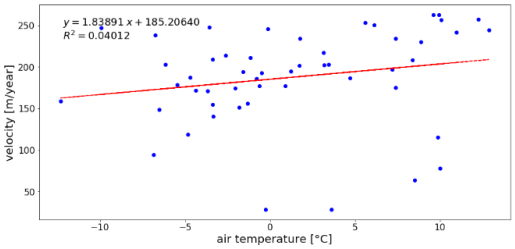

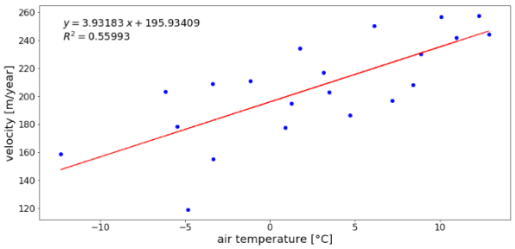

Point 6

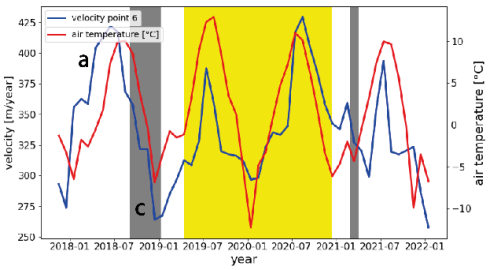

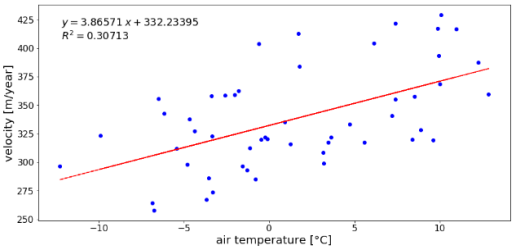

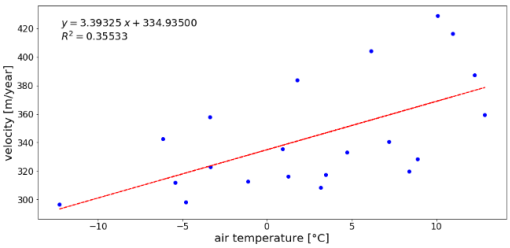

Point 7

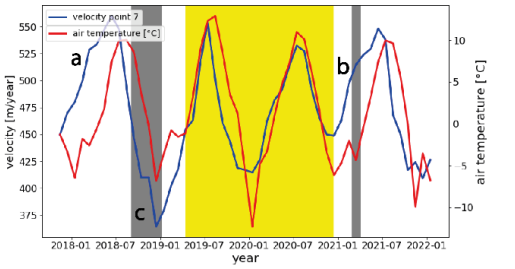

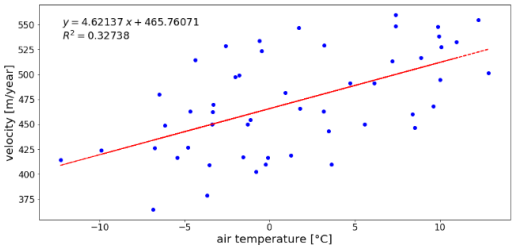

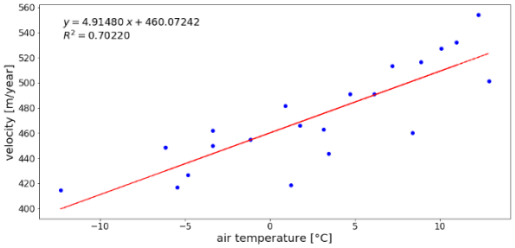

Point 8

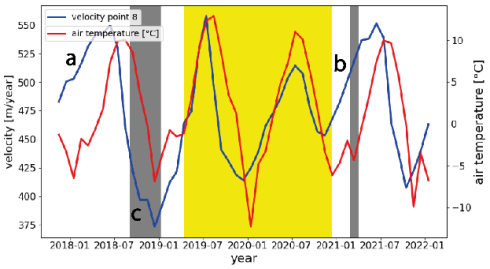

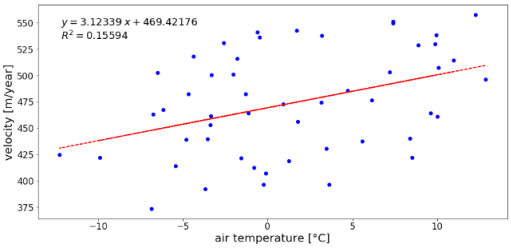

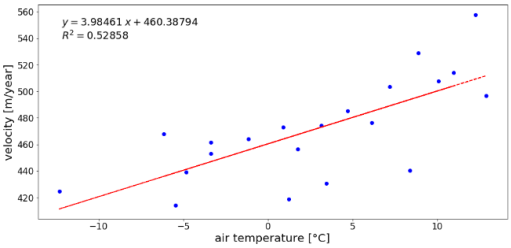

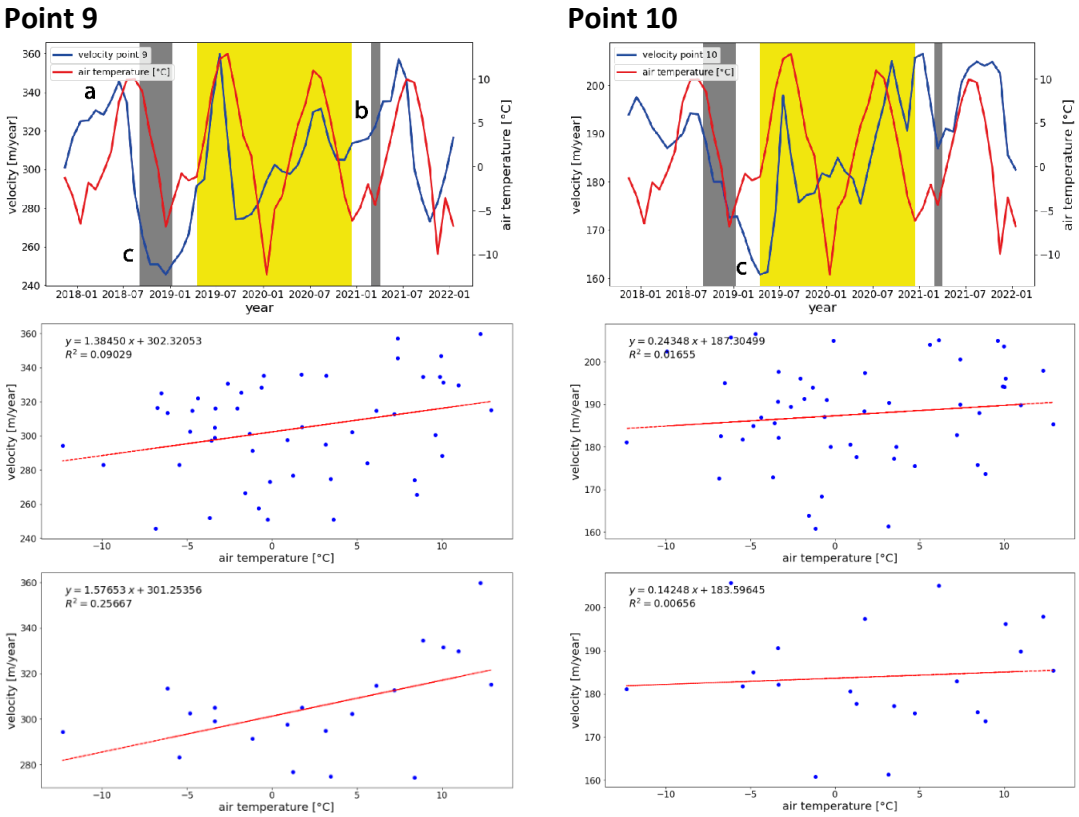

*Figure 2 Time-series velocities for points 1 to 10 versus air temperature. For each point, the **upper row** shows the monthly velocity time-series (blue line) and monthly air temperature (red line). Grey bars: reported periods of volcanic activity in 2018 and 2021. Yellow bars: presumed no volcanic activity phase. The **middle row** presents the correlation of velocity with air temperature for each point for the entire dataset. The **lower row** presents correlation of velocity with air temperature for each point for the time period with presumed no volcanic activity (yellow bars)*

Point 1

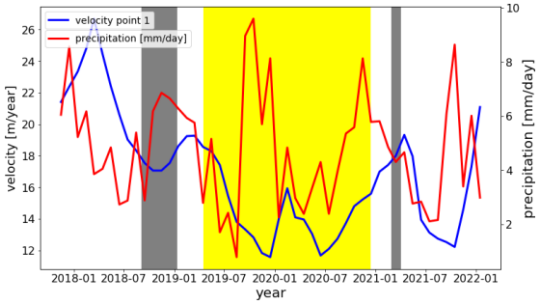

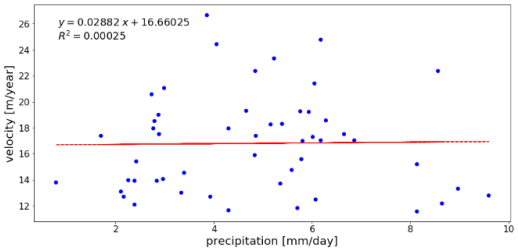

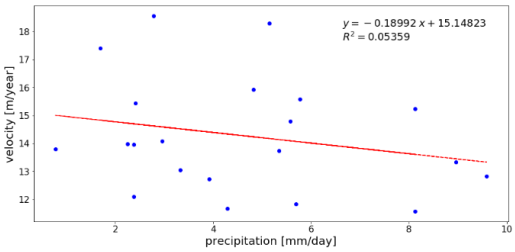

Point 2

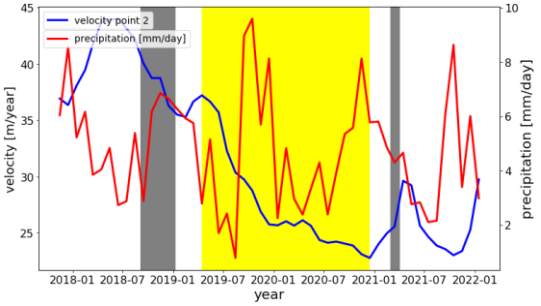

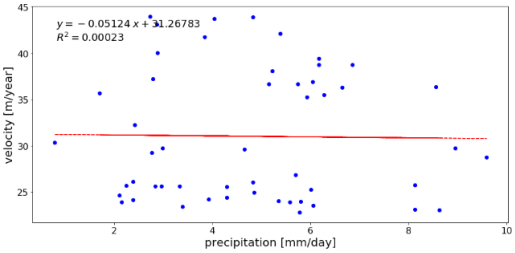

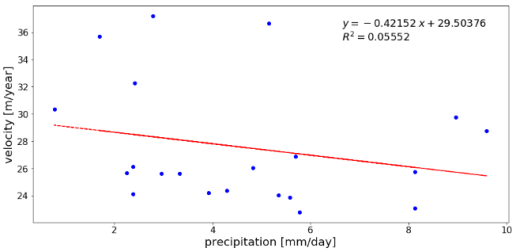

Point 3

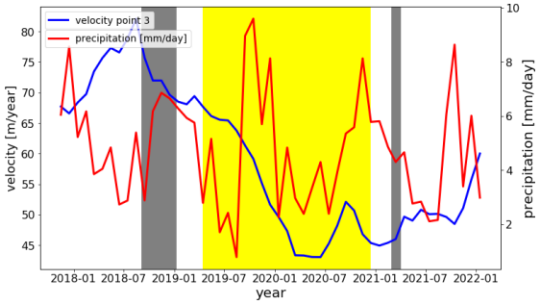

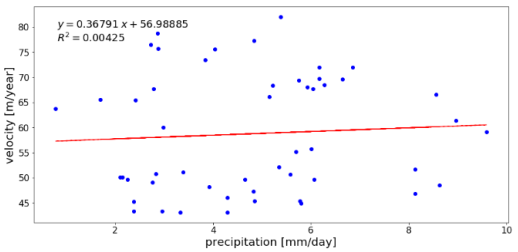

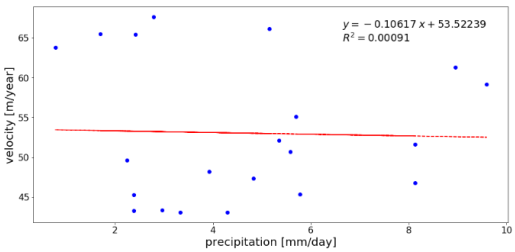

Point 4

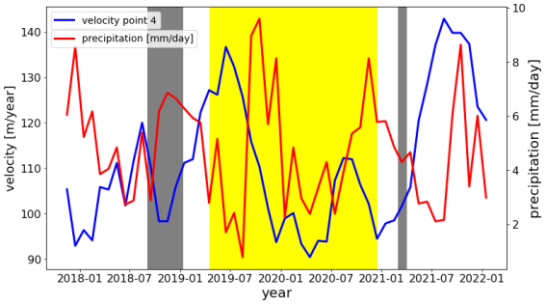

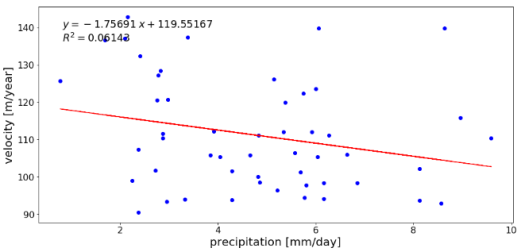

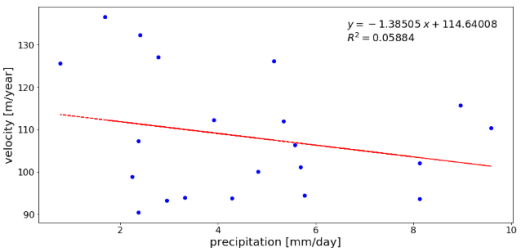

Point 5

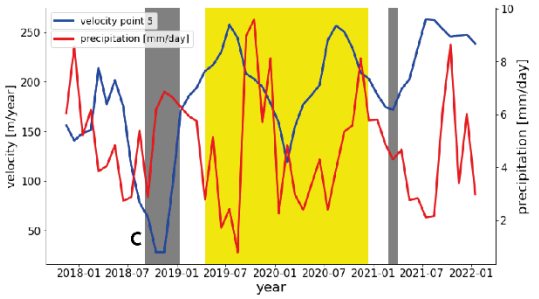

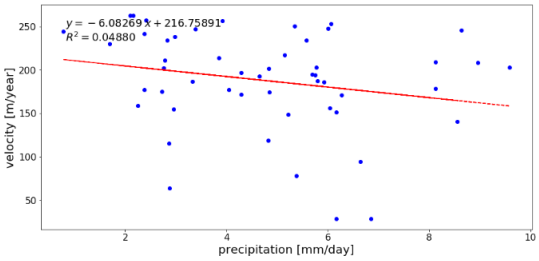

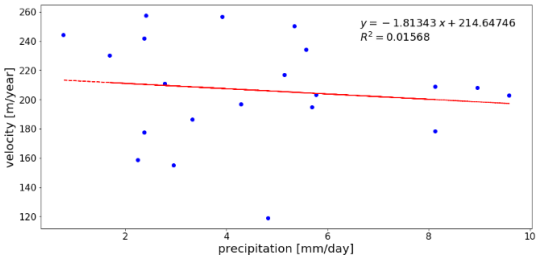

Point 6

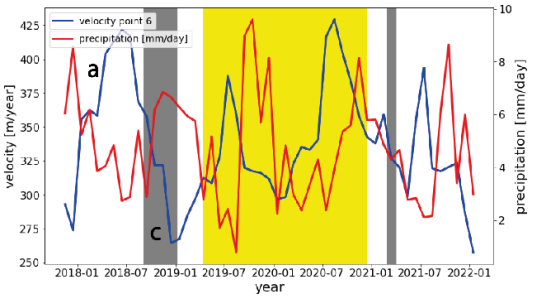

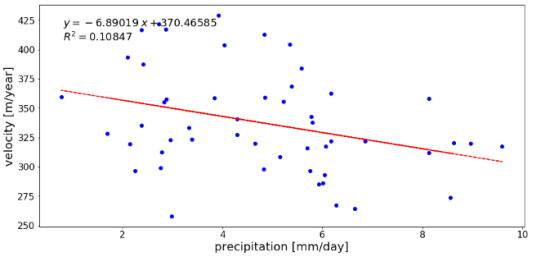

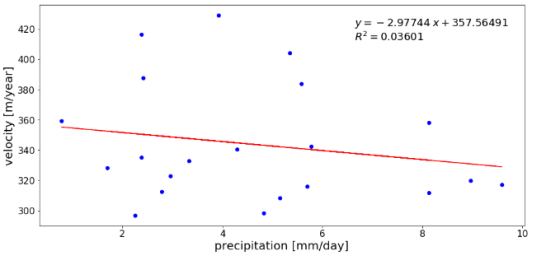

Point 7

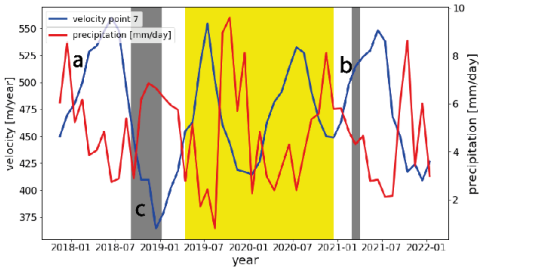

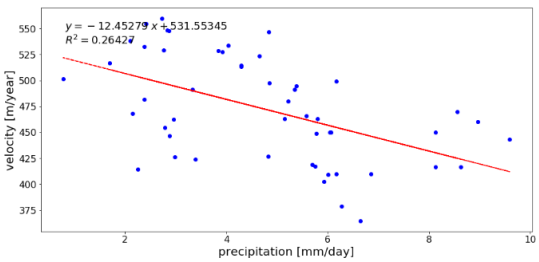

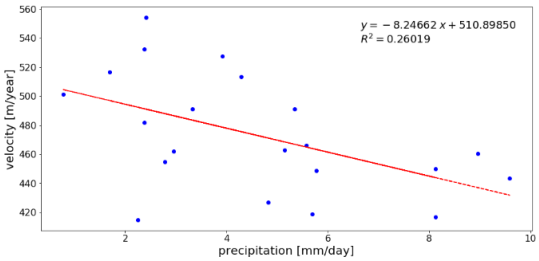

Point 8

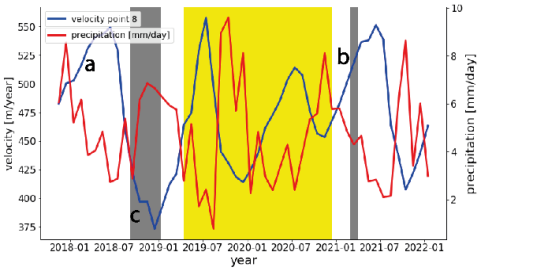

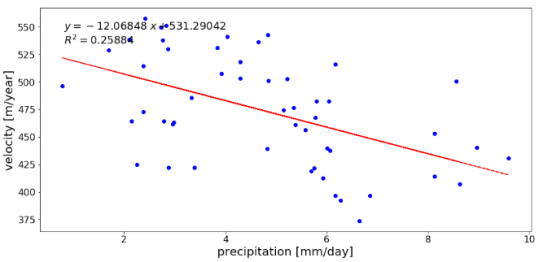

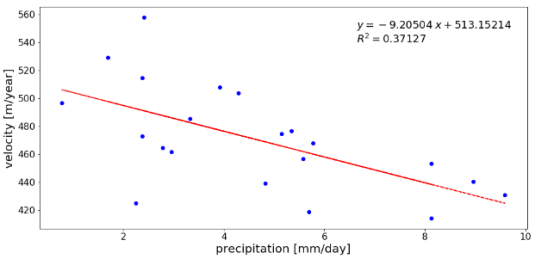

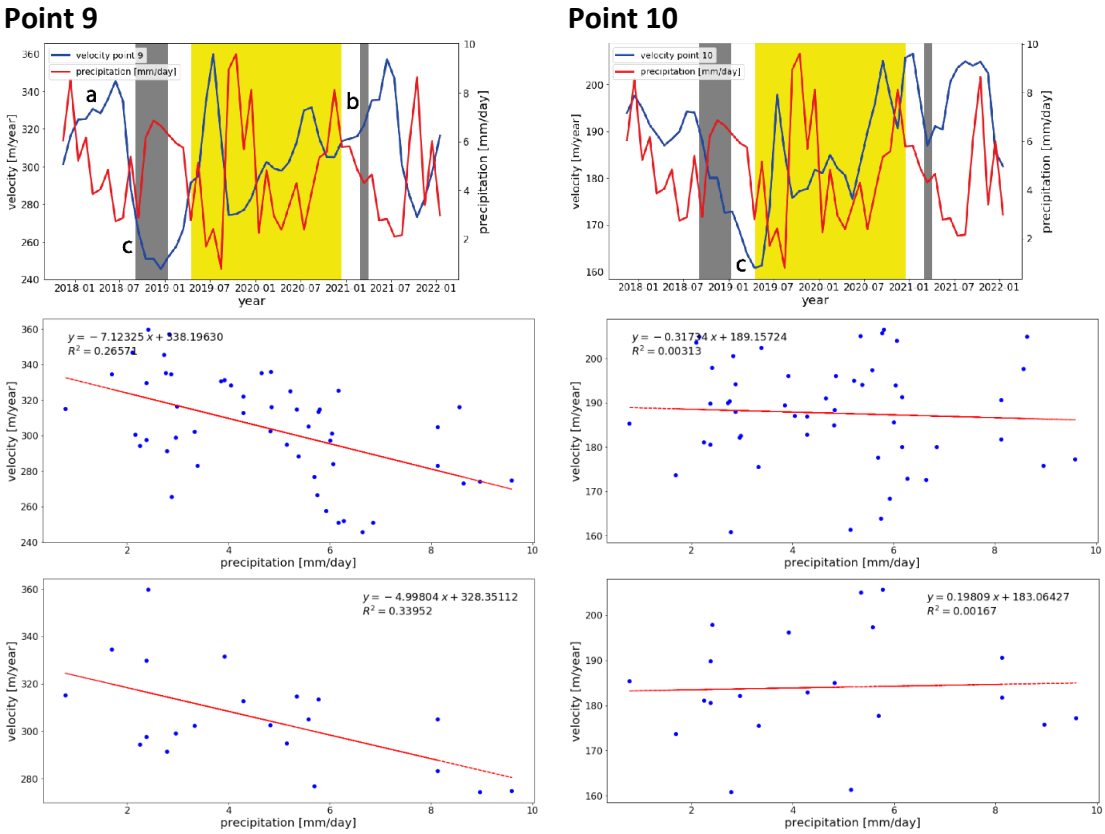

*Figure 3 Time-series velocities for points 1 to 10 versus precipitation. For each point, the **upper row** shows the monthly velocity time-series (blue line) and monthly precipitation (red line). Grey bars: reported periods of volcanic activity in 2018 and 2021. Yellow bars: presumed no volcanic activity phase. The **middle row** presents the correlation of velocity with precipitation for each point for the entire dataset. The **lower row** presents correlation of velocity with precipitation for each point for the time period with presumed no volcanic activity (yellow bars)*

November 2017

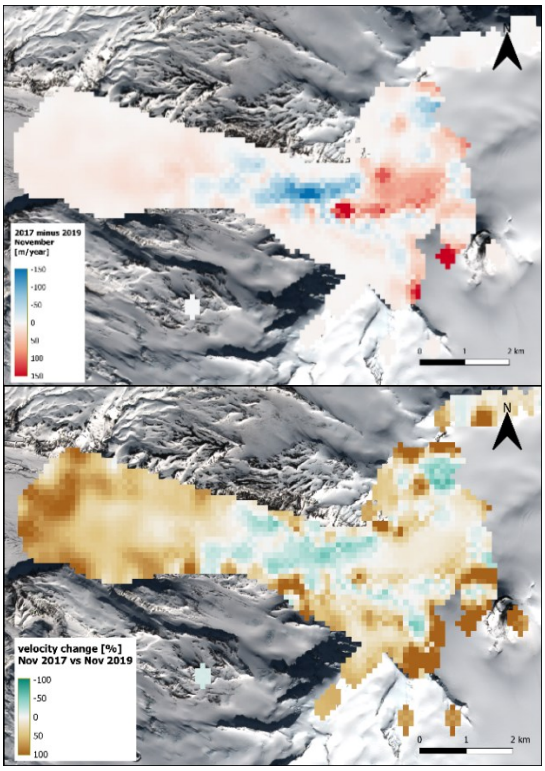

December 2017

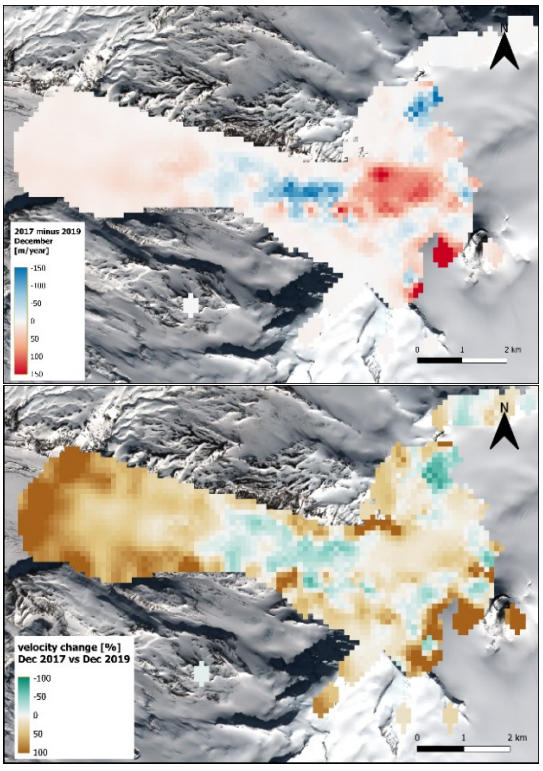

January 2018

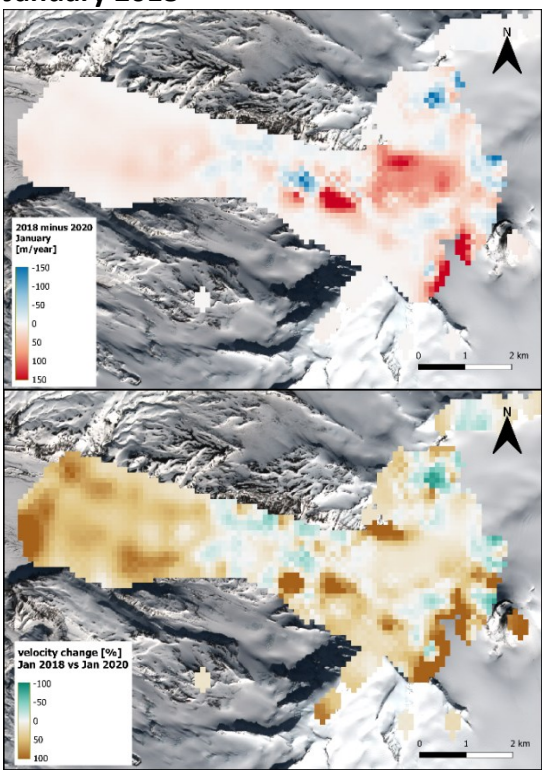

February 2018

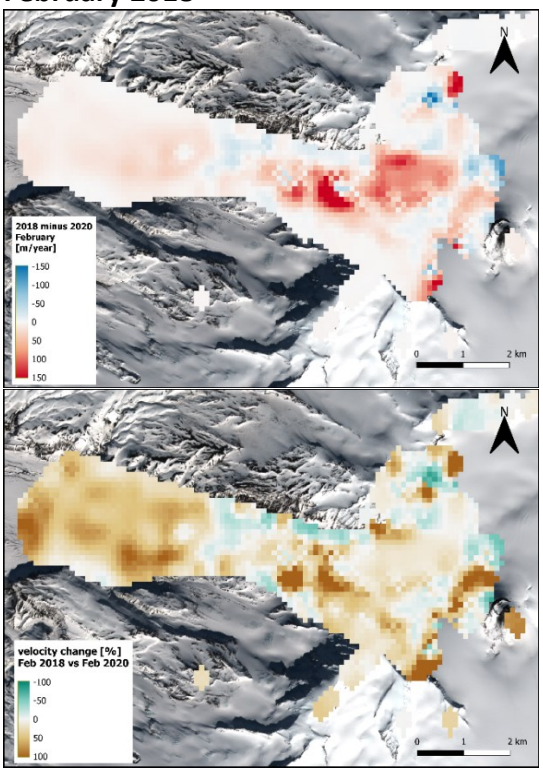

March 2018

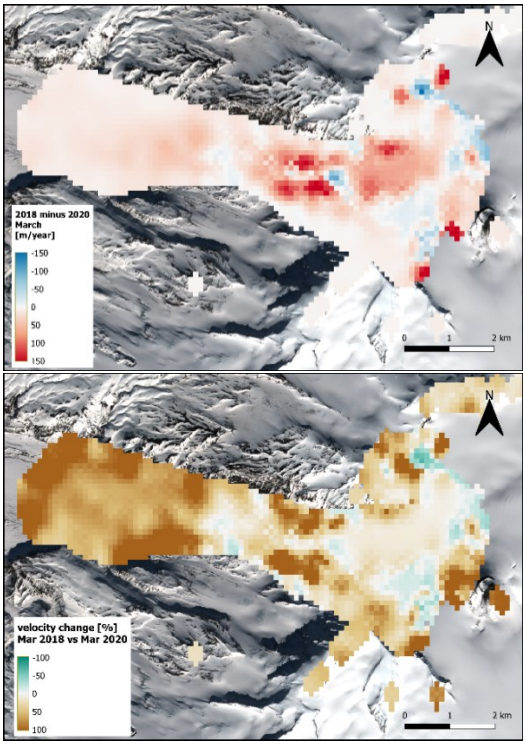

April 2018

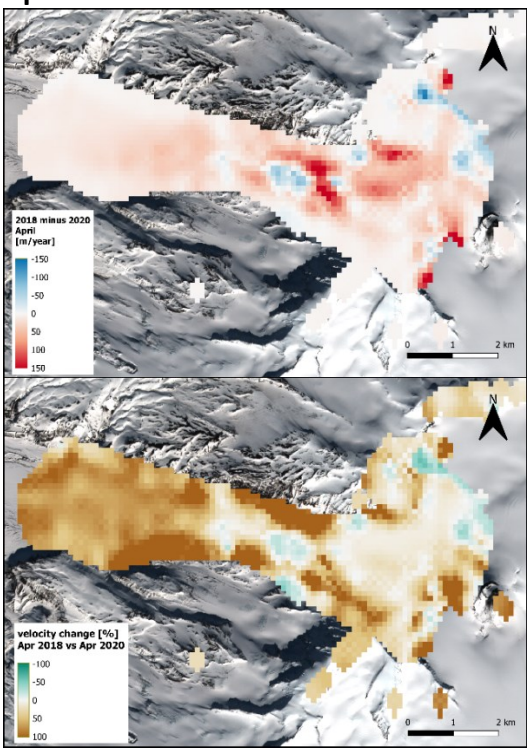

May 2018

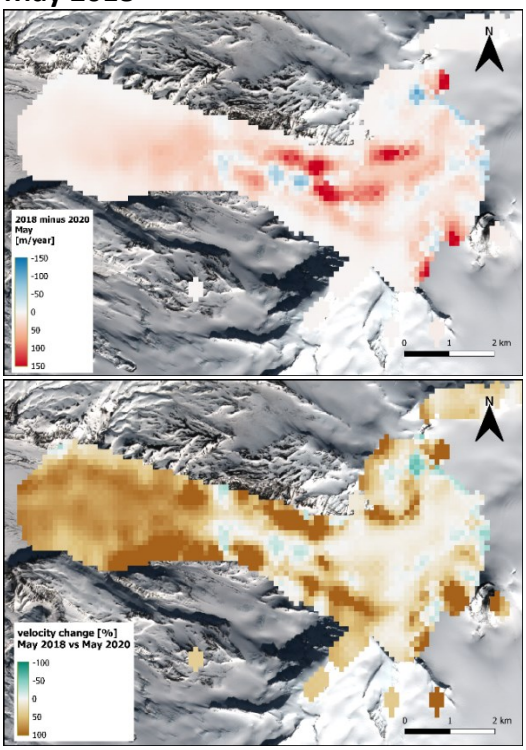

June 2018

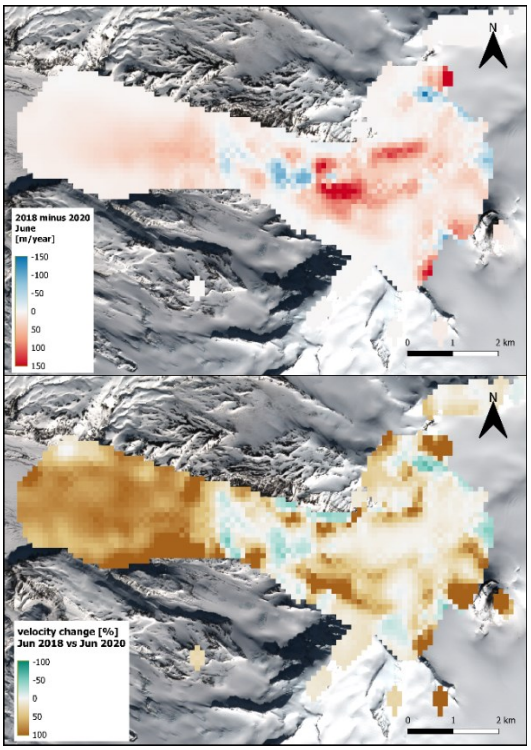

July 2018

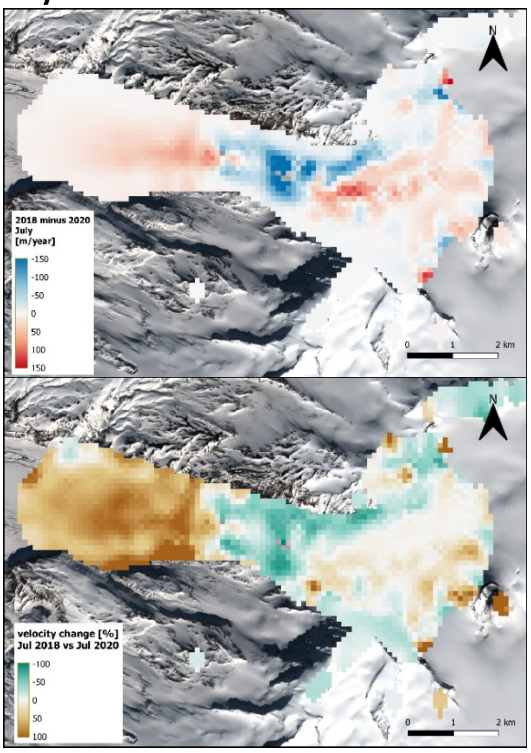

August 2018

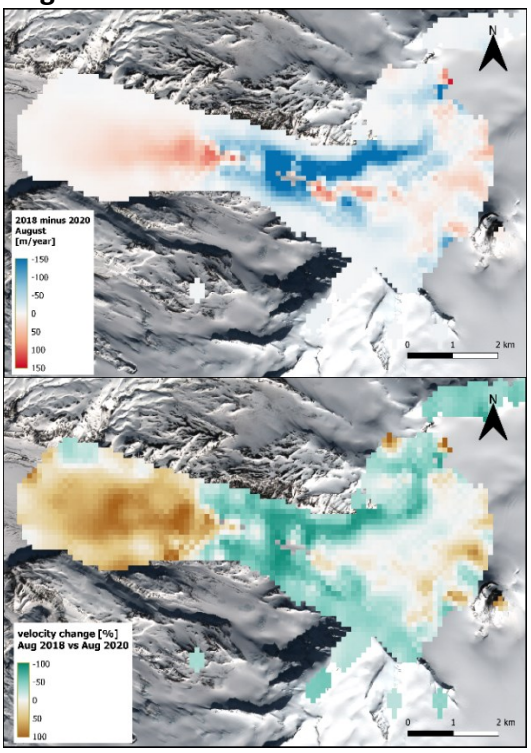

September 2018

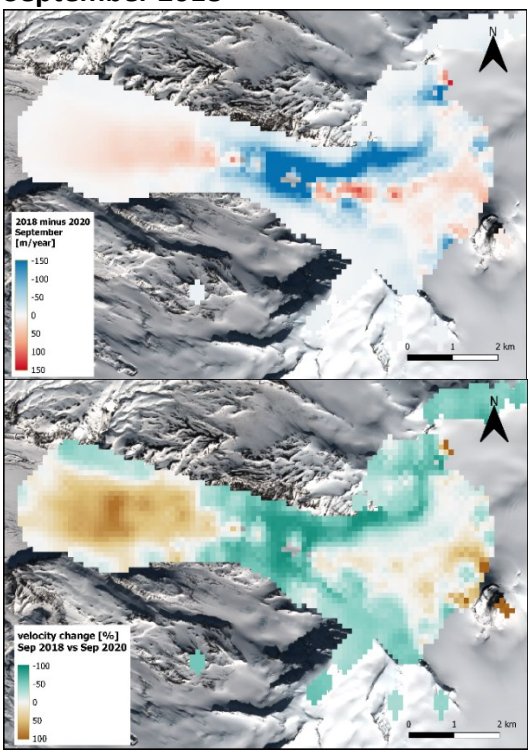

October 2018

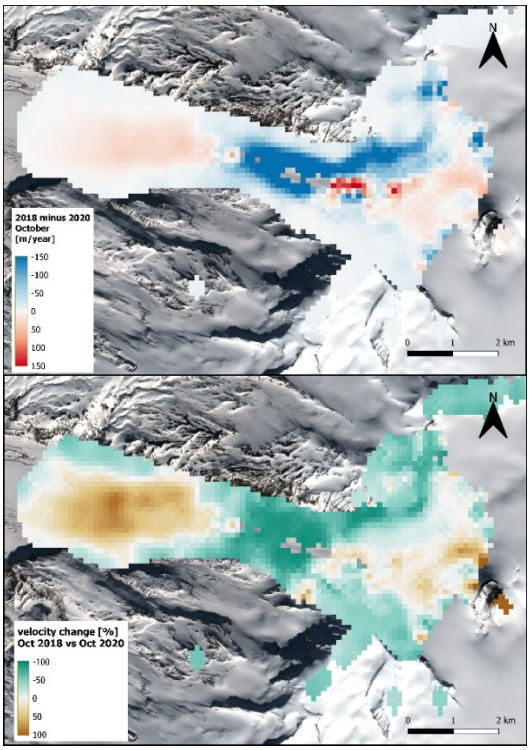

November 2018

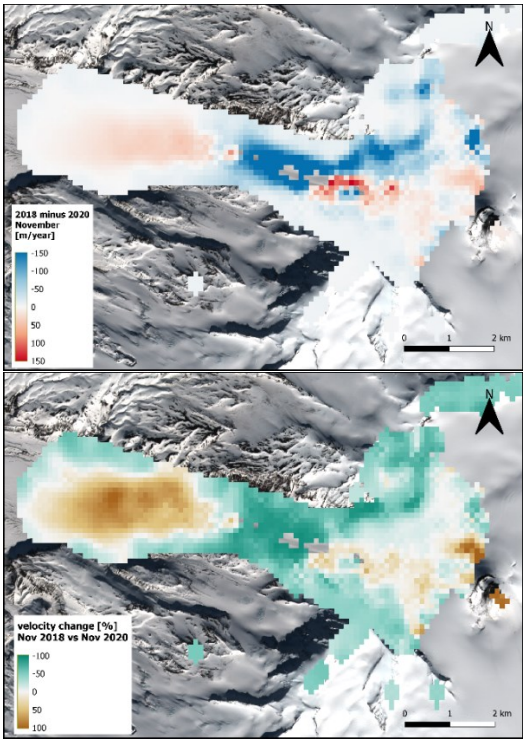

December 2018

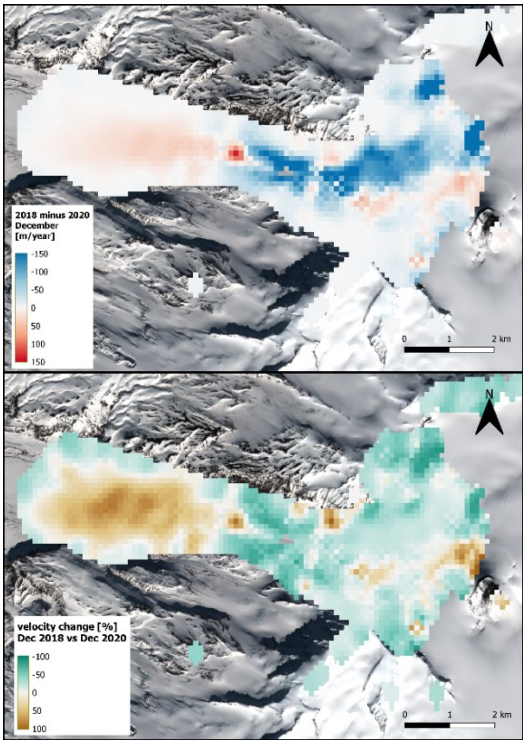

January 2019

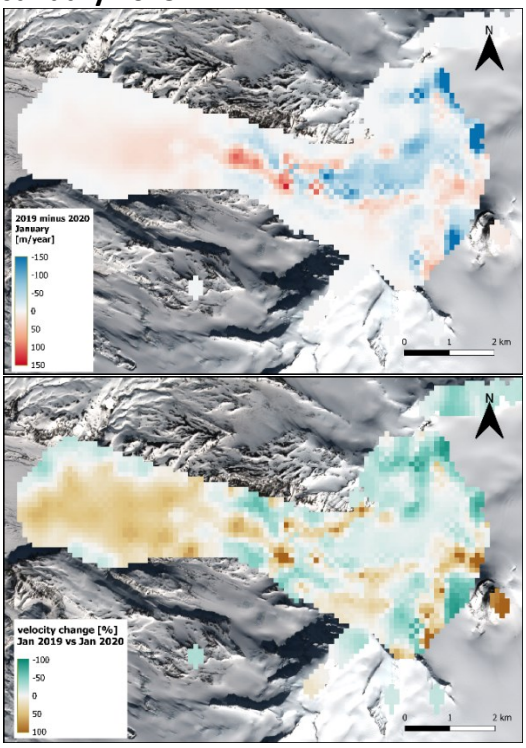

February 2019

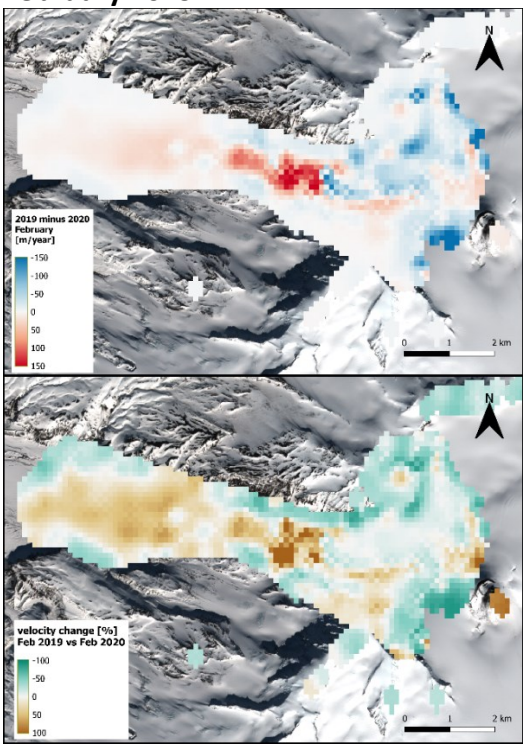

March 2019

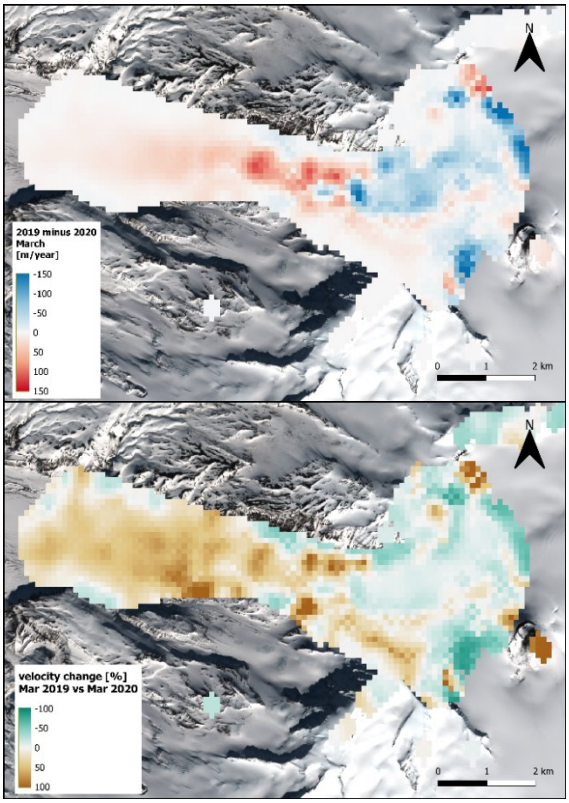

Figure 4 Velocity changes from November 2017 to March 2019 (covering the 2018 volcanically active phase) to the respective months in year 2019 and year 2020. Velocity differences are presented in the upper rows, relative velocity changes (%) in the lower rows for each month. Background image: Sentinel-2 true colour image from 25/03/2017.

January 2021

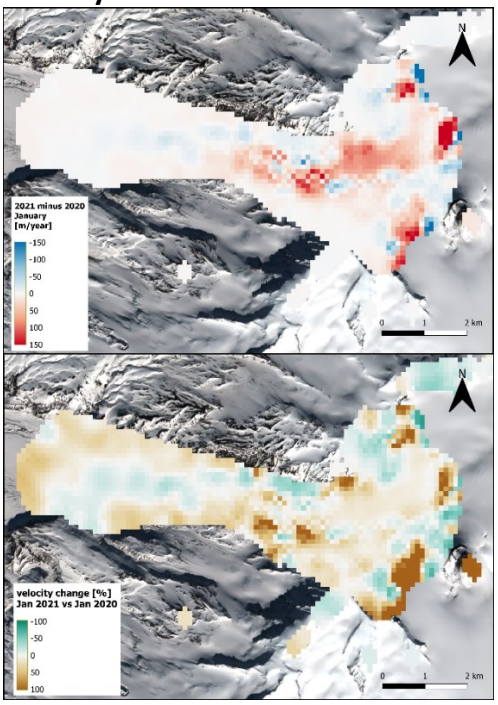

February 2021

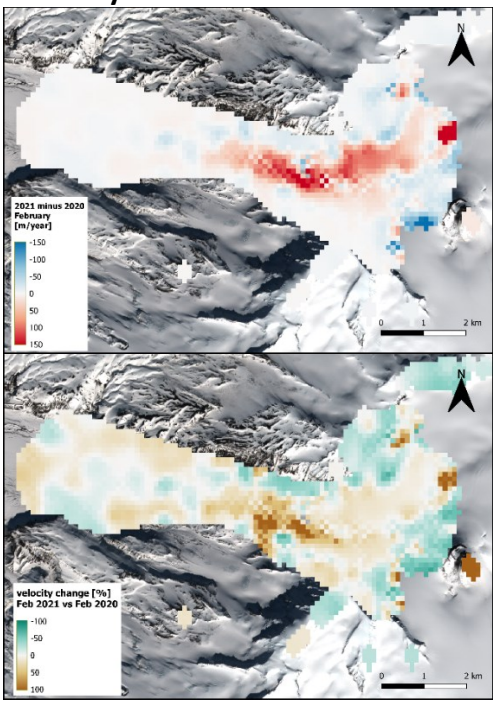

March 2021

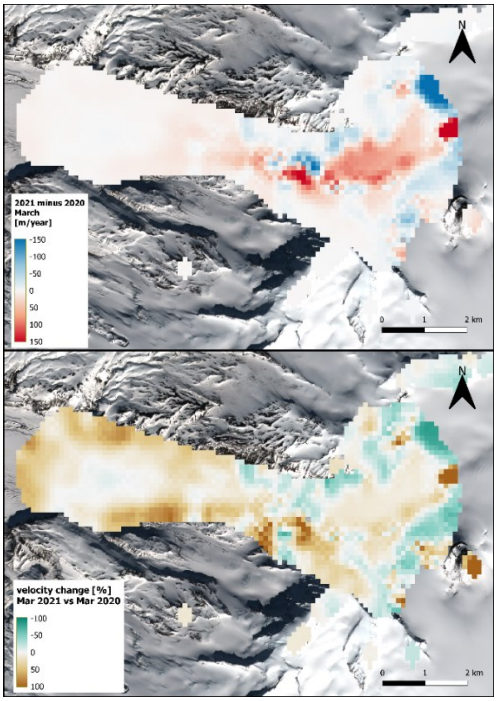

April 2021

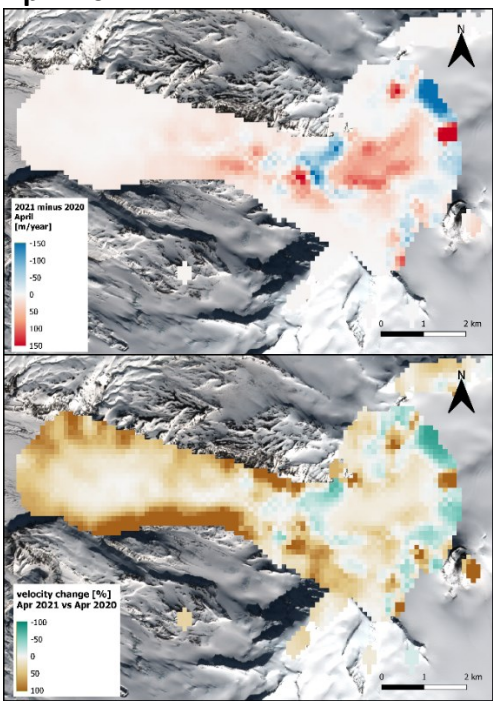

May 2021

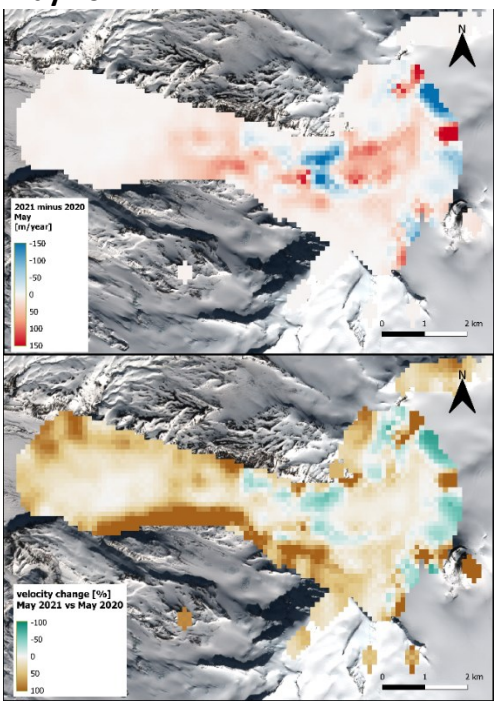

June 2021

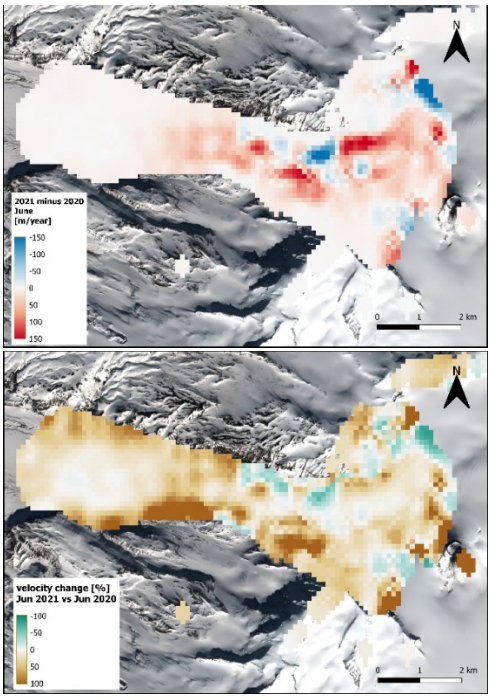

July 2021

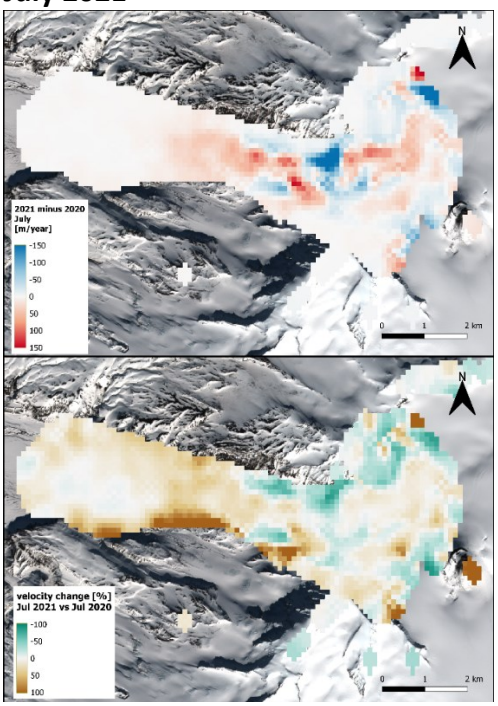

August 2021

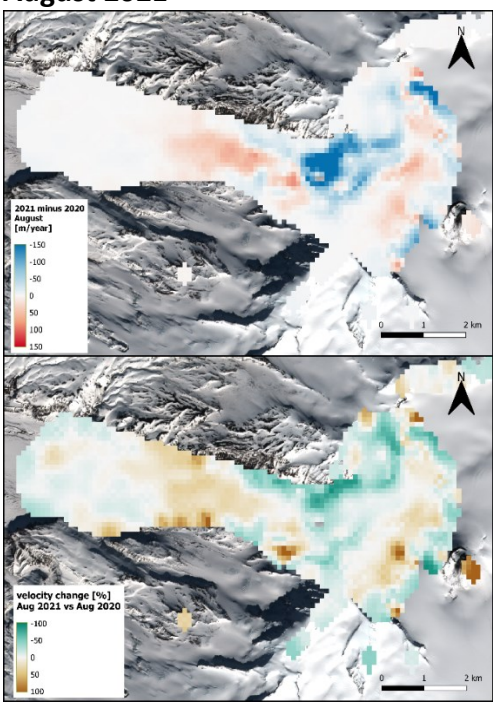

September 2021

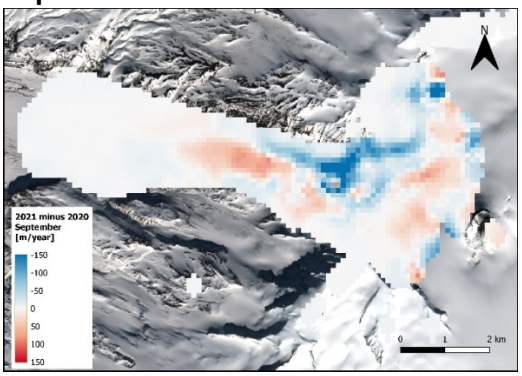

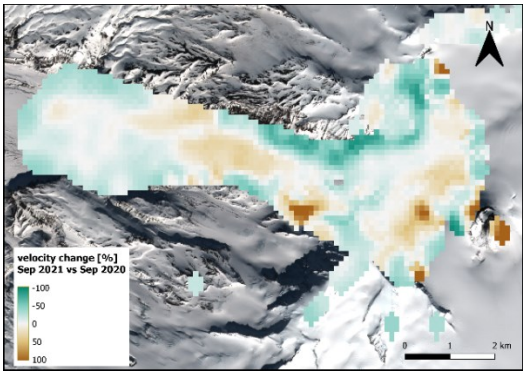

October 2021

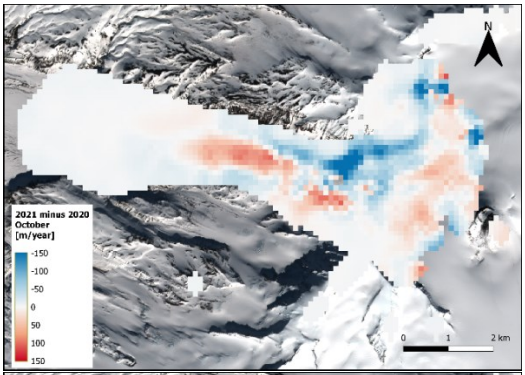

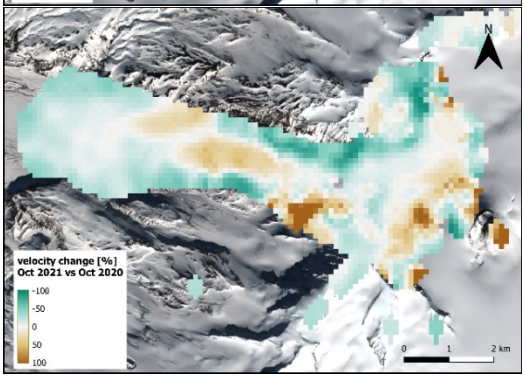

November 2021

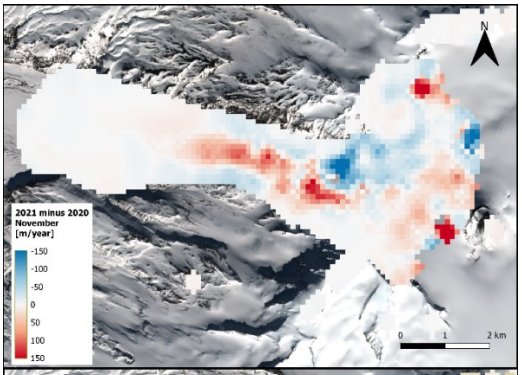

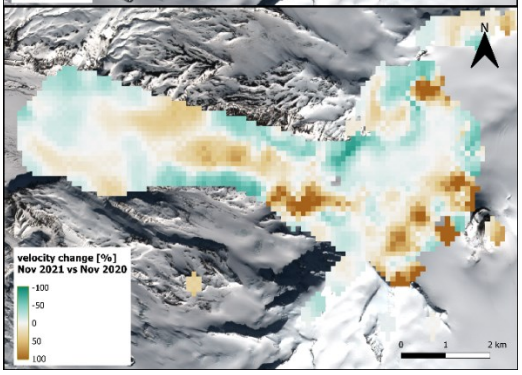

December 2021

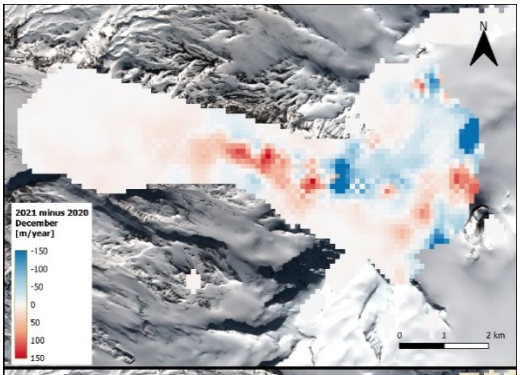

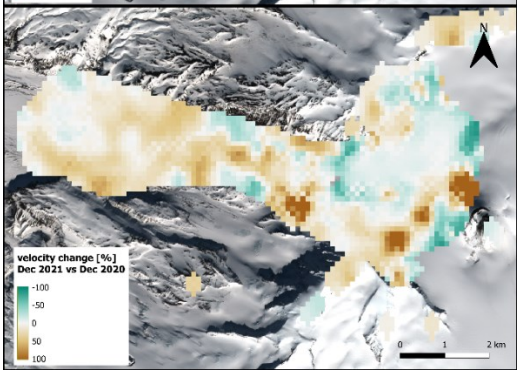

January 2022

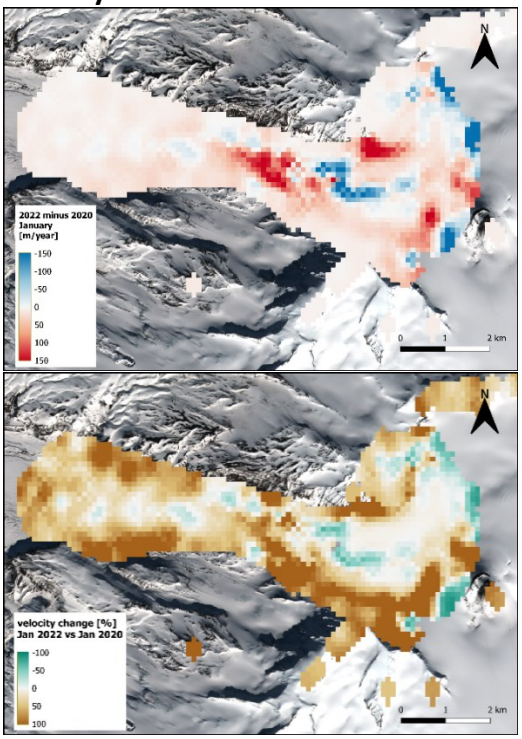

Figure 5 Velocity changes from Januar 2021 to January 2022 (covering the 2021 volcanically active phase) to the respective months in year 2020. Velocity differences are presented in the upper rows, relative velocity changes (%) in the lower rows for each month. Background image: Sentinel-2 true colour image from 25/03/2017

Table 5 Investigated glacier-clad volcanoes, respective eruption dates and geology/glaciology

volcano number	Volcano name	eruption date (start, end)	search period (start, end)	country/ region	lat/lon	volcano type	ice thickness [m]	geology/glaciology	Eruption characteristics (literature)	literature
1	**Mount Redoubt**	22/03/2009, 04/04/2009	30/04/2008, 30/09/2009	Alaska (United States)	60.485, -152.742	strato-volcano	80-190	glacier-clad, steep-sided stratovolcano with ice-filled summit caldera breached to the north by Drift glacier; location: 170 km southwest of Anchorage; volcano forms part of Aleutian volcanic arc, 10 km in diameter; ice thick-nesses up to 190 m in caldera region and ~ 80 m in upper Drift glacier region	abnormal heat flow in summit crater from late summer 2008; areas of exposed rock at top of 1966-1968 and 1990 lava domes; formation of 'subsidence areas', ice slurry flows, debris flows, holes in ice (ice cauldrons, below and above 1990 dome from 30 Jan 2009), crevasse formation	Trabant and Hawkins, 1997; Schaefer, 2011; Bleick et al., 2013; McGimsey et al., 2014

2	**Mount St. Helens**	27/03/1980, 06/10/1980	01/11/1979, 15/11/1980	United States (Washington state)	46.2, -122.18	strato-volcano	N/A	stratovolcano in the Cascade range; steep-sided stratovolcano; subduction of Juan-Fuca (oceanic) plate beneath North American (conti-nental) plate; before 1980 eruption: volcano covered by several glaciers; 1980 eruption: formation of large, north-facing 'amphitheater', ~ 2 km wide; after 1980 eruption: re-formation of a glacier in the summit until 2001: 200 m thick and 1km^2 in size	eruption in three phases, removal of 70% of ice volume (from initially 0.18km3); complete destruction of two glaciers; growth of volcanic bulge; deformation, earthquakes and oversteepenings caused crevassing and ice avalanches on the bulge; Shoestring glacier: sudden loss of accumulation area results in progressive decrease in velocity along entire remaining length of glacier; most of glaciers difficult to detect until late summer 1980 (due to ash cover)	Brugman and Post, 1981; USGS - Geology and Ecology of National Parks, URL: https://www.usgs.gov/science-support/osqi/yes/national-parks/geology-mount-st-helens-national-volcanic-monument (accessed: 08/05/2021)
		late September 2004 - summer 2006	01/08/2004, 30/09/2006				200		since October 2004 emplacement of a silicic lava dome through and then alongside glacier ice in crater of Mt St. Helens; crater glacier split in two halves, surface buckling of east-crater glacier with east-west trending crevasses, doubling of glacier thickness, East-Crater Glacier terminus advanced ~ 150 m	Schilling et al., 2004; Walder et al., 2007, 2008

3	**Nevado del Ruiz**	11/11/1985 and 13/11/1985	11/09/1984, 11/09/1986	Colom-bia	4.892, -75.324	strato-volcano	N/A	stratovolcano rising ~ 5390 m above sea level in Cordillera Central of Colombia, location: ~100 km west of Bogota	small Phreatic eruption on 11/11/1985 triggering a small lahar, which travelled 27 km down northern flank; small Plinian eruption on 13/11/1985 took place in summit crater (Crater Arenas), producing disastrous lahars travelling up to 104 km; ice cap of 25 km^2 area on summit before eruption	Naranjo et al., 1986; Pierson et al., 1990
4	**Nevado del Huila**	19/02/2007, 18/04/2007, 20/11/2008 - 05/2009	01/12/2006, 31/12/2011	Colom-bia	2.93, -76.03	strato-volcano	N/A	5364 m high stratovolcano with four ice-capped peaks; Glacier area ~10.7 km^2 before eruptions; area after eruption (2009): 9.8 km	large fissures formed up to 2 km long and ~80 m wide; lahar generation by melting of part of the summit ice and snow; formation of a 500 m wide crater between Central and South peaks; loss of a portion of El Oso Glacier tongue	Lopez Arenas and Ramirez Cadena, 2010; Monsalve et al., 2011; Granados et al., 2015

5	**Mount Hudson**	10/2011, 12/2011	01/01/2010, 31/12/2014	Chile	-45.9, -72.97	strato-volcano	hundreds of metres	10 km wide ice filled caldera; one of the most active vol-canoes in Southern Andes; eruptive period between October and December 2011 with VEI (1-2)	inflation between 2004 and 2010; seismic activity started October 25th; an eruptive column was visible the next day and some lahars had occurred in a valley; small event (VEI 1-2) with little apparent warning, on October 27th two craters near SW caldera rim with diameters 200 m to 500 m detected (Amigo et al. (2012) reported at least three new craters); end of eruption not clear	Amigo et al., 2012; Delgado et al., 2014
6	**Mount Belinda**	20/10/2001, 07/09/2007	20/10/2000, 30/03/2008	South Sand-wich Islands (United King-dom)	-58.445, -26.374	shield-volcano	N/A	Montagu Island in remote South Sandwich Islands: 10 by 12 km in size and rising 1370 m above sea level; subduction of South American plate beneath South Sandwich plate; Mount Belinda: small volcanic cone on larger shield volcano (Montagu Island), summit caldera (6 km in diameter) with very gently sloping icefield, tidewater glacier at NW corner of island	Low intensity explosive activity and several effusive events, persistent steam-ash plume (tephra cover), lava flows and gullies in glacier ice with crevassing (radiating from flow margin), formation of a 800 m wide lava delta, major disruptions to a glacier (widespread crevassing)	Patrick et al., 2005; Patrick and Smellie, 2013

7	**Eyja-fjalla-jökull**	20/03/2010, 08/06/2010	01/06/2009, 31/12/2012	Iceland	63.633, -19.633	central volcano	>100-400	central volcano ~ 1640 m high, located west of Vatnajökull ice cap; ice cap ~ 80 km^2, typically less than 100 m thick on slopes, thicker ice of ~200 m (up to 400 m) in caldera; Gígjökull glacier 4 km long and draining the summit caldera northwards	small flank eruption from 20 March to 12 April 2010 on Fimmvörduháls east of Eyjafjallajökull; main eruption on Eyjafjallajökull summit of modest size (VEI=3) and lasting for 39 days; dispersion of ash even to Europe; development of ice cauldrons within summit caldera (melting entire ice column) and development of supraglacial flood channels	Strachan, 2001; Gudmundsson et al., 2012; Magnússon et al., 2012
8	**Katla**	1999, 2005	01/11/2002, 01/10/2006	Iceland	63.633, -19.083	Sub-glacial central volcano	450-740	fourth largest ice cap in Iceland (600 km^2), between Eyjafjallajökull and Vatnajökull ice cap; 1300-1500 m high; caldera size: 100 km^2; location: southern tip of Eastern Volcanic Zone	permanent and semi-permanent ice cauldrons (10-50 m deep and ~1-1.5 km in diameter) related to subglacial geothermal activity	Björnsson and Guðmundsson, 2000; Guðmundsson et al., 2007; Scharrer et al., 2008
9	**Gríms-vötn (Gjálp)**	30/09/1996, 13/10/1996	15/07/1996, 15/11/1996	Iceland	64.416, -17.316	Sub-glacial volcanic fissure	500-750	6 km long volcanic fissure underneath Vatnajökull ice cap, midway between central volcanoes of Bárðarbunga and Grímsvötn	cauldron formation (width 8 km in June 1997); melting through 500 m thick ice in 30 hours other parts remained subglacial; meltwater drainage to Grímsvötn lake; subsidence and crevassing over eruptive	Gudmundsson et al., 1997, 2004

									fissure and meltwater path	
10	**Bárðar-bunga**	29/08/2014, 27/02/2015	01/01/2014, 31/05/2015	Iceland	64.633, -17.516	Sub-glacial central volcano	700-800	Bárðarbunga caldera: 10-11 km in max. diameter, 8 km in min diameter; located underneath Vatnajökull ice cap and between Bárðarbunga and Askja; emplacement of 45 km long regional dyke over period of 2 weeks in August 2014 at boundary between East and North Volcanic Zones in Iceland; central volcano belongs to Bárðarbunga-Veiðivötn system (including a fissure swarm)	eruption outside the ice cap at Holuhraun; Bárðarbunga caldera: ice subsidence with max. depth of 65 m and rates up to 50 cm/day; additional cauldron formation along path of the dyke: DK-01 (1.2 km diameter), DK-02 (780 m diameter) and DK-03 (elongated shape: 560 m to 250-300 m), (names of cauldrons according to Reynolds et al. (2017))	Gudmundsson et al., 2014; Rossi et al., 2016; Reynolds et al., 2017

Table 6 Details on (freely available) satellite remote sensing datasets used in this thesis for each volcano; total number investigated: ~1400 satellite images

volcano number	volcano name	search plat-form	data-provider	satellite/ source	sensor	dataset	spatial re-solut-ion	GEE dataset code (if applicable)	filter: CLOUDCOVER (%)	other filters	number of available images	number of (potentially) useful images
1	**Mount Redoubt**	GEE	NASA LP DAAC	Terra	ASTER	ASTER L1T Radiance	low	ASTER/AST_L1T_003	no	only images, in which bands B01, B02, B3N are present	22	8
		GEE	USGS EROS Archive	EO-1	ALI	EO-1 ALI L1Gst	low-med-ium	N/A	no	no	7	4
		Planet	Planet	Rapid-Eye*	REIS	RapidEye-OrthoTile, RapidEye-BasicScene	mediu m	N/A	no	no	2	0
		Google Earth Pro	Google Earth	N/A	N/A	N/A	N/A	N/A	N/A	N/A	0	0
2	**Mount St. Helens**	earth ex-plorer	USGS EROS Archive	Landsat2/ 3	MSS	Landsat 1-5 MSS C1 Level-1	low	N/A	no	no	49	12
		GEE	NASA LP DAAC	Terra	ASTER	ASTER L1T Radiance	low	ASTER/AST_L1T_003	no	only images, in which bands B01, B02, B3N are present	36	12
		Google Earth Pro	Google Earth	N/A	N/A	Maxar Tech-nologies, US Geological survey, USDA Farm	N/A	N/A	N/A	N/A	3	3

						Service Agency						
		earth-explorer	USGS EROS Archive	EO-1 ALI	ALI	EO-1 ALI L1Gst	low-med-ium	N/A	no	no	127	~10-15
3	**Nevado del Ruiz**	GEE	USGS/ Google	Landsat 5	TM	USGS Landsat 5 TM Collection 1 Tier 1 TOA Reflectance	low	LANDSAT/LT05/C01/T1_TOA	no	no	26	3
		GEE	USGS/ Google	Landsat 5	TM	USGS Landsat 5 TM Collection 1 Tier 2 TOA Reflect-ance	low	LANDSAT/LT05/C01/T2_TOA	no	no	18	0
		GEE	USGS	Landsat 5	MSS	USGS Landsat 5 MSS Collection 1 Tier 1 Raw Scenes	low	LANDSAT/LM05/C01/T1	no	no	0	0
		GEE	USGS	Landsat 5		USGS Landsat 5 MSS Collection 1 Tier 2 Raw Scenes	low	LANDSAT/LM05/C01/T2	no	no	53	6
4	**Nevado del Huila**	GEE	NASA LP DAAC	Terra	ASTER	ASTER L1T Radiance	low	ASTER/AST_L1T_003	no	only images in which bands B01, B02 and B3N present	22	3

		GEE	USGS/ Google	Landsat 7	ETM+	USGS Landsat 7 Collection 1 Tier 1 TOA Reflectance, USGS Landsat 7 Collection 1 Tier 1 Raw Scenes, USGS Landsat 7 Collection 1 Tier 2 TOA Reflectance	low	LANDSAT/LE07/C01/T1_TOA, LANDSAT/LE07/C01/T1, LANDSAT/LE07/C01/T2_TOA	no	no	8	3
		USGS earth explorer	USGS EROS Archive	EO-1	ALI	EO-1 ALI L1Gst	low-med-ium	N/A	no	no	1	0
		GEE	NASA LP DAAC	Terra	ASTER	ASTER L1T Radiance	low	ASTER/AST_L1T_003	no	no	14	0
		GEE	USGS/ Google	Landsat 7	ETM+	USGS Landsat 7 Collection 1 Tier 1 TOA Reflectance, USGS Landsat 7 Collection 1 Tier 1 Raw Scenes, USGS Landsat 7 Collection 1 Tier 2 TOA Reflectance	low	LANDSAT/LE07/C01/T1_TOA, LANDSAT/LE07/C01/T1, LANDSAT/LE07/C01/T2_TOA	no	no	13	4
		earth explorer	USGS EROS Archive	EO-1	ALI	EO-1 ALI L1Gst	low-med-ium	N/A	no	no	2	0

		Planet	Planet	RapidEye*	REIS	RapidEye OrthoTile, Rapid Eye Basic Scene	med-ium	N/A	no	no	0	0
		GEE	NASA LP DAAC	Terra	ASTER	ASTER L1T Radiance	low	ASTER/AST_L1T_003	no	no	33	4
		GEE	USGS/ Google	Landsat 7	ETM+	USGS Landsat 7 Collection 1 Tier 1 TOA Reflectance	low	LANDSAT/LE07/C01/T1_TOA	no	no	33	
		Planet	Planet	RapidEye	REIS	RapidEye-OrthoTile, RapidEye-BasicScene	mediu m	N/A	no	no	20	2
5	**Mount Hudson**	GEE	NASA LP DAAC	Terra	ASTER	ASTER L1T Radiance	low	ASTER/AST_L1T_003	no	only images, in which bands B01, B02, B3N are present	17	4
		Planet	Planet	RapidEye*	REIS	RapidEye-OrthoTile, RapidEye-BasicScene	mediu m	Basic Scene and OrthoTile	no	no	36	20
		GEE	USGS/ Google	Landsat_7	ETM+	USGS Landsat 7 Collection 1 Tier 1 TOA Reflectance	low	LANDSAT/LE07/C01/T1_TOA	less than 70	no	17	6
		earth explorer	USGS EROS Archive	EO-1	ALI	EO-1 ALI L1Gst	low-mediu m	ALI	no	no	3	3
		Google Earth Pro	Google Earth	Landsat/Copernicus	N/A	Landsat/Copernicus	N/A	N/A	N/A	N/A	5	0

6	**Mount Belinda**	GEE	USGS/ Google	Landsat 7	ETM+	USGS Landsat 7 Collection 1 Tier 1 Raw Scenes, USGS Landsat 7 Collection 1 Tier 1 TOA Reflectance, USGS Landsat 7 Collection 1 Tier 2 TOA Reflectance	low	LANDSAT/LE07/C01/T1_TOA, LANDSAT/LE07/C01/T1, LANDSAT/LE07/C01/T2_TOA	less than 90	no	22	5
		earth explorer	USGS EROS Archive	EO-1	ALI	EO-1 ALI L1Gst	low-medium	N/A	less than 80	no	31	12
		GEE	NASA LP DAAC	Terra	ASTER	ASTER L1T Radiance	low	ASTER/AST_L1T_003	less than 90	only images, in which bands B01, B02, B3N are present	17	8
		Google Earth Pro	Google Earth	N/A	N/A	Maxar Technologies	N/A	N/A	N/A	N/A	1	1
7	**Eyja-fjalla-jökull**	GEE	NASA LP DAAC	Terra	ASTER	ASTER L1T Radiance	low	ASTER/AST_L1T_003	no	only images, in which bands B01, B02, B3N are present	79	16

		GEE	USGS/ Google	Landsat 7	ETM+	Landsat 7 Collection 1 Tier 2 TOA	low	Landsat/LE07/ C01/T2_TOA	less than 90	no	18	0
		GEE	USGS/ Google	Landsat 7	ETM+	Landsat 7 Collection 1 Tier 1 TOA	low	Landsat/LE07/ C01/T1_TOA	less than 90	no	29	6
		Google Earth pro	Google Earth	N/A	N/A	Maxar Technologies	N/A	N/A	N/A	N/A	2	1
		Planet	Planet	RapidEye*	REIS	RapidEyeOrthoTile, RapidEye-BasicScene	medium	N/A	no	no	34	2
8	**Katla**	GEE	NASA LP DAAC	Terra	ASTER	ASTER L1T Radiance	low	ASTER/AST_L1T_003	no	no	149	20
9	**Gríms-vötn (Gjálp)**	GEE	USGS/ Google	Landsat 5	TM	USGS Landsat 5 TM Collection 1 Tier 1 TOA Reflectance	low	LANDSAT/LT05/C01/T1_TOA	no	no	6	1
		GEE	USGS/ Google	Landsat 5	TM	USGS Landsat 5 TM Collection 1 Tier 2 TOA Reflectance	low	LANDSAT/LT05/C01/T2_TOA	no	no	2	0
		GEE	USGS	Landsat 5	MSS	USGS Landsat 5 MSS Collection 1 Tier 1 and Tier 2 Raw Scenes	low	LANDSAT/LM05/C01/T1 and LANDSAT/LM05/C01/T2	no	no	0	0

		GEE	USGS /Google	Landsat 4	TM/MSS	USGS Landsat 4 TM Collection 1 Tier 1 and Tier 2 TOA Reflectance; USGS Landsat 4 MSS Collection 1 Tier 1 and Tier 2 Raw Scenes	low	LANDSAT/LT04/C01/T1_TOA and LANDSAT/LT04/C01/T2_TOA and LANDSAT/LM04/C01/T1 and LANDSAT/LM04/C01/T2	no	no	0	0
10	**Bárðarbunga**	GEE	NASA LP DAAC	Terra	ASTER	ASTER L1T Radiance	low	ASTER/AST_L1T_003	no	only images, in which bands B01, B02, B3N are present	203	12
		GEE	USGS/ Google	Landsat 7	ETM+	USGS Landsat 7 Collection 1 Tier 1 TOA Reflectance	low	LANDSAT/LE07/C01/T1_TOA	no	no	2	0
		GEE	USGS/ Google	Landsat 7		USGS Landsat 7 Collection 1 Tier 2 TOA Reflectance	low	LANDSAT/LE07/C01/T2_TOA	no	no	31	few
		Google Earth Pro	Google Earth	Landsat/Copernicus	N/A	Landsat/Copernicus	N/A	N/A	N/A	N/A	1	0
		Planet	Planet	RapidEye*	REIS	RapidEye OrthoTile, Rapid Eye Basic Scene	medium	N/A	no	no	12	4

		earth explorer	USGS EROS Archive	EO-1	ALI	EO-1 ALI L1Gst	low-medium	N/A	no	no	154	6
		GEE	USGS	Landsat 8	OLI	USGS Landsat 8 Collection 1 Tier 1 and Real-Time data OLI Raw Scenes	low	LANDSAT/LC08/C01/T1_RT, LANDSAT/LO08/C01/T1	less than 70	no	23	several

Table 7 Commercial images purchased for some of the investigated glacier-clad volcanoes; total number purchased: 19

volcano number	Volcano name	dataprovider	satellite	sensor	image acquisition date
1	**Mount Redoubt**	geocento	IKONOS-2	OSA	19/02/2009
		geocento	IKONOS-2	OSA	27/02/2009
		geocento	IKONOS-2	OSA	27/02/2009
		geocento	IKONOS-2	OSA	02/03/2009
		geocento	IKONOS-2	OSA	07/03/2009
2	**Mount St. Helens**	geocento	Quickbird-2	BGIS2000	02/10/2004
		geocento	Quickbird-2	BGIS2000	05/10/2004
		geocento	Quickbird-2	BGIS2000	13/03/2005
4	**Nevado del Huila**	geocento	Quickbird-2	BGIS2000	07/02/2007
		geocento	WorldView-1	WV60	11/03/2011
6	**Mount Belinda**	geocento	QuickBird-2	BGIS2000	27/03/2003
		geocento	Quickbird-2	BGIS2000	16/10/2003
		geocento	IKONOS-2	OSA	11/09/2004
7	**Eyjafjalla-jökull**	geocento	GeoEye-1	GIS	27/03/2010
		geocento	WorldView-2	WV110	17/04/2010
		geocento	WorldView-2	WV110	19/04/2010
		geocento	WorldView-1	WV60	21/04/2010
		geocento	WorldView-2	WV110	08/05/2010
		geocento	Quickbird-2	OSA	25/05/2010

Appendix 2 (Publication)

remote sensing

MDPI

Article

Assessing the Use of Optical Satellite Images to Detect Volcanic Impacts on Glacier Surface Morphology

Michael Dieter Martin [1,*], Iestyn Barr [1], Benjamin Edwards [2], Matteo Spagnolo [3], Sanaz Vajedian [1] and Elias Symeonakis [1]

[1] Department of Natural Sciences, Manchester Metropolitan University, Chester Street, Manchester M1 5GD, UK; i.barr@mmu.ac.uk (I.B.); s.vajedian@mmu.ac.uk (S.V.); e.symeonakis@mmu.ac.uk (E.S.)
[2] Department of Earth Sciences, Dickinson College, Carlisle, PA 17013, USA; edwardsb@dickinson.edu
[3] Department of Geography and Environment, University of Aberdeen, Aberdeen AB24 3UF, UK; m.spagnolo@abdn.ac.uk
* Correspondence: michael.d.martin2@stu.mmu.ac.uk

Abstract: Globally, about 250 Holocene volcanoes are either glacier-clad or have glaciers in close proximity. Interactions between volcanoes and glaciers are therefore common, and some of the most deadly (e.g., Nevado del Ruiz, 1985) and most costly (e.g., Eyjafjallajökull, 2010) eruptions of recent years were associated with glaciovolcanism. An improved understanding of volcano-glacier interactions is therefore of both global scientific and societal importance. This study investigates the potential of using optical satellite images to detect volcanic impacts on glaciers, with a view to utilise detected changes in glacier surface morphology to improve glacier-clad volcano monitoring and eruption forecasting. Roughly 1400 optical satellite images are investigated from key, well-documented eruptions around the globe during the satellite remote sensing era (i.e., 1972 to present). The most common observable volcanic impact on glacier morphology (for both thick and thin ice-masses) is the formation of ice cauldrons and openings, often associated with concentric crevassing. Other observable volcanic impacts include ice bulging and fracturing due to subglacial dome growth; localized crevassing adjacent to supraglacial lava flows; widespread glacier crevassing, presumably, due to meltwater-triggered glacier acceleration and advance. The main limitation of using optical satellite images to investigate changes in glacier morphology is the availability of cloud- and eruption-plume-free scenes of sufficient spatial- and temporal resolution. Therefore, for optimal monitoring and eruption prediction at glacier-clad volcanoes, optical satellite images are best used in combination with other sources, including SAR satellite data, aerial images, ground-based observations and satellite-derived products (e.g., DEMs).

Keywords: glaciovolcanism; volcano-glacier interactions; satellite remote sensing; volcanic hazards

Citation: Martin, M.D.; Barr, I.; Edwards, B.; Spagnolo, M.; Vajedian, S.; Symeonakis, E. Assessing the Use of Optical Satellite Images to Detect Volcanic Impacts on Glacier Surface Morphology. *Remote Sens.* **2021**, *13*, 3453. https://doi.org/10.3390/rs13173453

Academic Editor: Pietro Tizzani

Received: 14 July 2021
Accepted: 26 August 2021
Published: 31 August 2021

1. Introduction

Many (245 of 1413) Holocene volcanoes on Earth are currently ice-clad or have glaciers in close proximity [1,2], and interactions between volcanic activity and ice are therefore common (e.g., [3–7]). Such volcano-ice interactions are important since they often result in hazards, including floods, debris flows (lahars) and/or the distribution of fine-grained ash [3,4,8]. Some of the deadliest (e.g., Nevado del Ruiz, 1985) and most costly (e.g., Eyjafjallajökull, 2010) eruptions in recent history were associated with ice-clad volcanoes [9,10]. The former eruption killed ~23,000 people [3], and the latter heavily impacted air travel in large parts of Europe and caused considerable costs of about 1.3 billion euros (£1.1 billion, US$1.7 billion), due to the widespread dispersal of fine-grained ash [8,9]. Therefore, the investigation of volcano-ice interactions is of considerable social and economic importance. They are also significant for glaciology, since predicting the future behaviour of glaciers requires knowledge of their response to different forcing mechanisms. A notable example is the potential for

volcanic controls on the future stability of the West-Antarctic Ice Sheet (WAIS) [11]. Previous publications (e.g., [9,12,13]) reveal that glaciers can be affected by many volcanic processes including (but not limited to) enhanced geothermal heating, subglacial dome growth, sub- and supra-glacial lava flows, pyroclastic density currents and supraglacial flooding. These processes often have a visible impact on the glacier surface morphology as they can cause ice melt and destruction, ice-cauldron (depression) formation, localized ice fracturing and deformation and widespread glacier crevassing [13]. Given this morphological response, monitoring glaciers has the potential to indirectly indicate past, ongoing and imminent periods of volcanic unrest [6,13,14]. However, many ice-clad volcanoes are remote and difficult to access—e.g., Mount Hudson (Chile) or Mount Belinda (South Sandwich Islands)—partly due to the ice cover itself. In a number of cases, remote-sensing techniques have proved useful for indirectly monitoring volcanic activity by observing glaciers on ice-clad volcanoes. For example, with the help of satellite data and aerial photographs, Bleick et al. [6] observed glacier surface changes prior to the 2009 Mount Redoubt eruption. Despite their potential, such studies have often been limited by the cost and spatial coverage of suitable remotely sensed datasets (i.e., those with high spatial and temporal resolution). Therefore, observations of volcanic impacts on glaciers are often restricted to a limited number of specific events, specific volcanoes e.g., [4–7,15] or specific study areas e.g., [14,16–18]. In recent years, new satellite remote-sensing datasets, covering large parts of the globe, have become available (often free of charge), opening up the possibility for global-scale, systematic analyses [2,10,19]. Despite the potential of such data, their utility as a means of studying the effects of volcanism on the surface of glaciers, for the purpose of indirectly monitoring volcanic activity, has yet to be investigated. Our study addresses this gap in knowledge by testing the usefulness of optical remote sensing sources for identifying volcanic impacts on glacier surface morphology at a global scale. To achieve this, we assess the degree to which key, well documented volcanic impacts on glacier surface morphology, as reported in the literature (often based on field observations and aerial imagery), are identifiable from satellite imagery.

2. Background

The events presented in this study cover glaciovolcanic interactions from different geologic settings around the world. This implies variable ice thicknesses and eruption styles and intensities, which influence the way that ice masses are affected by volcanic activity. The ice masses studied in this paper range from comparably small, thin glaciers (commonly, but not exclusively, tens of metres thick) on top of stratovolcanoes, to hundreds of meters thick ice caps in Iceland. This section gives background information on the events presented in the Results section.

A common way that glaciers are affected by volcanoes is via subglacial heating and the formation of ice cauldrons e.g., [4,15,20]. The term ice cauldron covers the range from shallow, non-crevassed depressions in the ice surface to steep-sided, highly crevassed cylindrical chasms, which sometimes extend to bedrock (i.e., to the glacier bed). Cauldrons are generally caused by heat applied at the glacier base at the location of the vent. This rapid basal ice melting results in subsidence of the overlying ice and ice flow towards the vent. Some cauldrons are associated with meltwater accumulation that is rapidly released in jökulhlaups [20,21]. In contrast, openings are associated to meltwater flow through zones of weakness within the ice (e.g., pre-existing crevasses) due to high subglacial water pressures. The openings are formed locally if the meltwater finally reaches the glacier surface and continues flowing supraglacially [5,7]. The 2014–2015 rifting episode between Bárðarbunga and Askja in Iceland resulted in the formation of ice cauldrons (on Dyngjujökull glacier) along the path of a 45-km long subglacial dyke, and included the collapse of the Bárðarbunga caldera [15,22–24]. These cauldrons lie within a sector of ice 430–670 m thick [25]. In 1999–2005, geothermal activity on Katla (Iceland), beneath Mýrdalsjökull glacier, resulted in the formation of very large ice cauldrons, ~1–1.5 km in diameter above 400–700 m thick ice [21,26]. During the more violent eruption of Eyjafjallajökull (Iceland) in 2010, ice cauldrons formed in the summit crater and openings appeared in the ice surface

along a subglacial flood path down Gígjökull glacier [5,7]. Ice thicknesses are reported to be ~200 m for the caldera region, and typically less than 100 m for Gígjökull glacier [7,27]. Cauldron formation is not exclusive to subglacial volcanic activity in Iceland but has been observed on volcanoes elsewhere globally. For instance, on Mount Redoubt (Alaska), ice cauldrons were observed approximately two months before its eruption in March/April 2009, alongside a variety of other precursors such as crevassing, ice-slurry/debris flows and the emission of ejecta [6]. One of the cauldrons formed in the summit crater of the volcano, where ice is ~150 m thick [28], and was associated with near-vertical walls and clear concentric crevassing [6,29,30]. Cauldrons associated with the emission of gases and pyroclasts were also reported during the eruption of Mount Hudson (Chile) in October to December 2011 [31]. The March–April 2021 eruption of Mount Veniaminof in Alaska also produced a visible cauldron ~1 km in diameter, east of the prominent and active intra-caldera cone within ice that is ~100 m thick [32,33]. During this period, the emission of ash-plumes, (potential) lava effusion under the intra-caldera glacier and subsidence of glacier ice were reported [33].

Crevassing of glacier ice due to volcanic activity, but without cauldron formation has been reported from Mount Belinda (Montagu Island) in the South Sandwich Islands. Mount Belinda is a small volcanic cone in a 6-km wide ice-filled caldera, with a tidewater glacier draining its northern margin. Mount Belinda experienced a low-intensity volcanically-active period from 2001 to 2007. This included active lava flows and subglacial melt, which is presumed to have promoted glacier acceleration (due to basal lubrication), causing the outlet glacier's surface to become extensively crevassed [34,35]. An example of an ice mass being affected by subglacial dome growth comes from Mount St Helens (United States) during an active period from 2004 to 2006. At this time, a 1 km^2 and 200 m thick glacier occupied the volcano's "amphitheater"-like crater [36]. During the active period, a lava dome extruded in several spines and squeezed the glacier against the crater wall. The dome extrusion finally split the glacier apart and resulted in heavy crevassing and glacier bulging [37,38].

3. Materials and Methods

In this study, ~1400 freely-available low- to medium-resolution, and a limited number of commercial high-resolution, optical satellite images were investigated. We focused on optical satellite data (rather than other datasets, including Synthetic Aperture Radar (SAR)) since only optical satellite data cover almost half a century and the past decade has seen a rapid increase in the variety of free and commercial datasets potentially suitable for glacier-volcano monitoring. Following Elliot et al. [39], we use the term "low-resolution" for image resolutions of 10–100 m, "medium-resolution" for image resolutions of 1–10 m and "high resolution" for images of less than 1 m resolution. The literature reveals ~66 instances of documented volcanic impacts on glaciers at ~42 volcanoes globally during the optical satellite era (i.e., 1972 to present) [13]. Following detailed analysis of each of these events, we focused on a selection of the best-documented examples that represent major potential volcanic impacts on glacier surface morphology and are therefore considered representative (see Figure 1 and Table 1). Supplementary Table S1 reports the characteristics of all investigated events as reported in the literature and provides an overview of all satellite image sources (commercial and non-commercial) used. Satellite images were obtained through geocento (https://geocento.com/, accessed on 18 November 2020), Google Earth Engine Code Editor" (GEE) [40], USGS EarthExplorer (earthexplorer.com, accessed on 24 February 2021) and Planet (planet.com, accessed on 26 May 2021), and images were viewed in the visible and near-infrared range of the electromagnetic spectrum (including panchromatic bands). Images were enhanced for better visibility using contrast enhancement/histogram stretch (where appropriate) in QGIS 3.10. (QGIS.org, 2021. QGIS Geographic Information System. QGIS Association. (http://www.qgis.org, accessed on 07 July 2021).

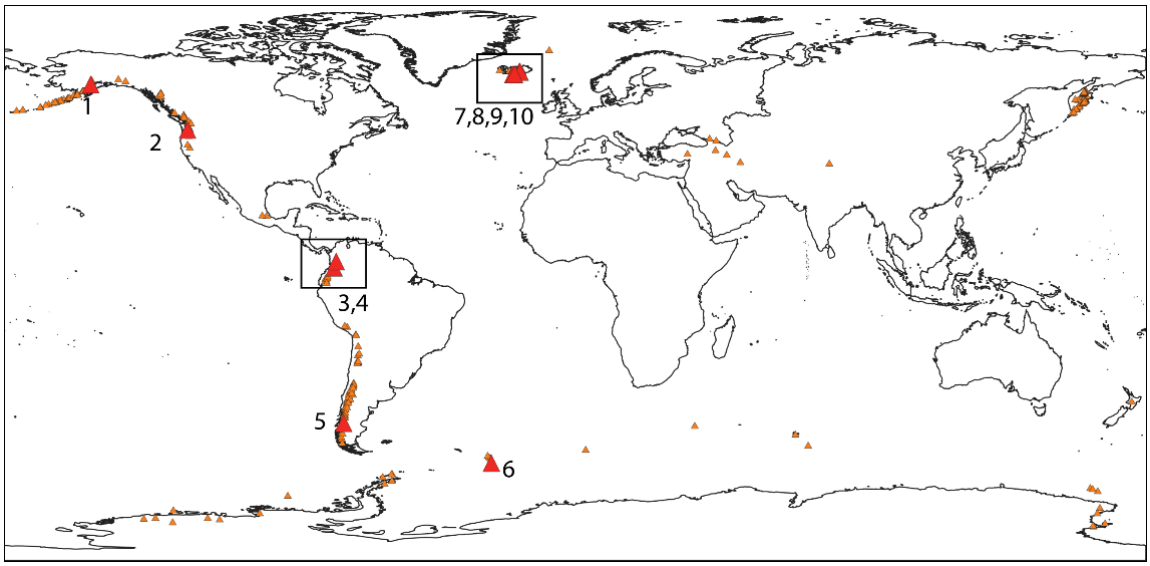

Figure 1. Glacierized volcanoes around the globe (small orange triangles, [2]) and volcanoes investigated in this study (red triangles, numbered). For some volcanoes, multiple events were investigated. Volcano numbers are detailed in Table 1. Basemap: "World Continents" (accessed on 10 March 2021).

Table 1. Volcanoes and corresponding eruptive activity investigated in this study (volcano numbers relate to Figure 1). Examples illustrated in figures within the present study, are shown in bold.

Volcano Number	Volcano Name	Volcano Type	Region/Country	Coordinates (Lat, Lon)	Period of Activity
1	**Mount Redoubt**	**stratovolcano**	**Alaska (US)**	**60.485, −152.742**	**03/2009–04/2009**
2	**Mount St Helens**	**stratovolcano**	**United States**	**46.2, −122.18**	03/1980–10/1980 **09/2004–2006**
3	Nevado del Ruiz	stratovolcano	Colombia	4.892, −75.324	11/1985
4	Nevado del Huila	stratovolcano	Colombia	2.93, −76.03	02/2007–05/2009
5	**Mount Hudson**	**stratovolcano**	**Chile**	**−45.9, −72.97**	**10/2011–12/2011**
6	**Mount Belinda (Montagu Island)**	**shieldvolcano**	**South Sandwich-Islands (UK)**	**−58.445, −26.374**	**10/2001–09/2007**
7	**Eyjafjallajökull**	**central vocano**	**Iceland**	**63.633, −19.633**	**03/2010–06/2010**
8	**Katla (Mýrdals-jökull)**	**subglacial central vocano**	**Iceland**	**63.633, −19.083**	**1999–2005**
9	Grímsvötn (Gjálp)	subglacial volcanic fisure	Iceland	64.416, −17.316	09/1996–10/1996
10	**Bárðarbunga**	**subglacial central vocano**	**Iceland**	**64.633, −17.516**	**08/2014–02/2015**

4. Results

4.1. Ice Cauldron Formation

In principle, ice cauldrons are readily detectable with low-resolution satellite imagery, particularly within thick ice. With satellite sensors operating in the visible and near-infrared range (including multispectral and panchromatic bands), cauldrons appear as dark (shaded) areas against the bright ice surface. A period of geothermal activity beneath Mýrdalsjökull between 1999 and 2005 led to the formation of large ice cauldrons, which were identifiable on ASTER visible and near-infrared (VNIR) images (15 m resolution,

Figure 2). During the 2014–2015 Bárðarbunga eruption, three cauldrons developed on the surface of Dyngjujökull glacier in the northern part of the Vatnajökull ice cap. These cauldrons are clearly visible as shadows against the snow-covered ice in a true-colour composite EO-1 ALI image (30 m resolution; Figure 3b). However, in a snow-free EO-1 ALI image (Figure 3c), the cauldrons are not visible, since transmitted radiance from the cauldrons region is not distinguishable from the surrounding dirty ice (even though the cauldrons are present at the time of image capture, as shown by Reynolds et al. [15] using aerial- and TerraSAR-X imagery). An enlarged view of the northernmost cauldron shows evidence of faint concentric crevassing (Figure 3d).

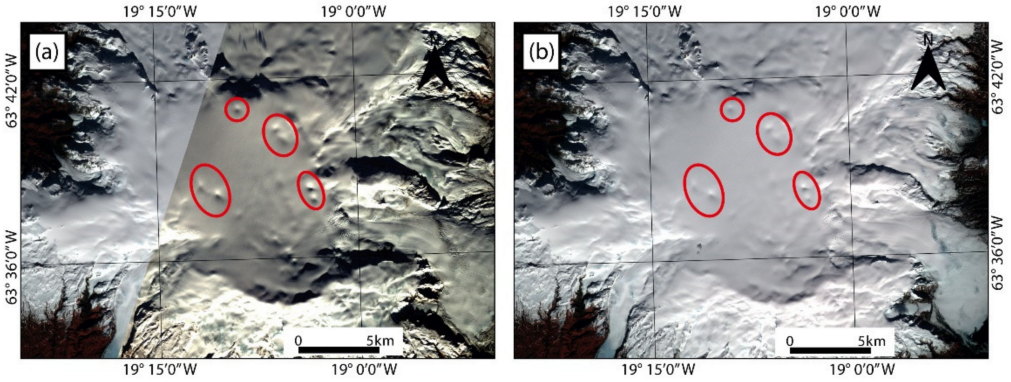

Figure 2. ASTER VNIR images (15 m resolution) of Mýrdalsjökull (Katla volcano beneath ice cap). (**a**) from 7 November 2002 and (**b**) from 17 March 2004. Both images show cauldrons over-active geothermal areas (encircled in red).

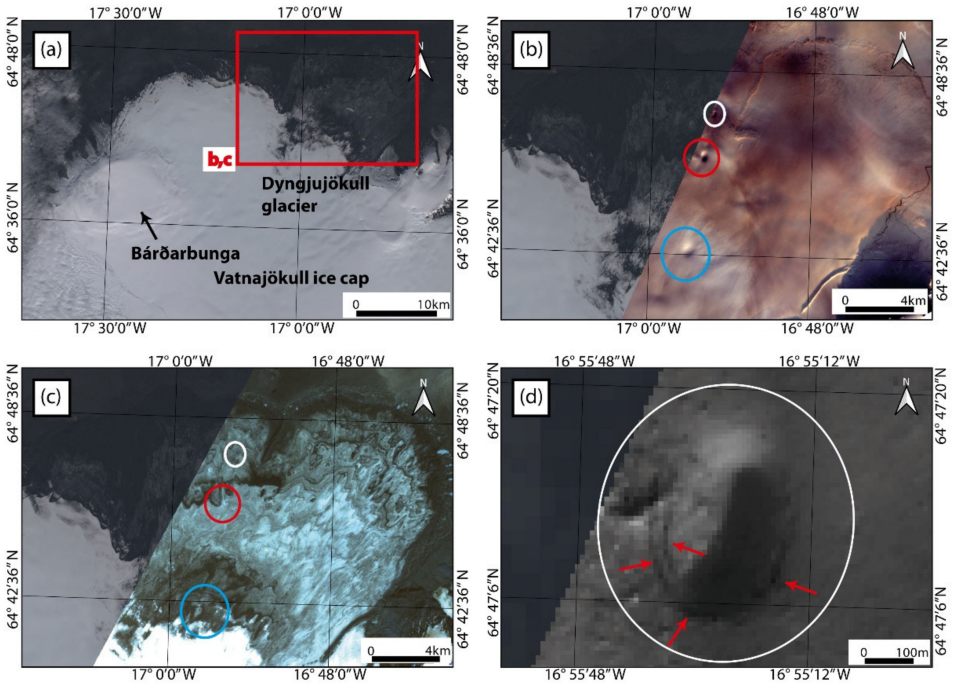

Figure 3. (**a**) Landsat 8 overview image (30 m resolution) of the northern part of Vatnajökull ice cap. Red rectangle shows the study area on Dyngjujökull glacier (subfigures b and c). (**b**) EO-1 ALI true-colour composite images (30 m resolution) from 4 November 2014 (snow-covered) and (**c**) 20 September 2014 (non- snow-covered) showing Dyngjujökull glacier. For both images, three cauldrons are encircled in white, red and blue. Background image (non snow-covered) from Landsat 8 for all images (**b**–**d**). (**d**) EO-1 ALI panchromatic image (10 m resolution) from 4 November 2014, enlarged to show a cauldron with faint concentric crevassing (crevasses indicated with red arrows).

4.2. Opening Formation

Volcanically triggered openings on the glacier surface are in principle observable with low-resolution images (>15 m resolution), however, they are best observed with at least medium-resolution images (~5 m resolution or better) due to the surface texture making it difficult to distinguish between openings and other features on the glacier surface. A notable example comes from Eyjafjallajökull (Figure 4a), where the 2010 eruption, besides melting through the entire ice column in the main crater, produced openings on Gígjökull glacier (Figure 4b,c). A view from April 2010 shows the intact surface of the glacier before the explosive phase of the eruption (inset Figure 4a). Several openings (without concentric crevassing) developed in the upper part of Gígjökull glacier during the eruption due to subglacial meltwater flow [7], and are visible in low-resolution ASTER images (Figure 4b), but better seen with WorldView-1 imagery (2 m resolution) acquired on the same day (red arrows, Figure 4c).

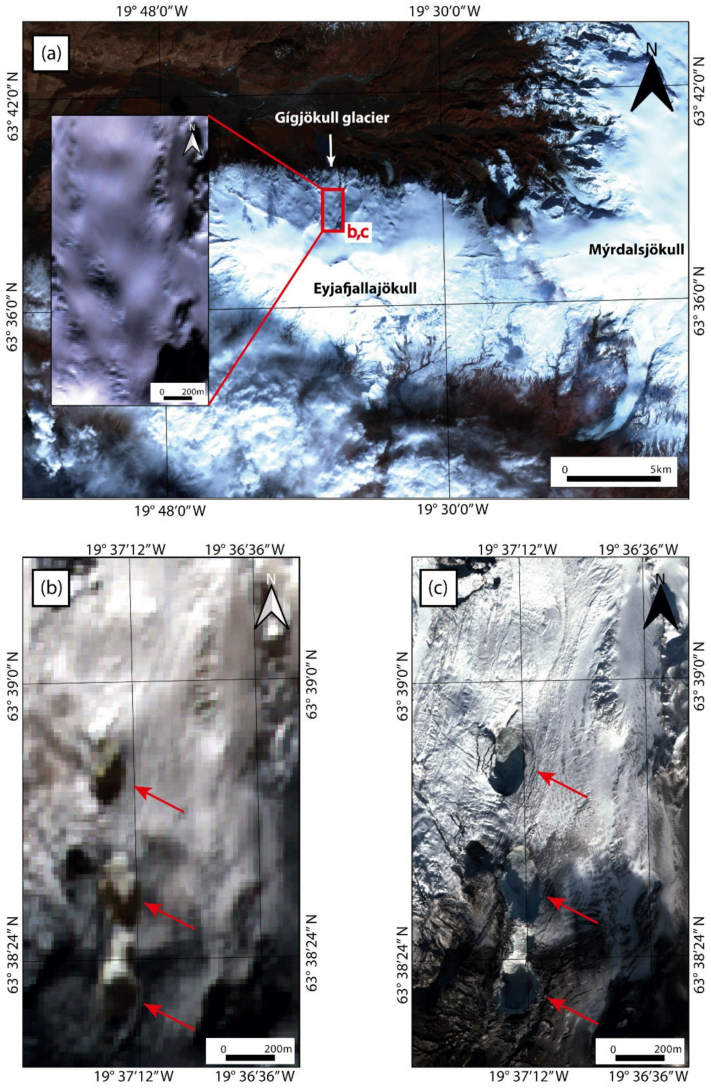

Figure 4. (**a**) ASTER VNIR (15 m resolution) overview image of Eyjafjallajökull from 01 April 2010, with a small box showing the study area on Gígjökull glacier. The ASTER VNIR image (15 m resolution) in the inset shows the intact glacier surface before the summit eruption. (**b**) ASTER VNIR (15 m resolution) image and (**c**) WorldView-1 visible image (2 m resolution), both acquired on 19 April 2010 during the summit eruption showing at least three openings on the glacier surface (red arrows); WorldView-1 image: DigitalGlobe Products. WorldView-1 © 2010 DigitalGlobe, Inc., a Maxar company, Westminster, CO, USA.

4.3. Glacier Crevassing

In this section, glaciovolcanic factors/events that lead to crevassing of glacial ice are considered. Ice cauldron formation is often associated with concentric crevassing (Section 4.3.1). Other volcanic factors that can lead to glacier crevassing include subglacial lava dome growth (Section 4.3.2), localized crevassing adjacent to supraglacial lava flows (Section 4.3.3) and widespread (glacier-wide) crevassing due to glacier acceleration/advance triggered by increased meltwater at the ice-bed interface (Section 4.3.4).

4.3.1. Concentric Crevassing Due to Ice Cauldron Formation

Concentric crevasses related to cauldron formation on ice-covered stratovolcanoes are observed with medium- to high-resolution images, but are too small to be identified with low-resolution images alone. In principle, crevasses can be identified in satellite images as dark fissures on the bright coloured glacial ice and snow. Figure 5a shows Mount Redoubt shortly before its eruption in March 2009, and Figure 5b–d reveal the capabilities of medium- and high-resolution images for ice-cauldron/crevassing detection at this volcano. In this example, the low-resolution ASTER image (Figure 5c) and high-resolution IKONOS-2 image (Figure 5d, 0.8 m resolution) were acquired on the same day. The ice cauldron and concentric crevasses are more clearly visible in the IKONOS-2 image than in the ASTER image due to its high spatial resolution. With high-resolution images, it is not only possible to identify concentric crevasses, but also to accurately monitor their evolution (including changes in their number, length and width). This becomes clear if Figure 5b is compared to Figure 5d. The satellite image in Figure 5b was acquired several days before those of Figure 5c,d and shows a smaller, less evolved cauldron and fewer/smaller crevasses (blue arrows).

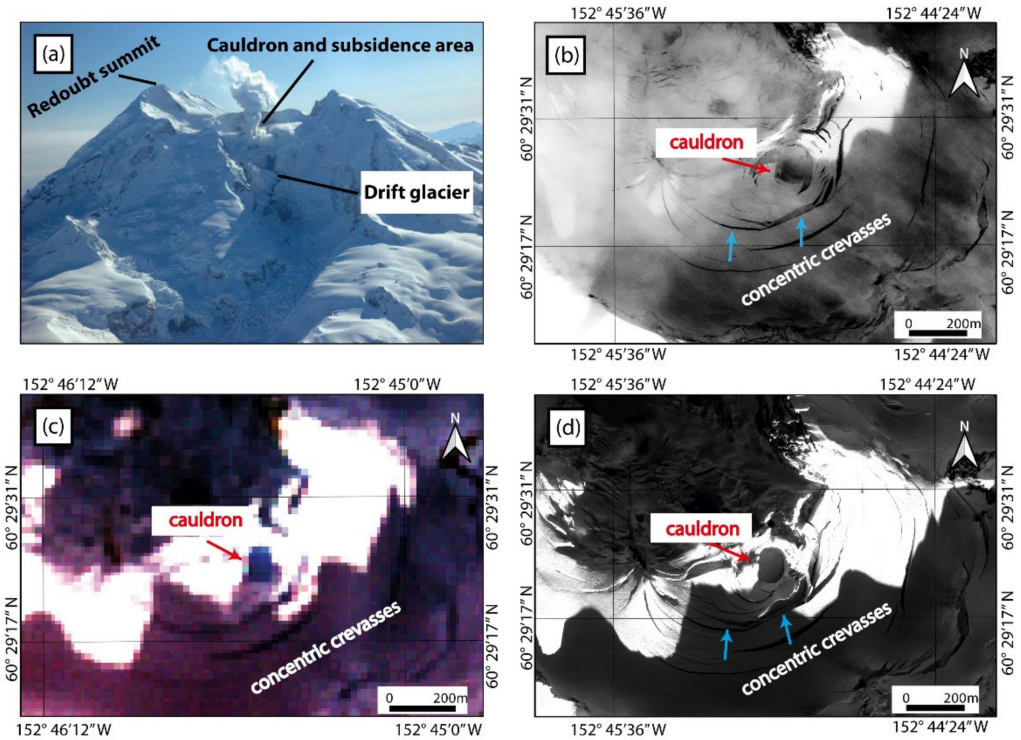

Figure 5. (**a**) photograph of north flank of Mount Redoubt from 15 March 2009 (shortly before its eruption; photo by H. Bleick AVO/USGS). The study site shown in panels (**b**–**d**) lies within the cauldron and subsidence area. (**b**) IKONOS-2 panchromatic image (0.8 m resolution) from 19 February 2009 showing an ice-cauldron and concentric crevasses. (**c**) ASTER VNIR image (15 m resolution). (**d**) IKONOS-2 panchromatic image (0.8 m resolution) showing a large ice-cauldron and concentric crevassing. Blue arrows show the locations of growing crevasses/increased number of crevasses. Images (**c**) and (**d**) were both acquired on 02 March 2009, and all subfigures (**b**–**d**) cover the same spatial area. IKONOS-2 products: DigitalGlobe Products. IKONOS-2 © 2009 DigitalGlobe, Inc., a Maxar company, Westminster, CO, USA.

In contrast to the cauldrons on Mount Redoubt presented above, in some cases, cauldrons lack a clearly-identifiable central melt-pit and are therefore only indicated by concentric crevassing. This was the case for Mount Hudson during its 2011 eruption, as revealed by Rapid-Eye imagery (5 m resolution, Figure 6).

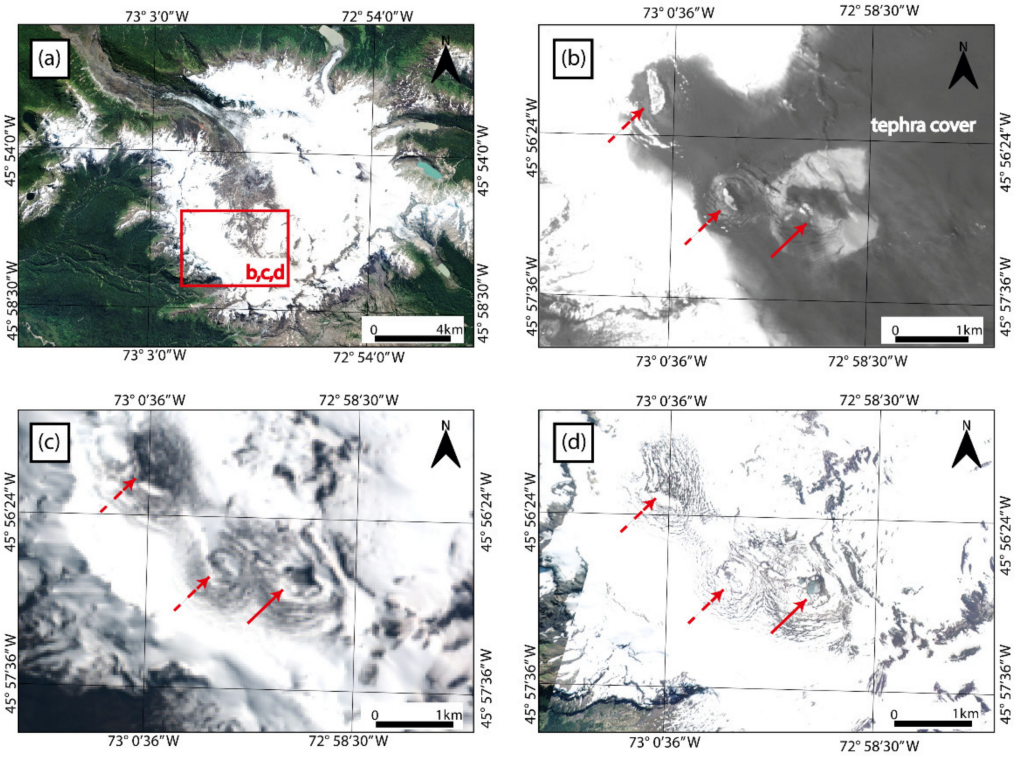

Figure 6. (**a**) Rapid-Eye true-colour overview image (5 m resolution) of Mount Hudson from 19 February 2011, (**b**) EO-1 ALI panchromatic image (10 m resolution) from 01 Novemer 2011, (**c**) EO-1 ALI true-colour image (30 m resolution) from 30 Novemer 2011 and (**d**) Rapid-Eye true-colour image (5 m resolution) from 01 December 2011. All subfigures (**b**–**d**) show the same extent and show one cauldron (red bold arrow) and the (possible) location of two more cauldrons (red dashed arrows); Rapid-Eye image: Planet Team (2017), https://api.planet.com (accessed on 22 October 2019).

4.3.2. Crevassing Due to Subglacial Lava Dome Growth

Subglacial dome growth on ice-covered stratovolcanoes commonly results in small-scale crevassing, which is often only visible in medium- to high-resolution images. During the eruption of Mount St Helens from 2004 to 2006, a lava dome gradually developed beneath a small crater-occupying glacier. In the initial stage of the eruption in early October 2004, a melt hole formed in the glacier surface (red arrow in Figure 7b) and parts of East Crater glacier became crevassed due to the onset of lava dome growth (Figure 7b). As the lava dome continued to grow, it extruded through the ice, resulting in the deformation and heavy crevassing of East Crater glacier (Figure 7c,d). The impact of dome growth (ice displacement, crevassing and melt-hole formation) on very small glaciers (~1 km^2, 200 m thick) such as the one described are best viewed with at least medium-resolution images such as QuickBird 2 (Figure 7c, 2.4 m). High-resolution images (such as QuickBird-2 panchromatic, 0.6 m) might be required particularly when it comes to small scale crevassing (Figure 7b). The impacts mentioned are less clear in medium-resolution EO-1 ALI panchromatic images (10 m resolution, Figure 7d), and almost impossible to observe in low-resolution imagery (>10 m resolution).

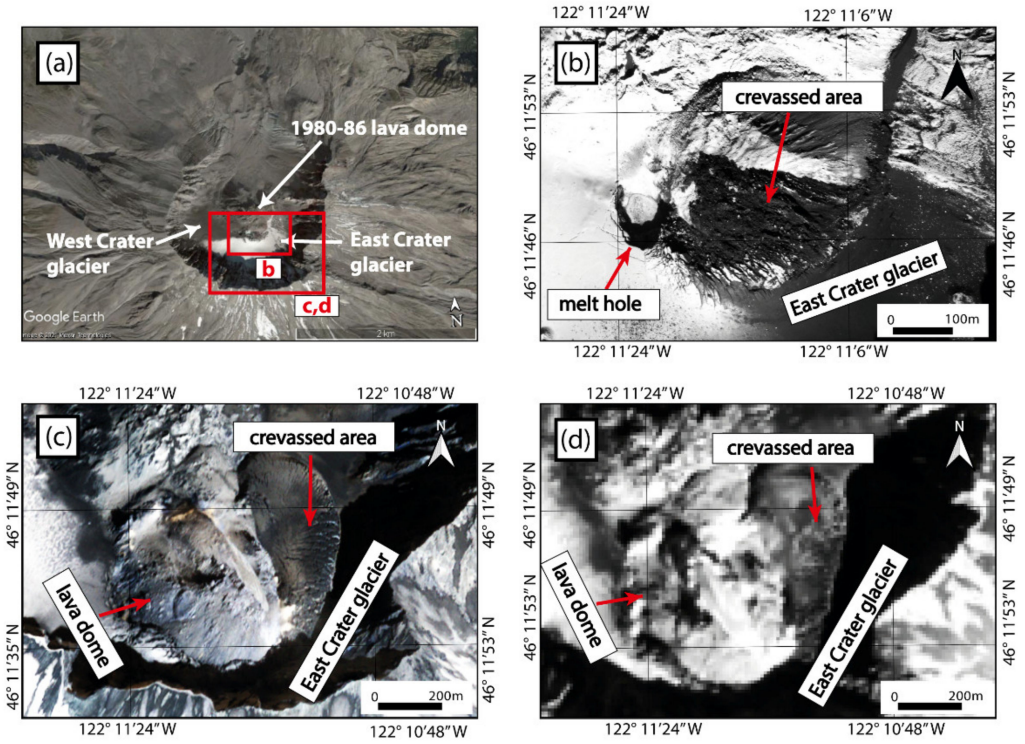

Figure 7. (**a**) GoogleEarth image from 03 October 2004 showing the Mount St. Helens summit crater (© 2021 Maxar Technologies). (**b**) QuickBird 2 panchromatic image (0.6 m resolution) from 05 October 2004. (**c**) QuickBird-2 visible image (2.4 m resolution) from 13 March 2005. (**d**) EO-1 ALI panchromatic image (10 m resolution) from 15 March 2005. All images show the impacts (crevassing, melt-hole formation) on East Crater glacier due to subglacial lava dome growth (DigitalGlobe Products. QuickBird-2 © 2004, 2005 DigitalGlobe, Inc., a Maxar company, Westminster, CO, USA).

4.3.3. Localized Crevassing Due to Supraglacial Lava Flows

Medium-resolution satellite images (i.e., with resolutions of ~10 m or better) are sufficient to detect crevasses caused by supraglacial lava flows. For example, from 2001–2007, a (mostly effusive) eruption at Mount Belinda (Montagu Island) (Figure 8a) resulted in supraglacial lava flows, which are clearly visible in medium-resolution EO-1 ALI panchromatic imagery (Figure 8b). This medium-resolution imagery also reveals localised crevasses surrounding the supraglacial lava flow (reported by [35]; see Figure 8b). These crevasses presumably indicate that the lava melted deep channels/gullies into the glacier surface [9,34,35]. These melt-gullies are difficult to observe directly, but their impact on the surrounding ice is observed in medium-resolution imagery.

4.3.4. Widespread Crevassing Due to Glacier Acceleration/Advance

During the 2001–2007 eruption at Mount Belinda, the outlet glacier which drains the volcano's northern flank experienced widespread (i.e., glacier-wide) crevassing. This crevassing is thought to reflect glacier acceleration and advance (i.e., "surging") in response to subglacial meltwater release during the eruption [9]. The Landsat-7 panchromatic image (15 m resolution) in Figure 8a shows the largely intact (i.e., minimally crevassed) glacier surface ~9 months before the onset of volcanic activity. By contrast, the EO-1 ALI panchromatic images in Figure 8c,d, acquired during the eruptive period, shows widespread crevassing of the glacier surface. Thus, unlike localized crevassing related to ice cauldrons or volcanic dome growth (e.g., Sections 4.3.1 and 4.3.2), widespread glacier crevassing at Mount Belinda is identifiable even without access to high-resolution imagery.

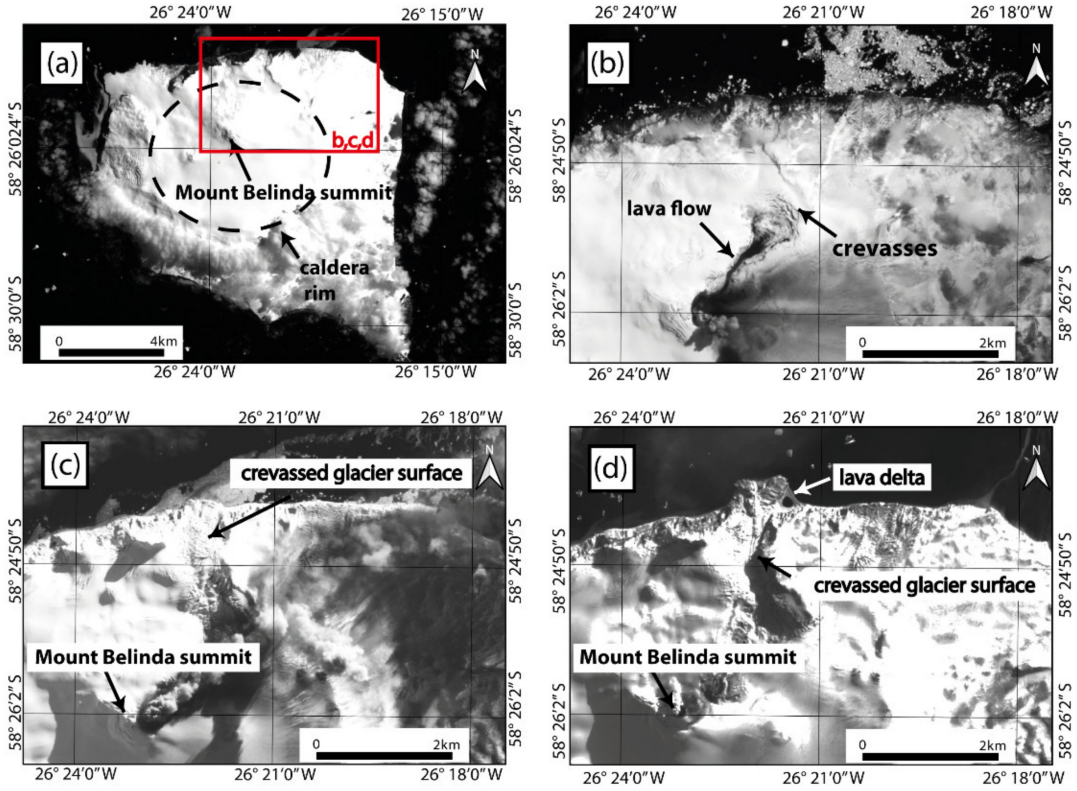

Figure 8. (**a**) Landsat 7 panchromatic image (15 m resolution) acquired on 24 January 2001 showing Montagu Island before the start of an eruptive period at Mount Belinda. (**b**) EO-1 ALI panchromatic image (10 m resolution) from 07 December 2003 showing a supraglacial lava flow, and associated crevassing. (**c**) EO-1 ALI panchromatic image (10 m resolution) from 06 August 2005. (**d**) EO-1 ALI panchromatic image (10 m resolution) from 18 August 2007. Subfigures (**c**) and (**d**) show widespread glacier crevassing. All subfigures (**b**–**d**) cover the same region of the northern part of the caldera.

5. Discussion

From our analysis of the preceding examples of volcano-glacier interactions using optical imagery, we have identified the most readily observed volcanic impacts on glaciers, identified several key challenges to making these observations, and developed some "best practice" guidelines.

5.1. Observable Volcanic Impacts on Glaciers

5.1.1. Ice Cauldron/Opening Formation

Ice cauldrons are the most common volcanic impact on glaciers observable from optical satellite images. For small subglacial eruptions (e.g., Bárðarbunga 2014–2015) or above geothermally active regions (e.g., Mýrdalsjökull) with large ice-thickness, these cauldrons tend not to extend to bedrock (i.e., to the glacier bed), but form depressions that are much wider than deep, typically up to 3-km in diameter see [21]. In optical images, these glacier surface depressions are often observable due to shadowing, which results in areas (inside parts of the ice cauldrons) that are distinct from the usually brighter glacier surface. Due to these often-conspicuous contrasts in surface shading, large surface cauldrons are, in principle, readily observable even in low-resolution satellite images (Figure 3). In some cases, more energetic eruptions can produce ice cauldrons that extend to bedrock. For example, at Gjálp in 1996 ice cauldrons melted through up to 500 m of ice [4]. Though large, these cauldrons can be difficult to observe during, or shortly after eruptions, since the explosive events that lead to their formation also produce ash-laden eruption plumes, preventing direct observation of the ice surface using optical remote sensing sources (e.g., no suitable optical images show the cauldron in the main caldera at Eyjafjallajökull in 2010). Ice cauldron formation is also common at volcanoes with

thinner and less extensive ice cover, and cauldrons often extend to bedrock. Using optical satellite images, it is possible to detect these cauldrons on Mount Redoubt during and following its active period in 2009 (Figure 5) and on Mount Hudson during and following its active period in 2011 (see Figure 6). The detection of cauldrons on only partially ice-covered volcanoes creates some difficulties due to an often restricted cauldron size (see Figure 5), combined with a highly variable surface texture, topography and colour at the summit (also see Section 5.2). However, cauldrons are often visible in medium- and high-resolution imagery and appear as either dark spots (<a few pixels) or regions (multiple pixels), depending on image resolution (see Figures 3 and 4). Particularly large lahars might be generated by eruptions through crater lakes depending on the amount of lake water involved [12]. Similarly, large amounts of water stored in ice cauldrons formed before a large eruptive event might increase the likelihood of large lahars, emphasising the importance of identifying ice cauldrons.

5.1.2. Crevassing

Glacier crevassing is another volcanic impact on glaciers commonly observable from optical satellite images. These crevasses are often localized and concentric (e.g., encircling ice cauldrons), but can also be more widespread, and irregular or linear in form. In fact, all volcanic impacts on glaciers discussed in this paper are, to some degree, associated with crevassing. In principle, crevasses are visible as dark stripes in optical satellite images (Figure 8c), though their detection depends on a notable colour contrast between the crevasse and the surrounding glacial ice and snow. Various approaches have been used to detect widespread regions of crevassing on "non-volcanic" glaciers, using low- to high-resolution optical satellite images [41–46]. However, some volcanically-generated glacier crevasses (e.g., those forming around the margins of ice caldrons or those forming related to subglacial dome growth) are often small and comparatively isolated (rather than widespread), meaning that individual landform identification can be challenging, and requires medium- to high-resolution imagery. In addition, when investigating glacierized volcanoes, being able to monitor crevasse development (e.g., crevasses appearing where they were formerly absent) and evolution (e.g., growth) is important. This generally requires imagery with both high spatial and temporal resolution, and is easier for glaciers that are not already heavily crevassed (see Figure 8).

5.2. Difficulties with Observing Volcanic Impacts on Glaciers

In this study, we have identified some key challenges of using optical satellite images to study volcanic impacts on glaciers. Often, extensive cloud cover and eruption plumes limit the temporal resolution of useful imagery for a specific volcano. This is a problem common to optical remote sensing of many volcanoes globally, not just those that are glacier-clad. One potential solution (though not the focus of this study) is to use SAR satellite data operating in the microwave region of the electromagnetic spectrum, which can penetrate clouds due to a larger wavelength used. For example, crevassing of the glacier surface yields an increased backscatter of amplitude SAR data used to identify ice cauldrons and meltwater tunnels on Mýrdalsjökull [47]. Supraglacial snow cover also introduces difficulties with observing volcanic impacts on glaciers from optical imagery, since details of the ice surface are often obscured. This is particularly relevant for volcanic events that occur during winter (or the snow season). However, in some cases, snow cover can be an advantage, since it creates a homogeneous surface of low contrast, making subtle changes in topography (e.g., ice surface cauldrons) easier to identify (see Figure 3).

In general, low-resolution optical imagery is useful for identifying and monitoring some larger volcanic impacts on glacier surface morphology, but is unable to resolve smaller features including some crevasses, cauldrons, ice domes and supraglacial channels. Observing volcanic impacts on small (thin) glaciers can also be particularly challenging, since these glaciers typically have steep, and heavily crevassed surfaces (due to the influence of steep and undulating bed topography), with frequent bedrock protrusions sometimes

difficult to distinguish from glacial ice and/or volcanic extruding features. Given these issues with scale, detailed investigation of volcanic impacts on glaciers often requires medium-resolution imagery of at least ~5 m. At present, this has cost implications, since freely-available imagery often is of low resolution. A further problem of image availability is that historical eruptions are typically poorly covered by satellite imagery. This applies most notably to events that occurred prior to the widespread availability of imagery from Landsat 7 and ASTER satellites (both launched in 1999). This leads to a strong temporal bias towards more recent eruptions (see examples presented in this study).

In addition to these challenges with image availability, it is also difficult to assess the required (or optimal) frequency of image acquisition for successful monitoring of glacier-clad volcanoes. The timescales that apply for the formation of the features discussed in this paper vary considerably from several minutes to months/years. For instance, the formation of new ice cauldrons in the summit area of Eyjafjallajökull in 2010 took place within minutes [5], whereas squeezing of glacier ice and related crevasse formation on the Crater glacier during the extrusion of a volcanic dome on Mount St. Helens continued for about two years [37,38]. The time-frame for widespread crevassing of a glacier due to increased generation of basal meltwater (as observed on Mount Belinda) likely lies somewhere between those two endmembers. Therefore, in some quickly evolving instances images would ideally be acquired very frequently (~several per day), whereas other instances could, in principle, be sufficiently well monitored based on the common repeat cycle of ~16 days for Landsat or ASTER, though issues with cloud cover and eruption plumes remain.

Finally, when viewing optical satellite imagery, it is sometimes difficult to discern the precise nature of volcano-glacier interactions. For example, supraglacial flow paths of volcanically-triggered floods and lahars are typically easy to distinguish because the debris deposited contrasts with the bright glacier surface. However, using satellite imagery alone, it is difficult to establish whether these events incised channels into the ice, or just flowed across the glacier surface. This also applies to supraglacial lava flows, which are often notably darker than the surrounding ice, but optical images provide little information about whether the glacier surface has been melted/incised. In this latter example, crevasses radiating from a lava flow's terminus (e.g., Mount Belinda, Figure 8b) can provide some indication that, through melting, the lava has had an impact on the glacier surface morphology (also see [35]). Part of this challenge in observing volcanic impacts on glaciers using optical satellite imagery is the lack of quantitative information on changing ice surface elevations (a key indicator of ice melt, fracture, doming, etc.). This clearly points to digital elevation models (DEMs) as potentially useful sources (though not the focus of this study), particularly when multiple high-resolution DEMs representing conditions before and after periods of volcanic unrest are available. For example, Rossi et al. [24] used pre- and post-event DEMs to identify and measure supraglacial ice cauldrons formed during the 2014–2015 Bárðarbunga eruption.

5.3. Guidelines for Best Practice

For the purposes of monitoring glacier-clad volcanoes, being able to detect volcanic impacts on the surface morphology of glaciers is important. With that in mind, here we outline a set of general guidelines for anyone undertaking (or wishing to undertake) this task using optical satellite imagery.

5.3.1. Site Overview and Image Availability

For a particular volcano, glacier and/or event, satellite image availability is a key factor determining which volcanic impacts on glaciers are identifiable. For historical analysis (rather than monitoring), this is primarily determined by the period of interest. For example, for older events (but still within the satellite era), e.g., those that occurred between 1972 (the launch year of Landsat 1) and 1999, imagery is mostly of low spatial resolution, and choice of satellites is very limited (e.g., Landsat 1-5 and SPOT 1-4) [39]. For

events that have occurred since 1999, the range and resolution (spatial and temporal) of available images improves dramatically, particularly in recent years. Some free, but low-resolution, sources (e.g., Landsat 7, ASTER) are available throughout this period. Medium- and high-resolution images are also available (e.g., since the launch of IKONOS in 1999), but are typically commercial, rather than accessible for free.

Given the costs associated with obtaining high-resolution imagery, for the purposes of observing volcanic impacts on glaciers, lower resolution, but freely available, imagery can serve as a foundation. These images can then be supplemented with "targeted" and judiciously selected (i.e., covering specific areas and/or time periods) commercial imagery.

Free and commercial imagery is available via various websites, and some image types (e.g., Landsat and ASTER) are often easiest to access through platforms such as Google Earth Engine [40]. In some cases, freeware virtual globes (e.g., Google Earth and NASA Worldwind) and web mapping services (e.g., Bing Maps and Google Maps) can provide access to high-resolution images (with plugins available to export images into GIS packages such as QGIS). Thus, virtual globes and web mapping services allow access to high-resolution imagery, without the costs associated with commercial data. However, due to the limited availability of images, and the lack of user choice in image selection, these platforms rarely have images (and certainly not multiple images) covering a particular time period of interest (c.f., [13]), and are of limited use when considering highly dynamic environments (such as those associated with active volcanism).

5.3.2. User Experience

The ability to identify volcanic impacts on glaciers using optical satellite imagery partly depends on user experience. For most users (particularly those with comparatively limited experience), examining "known" (or documented) examples, such as those highlighted in this paper, is likely to be useful. This might involve observing volcanic impacts in the field, from existing ground-based or aerial photographs, or by looking at medium- to high-resolution satellite imagery. This is likely to be particularly useful for distinguishing between bedrock protrusions and features related to volcanic activity. Once familiar with the types of features that are present, previously undocumented volcanic impacts on glaciers can be searched for, using lower resolution imagery if necessary.

5.3.3. Using Multi-Temporal Images

Since observing volcanic impacts on glaciers effectively involves change detection (e.g., the development of glacier crevasses where they were previously absent), observing satellite images from a range of time periods (pre-, syn- and post-volcanic activity) is important. This is often possible by generating a time-series of images (in native resolution), e.g., using Google Earth Engine Code Editor, which requires some java script knowledge [40]. When producing such a time series, image availability (see Section 5.3.1) might be a limiting factor; however, where possible, images which show the glacier surface in its "natural" (i.e., non-volcanically impacted) state are key. This is particularly true of images from the same season (but perhaps a different year) as the period of volcanic unrest. How long before, or after, a period of activity images are useful/relevant is unclear, though some glaciers are known to have experienced changes in surface morphology months prior to eruptions (e.g., Mount Redoubt, 2009), and many impacts were still observable years after [13].

As the spatial and temporal resolution of imagery continue to improve over coming years, monitoring volcanic impacts on glaciers will likely be easier (particularly obtaining cloud-free images) and possible with greater detail than for historical events. In many cases, images are likely to be available on cloud-based platforms such as Sentinel Hub Playground (https://apps.sentinel-hub.com/sentinel-playground/, accessed on 18 March 2021), which allow data visualisation and manipulation (e.g., producing different band combinations) without having to download.

5.4. Mount Veniaminof: A Recent Example

Section 5.3, presented guidelines for best practice for monitoring of glacier-clad volcanoes. In this section, we apply these guidelines to document changes in glacier surface morphology on Mount Veniaminof (Alaska) during its very recent active period from March–April 2021. Emission of ash-plumes, (potential) lava effusion under the intra-caldera glacier and subsidence of glacier ice were reported [33]. Both low spatial resolution Landsat-8 panchromatic images (15 m resolution) and medium spatial resolution Sentinel-2 images (10 m resolution) are sufficient to detect a newly developed ice cauldron and concentric crevasses in the glacier surface (Figure 9). Due to repeated image acquisition (i.e., the 5-day repeat cycle of the Sentinel-2 satellites), ice-cauldron evolution could be monitored with a much better temporal and spatial resolution than most of the other cases presented in this work. This example clearly demonstrates the improved potential of recently launched optical satellites for monitoring of glacier-clad volcanoes.

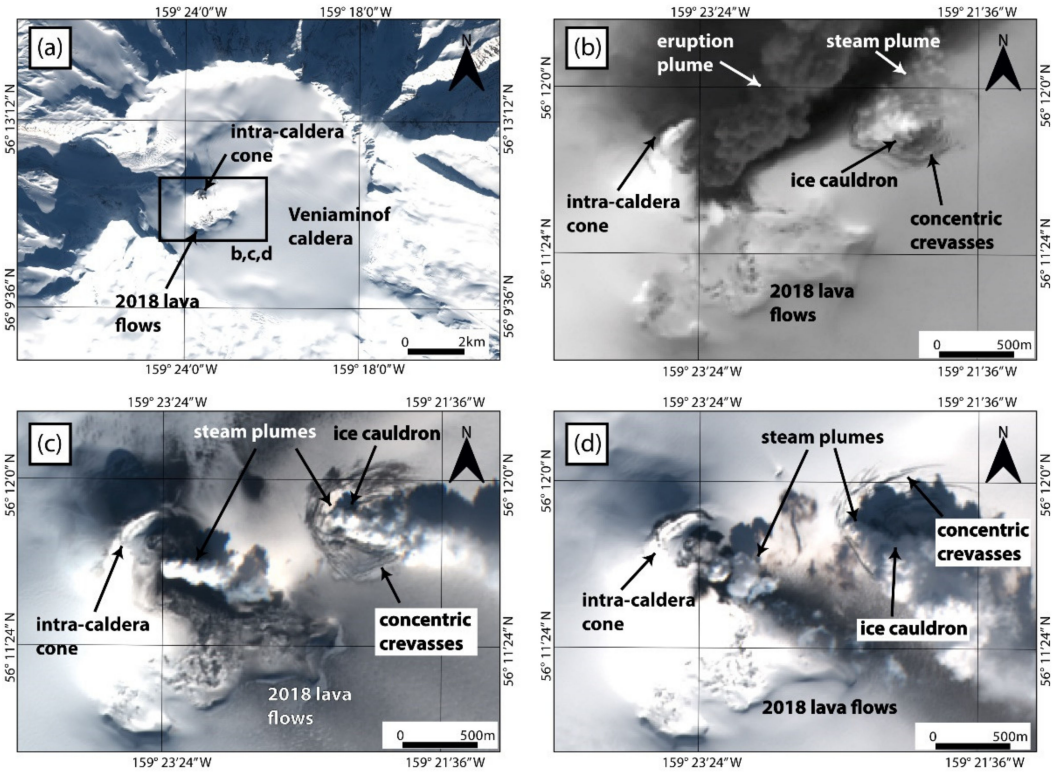

Figure 9. Recent volcanic activity on Mount Veniaminof: (**a**) Sentinel-2 true-colour overview image (10 m resolution) of the Veniaminof caldera from 04 February 2021 with an intra-caldera volcanic cone and (mostly snow-covered) 2018 lava flows; (**b**) Landsat-8 panchromatic image from 09 March 2021 (15 m resolution); (**c**,**d**) Sentinel-2 true-colour images from 11 March 2021 and 21 March 2021, respectively (both 10 m resolution). All subfigures (**b**–**d**) show an ice-cauldron and concentric crevasses related to the March 2021 active period as zoom-ins on the intra-caldera volcanic cone. Sentinel-2 data: Copernicus Sentinel data (2021).

6. Conclusions

Recent years have seen a rapid increase in freely available and commercial optical satellite images, covering large parts of the Earth. In this study, this global data source has been searched for evidence of volcanic impacts on glacier surface morphology, with a focus on well-known (documented) examples from the literature. The main conclusions are:

- The most common volcanic impact on glacier surface morphology observable in optical satellite imagery is the formation of ice cauldrons (i.e., depressions in the glacier surface). Depending on eruption energy/type, ice thickness and image resolution,

these cauldrons often appear as dark points/areas or as regions of distinct shadowing which contrast with the usually bright glacier surface.

- Other observable volcanic impacts on glacier surface morphology are widespread glacier crevassing, localized crevassing (e.g., adjacent to supraglacial lava flows or ice cauldrons) and ice bulging and fracturing due to subglacial dome growth.
- All volcanic impacts on glaciers investigated in this work are, to some degree, associated with crevassing, which is commonly visible as dark stripes on optical satellite images.
- The key challenge when using optical satellite images to study volcano-glacier interactions is the availability of cloud- and plume-free images with sufficient spatial and temporal resolution to observe (and monitor) the evolution of (sometimes) small-scale changes in glacier surface morphology. Useful imagery is increasingly available, but this does not help when observing historical eruptions, and the widespread use of commercial imagery is usually prohibitively expensive. Lower resolution imagery is often freely available, but identifying and interpreting changes in glacier morphology from these sources requires greater user experience.
- Overall, optical satellite imagery is a useful source for studying changes in glacier morphology caused by volcanic activity, particularly in remote and inaccessible parts of the world. This suggests that global-scale analysis and monitoring are possible. However, due to the costs of high-resolution (spatial and temporal) imagery, and the limited quantitative information that can be extracted, optical satellite imagery is best used in combination with DEMs, radar data, aerial images (derived from planes and/or drones) and ground-based observations.

Supplementary Materials: The following are available online at https://www.mdpi.com/article/10.3390/rs13173453/s1, Figure S1: title, Table S1, References [48–54] are cited in Supplementary Table S1. Table S1 presents the characteristics of all the glacier-clad volcanoes investigated in this study and presents the numbers of available/useful images for non-commercial satellite images (Sheet: "non-commercial satellite images") and the numbers of ordered commercial satellite image (Sheet: "commercial satellite images"). A third Sheet ("satellite specifications") details characteristics (spatial resolution and revisit time) of the respective satellite sources used.

Author Contributions: Conceptualization, I.B., B.E., E.S. and M.S.; methodology, M.D.M.; investigation, M.D.M.; writing—original draft preparation, M.D.M. and I.B.; writing—review and editing, B.E., E.S., M.S. and S.V.; supervision, I.B., B.E., E.S. M.S.; funding acquisition, I.B., B.E., E.S. and M.S. All authors have read and agreed to the published version of the manuscript.

Funding: This research and APC were funded by a Leverhulme Trust Research Project Grant: RPG-2019-093.

Data Availability Statement: Landsat and EO-1 data available from the USGS Earth Resources Observation and Science (EROS) Center; ASTER data are distributed by the Land Processes Distributed Active Archive Center (LP DAAC), located at USGS/EROS, Sioux Falls, SD. http://lpdaac.usgs.gov (accessed on 26 May 2021); Sentinel-2 data available from European Space Agency (ESA)/Copernicus; RapidEye and PlanetScope images obtained via planet: Planet Team (2017), Planet Application Program Interface: In Space for Life on Earth. San Francisco, CA. https://api.planet.com (accessed on 26 May 2021).

Conflicts of Interest: The authors declare no conflict of interest. The funders had no role in the design of the study; in the collection, analyses, or interpretation of data; in the writing of the manuscript, or in the decision to publish the results.

References

1. Smithsonian Institution. *Volcanoes of the World, Version 4.10.2*; Venzke, E., Ed.; Smithsonian Institution: Washington, DC, USA, 2013.
2. Edwards, B.; Kochtitzky, W.; Battersby, S. Global Mapping of Future Glaciovolcanism. *Glob. Planet. Chang.* **2020**, *195*, 103356. [CrossRef]
3. Pierson, T.C.; Janda, R.J.; Thouret, J.-C.; Borrero, C.A. Perturbation and Melting of Snow and Ice by the 13 November 1985 Eruption of Nevado Del Ruiz, Colombia, and Consequent Mobilization, Flow and Deposition of Lahars. *J. Volcanol. Geotherm. Res.* **1990**, *41*, 17–66. [CrossRef]
4. Gudmundsson, M.T.; Sigmundsson, F.; Björnsson, H. Ice–Volcano Interaction of the 1996 Gjálp Subglacial Eruption, Vatnajökull, Iceland. *Nature* **1997**, *389*, 954–957. [CrossRef]
5. Magnússon, E.; Gudmundsson, M.T.; Roberts, M.J.; Sigurðsson, G.; Höskuldsson, F.; Oddsson, B. Ice-Volcano Interactions during the 2010 Eyjafjallajökull Eruption, as Revealed by Airborne Imaging Radar: Ice-Volcano Interactions. *J. Geophys. Res. Solid Earth* **2012**, *117*. [CrossRef]
6. Bleick, H.A.; Coombs, M.L.; Cervelli, P.F.; Bull, K.F.; Wessels, R.L. Volcano–Ice Interactions Precursory to the 2009 Eruption of Redoubt Volcano, Alaska. *J. Volcanol. Geotherm. Res.* **2013**, *259*, 373–388. [CrossRef]
7. Oddsson, B.; Gudmundsson, M.T.; Edwards, B.R.; Thordarson, T.; Magnússon, E.; Sigurðsson, G. Subglacial Lava Propagation, Ice Melting and Heat Transfer during Emplacement of an Intermediate Lava Flow in the 2010 Eyjafjallajökull Eruption. *Bull. Volcanol.* **2016**, *78*, 48. [CrossRef]
8. Gudmundsson, M.T.; Thordarson, T.; Höskuldsson, Á.; Larsen, G.; Björnsson, H.; Prata, F.J.; Oddsson, B.; Magnússon, E.; Högnadóttir, T.; Petersen, G.N.; et al. Ash Generation and Distribution from the April–May 2010 Eruption of Eyjafjallajökull, Iceland. *Sci. Rep.* **2012**, *2*, 572. [CrossRef] [PubMed]
9. Smellie, J.L.; Edwards, B.R. *Glaciovolcanism on Earth and Mars: Products, Processes and Palaeoenvironmental Significance*; Cambridge University Press: Cambridge, UK, 2016; ISBN 978-1-139-76438-4.
10. Curtis, A.; Kyle, P. Methods for Mapping and Monitoring Global Glaciovolcanism. *J. Volcanol. Geotherm. Res.* **2017**, *333*, 134–144. [CrossRef]
11. Van Wyk de Vries, M.; Bingham, R.G.; Hein, A.S. A New Volcanic Province: An Inventory of Subglacial Volcanoes in West Antarctica. *Geol. Soc. Lond. Spec. Publ.* **2018**, *461*, 231–248. [CrossRef]
12. Major, J.J.; Newhall, C.G. Snow and Ice Perturbation during Historical Volcanic Eruptions and the Formation of Lahars and Floods: A Global Review. *Bull. Volcanol.* **1989**, *52*, 1–27. [CrossRef]
13. Barr, I.D.; Lynch, C.M.; Mullan, D.; De Siena, L.; Spagnolo, M. Volcanic Impacts on Modern Glaciers: A Global Synthesis. *Earth-Sci. Rev.* **2018**, *182*, 186–203. [CrossRef]
14. Rivera, A.; Bown, F.; Carrión, D.; Zenteno, P. Glacier Responses to Recent Volcanic Activity in Southern Chile. *Environ. Res. Lett.* **2012**, *7*, 014036. [CrossRef]
15. Reynolds, H.I.; Gudmundsson, M.T.; Högnadóttir, T.; Magnússon, E.; Pálsson, F. Subglacial Volcanic Activity above a Lateral Dyke Path during the 2014–2015 Bárdarbunga-Holuhraun Rifting Episode, Iceland. *Bull. Volcanol.* **2017**, *79*, 38. [CrossRef]
16. Muraviev, A.Y.; Muraviev, Y.D. Fluctuations of Glaciers of the Klyuchevskaya Group of Volcanoes in the 20th–21st Centuries. *Led I Sneg-Ice Snow* **2016**, *56*, 480–492. [CrossRef]
17. Barr, I.; Dokukin, M.; Kougkoulos, I.; Livingstone, S.; Lovell, H.; Małecki, J.; Muraviev, A. Using ArcticDEM to Analyse the Dimensions and Dynamics of Debris-Covered Glaciers in Kamchatka, Russia. *Geosciences* **2018**, *8*, 216. [CrossRef]
18. Reinthaler, J.; Paul, F.; Granados, H.D.; Rivera, A.; Huggel, C. Area Changes of Glaciers on Active Volcanoes in Latin America between 1986 and 2015 Observed from Multi-Temporal Satellite Imagery. *J. Glaciol.* **2019**, *65*, 542–556. [CrossRef]
19. Pfeffer, W.T.; Arendt, A.A.; Bliss, A.; Bolch, T.; Cogley, J.G.; Gardner, A.S.; Hagen, J.-O.; Hock, R.; Kaser, G.; Kienholz, C.; et al. The Randolph Glacier Inventory: A Globally Complete Inventory of Glaciers. *J. Glaciol.* **2014**, *60*, 537–552. [CrossRef]
20. Gudmundsson, M.T.; Sigmundsson, F.; Björnsson, H.; Högnadóttir, T. The 1996 Eruption at Gjálp, Vatnajökull Ice Cap, Iceland: Efficiency of Heat Transfer, Ice Deformation and Subglacial Water Pressure. *Bull. Volcanol.* **2004**, *66*, 46–65. [CrossRef]
21. Guðmundsson, M.S.T.; Högnadóttir, Þ.; Kristinsson, A.B.; Guðbjörnsson, S. Geothermal Activity in the Subglacial Katla Caldera, Iceland, 1999–2005, Studied with Radar Altimetry. *Ann. Glaciol.* **2007**, *45*, 66–72. [CrossRef]
22. Gudmundsson, A.; Lecoeur, N.; Mohajeri, N.; Thordarson, T. Dike Emplacement at Bardarbunga, Iceland, Induces Unusual Stress Changes, Caldera Deformation, and Earthquakes. *Bull. Volcanol.* **2014**, *76*, 869. [CrossRef]
23. Riel, B.; Milillo, P.; Simons, M.; Lundgren, P.; Kanamori, H.; Samsonov, S. The Collapse of Bárðarbunga Caldera, Iceland. *Geophys. J. Int.* **2015**, *202*, 446–453. [CrossRef]
24. Rossi, C.; Minet, C.; Fritz, T.; Eineder, M.; Bamler, R. Temporal Monitoring of Subglacial Volcanoes with TanDEM-X—Application to the 2014–2015 Eruption within the Bárðarbunga Volcanic System, Iceland. *Remote Sens. Environ.* **2016**, *181*, 186–197. [CrossRef]
25. Farinotti, D. A Consensus Estimate for the Ice Thickness Distribution of All Glaciers on Earth. *Nat. Geosci.* **2019**, *12*, 168–173. [CrossRef]
26. Björnsson, H.; Guðmundsson, M.T. Surface and Bedrock Topography of Mýrdalsjökull, Iceland: The Katla Caldera, Eruption Sites and Routes of Jökulhlaups. *Jökull* **2000**, *49*, 29–46.
27. Strachan, S.M. A Geophysical Investigation of the Eyjafjallajökull Glaciovolcanic System, South Iceland, Using Radio Echo Sounding. Ph.D. Thesis, University of Edingburgh, Edingburgh, UK, 2001.

28. Trabant, D.C.; Hawkins, D.B. Glacier Ice-Volume Modeling and Glacier Volumes on Redoubt Volcano, Alaska. *Water-Resour. Investig.* **1997**, *97*, 4187.
29. Schaefer, J.R. The 2009 Eruption of Redoubt Volcano, Alaska. *Rep. Investig.* **2011**, *5*, 45.
30. McGimsey, R.G.; Neal, C.A.; Girina, O.A.; Chibisova, M.V.; Rybin, A.V. 2009 Volcanic Activity in Alaska, Kamchatka, and the Kurile Islands—Summary of Events and Response of the Alaska Volcano Observatory. 2014. Available online: http://repository.geologyscience.ru/handle/123456789/1652 (accessed on 24 February 2021).
31. Amigo, Á.; Silva, C.; Orozo, G.; Bertin, D.; Lara, L.E. La Crisis Eruptiva Del Volcán Hudson Durante Octubre-Noviembre 2011. *XII Congr. Geol. Chil. Antofagasta* **2012**, 457–459.
32. Welch, B.C.; Dwyer, K.; Helgen, M.; Waythomas, C.F.; Jacobel, R.W. Geophysical Survey of the Intra-Caldera Icefield of Mt Veniaminof, Alaska. *Ann. Glaciol.* **2007**, *45*, 58–65. [CrossRef]
33. Global Volcanism Program, 2021. Report on Veniaminof (United States). In *Weekly Volcanic Activity Report*; 03 March-06 April 2021; Smithsonian Institution: Washington, DC, USA; US Geological Survey: Reston, VA, USA, 2021.
34. Patrick, M.R.; Smellie, J.L.; Harris, A.J.L.; Wright, R.; Dean, K.; Izbekov, P.; Garbeil, H.; Pilger, E. First Recorded Eruption of Mount Belinda Volcano (Montagu Island), South Sandwich Islands. *Bull. Volcanol.* **2005**, *67*, 415–422. [CrossRef]
35. Patrick, M.R.; Smellie, J.L. Synthesis A Spaceborne Inventory of Volcanic Activity in Antarctica and Southern Oceans, 2000–2010. *Antarct. Sci.* **2013**, *25*, 475–500. [CrossRef]
36. Schilling, S.P.; Carrara, P.E.; Thompson, R.A.; Iwatsubo, E.Y. Posteruption Glacier Development within the Crater of Mount St. Helens, Washington, USA. *Quat. Res.* **2004**, *61*, 325–329. [CrossRef]
37. Walder, J.S.; LaHusen, R.G.; Vallance, J.W.; Schilling, S.P. Emplacement of a Silicic Lava Dome through a Crater Glacier: Mount St Helens, 2004–2006. *Ann. Glaciol.* **2007**, *45*, 14–20. [CrossRef]
38. Walder, J.S.; Schilling, S.P.; Vallance, J.W.; LaHusen, R.G. *A Volcano Rekindled: The Renewed Eruption of Mount St. Helens, 2004–2006*; Sherrod, D.R., Scott, W.E., Stauffer, P.H., Eds.; Professional paper; U.S. Dept. of the Interior; U.S. Geological Survey: Reston, VA, USA, 2008; pp. 257–276, ISBN 978-1-4113-2401-5.
39. Elliott, J.R.; Walters, R.J.; Wright, T.J. The Role of Space-Based Observation in Understanding and Responding to Active Tectonics and Earthquakes. *Nat. Commun.* **2016**, *7*, 13844. [CrossRef]
40. Gorelick, N.; Hancher, M.; Dixon, M.; Ilyushchenko, S.; Thau, D.; Moore, R. Google Earth Engine: Planetary-Scale Geospatial Analysis for Everyone. *Remote Sens. Environ.* **2017**, *202*, 18–27. [CrossRef]
41. Krimmel, R.M.; Meier, M.F. Glacier Applications of Erts Images. *J. Glaciol.* **1975**, *15*, 391–402. [CrossRef]
42. Glasser, N.F.; Scambos, T.A. A Structural Glaciological Analysis of the 2002 Larsen B Ice-Shelf Collapse. *J. Glaciol.* **2008**, *54*, 3–16. [CrossRef]
43. Colgan, W.; Steffen, K.; McLamb, W.S.; Abdalati, W.; Rajaram, H.; Motyka, R.; Phillips, T.; Anderson, R. An Increase in Crevasse Extent, West Greenland: Hydrologic Implications: Increased Crevasse Extent West Greenland. *Geophys. Res. Lett.* **2011**, *38*. [CrossRef]
44. Colgan, W.; Rajaram, H.; Abdalati, W.; McCutchan, C.; Mottram, R.; Moussavi, M.S.; Grigsby, S. Glacier Crevasses: Observations, Models, and Mass Balance Implications: Glacier Crevasses. *Rev. Geophys.* **2016**, *54*, 119–161. [CrossRef]
45. Rivera, A.; Cawkwell, F.; Wendt, A.; Zamora, R. Mapping Blue-Ice Areas and Crevasses in West Antarctica Using ASTER Images, GPS, and Radar Measurements. In *Global Land Ice Measurements from Space*; Kargel, J.S., Leonard, G.J., Bishop, M.P., Kääb, A., Raup, B.H., Eds.; Springer: Berlin/Heidelberg, Germany, 2014; pp. 743–757, ISBN 978-3-540-79817-0.
46. Bhardwaj, A.; Sam, L.; Singh, S.; Kumar, R. Automated Detection and Temporal Monitoring of Crevasses Using Remote Sensing and Their Implications for Glacier Dynamics. *Ann. Glaciol.* **2016**, *57*, 81–91. [CrossRef]
47. Scharrer, K.; Spieler, O.; Mayer, C.; Münzer, U. Imprints of Sub-Glacial Volcanic Activity on a Glacier Surface—SAR Study of Katla Volcano, Iceland. *Bull. Volcanol.* **2008**, *70*, 495–506. [CrossRef]
48. Delgado, F.; Pritchard, M.; Lohman, R.; Naranjo, J.A. The 2011 Hudson Volcano Eruption (Southern Andes, Chile): Pre-Eruptive Inflation and Hotspots Observed with InSAR and Thermal Imagery. *Bull. Volcanol.* **2014**, *76*, 815. [CrossRef]
49. Brugman, M.M.; Post, A. Effects of Volcanism on the Glaciers of Mount St. Helens. *Geol. Surv. Circ.* **1981**, *850*, 1–11.
50. Granados, H.D.; Miranda, P.J.; Núñez, G.C.; Alzate, B.P.; Mothes, P.; Roa, H.M.; Cáceres Correa, B.E.; Ramos, J.C. Hazards at Ice-Clad Volcanoes. In *Snow and Ice-Related Hazards, Risks and Disasters*; Elsevier: Amsterdam, The Netherlands, 2015; pp. 607–646, ISBN 978-0-12-394849-6.
51. Monsalve, M.L.; Pulgarín, B.A.; Mojica, J.; Santacoloma, C.C.; Cardona, C.E. Interpretación de la Actividad Eruptiva del Volcán Nevado del Huila (Colombia), 2007–2009: Análisis de Componentes de Materiales Emitidos. *Bol. Geol.* **2011**, *33*, 73–93.
52. Púlgarin, B.; Cardona, C.E.; Santacoloma, C.C.; Agudelo, A.; Calvache, M.; Monsalve, M.L. Erupciones del volcan Nevado del Huila (Colombia) en febrero y abril de 2007 y cambios en su masa glaciar. In *Glaciares, Nieves y Hielos de America Latina: Cambio Climatico y Amenezas Glaciares*; Lopez, C.D., Ramirez, J., Eds.; INGEOMINAS: Bogotá, Colombia, 2010; pp. 279–305.
53. Naranjo, J.L.; Sigurdsson, H.; Carey, S.N.; Fritz, W. Eruption of the Nevado Del Ruiz Volcano, Colombia, On 13 November 1985: Tephra Fall and Lahars. *Science* **1986**, *233*, 961–963. [CrossRef] [PubMed]
54. Esri. "World Continents" [basemap]. Scale not Given. "World Continents." Centre d'enseignement Saint-Joseph de Chimay. 31 August 2017. Available online: https://hub.arcgis.com/datasets/CESJ::world-continents/explore?location=-0.076095%2C0.000000%2C1.00 (accessed on 10 March 2021).